UNIVERSITÀ
DEGLI STUDI
DI PADOVA

Head Office: Università degli Studi di Padova

Department of Chemical Sciences

Ph.D. COURSE IN: Science and Engineering of Materials and Nanostructures

SERIES: XXXI

Crashing Flatland: Defective and Hybrid 2D-Materials for (Electro)Catalysis

Coordinator: Ch.mo Prof. Giovanni Mattei

Supervisor: Ch.mo Prof. Gaetano Granozzi

Ph.D. Student: Dario Mosconi

Index

Abstract

This Ph.D. project is aimed to discover new strategies to develop materials to utilize in the fields of *Green Energy* and *Green Chemistry* and it was directed at the application of 2D Materials in particular. This thesis is divided into five main chapters where we presented five exemplary systems in which we focused our attention on different aspects of materials design. Each chapter comprises an introduction and a conclusion section, in which we tried to go into the details of each targeted application and of the specific design strategy employed. However, at the beginning and at the end of the thesis, the reader can find an Introduction and a Conclusion section where we tried to collocate the goals and challenges of this work within a broader context of materials science and catalysis/electrocatalysis.

In our studies in the *Green Energy* area, we focused on the use of MoS_2-based materials in water splitting cathodic half-reaction in order to obtain the best possible performance in hydrogen generation in different conditions. To do that, different strategies were developed to drive the original material to adapt to specific application. In detail, in Chapter Two we investigated the design of three-dimensional MoS_2 structures doped with different amount of Ni in order to activate MoS_2 for the Hydrogen Evolution Reaction (HER) performed in alkaline environment, which typically hinder this reaction. We carried out an extensive structural characterization in order to establish the role of each type of active sites formed on the material in the HER activity and kinetics. In Chapter Three, we developed an electrodeposition method for preparing amorphous MoS_2/Ag_2S hybrid using recycled DVD as the support; this revealed as a viable opportunity to turn an abundant waste into an added-value material. After a suitable investigation to understand what kind of material was formed upon electrodeposition, MoS_2/Ag_2S/DVD was tested for HER in acidic medium. In Chapter Four another kind of hybrid was prepared by designing a one-pot solvothermal synthesis of $MoS_{2(1-x)}Se_{2x}$ nanosheets grown on N-doped reduced Graphene Oxide (N-rGO). The goal was the control of the optoelectronic properties of the final material, since the combination of $MoS_{2(1-x)}Se_{2x}$ and N-rGO allows to form p-n nanojunctions, which induce an enhancement of HER activity upon illumination with visible light. Then we used different techniques to prove what was the best Se:S ratio to optimize both the absolute performances in HER and the enhancement upon light irradiation.

Regarding *Green Chemistry* area, we used Graphene Acid (GA) as starting material and we exploited its uniform surface functionalization to prepare materials for heterogeneous catalysis for different reactions, comparing them with the benchmark Graphene Oxide (GO), modified with the same protocol. In Chapter Five, we synthesized a heterogeneous catalyst by covalently grafting Ferrocene (Fc) moieties to –COOH surface groups of GA and GO. The resulting Fc-modified graphene derivatives have been tested as heterogeneous catalysts for the C-H insertion of aryl diazonium salts into several arene substrates. The tests revealed a strong influence of the support, which we could attribute the intrinsic properties of GA. In Chapter Six, we have grown Pd nanoparticles on GA to prepare a catalyst for Suzuki-Miyaura cross coupling reaction. We have studied the effect of surface functionalization on the nanoparticles formation process and on the derived capability on the controlling the size distribution. The catalysts were tested in Suzuki cross coupling in green conditions and we could highlight the influence of nanoparticles size on activity. Moreover, we studied the same catalysts also for boronic acid homocoupling reaction, that can provide similar final products, but in a more atom economically way.

Chapter One:

Introduction

1.1 Introduction

Nowadays, energy is one of the main challenge of our society. Indeed, the continuous population raising, the colossal economy growth of several countries and the more and more energy demanding lifestyles are severely struggling the actual energetic policy based on fossil fuels. Moreover, also the way we manage the energetic resources is under debate, because, even if the actual energetic resources based on fossil fuels would be enough, the consequences of their use are devastating the world welfare by increasing pollution and global warming. The transition to a more sustainable energetic policy is a dramatically urgent issue that the whole scientific community is addressing in a common multidisciplinary way. In this *scenario*, materials scientists, chemists and physicists are in the forefront, and main efforts are currently focused both on renewable primary energy sources, sustainable methods for energy conversion and more efficient ways to manage the energy services (see scheme below). The International Energy Agency (IEA) yearly releases the World Energy Outlook (WEO), which can be considered the main reference for the world energetic policy.[1]

A schematic diagram illustrating the concept of conversion of primary energy sources into energy services

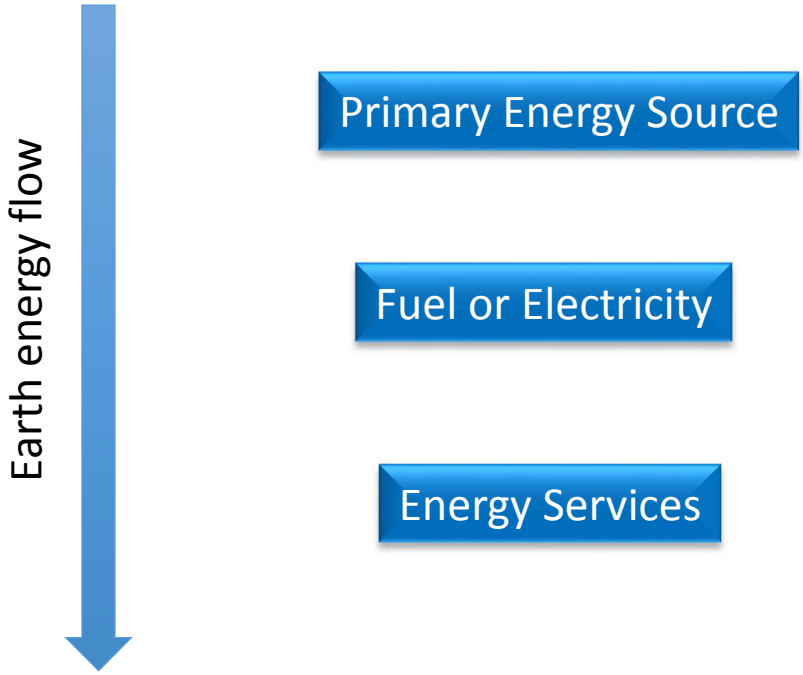

Switching to renewable energy sources (i.e. energy that comes from resources which are naturally replenished on a human timescale) is the unique perspective answer that scientific community has found as effective to find a solution to the mentioned world problems. Especially in the last decade, an extraordinary amount of resources have been spent in order to find viable substitutes to fossil fuels. As already anticipated by Jules Verne in its prophetic fantasy book "The Mysterious Island" (1874, where he says that *water will be the coal of the future*), water is the most abundant source for hydrogen, and molecular hydrogen is actually retained the most promising alternative fuel, since its reaction with oxygen provides clean energy, being

water the unique exhaust product. In this context, a sustainable, clean and cost-effective way to produce hydrogen is required to make the so called *hydrogen economy* feasible.[2,3]

The most common method to produce large quantities of hydrogen, *i.e.* steam reforming of methane or light alcohols, is neither clean nor sustainable. In addition, the final product contains small amounts of CO that constitutes a poison for the Pt-based catalysts used in Fuel Cells (FCs), limiting their lifecycles.[4]

Electrolyzers, based on the electrocatalytic water splitting (WS), are emerging as the best devices to obtain clean hydrogen through hydrogen evolution reaction (HER).[5] However, to be exploitable, WS must be boosted by suitable electrocatalysts. Consequently, preparation and optimization of new electrocatalysts for sustainable electrochemical conversion devices is fundamental to bring innovative solution from laboratory to industrial scale and improve the quantity and the quality of the energy we use.

In this context, Materials Science plays a pivotal role, since it can provide an effective approach to prepare and study completely new materials and all the related properties, up to applications. Graphene is the perfect example of this roadmap: it completely shook up scientific community 15 years ago and now it is progressively going toward commercial productions and applications. As reported in *Nature Nanotechnology* for the 10th anniversary from the seminal work of Geim and Novoselov,[6–8] in 2004-2014 decade, from the first isolation of graphene from graphite by using adhesive tape, graphene has been prepared by many different methods (see Figure 1.1) and graphene sheets are now produced in hundreds of tonnes and tens of thousands of square metres. In 2009, only a few USA-based small start-up companies were making large volumes of small graphene sheets. In the following five years, tens of graphene manufacturing companies have sprung up all over the world, which produce not only micrometric graphene sheets but also large-area, high-quality graphene films on an industrial scale. In particular, the production industry of graphene materials in China has been developing very rapidly, and its total annual production capacity of small graphene sheets and graphene films exceeds 400 tonnes and 110,000 m^2, respectively, demonstrating how the drastic approach above mentioned can kick off the business of companies.

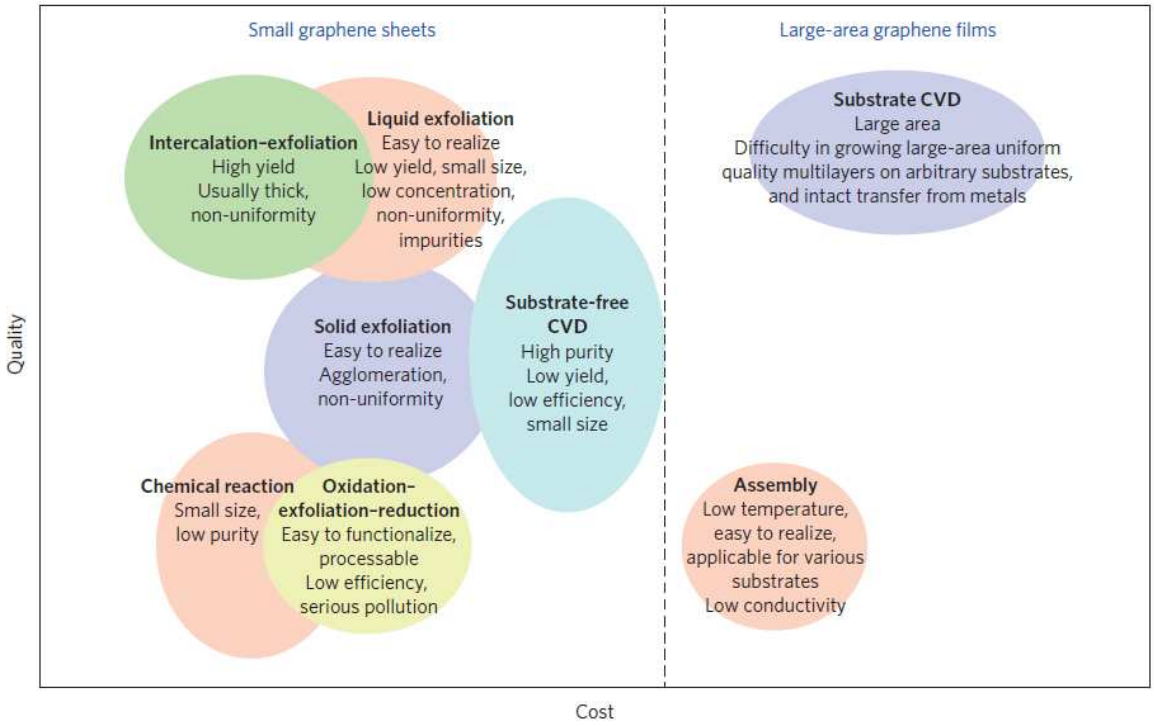

Figure 1.1. Comparison of the quality and cost of graphene products manufactured by different methods. Reproduced from Ref. 4.

1.2 Motivations of Ph.D. Project

Considering the unsustainable energetic situation, the development of innovative materials to facilitate the transition to fully sustainable energetics is necessary. Generally speaking, the most popular definition of sustainability is that from the Brundtland Report (Our Common Future, by the World Commission on Environment and Development, 1987, p. 43.) which says:

"Sustainable development is development that meets the needs of the present without compromising the ability of future generations to meet their own needs."

This very general definition of sustainability can be supported by dividing it in three categories:

- *Environmental sustainability* is the ability to maintain rates of renewable resource harvest, pollution creation, and non-renewable resource depletion that can be continued indefinitely;
- *Economic sustainability* is the ability to support a defined level of economic production indefinitely;
- *Social sustainability* is the ability of a social system, such as a country, to function at a defined level of social well-being indefinitely.

This Ph.D. project clearly is aimed at large at developing a *Green Economy*, whose general definition is: *an economy that aims at reducing environmental risks and ecological scarcities, and that aims for sustainable development without degrading the environment.* More specifically the project can be fitted in the sub-fields of *Green Energy* and *Green Chemistry*.

1.2.1 Green Energy: Fuel Cells and Electrochemical Water Splitting

The concept of *Green Energy* is as simple in theory as difficult in practice, and it is made by three key components:

- ***Production***: the way we convert the primary sources for our needs. For example, if we produce electricity *via* combustion of coal, it may be effective but surely not *green* because the byproducts of the reaction will pollute seriously the atmosphere, harming people and environment. So a *green* energy production should be effective without generating dangerous byproducts. Renewable energy sources are the best primary sources since they respect our future because they are naturally replenished on a human timescale, such as sunlight, wind, rain, tides, waves, and geothermal heat.[9]
- ***Utilization***: it is related to the efficiency and the energy saving of the devices needed by our life-styles. Being at the moment renewable sources still more expensive than fossil ones (there is a great debate on this point), it is crucial anyway to use the energy we produce in the most effective way.
- ***Environmental Impact***: if the energy production should not impact on the environment, devices that consume that energy should not do it as well. This component is strongly related to utilization, since typically energy saving induce a lower environmental impact (e.g. a car that burns less fuel will release less CO_x into the atmosphere). In this context, recycling plays a pivotal role since it provides a value to wastes, allowing to save primary resources. The way to consider properly the balance is considering the whole life-cycle assessment of the products and production methods.

In the last two decades, the scientific community is making great efforts to find out realistic and scalable solutions to effectively substitute fossil fuels and conversion energy systems (e.g. fuel cells, FCs), both for stationary and mobile applications. Molecular hydrogen is nowadays retained the most promising alternative fuel since its reaction with oxygen provides clean energy, being water the unique exhaust product. Indeed, FCs work according to the following half-reactions, that are Oxygen Reduction Reaction (ORR) at the cathode and Hydrogen Oxidation Reaction (HOR) at the anode:

$$O_2 + 4H_3O^+ + 4e^- \rightarrow 2H_2O$$

$$2H_2 \rightarrow 4H_3O^+ + 4e^-$$

Generally, ORR is the main challenging reaction, due to the difficulty of transferring simultaneously 4 electrons from the catalyst to the adsorbed species, causing kinetics hindrance. In the ORR process, Pt-based catalysts are the benchmarks for what concern peak performances, but, having low tolerance to byproducts such as methanol/CO, they undergo to a limited operating life (durability), highlighting the urgency for more durable ORR electrocatalysts.[10–12] In addition, platinum group metals (PGMs) are nowadays considered as critical raw materials and their replacement is needed as well.[13,14]

In this context, a sustainable, clean and cost-effective way to produce hydrogen is required to put the basis for the already mentioned *hydrogen economy*[15]. Electrolyzers, based on the electrocatalytic WS, are nowadays commercial devices (still in the phase of optimization) to obtain clean hydrogen through HER at the cathode,[5] giving as "byproduct" molecular O_2 at the counter electrode through Oxygen Evolution Reaction (OER). Therefore, the ideal technological loop consists of WS in an electrolyzer through the HER and

OER for fuel generation, followed by power generation through the ORR and HOR in fuel cells, giving *green* solutions for energy production and utilization (see Figure 1.2) .

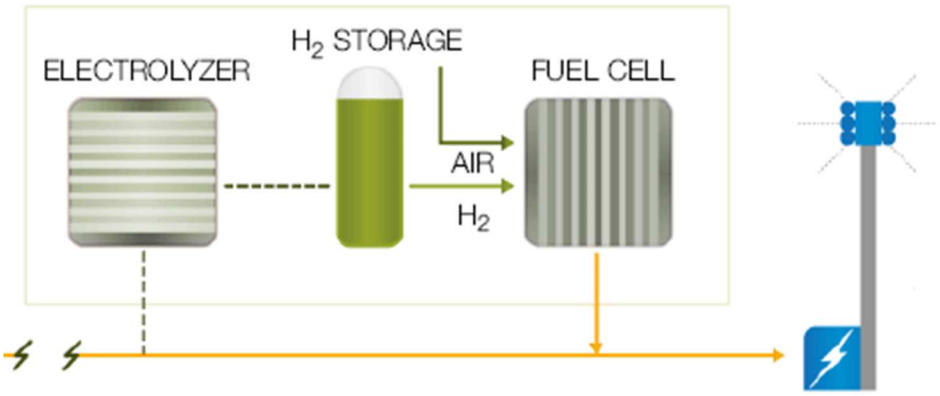

Figure 1.2. Scheme of ideal energy loop based on hydrogen generation/storage/utilization.

The overall electrocatalytic reaction of WS is very simple in principle:

$$Overall: \qquad H_2O \rightarrow H_2 + O_2 \qquad \Delta G = 1.23\ V$$

Where ΔG is equilibrium for water electrolysis (i.e. the thermodynamical limit), therefore in ideal conditions with ideal electrodes WS could be achieved by applying a small overpotential above 1.23 V. But kinetics can complicate such a simplicity.

The overall reaction can be split in two half-reactions, HER is the cathodic process, whereas OER is the anodic one. Even if overall reaction remain the same, half-reactions are pH-dependent because of the change of species to react in the electrolyte.

In alkaline conditions (pH 14) the corresponding half-reactions are:[16]

$$4H_2O + 4e^- \rightarrow 2H_2 + 4OH^- \qquad E_c^\circ = -0.826\ V$$

$$4OH^- \rightarrow O_2 + 2H_2O + 4e^- \qquad E_a^\circ = 0.404\ V$$

where $E°_c$ and $E°_a$ are the equilibrium half-cell potentials at standard conditions of 1 atm and 25 °C.

In neutral solutions (pH 7):

$$4H_2O + 4e^- \rightarrow 2H_2 + 4OH^- \qquad E_c^\circ = -0.413\ V$$

$$2H_2O \rightarrow O_2 + 4H_3O^+ + 4e^- \qquad E_a^\circ = 0.817\ V$$

In acidic electrolyte (pH 0):

$$4H_3O^+ + 4e^- \rightarrow 2H_2 \qquad E_c^\circ = 0.00\ V$$

$$2H_2O \rightarrow O_2 + 4H_3O^+ + 4e^- \qquad E_a^\circ = 1.23\ V$$

Actually, the main problem of WS is water itself, because of its stability. Indeed, water electrolysis is relatively favourable in acid and alkaline conditions due to the presence of deprotonated water molecules available for OER in alkaline solutions or protonated water molecules for HER in acid solutions. Therefore, in acidic

environment HER would be favoured because the active species would be H_3O^+ while OER is slowed down and *viceversa* in basic conditions. This also explains why water electrolysis in neutral condition is kinetically more difficult.

However, since the OER is kinetically more critical than HER, the complete WS has not the same overall efficiency in acid or base. Indeed, OER has to go through a kinetically sluggish 4 electrons process, being unfavourable for removing of four electrons to form O=O bond.[17] Therefore, the tendency is to optimize the electrocatalysts for WS in basic conditions. So, to summarize, the more urgent reactions to study are OER and HER in alkaline environment to achieve a feasible large-scale WS. However, HER in acidic electrolyte has to be considered as well, since, in principle, is possible to achieve excellent H_2 generation, but substitution of rare and expensive PGMs is mandatory in order to enlarge the production scale.

At the moment, noble metals are the benchmarks for these reactions, in particular Pt is the reference for HER, while Ir- and Ru-based oxides are for the OER. However, as already mentioned, there is a strong issue in maintaining PGMs at the basis of sustainable electrocatalytic processes. This has given rise to a global race for developing innovative electrocatalysts based on non-PGMs materials, which would be also difficult to manage in acidic conditions.

In the present thesis we are focusing on 2D materials for WS. As will be deeper discussed below, these materials, compared to others such as nanowires or nanoparticles, show two important features when considered as electrocatalysts: they are tunable and uniformly expose lattice plane while having unique electronic properties.[18] Moreover, 2D materials have significantly high specific surface areas and robust mechanical properties, ideal properties for platforms for practical applications.[19] For instance, most layered materials are easily fabricated into freestanding films with uniform thickness.[20,21] Compared to powdered catalysts, freestanding electrodes are much more suitable for actual utilization as they can prevent catalyst agglomeration and exfoliation from supports.[22] In section 1.3 we will outline the current status of such materials, particularly aiming at their use in electrocatalysis and catalysis.

1.2.2 Green Chemistry: Catalyst Heterogenization

Green Chemistry is a branch of chemistry and chemical engineering that regards the design of chemical reactions and processes with the goal of lowering the environmental impact of chemistry and applies across the life cycle of a chemical product, including its design, manufacture, use, and ultimate disposal. Clearly, this process goes through the utilization of safer and environmental friendly chemicals and the reduction or the elimination of hazardous byproducts.[23]

Moreover, the use of renewable material feedstocks and energy sources and the design of energy efficient processes are required. This fact becomes more evident considering that one of the largest energy demands of our society is due to the production of fine chemicals, which accounts for approximately 25% of industrial energy consumption.[24]

Developed by Paul Anastas and John Warner,[25] the following list of 12 principles outlines an early conception of what would make a greener chemical, process, or product:

1. *Prevention*

   It is better to prevent waste than to treat or clean up waste after it has been created.

2. *Atom Economy*

   Synthetic methods should be designed to maximize the incorporation of all materials used in the process into the final product.

3. *Less Hazardous Chemical Syntheses*

   Wherever practicable, synthetic methods should be designed to use and generate substances that possess little or no toxicity to human health and the environment.

4. *Designing Safer Chemicals*

   Chemical products should be designed to affect their desired function while minimizing their toxicity.

5. *Safer Solvents and Auxiliaries*

   The use of auxiliary substances (e.g., solvents, separation agents, etc.) should be made unnecessary wherever possible and innocuous when used.

6. *Design for Energy Efficiency*

   Energy requirements of chemical processes should be recognized for their environmental and economic impacts and should be minimized. If possible, synthetic methods should be conducted at ambient temperature and pressure.

7. *Use of Renewable Feedstocks*

   A raw material or feedstock should be renewable rather than depleting whenever technically and economically practicable.

8. *Reduce Derivatives*

   Unnecessary derivatization (use of blocking groups, protection/deprotection, temporary modification of physical/chemical processes) should be minimized or avoided if possible, because such steps require additional reagents and can generate waste.

9. *Catalysis*

   Catalytic reagents (as selective as possible) are superior to stoichiometric reagents.

10. *Design for Degradation*

    Chemical products should be designed so that at the end of their function they break down into innocuous degradation products and do not persist in the environment.

11. *Real-time analysis for Pollution Prevention*

    Analytical methodologies need to be further developed to allow for real-time, in-process monitoring and control prior to the formation of hazardous substances.

12. *Inherently Safer Chemistry for Accident Prevention*

    Substances and the form of a substance used in a chemical process should be chosen to minimize the potential for chemical accidents, including releases, explosions, and fires.

As it can be observed, the 9th principle said that the utilization of catalysts is welcome, since typically catalysed reactions provides higher yield and selectivity. Often the best-performing catalysts are homogeneous, meaning that are in the same phase of the reactants. The classical example are soluble metal complexes, whose catalytic sites are all accessible and they grant the possibility to tune the chemo-, regio- and enantioselectivity of the catalyst.[26] Moreover, homogeneous catalysts have a number of other advantages such as better yields, and easy optimization of catalytic systems by modification of ligand and metals. This catalyst category is extensively used in a number of commercial applications, but the problematic separation from the final product creates economic and environmental barriers to broadening their scope. Despite their advantages and their wide use, many homogeneous catalytic systems have not been commercialized because of the difficulty encountered in separating the catalyst from the final reaction product. Removal of trace amounts of catalyst from the target chemical is crucial since metal contamination is strongly regulated, especially in pharmaceutical industry. Even with the extensive and careful use of various techniques such as distillation, chromatography, or extraction, removal of trace amounts of catalyst remains a challenge. Evidently, the contamination issue is in contrast with the *Green Chemistry* policy and the necessity of further purification steps as well generates more wastes and increases the costs of the process. Moreover, homogenous catalyst are usually not reusable because of the recovery issues, which is cause of further increment of costs and resources utilization.

To overcome the separation problems in homogeneous catalysis, chemists and engineers have investigated a wide range of strategies and the use of heterogeneous catalyst systems looks as the best logical solution.[27–29] The common structural feature of these materials is the anchoring of the catalytic moiety on a scaffold that must have a good stability (thermal and chemical) and high surface area to ensure enough contact between active species and reactants (e.g. mesoporous silica scaffold).[30,31] Anchoring can be achieved by covalent binding of the molecules or by simple adsorption, but covalent anchoring is clearly more robust and it can withstand harsh reaction conditions and it allows reusing the material several times. Although attempts have been made to make all active sites on solid supports accessible for reaction, allowing rates and selectivities comparable to those obtained with homogeneous catalysts, only sites on the surface are available for catalysis, which decreases the overall reactivity of the catalyst system. Therefore, the use of scaffolds that grant the best accessibility to catalytic centres is a smart route to push the application of heterogeneous catalysts.

In this view, 2D-Materials are very appealing just because of their bidimensional nature, which makes coinciding their surface chemistry with the bulk one and consequently making all the catalytic centres equally available. For instance, graphene combines this advantage to the typical characteristics required for a catalyst support such mechanical strength, tunable porosity and chemical inertness in most reaction media.[32] Moreover, as will be discussed in section 1.3, graphene exhibits properties like high electronic[33] and thermal conductivity,[34–38] that can boost catalytic processes. A large variety of graphene derivatives has been developed recently, offering a large gamut of materials characterized by an extremely rich surface chemistry, which can be exploited for advanced functionalization protocols. Among these, graphene oxide (GO) is the most widely used, given its easy and scalable synthesis and because of plenty of surface oxygenated groups (i.e. tertiary alcohols, epoxide, carboxyl and carbonyl groups), [39] but other scaffold have been developed as well.

1.3 Evolution of 2D Materials and State of the Art

1.3.1 First Generation of Graphene: Aiming the Perfection

The conceptual evolution on graphene was so intense and rich of extraordinary ideas that there have been three generations of graphene related materials with different properties, aims and purposes in less than 15 years. Indeed graphene started to be discussed theoretically since the 1947 by Wallace,[40] but it took almost 60 years to isolate the first sample to characterize experimentally. At the discovery of *Flatland,* the outstanding properties of graphene came out instantly: for instance, high optical transparency (*ca*. 98% of transmitted light in the visible range),[41,42] superior and anisotropic thermal conductivity (up to 2500 $W \cdot m^{-1} \cdot K^{-1}$)[34–38] and the highest mechanical strength ever measured (1 TPa Young's modulus and 130.5 GPa tensile strength)[43] made immediately appear graphene as a revolutionary material. Nevertheless, the more intriguing properties were uncovered when the electronic structure was studied. According to its band structure, graphene was found to be a zero-gap semiconductor, since valence and conduction bands meet at the six *K*-points of the Brillouin zone, generating the so-called Dirac cones structure.[6,33,44–47] Thanks to the linear dispersion relation, graphene exhibits a huge in-plane carrier mobility, because fermions results to be substantially massless, allowing the hole and electron mobility to exceed 15000 $cm^2 \cdot V^{-1} \cdot s^{-1}$.[33] The combination of these properties made the material appearing as ideal for application in microelectronics, such as fabrication of ultrathin field effect transistors, inducing physics community to take the lead of graphene research main lines. Indeed, after finding that the dominant scattering mechanism is the one from defects and that the intrinsic limits of room temperature mobility is $2 \cdot 10^5\ cm^2 \cdot V^{-1} \cdot s^{-1}$, the research focused on scaling up the production and on obtaining the most perfect graphene possible, with the aim of getting as near as possible to the hypothetical limit.[48]

1.3.2 Second Generation of Graphene: Chemically Modified and 3D-Structured Graphene

From the chemical point of view, defects are high-energy spots in the material scaffold that may be exploited to catalyse chemical or electrochemical reactions. Moreover, the theoretical surface area of monolayer graphene was calculated to be 2630 m^2/g, a huge value that, combined with graphene electronic properties, makes this material an ideal support for catalysts and other materials to use in energy conversion and storage.[49] Therefore, Material Scientists began a parallel study (that is Second Generation Graphene) on methods to prepare graphene in suitable quantities to use in the typical wet chemistry procedures. The following natural step was to insert intentionally defects in controlled ways in order to tune graphene properties with the aim, in this case, to enhance the catalytic properties.[50] These studies allowed to develop a wide gamut of techniques to obtain larger and more processable quantities of modified graphene, with tunable properties and higher defectivity. Roughly, materials that came out from these second research branch may be divided in two main categories:

- Chemical Modified Graphene (CMG), that are materials made of graphene sheets modified by doping, so with relatively small quantity of substitutional heteroatoms (B, N, S, P,…) or even decorated with different functional groups;[51–53]
- 3D Graphene Architectures (3DG), where graphene or CMG morphology is controlled in order to obtain a three-dimensional network, for instance to expose higher active area, to activate some

catalytic sites or in general to use as base for more complex hybrids.[54]

Surely the most popular CMG is Graphene Oxide (GO): being typically produced by modified Hummer's method,[55] that consists of treating graphite with strongly oxidizing agents (such as H_2SO_4, H_3PO_4, H_2O_2 and $KMnO_4$), GO usually shows different functional groups on its surface, like epoxides, hydroxyl, carbonyl and carboxylic acid moieties.[56] The presence of these oxygenated groups makes graphene sheets much more processable, since the increased polarity allows to suspend GO in polar solvent such as water, N,N-dimethylformamide (DMF) and N-methylpyrrolidone (NMP). The defectivity of GO tends to hamper the properties promoted by crystallinity (*i.e.* electrical conductivity), but they can be restored by reducing GO to reduced-GO (rGO) following several different methods (chemical, electrochemical or thermal). For this flexibility, GO actually became the benchmark for graphene-like materials. The main disadvantage of GO is however is ill-defined structure and inhomogeneity.

Very recently, another surface functionalized CMG, conceptually similar to GO, has been prepared, the so-called Graphene Acid (GA), synthesized by Otyepka and coworkers.[57] GA is prepared from commercial fluorographite, whose C-F bonds undergo to nucleophilic substitution by reacting with sodium cyanide, giving the intermediate cyanographene. In the following step, nitrile moieties are converted to –COOH *via* acidic hydrolysis. Thanks to this well-designed synthesis route, GA has more homogeneous surface functionalization compared to GO, both as composition (mainly –COOH are present) and as distribution, being distributed uniformly on basal plane, in contrast with GO where functional moieties are especially on the edges. More interestingly, GA combines high surface functionalization with excellent electrical properties, comparable to rGO. Hence, GA is, in principle, a perfect substrate for catalyst heterogenization, giving an elegant example of how conventional chemistry can be applied on graphene to obtain the aimed properties.

The other family in CMGs is heteroatoms-doped graphene, where, instead of acting on surface functionalization, atoms like B, N, S, P are inserted in substitutional position in the graphene sheet.[52,53,58–61] As for other semiconductor, the introduction of the heteroatom may strongly influence the electronic properties, for instance giving a preferential conductivity (*n* or *p*-type) and generating defects that can catalyse chemical or electrochemical reactions.

Among doped graphene materials, certainly N-doped graphene is the more deeply investigated.[62–64] Typically, N-Graphene has been produced by Chemical Vapour Deposition (CVD) methods (annealing of GO or graphene in NH_3 or other precursors), in solution or *via* electrochemical reduction.

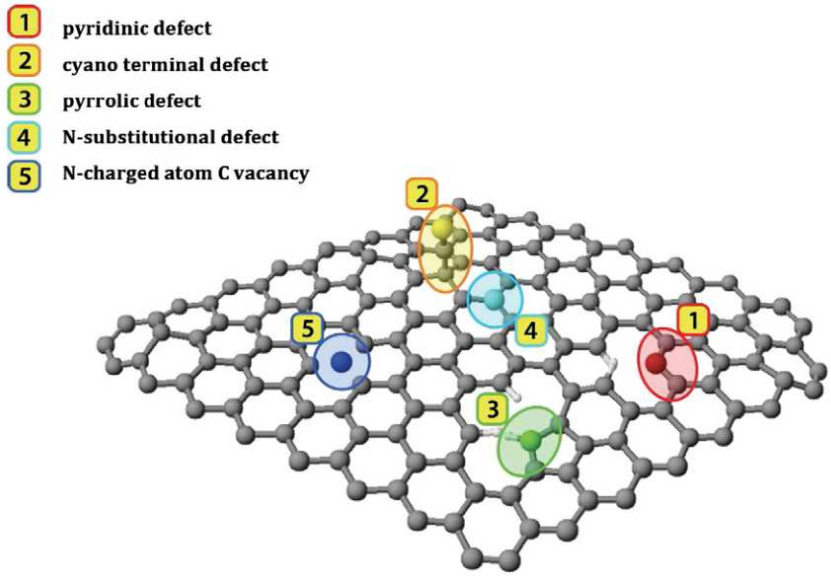

Figure 1.3. Schematic representation of N-doped graphene with highlighted the typical defects produced in the honeycomb lattice. Reproduced from ref. 21.

As shown in Figure 1.3, several kind of defects can be generated in the lattice and actually one of the challenges of this materials is to generate selectively just one type of defect, even if some procedure to obtain prevalent pyridinic or quaternary N-doping have been developed in recent years.[65,66] This achievement is very important, since it has been proven that these defects can be exploited in appropriate applications, since, for instance, graphitic nitrogen is the main responsible for the n-conductivity of N-graphene and pyridinic nitrogen was found to be an active site for Oxygen Reduction Reaction (ORR).[66]

As mentioned above, the other massive category of materials of Second Generation Graphene is the 3D-Graphene Architectures (3DG). In the case of 3DG, graphene or CMG are shaped in order to exploit the properties of graphene in systems with high surface area. The prototypical 3DG is graphene aerogel produced by freeze-drying or supercritical CO_2 drying of CMG suspension, generating self-standing 3D-networks with Brauner-Emmett-Teller (BET) surface area higher than 1000 m^2/g.[67–71] However, even other structures can be synthesized, like hollow nanospheres, crumpled sheets and capsules.[54,72–76]

Often, metallic templates have been used to shape up 3DGs: for instance, commercial Ni foams were used to produce supported graphene networks that, thanks to ultra-low density and high electrical conductivity, are appealing composites for a wide range of applications, like electrodes, supercapacitors and batteries.[77–79]

In other cases, metals are used as sacrificial templates, so are chemically removed after synthesis in order to further increase the exposed area of the graphene. Nice examples are the works from research groups of Choi and Qu.[80,81] In the early case, Ni nanoparticles (NPs) were coated with a polyol molecules, that were incorporated in the NiNPs by carburization at 250 °C. The following steps, annealing at 500 °C and treatment in HCl, allowed to form the multi-layer graphene on NiNPs surface and dissolve the template, respectively, achieving the final hollow graphene spheres. In the work of Qu, GO suspension was put in a glass pipeline, where a Cu wire was previously inserted. To form the extremely sharp shaped microtubes presented, the

glass pipeline was heated at 230 °C to hydrothermally reduce GO, followed by a treatment in aqueous $FeCl_3$ to dissolve the Cu. This strategy allowed the authors to grow metal NPs selectively on the outer or on the inner wall, paving the way to multiple functionalities integrated on the same 3DG.

Clearly, these strategies are just some examples of an impressive number of papers in literature for preparing 3DGs and, in principle, each of these strategies can be applied to all CMGs with a huge number of possible combinations, depending on the final application the material is aimed to.

It is quite evident that CMGs and 3DGs are more relevant for energy applications compared to First Generation Graphene. The fine tuning of morphological, structural and electronic properties grants the possibility to adapt these materials to different research scopes, like the already mentioned catalysis, electrocatalysis, supercapacitance and other forms of energy storage and conversion. Naturally, the extreme flexibility exhibited by graphene-based materials put in the spotlight also other 2D layered materials and transferring the knowledge acquired from graphene to other 2D-materials pulled the trigger on the Third Generation Graphene.

1.3.3 Third Generation of Graphene: Graphene Related Materials

Despite the outstanding properties shown by graphene, CMGs and 3DGs, it was unavoidable to face a failure in some applications. Curiously, graphene is still missing promises in one of the earlier application of the First Generation, which is the use as channel material in Field Effect Transistors (FETs). Indeed, the electronic properties that attracted electron-device community are also the main issue for FET applications. Briefly, as showed by Schwierz,[82] if graphene is used as channel semiconductor, it becomes troublesome to turn off the FET, since the absence of the band gap implies that, even if no potential is applied to the FET gate, the material switches from electron to hole conductivity instead of stopping the carriers flow. The consequence is the On/Off current ratio was found to be between 2 and 20, which is completely insufficient considering that the minimum recommended value is 10^3. In principle, using CMGs is possible to tune the gap from 0 to 0.5 eV, but On/Off current ratio is still far from values suitable for practical applications and for competing with mainstream silicon technologies.[83] The immediate consequence was that other “continents” of the *Flatland* started being explored in order to have a channel material with a real band gap, but also some fascinating properties of 2D-materials like the definite layer structure without dangling bonds and atomic-level thickness.

Even if this is just an example, a similar evolution occurred also in other research fields. In electrocatalysis, graphene itself showed bad activity in electrochemical WS, having actually no active sites for Hydrogen Evolution Reaction (HER) and Oxygen Evolution Reaction (OER). *Ab initio* calculations[84] showed that better performances could be obtained by coupling graphene with metal surfaces or by using CMGs, since the interruption of the lattice due to the presence of heteroatoms may acts as catalytic site for WS. However, it has to be considered that not all the defects are prone to perform the same electrocatalytic reaction, so chemical modification has to come together with a fine defects tuning in order to obtain competitive performances. For these objective difficulties, very few works have been published on the experimental utilization of pure CMGs in electrochemical WS. Zhang and Dai recently prepared and tested N,P,F-Tri-doped graphene as multifunctional catalyst for ORR and WS,[85] but more than 2 V were necessary to drive 10

mA/cm^2, that is 0.8 V above the thermodynamical limit of 1.23 V for WS. Better results were obtained in Yao's research group, where graphene with high concentration of topological defects was synthesized and tested for ORR and overall WS.[86] With respect to previous case, defective graphene in WS needs 0.6 V overpotential to reach 10 mA/cm^2, that it is a good result for a metal-free catalyst, but far from the benchmarks, especially in alkaline HER. Consequently, at the state of the art of WS, graphene and CMGs are mostly used as support for other metal-based materials, with the aim of exploiting electrical properties or to implement some synergies by forming a junction with the active material.

As demonstrated by these cases, graphene and CMGs, even if revolutionary materials, are not the magic bullet to all the challenges that scientific community has been facing in the last decade. However, the impressive knowledge acquired on graphene was decisive in processing, characterizing and improving performance of the other 2D-materials. Actually, graphene-related materials (GRMs) are complementary to graphene: GRMs are associated to CMGs and graphene being layered, on the other hand they have completely different electronic structure and chemical composition. The most notorious members of GRMs family are depicted in Figure 1.4.

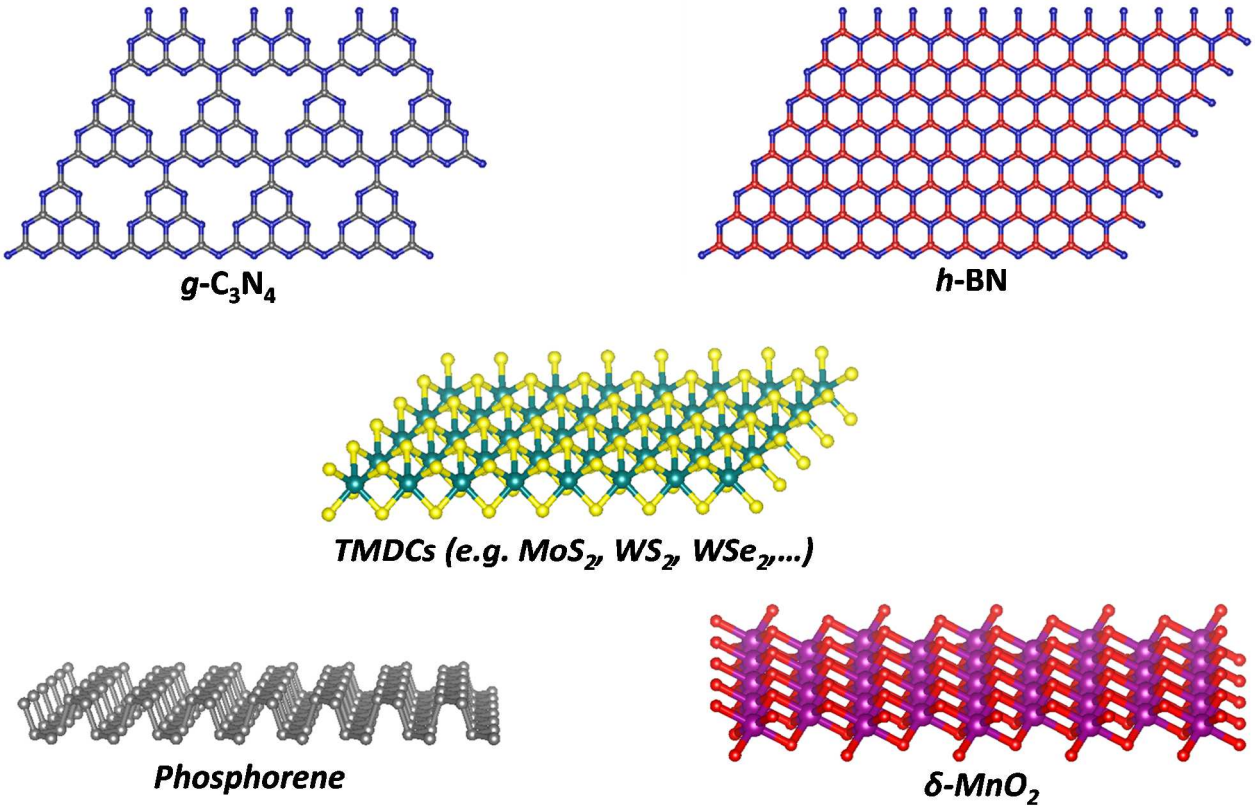

Figure 1.4. Ball and stick models of best known GRMs.

As written above, all these materials have some common peculiarities due to their 2D nature:

- Atomic-level thickness;
- Definite layer structure;
- No dangling bonds: carriers conducted on the surface of the material encounter very low roughness, reducing the scattering probability;
- Tunability of optoelectronic properties with of layers;
- Application of similar protocols for processing materials (*e.g.* exfoliation, purification, morphology modification).

However, their chemical composition is really very heterogeneous: Graphitic Carbon Nitride (g-C_3N_4) is still a carbon based materials, Hexagonal Boron Nitride (h-BN) and Phosphorene has no carbon in their structures but they are metal-free, Transition Metal Dichalcogenides (TMDCs) and layered MnO_2 can exploit the chemistry of metals, but being chalcogenides and oxides, respectively, direct them in completely different applications. Curiously, considering graphene, CMGs and GRMs, 2D semiconductors band gaps can cover continuously the energy range from 0 to 2.6 eV (from far-IR to cyan light) plus an insulator like h-BN (*ca*. 5.9 eV),[87] giving a wide selection of optoelectronic properties for the use of 2D-materials in specific applications (see Figure 1.5).

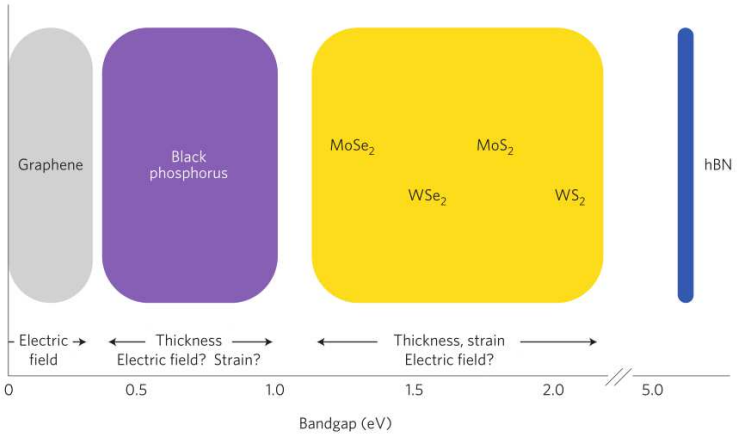

Figure 1.5. Schematic diagram of 2D-Materials band gaps. Reproduced from 57.

Among GRMs, Graphitic Carbon Nitride (g-C_3N_4) can be considered the most similar to graphene, since its structure can be associated with that of a strongly N-doped graphene. g-C_3N_4 is a good electrocatalyst and, thanks to its 2.6 eV band gap, its performances can be boosted *via* visible light irradiation.[88,89] For instance, g-C_3N_4 is a promising catalysts for the ORR due to the high content of pyridinic and graphitic N and abundant edge amine sites, but it was also successfully tested in photocatalytic CO_2 Reduction Reaction (CRR) to further processable organic feedstocks (CO, formic acid, formaldehyde,…).[90,91] Moreover, the natural vacancies in g-C_3N_4 can be patched by growing highly monodispersed nanoparticles, resulting in interesting synergistic effects.[88] However, g-C_3N_4, being a sort of defective graphene, suffers of poor electronic conductivity, limiting large scale applications, so this material is often used in combination with conductive 2D-materials (i.e. graphene or CMGs) in order to improve electrochemical performances.[92]

Also h-BN has the same honeycomb lattice of graphene and it is isoelectronic as well, but the polar nature of B–N bonds make the band gap to pass from 0 to almost 6 eV. Obviously, the insulating behaviour of h-BN seriously hamper applications in electrochemistry, so it is mostly used as dielectric substrate for other GRMs or as substitute of SiO_2 in all-2D FETs.[93–95] However, recent works showed that *via* chemical doping is possible to reduce the h-BN gap down to 2 eV.[96]

Phosphorene is the black allotrope of phosphorous, reduced to the monolayer thickness. Phosphorene structure notably differs from graphene's honeycomb, because of the presence of 5 electrons in P 3p orbitals that gives rise to sp^3 hybridization, explaining the non-planarity of the 2D sheet.[97] This particular GRMs is interesting because of the combination of a small band gap (from 0.3 eV in bulk to 1.88 eV in monolayer) with a good electrical conductivity.[98] Indeed, in recent years some works have been published on the use phosphorene both as electrocatalyst and photoelectrocatalyst, showing some interesting results in HER and OER.[99–101] Unfortunately, the main drawback of using black phosphorous in electrocatalysis is the low stability in atmospheric conditions, since it degrades in contact with water and oxygen, which is also a visible light pronounced process. Therefore, at the moment, the main application scopes of phosphorene are the ones in controlled atmosphere, like fabrication of FETs and batteries.[102,103]

δ-MnO_2 is the only layered of six polymorphs of MnO_2, and it comes with a 2.1 eV band gap in bulk crystals,[104,105] meaning that this oxide may be used as visible light activated photocatalyst.[106] Interestingly, δ-MnO_2 tends to intercalate cations and water molecules in the interlayer space, modifying both the band gap and the electrochemical performances.[106] Being an oxide, δ-MnO_2 suffers of low conductivity, but compared with other GRMs it exhibits excellent stability in oxidative conditions.[107] Therefore, δ-MnO_2 has been found to catalyse OER and photo-OER with moderate overpotentials.[105,108,109] However, δ-MnO_2 catalytic activity is not limited to water oxidation, but it was found to be a well-performing catalyst also in ORR and in other reactions, like formaldehyde oxidation.[107,110] Typically, δ-MnO_2 was considered to be inactive for the WS cathodic half-reaction, due to its unsuitable electronic structure and low conduction band level. However, as demonstrated by the Second Generation of Graphene, defects engineering can pave the way to generate new active sites in the same material, and this was for MnO_2. Wang *et al.* observed half-metallic character in monolayer nanosheets doped with Mn and O vacancies, a property not observed in bulk counterparts, providing a new strategy for improving the electronic properties and conductivity of δ-MnO_2 for overall WS.[111] In a following work, Zhao *et al.* synthesized a hierarchical composite δ-MnO_2/Ni-foam with high vacancies abundance:[112] during tests for WS, a remarkable 0.5 V global overpotential at 10 mA/cm^2 was recorded, with about 560 mV improving of HER onset with respect to bulk δ-MnO_2.

Finally, TMDCs are the most investigated GRMs (together with graphene-based materials), as established by the about 10^4 publications in 2016.[102] TMDCs are a wide family of materials with a common rough formula MX_2 (M = Mo, W, V, Nb, Ta, Ti, Re, Zr,… and X = S, Se or Te) and a sandwich-like hexagonal structure with a layer of metal atoms enclosed between two chalcogenide atoms layer (see Figure 1.4). Consequently, with respect to most GRMs, in TMDCs there is possibility to tune optoelectronic properties also by composition: considering the prototypical TMDC (*i.e.* MoS_2), studies were carried out to proof the excellent controlling of properties by making alloys mixing both metals (*e.g.* $Mo_{(1-x)}W_xS_2$) and chalcogenides (*e.g.* $MoS_{2(1-x)}Se_{2x}$),[113–118] coming up with precise band gap engineering and modulation of related properties, like photoluminescence.

Moreover, all TMDCs has more than one polymorph, with different properties and activities, and also amorphous material were found to be very active in some electrocatalytic reactions. Considering again MoS_2, it can exist in three polymorphic forms, schematically represented in Figure 1.6. The most common is the hexagonal 2H-phase, which exhibits semiconducting behaviour with band gap from 1.2 to 1.9 eV when decreasing the number of layers. The distorted tetragonal 1T-phase is typically obtained upon alkali intercalation and following exfoliation into nanosheets, it is metallic and basically metastable and very defective, characteristics that grant to this polymorph to perform extremely well in HER.[20,119] The rarest polytype is the rombohedral 3R-phase, that has to be synthesized through specific growing procedures and behave like a semiconductor (indirect band gap 1.3 eV).[120–122] Each of these polymorphs possesses unique structures and electronic properties from where different catalytic properties can emerge due to the different active sites.

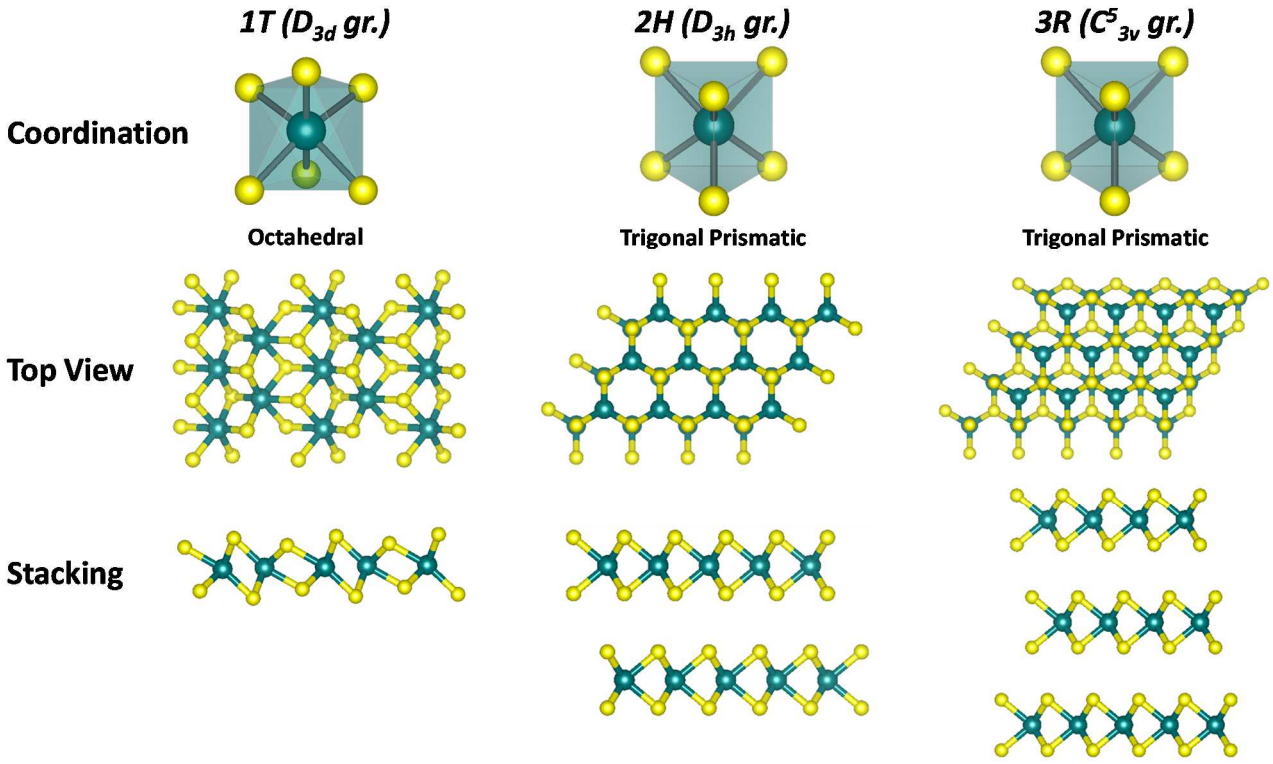

Figure 1.6. 3D models of different 1T, 2H and 3R MoS_2 polymorphs, respectively. The symmetry group of the crystallographic unit cell is reported in brackets.

Moreover, amorphous MoS_2 and non-stoichiometric MoS_x ($2 < x < 3$) can be easily synthesized from suitable precursors and, thanks to high number of defects, they may have different active sites, exhibiting also in this case very interesting activity in electrocatalysis.[123–126]

It is quite evident that the intrinsic activity of TMDCs, combined with the huge tuning possibilities, is the reason for the high focus on these GRMs, considering that all the strategies applicable to other 2D-materials can be actualized (*i.e.* doping, 3D-structuring, hybrids, …) as well. Actually, the application of TMDCs spans substantially in every field where an electroactive material is required, thanks to their versatility comparable to graphene one. For example, in microelectronics field MoS_2 has been successfully tested as channel material in FETs and logic devices,[94,95,127–129] and as part of MoS_2/Graphene heterostructure for non-volatile

memory cells[130] and photodetectors.[131] Similarly, TMDCs were largely tested in lithium ion batteries[132–134] and supercapacitors,[20,135–138] taking advantage of all the approaches developed for graphene and CMGs for selectively improving the required properties. Concerning electrocatalysis, TMDCs are among the benchmark materials in HER. Indeed, especially MoS_2 and $MoSe_2$ based electrocatalysts exhibited extremely good performances even if the HER reaction was mostly tested in not ideal conditions (*i.e.* in basic electrolyte). Considering HER in the typical conditions (0.5 M H_2SO_4), it is well-known that 1T-MoS_2 can perform HER with low overpotentials and kinetics close to Pt, which is believed being related to the high number of defects generated during the stressing exfoliation process.[119] Another example is a 3D-structured composite prepared by growing $MoS_{2(1-x)}Se_{2x}$ on a selenized Ni-foam. Even if three steps were necessary to achieve the final material, an outstanding 69 mV overpotential was sufficient to draw 10 mA/cm^2 and about 110 mV for 100 mA/cm^2.[139] In OER the activity of MoS_2 is low due to a certain lack of stability, but a nice work from Mattevi's group showed improved performance making a bulk heterojunctions combining MoS_2 and WS_2.[140] Finally, TMDCs showed excellent performances also in CRR, with just the help of some ionic liquid in the electrolyte to suppress HER, being two competitive process in the same potential window.[141,142] In this case the best performing material was found to be WSe_2, whose overpotential for CRR was found to be 54 mV.

1.4 Ph.D. Thesis Structure

This Ph.D. project, as extensively discussed in section 1.2, is aimed to discover new strategies to develop materials to utilize in the fields of *Green Energy* and *Green Chemistry* and it was directed at the application of 2D Materials in particular. Section 1.3 reported part of the huge work made by scientific community on these materials and underlined the still unexpressed potential that lies in them.

In our studies in the *Green Energy* area, we focused on the use of MoS_2-based materials in WS cathodic half-reaction in order to obtain the best possible performance in hydrogen generation in different conditions. To do that, different strategies were developed (i.e. metal doping, inorganic and organic/inorganic hybrids) to drive the original material to adapt to specific application.

Regarding *Green Chemistry* area, we used a specific CMG, that is the already mentioned Graphene Acid (GA), and we exploited its uniform surface functionalization to prepare materials for heterogeneous catalysis for different reactions, comparing them with the benchmark GO, modified with the same protocol.

The Thesis work is divided in 5 main chapters. In Chapter Two we investigated the design of three-dimensional MoS_2 structures doped with several amount of Ni in order to activate MoS_2 for the HER performed in alkaline environment, which typically hinder this reaction. Nevertheless, the introduction of a different cation in the lattice can causes the modification of the structure, which can also influence the HER. We prepared 3D-structured MoS_2 samples (hereafter 3D-MoS_2) obtained starting from ammonium tetrathiomolybdate (ATM) using a procedure that also allows to easily introduce the dopant in a single pot. We tested several conditions in order to find the procedure that would allow to expose as much active sites as possible. We then studied the effects of different amount of Ni doping both on the 3D-MoS_2 structure and the catalytic performances in HER, both in acidic and in basic media. The investigation was carried on combining several techniques. Morphology was examined by electronic microscopies, both Scanning (SEM) and Transmission Electron Microscopy (TEM). During the same measurements, we also performed Energy

Dispersive X-Ray analysis (EDX) to verify the effective distribution of the dopant, since eventual inhomogeneity would indicate the segregation of distinct dopant-based species (M_xO_y or M_xS_y), a process that may happen especially with relatively high loadings. The influence of Ni on MoS_2 lattice was investigated by mean of X-Ray Diffraction Analysis (XRD) and Raman Spectroscopy. The combination of these techniques was helpful to reveal the dopant influence on the lattice parameters and the defectivity and stacking of the MoS_2 layers. X-Ray Photoemission Spectroscopy (XPS) was decisive in bridging the structural information with HER activity. Indeed, XPS was helpful to observe the dopant chemical environment, figuring out the different kind of active sites produced on the material. Moreover, the shifts in Binding Energy (BE) of the signals relative to the scaffold showed how the dopant influenced the MoS_2 electronic structure. We performed an extensive electrochemical characterization in acidic (0.5M H_2SO_4) and alkaline (1.0M KOH) electrolytes to find out the role of each active species in catalysing HER depending on the available species to react, both in terms of pure performances and of reaction kinetics. The result was a contrasting behaviour of the materials due to the different abundance of active sites generated by Ni on MoS_2 edge or basal plane.

In Chapter Three, we developed a method for preparing amorphous MoS_2/Ag_2S hybrid using recycled DVD as the substrate; this revealed as a viable opportunity to turn an abundant waste into an added-value material. We produced the hybrid materials by exposing the Ag patterned layer of commercial DVD and by electro-depositing the material from a 50 mM ATM aqueous solution for 3 minutes. The reduction of ATM simultaneously cause the deposition of MoS_2 and the generation of SH^- anions that sulphidize metallic Ag to Ag_2S, forming MoS_2/Ag_2S n-p nanojunctions. To proof the role of MoS_2, we grown pure Ag_2S and MoO_2 films as blank experiments. The evolution of the DVD support was followed by using SEM, XRD and Raman Spectroscopy, for morphology, crystal phases and structural modifications, respectively. SEM showed a strongly increased roughness of the DVD substrate, while XRD and Raman measurements revealed the amorphous nature of materials deposited through this protocol. XPS further confirmed the amorphous nature of the films and allowed to quantify the ratio among the sulphides. We operated electrochemical tests by combining polarization curves, Electrochemical Impedance Spectroscopy (EIS) and double-layer capacitance measurements, resulting in a very cheap and effective catalyst for HER. Moreover, thanks to the presence of n-p junctions (proofed by Mott-Schottky analysis), a nice 10% performance enhancement under visible light irradiation was observed.

In Chapter Four another kind of hybrid was prepared by designing a one-pot hydrothermal synthesis of $MoS_{2(1-x)}Se_{2x}$ nanosheets grown on N-doped reduced Graphene Oxide (hereafter N-rGO). This study was focused on optimizing a synthesis that allows a precise and easy-to-tune Se:S ratio, with the goal of controlling optoelectronic properties. In the synthesis we utilized ATM as MoS_2 precursor in the presence of Dimethyl Diselenide (DMDSe) as selenizing agent. Through a series of blank experiments, we found that a two-temperatures synthesis was the best to obtain the target material: a first step at 180°C to allow the growth of MoS_x slabs without the competition with selenization reaction and subsequently a step at 200 °C to activate DMDSe and substituting S anions on the nanosheets. The materials that we obtained were found to be amorphous due to low process temperature. Therefore two different goals were chased: the as-produced materials were tested for HER in acidic environment, while crystalline materials, obtained by annealing at 600 °C, were destined to photoinduced HER. The reason resides on the different crystallinity: the amorphous samples, being highly defective, were expected to have higher intrinsic catalytic activity but

worse interaction with light because of defects-mediated exciton recombination; on the other hand, crystallizing the materials would allow losing pure performance but improving the exciton lifetime, favouring the photoinduced reaction. Indeed, this hybrid material is based on the interaction between two moieties that are responsible for the creation of a p-n nanojunction and have two synergistic roles (imparting good electric conduction the N-rGO, and granting a low overpotential the $MoS_{2(1-x)}Se_{2x}$) inside a unique catalytic reaction. The tuning of Se:S ratio was followed by the evolution of Raman modes with the changes in composition, as in the case of XPS, that was used to determine the Se:S ratio. HER activity and kinetics was firstly investigated for all the produced samples, revealing that, in the case of amorphous samples, the introduction of Se had no beneficial effects, since amorphous MoS_2/N-rGO was the best performing material. On the other hand, after annealing the intrinsic defectivity of Se-containing samples completely reverted the trends. Subsequently, photoinduced HER was studied for selected samples: as expected, amorphous samples were found to be much less responding to light irradiation compared to crystalline counterparts. On the latter, UV-Vis, transient photocurrent and Incident Photons to Current Efficiency (IPCE) studies were made to observe the evolution of performance with different Se contents.

The contents of Chapter Five move from electrocatalysis to heterogeneous catalysis. We synthesized a heterogeneous catalyst by covalently grafting Ferrocene (Fc) moieties to –COOH surface groups of GA and GO. The resulting Fc-modified graphene derivatives have been tested as heterogeneous catalysts for the C-H insertion of aryl diazonium salts into several arene substrates, a reaction of pivotal importance for organic chemistry since it activates a rather inert system, opening new reaction pathways in the synthetic research. The materials were extensively characterized along every synthetic step. SEM and TEM experiments were performed to check the morphology, Raman spectroscopy was used to calculate the I_D/I_G ratio and we observed in UV-Vis spectra the appearance of Fc bands. Thanks to XPS measurements we were able to follow the evolution of C core level along the functionalization steps. XPS was used as well to determine the amount of Fe in the final materials, crosschecking the results with EDX analysis and with charge integration measurement in Cyclic Voltammetry (CV) experiments. Once the successful functionalization of the GA and GO supports with Fc was demonstrated, and considering that molecular Fc shows a good catalytic activity in the C-H insertion of diazonium salts into arene substrates reaction, the GA- and GO-based materials were tested as heterogeneous catalysts for the same reaction. The catalytic activity and kinetics were observed via Nuclear Magnetic Resonance (NMR), resulting not only in a successful heterogenization of Fc, but also in a clear superiority of GA as scaffold with respect to GO.

A different type of graphene-based catalyst was investigated in Chapter Six, in particular we have grown Pd nanoparticles on GA and GO to create a material for Suzuki-Miyaura cross coupling reaction. The literature is full of reports where researchers tackle the combination of Pd and graphene in form of small metallic dots, with diameter ranging from big clusters (less than 2 nm) to big nanoparticles (80-100 nm). However, the mechanism on how the nanoparticles grow on surface is not addressed. It is believed that surface oxygen groups on GO or rGO play a role. In order to shed light about this fundamental question, we employed GA as platform to grow Pd nanoparticles. The uniform surface chemistry become crucial to understand the chemical transformation involved in the nucleation and growing of the supported metallic nanoparticles. We characterized the synthesized materials by mean of XPS, which was essential in observing the changings of C line upon impregnation and of Pd core level, where both chemical state and capacitive effects due to

quantum confinement could be observed. Moreover, an estimation of Pd loading could be calculated and further confirmed by EDX and Inductively Coupled Plasma Mass Spectrometry (ICP-MS). On GA, different Pd loadings were essayed to obtain smaller (i.e. more active) Pd nanoparticles. TEM analysis demonstrated that much narrower Pd nanoparticles size distribution could be obtained on GA with respect to GO, proofing the importance of surface moieties in controlling nanoparticles growth. Also UV-Vis spectroscopy confirmed these hypothesis, since it is known that the size of the Pd nanoparticle can affect the optical properties regarding the corresponding maximum of the plasmonic effect. Regarding the catalytic activity, the Suzuki-Miyaura reaction is one of the most widespread employed cross-coupling reactions to form C-C bonds. Pd nanoparticles supported on graphene derivatives have already been reported to have activity on the cross coupling of boronic acids with different halides, demonstrating good catalytic performance with high stability, cyclability and versatility even working under green conditions. Other authors, however, reported the synthesis of homocoupling catalysts of boronic acids instead of the cross-coupling ones. Thanks to Pd nanoparticles homogeneity, derived from uniform surface functionalization of GA, we found that our GA-Pd system is able to perform selectively and in green conditions both reactions with a simple control of the reagents involved.

References

(1) International Energy Agency. World Energy Outlook (WEO) www.iea.org/weo.

(2) United Nations Environment Programme. Division of Technology, I. *Hydrogen Economy : A Non-Technical Review.*; 2006.

(3) McDowall, W.; Eames, M. Forecasts, Scenarios, Visions, Backcasts and Roadmaps to the Hydrogen Economy: A Review of the Hydrogen Futures Literature. *Energy Policy* **2006**, *34* (11), 1236–1250.

(4) Balasubramanian, B.; Ortiz, A. L.; Kayatakoglu, S.; Harris, D. P. Hydrogen from Methane in a Single-Step. *Process. Chem. Eng. Sci.* **1999**, *54*, 3543.

(5) Faber, M. S.; Jin, S. Earth-Abundant Inorganic Electrocatalysts and Their Nanostructures for Energy Conversion Applications. *Energy Environ. Sci.* **2014**, *7* (11), 3519–3542.

(6) Novoselov, K. S.; Geim, A. K.; Morozov, S. V.; D. Jiang, Y. Z.; Dubonos, S. V.; Grigorieva, I. V.; Firsov, A. A. Electric Field Effect in Atomically Thin Carbon Films. *Science* **2004**, *306* (5696), 666–669.

(7) Zurutuza, A.; Marinelli, C. Challenges and Opportunities in Graphene Commercialization. *Nat. Nanotechnol.* **2014**, *9* (10), 730–734.

(8) Ren, W.; Cheng, H. M. The Global Growth of Graphene. *Nat. Nanotechnol.* **2014**, *9* (10), 726–730.

(9) Ellabban, O.; Abu-Rub, H.; Blaabjerg, F. Renewable Energy Resources: Current Status, Future Prospects and Their Enabling Technology. *Renew. Sustain. Energy Rev.* **2014**, *39*, 748–764.

(10) Xia, W.; Mahmood, A.; Liang, Z.; Zou, R.; Guo, S. Earth-Abundant Nanomaterials for Oxygen Reduction. *Angew. Chemie - Int. Ed.* **2016**, *55* (8), 2650–2676.

(11) Shao, M.; Chang, Q.; Dodelet, J.-P.; Chenitz, R. Recent Advances in Electrocatalysts for Oxygen Reduction Reaction. *Chem. Rev.* **2016**, *116* (6), 3594–3657.

(12) Xia, B. Y.; Yan, Y.; Wang, X.; Lou, X. W. Recent Progress on Graphene-Based Hybrid Electrocatalysts. *Mater. Horizons* **2014**, *1* (4), 379–399.

(13) European Commission. Critical Raw Materials ec.europa.eu/growth/sectors/raw-materials/specific-interest/critical_en.

(14) Mathieux, F.; Ardente, F.; Bobba, S.; Nuss, P.; Blengini, G.; Alves Dias, P.; Blagoeva, D.; Torres De Matos, C.; Wittmer, D.; Pavel, C.; Hamor, T.; Saveyn, H.; Gawlik, B.; Orveillon, G.; Huygens, D.; Garbarino, E.; Tzimas, E.; Bouraoui, F.; Solar, S. *Critical Raw Materials and the Circular Economy - Background Report*; 2017.

(15) Muradov, N. Z.; Veziroğlu, T. N. From Hydrocarbon to Hydrogen-Carbon to Hydrogen Economy. *Int. J. Hydrogen Energy* **2005**, *30* (3), 225–237.

(16) Cheng, Y.; Jiang, S. P. Advances in Electrocatalysts for Oxygen Evolution Reaction of Water Electrolysis-from Metal Oxides to Carbon Nanotubes. *Prog. Nat. Sci. Mater. Int.* **2015**, *25* (6), 545–553.

(17) Meyer, T. J. The Art of Splitting Water. *Nature* **2008**, *451*, 778.

(18) Tao, H.; Gao, Y.; Talreja, N.; Guo, F.; Texter, J.; Yan, C.; Sun, Z. Two-Dimensional Nanosheets for Electrocatalysis in Energy Generation and Conversion. *J. Mater. Chem. A* **2017**, *5* (16), 7257–7284.

(19) Tan, C.; Cao, X.; Wu, X.-J.; He, Q.; Yang, J.; Zhang, X.; Chen, J.; Zhao, W.; Han, S.; Nam, G.-H.; Sindoro, M.; Zhang, H. Recent Advances in Ultrathin Two-Dimensional Nanomaterials. *Chem. Rev.* **2017**, *117* (9), 6225–6331.

(20) Acerce, M.; Voiry, D.; Chhowalla, M. Metallic 1T Phase MoS_2 Nanosheets as Supercapacitor Electrode

Materials. *Nat. Nanotechnol.* **2015**, *10* (4), 313–318.

(21) Torrisi, F.; Coleman, J. N. Electrifying Inks with 2D Materials. *Nat. Nanotechnol.* **2014**, *9* (10), 738–739.

(22) Duan, J.; Chen, S.; Jaroniec, M.; Qiao, S. Z. Heteroatom-Doped Graphene-Based Materials for Energy-Relevant Electrocatalytic Processes. *ACS Catal.* **2015**, *5* (9), 5207–5234.

(23) United States Environmental Protection Agency. Green Chemistry www.epa.gov/greenchemistry.

(24) ExxonMobil. Outlook for Energy: A View to 2040. **2015**.

(25) Anastas, P. T.; Warner, J. C. *Green Chemistry: Theory and Practice.*; Oxford University Press: New York, 1998.

(26) Polshettiwar, V.; Varma, R. S. Green Chemistry by Nano-Catalysis. *Green Chem.* **2010**, *12* (5), 743–754.

(27) Mizuno, N.; Misono, M. Heterogeneous Catalysis. *Chem. Rev.* **1998**, *98* (1), 199–218.

(28) Copéret, C.; Chabanas, M.; Petroff Saint-Arroman, R.; Basset, J.-M. Homogeneous and Heterogeneous Catalysis: Bridging the Gap through Surface Organometallic Chemistry. *Angew. Chem. Int. Ed. Engl.* **2003**, *42* (2), 156–181.

(29) Lefebvre, F.; Basset, J.-M. Recent Applications in Catalysis of Surface Organometallic Chemistry. *J. Mol. Catal. A Chem.* **1999**, *146* (1–2), 3–12.

(30) Polshettiwar, V.; Molnár, Á. Silica-Supported Pd Catalysts for Heck Coupling Reactions. *Tetrahedron* **2007**, *63* (30), 6949–6976.

(31) Polshettiwar, V.; Len, C.; Fihri, A. Silica-Supported Palladium: Sustainable Catalysts for Cross-Coupling Reactions. *Coord. Chem. Rev.* **2009**, *253*, 2599–2626.

(32) Akhavan, O.; Ghaderi, E. Toxicity of Graphene and Graphene Oxide Nanowalls against Bacteria. *ACS Nano* **2010**, *4* (10), 5731–5736.

(33) Geim, A. K.; Novoselov, K. S. The Rise of Graphene. *Nat. Mater.* **2007**, *6* (3), 183–191.

(34) Lee, J. U.; Yoon, D.; Kim, H.; Lee, S. W.; Cheong, H. Thermal Conductivity of Suspended Pristine Graphene Measured by Raman Spectroscopy. *Phys. Rev. B - Condens. Matter Mater. Phys.* **2011**, *83* (8), 1–4.

(35) Xu, X.; Pereira, L. F. C.; Wang, Y.; Wu, J.; Zhang, K.; Zhao, X.; Bae, S.; Tinh Bui, C.; Xie, R.; Thong, J. T. L.; Hong, B. H.; Loh, K. P.; Donadio, D.; Li, B.; Özyilmaz, B. Length-Dependent Thermal Conductivity in Suspended Single-Layer Graphene. *Nat. Commun.* **2014**, *5*, 1–6.

(36) Faugeras, C.; Faugeras, B.; Orlita, M.; Potemski, Ḿ. M.; Nair, R. R.; Geim, A. K. Thermal Conductivity of Graphene in Corbino Membrane Geometry. *ACS Nano* **2010**, *4* (4), 1889–1892.

(37) Cai, W.; Moore, A. L.; Zhu, Y.; Li, X.; Chen, S.; Shi, L.; Ruoff, R. S. Thermal Transport in Suspended and Supported Monolayer Graphene Grown by Chemical Vapor Deposition. *Nano Lett.* **2010**, *10* (5), 1645–1651.

(38) Yousefzadi Nobakht, A.; Shin, S. Anisotropic Control of Thermal Transport in Graphene/Si Heterostructures. *J. Appl. Phys.* **2016**, *120* (22).

(39) Chen, D.; Feng, H.; Li, J. Graphene Oxide: Preparation, Functionalization, and Electrochemical Applications. *Chem. Rev.* **2012**, *112* (11), 6027–6053.

(40) Wallace, P. R. The Band Theory of Graphite. *Phys. Rev.* **1947**, *71* (9), 622–634.

(41) Kim, K. S.; Zhao, Y.; Jang, H.; Lee, S. Y.; Kim, J. M.; Kim, K. S.; Ahn, J. H.; Kim, P.; Choi, J. Y.; Hong, B. H. Large-Scale Pattern Growth of Graphene Films for Stretchable Transparent Electrodes. *Nature* **2009**,

457 (7230), 706–710.

(42) Nair, R. R.; Blake, P.; Grigorenko, A. N.; Novoselov, K. S.; Booth, T. J.; Stauber, T.; Peres, N. M. R.; Geim, A. K. Universal Dynamic Conductivity and Quantized Visible Opacity of Suspended Graphene. *Science* **2008**, *320*, 1308.

(43) Lee, C.; Wei, X.; Kysar, J. W.; Hone, J. Measurement of the Elastic Properties and Intrinsic Strength of Monolayer Graphene. *Science* **2008**, *321*, 385–388.

(44) Cooper, D. R.; D'Anjou, B.; Ghattamaneni, N.; Harack, B.; Hilke, M.; Horth, A.; Majlis, N.; Massicotte, M.; Vandsburger, L.; Whiteway, E.; Yu, V. Experimental Review of Graphene. *ISRN Condens. Matter Phys.* **2012**, *2012*.

(45) Novoselov, K. S.; Geim, A. K.; Morozov, S. V.; Jiang, D.; Katsnelson, M. I.; Grigorieva, I. V.; Dubonos, S. V.; Firsov, A. A. Two-Dimensional Gas of Massless Dirac Fermions in Graphene. *Nature* **2005**, *438*, 197–200.

(46) Morozov, S. V.; Novoselov, K. S.; Katsnelson, M. I.; Schedin, F.; Elias, D. C.; Jaszczak, J. A.; Geim, A. K. Giant Intrinsic Carrier Mobilities in Graphene and Its Bilayer. *Phys. Rev. Lett.* **2008**, *100* (1), 11–14.

(47) Neto, A. H. C.; Guinea, F.; Peres, N. M. R.; Novoselov, K. S.; Geim, A. K. The Electronic Properties of Graphene. *Rev. Mod. Phys.* **2009**, *81*, 109.

(48) Chen, J. H.; Jang, C.; Xiao, S.; Ishigami, M.; Fuhrer, M. S. Intrinsic and Extrinsic Performance Limits of Graphene Devices on SiO_2. *Nat. Nanotechnol.* **2008**, *3* (4), 206–209.

(49) Bonaccorso, F.; Colombo, L.; Yu, G.; Stoller, M.; Tozzini, V.; Ferrari, A. C.; Ruoff, R. S.; Pellegrini, V. Graphene, Related Two-Dimensional Crystals, and Hybrid Systems for Energy Conversion and Storage. *Science* **2015**, *347* (6217).

(50) Agnoli, S.; Granozzi, G. Second Generation Graphene : Opportunities and Challenges for Surface Science. *Surf. Sci.* **2013**, *609*, 1–5.

(51) Ruoff, R. S. Chemically Modified Graphenes. *J. Mater. Chem.* **2011**, *21* (10), 3272.

(52) Agnoli, S.; Favaro, M. Doping Graphene with Boron: A Review of Synthesis Methods, Physicochemical Characterization, and Emerging Applications. *J. Mater. Chem. A* **2016**, *4* (14), 5002–5025.

(53) Sheng, Z.-H.; Shao, L.; Chen, J.-J.; Bao, W.-J.; Wang, F.-B.; Xia, X.-H. Catalyst-Free Synthesis of Nitrogen-Doped Graphene via Thermal Annealing Graphite Oxide with Melamine and Its Excellent Electrocatalysis. *ACS Nano* **2011**, *5* (6), 4350–4358.

(54) Carraro, F.; Calvillo, L.; Cattelan, M.; Favaro, M.; Righetto, M.; Nappini, S.; Píš, I.; Celorrio, V.; Fermín, D. J.; Martucci, A.; Agnoli, S.; Granozzi, G. Fast One-Pot Synthesis of MoS_2/Crumpled Graphene p-n Nanonjunctions for Enhanced Photoelectrochemical Hydrogen Production. *ACS Appl. Mater. Interfaces* **2015**, *7* (46), 25685–25692.

(55) Marcano, D. C. D.; Kosynkin, D. D. V.; Berlin, J. M. J.; Sinitskii, A.; Sun, Z.; Slesarev, A.; Alemany, L. B.; Lu, W.; Tour, J. M. Improved Synthesis of Graphene Oxide. *ACS Nano* **2010**, *4* (8), 4806–4814.

(56) Favaro, M.; Agnoli, S.; Di Valentin, C.; Mattevi, C.; Cattelan, M.; Artiglia, L.; Magnano, E.; Bondino, F.; Nappini, S.; Granozzi, G. TiO_2/Graphene Nanocomposites from the Direct Reduction of Graphene Oxide by Metal Evaporation. *Carbon N. Y.* **2014**, *68*, 319–329.

(57) Bakandritsos, A.; Pykal, M.; Boński, P.; Jakubec, P.; Chronopoulos, D. D.; Poláková, K.; Georgakilas, V.; Čépe, K.; Tomanec, O.; Ranc, V.; Bourlinos, A. B.; Zbořil, R.; Otyepka, M. Cyanographene and Graphene Acid: Emerging Derivatives Enabling High-Yield and Selective Functionalization of Graphene. *ACS Nano* **2017**, *11* (3), 2982–2991.

(58) Wang, X.; Sun, G.; Routh, P.; Kim, D.-H.; Huang, W.; Chen, P. Heteroatom-Doped Graphene Materials:

Syntheses, Properties and Applications. *Chem. Soc. Rev.* **2014**, *43* (20), 7067–7098.

(59) Routh, P.; Shin, S. H.; Jung, S. M.; Choi, H. J.; Jeon, I. Y.; Baek, J. B. Boron-Nitrogen-Phosphorous Doped Graphene Nanoplatelets for Enhanced Electrocatalytic Activity. *Eur. Polym. J.* **2018**, *99* (January), 511–517.

(60) Yang, Z.; Yao, Z.; Li, G.; Fang, G.; Nie, H.; Liu, Z.; Zhou, X.; Chen, X.; Huang, S. Sulfur-Doped Graphene as an Efficient Metal-Free Cathode Catalyst for Oxygen Reduction. *ACS Nano* **2012**, *6* (1), 205–211.

(61) Zhang, C.; Mahmood, N.; Yin, H.; Liu, F.; Hou, Y. Synthesis of Phosphorus-Doped Graphene and Its Multifunctional Applications for Oxygen Reduction Reaction and Lithium Ion Batteries. *Adv. Mater.* **2013**, *25* (35), 4932–4937.

(62) Geng, D.; Yang, S.; Zhang, Y.; Yang, J.; Liu, J.; Li, R.; Sham, T. K.; Sun, X.; Ye, S.; Knights, S. Nitrogen Doping Effects on the Structure of Graphene. *Appl. Surf. Sci.* **2011**, *257* (21), 9193–9198.

(63) Li, X.; Wang, H.; Robinson, J. T.; Sanchez, H.; Diankov, G.; Dai, H. Simultaneous Nitrogen-Doping and Reduction of Graphene Oxide. *J. Am. Chem. Soc.* **2009**, *131* (13), 15939–15944.

(64) Panchakarla, L. S.; Subrahmanyam, K. S.; Saha, S. K.; Govindaraj, a.; Krishnamurthy, H. R.; Waghmare, U. V.; Rao, C. N. R. Synthesis, Structure and Properties of Boron and Nitrogen Doped Graphene. **2009**, 12.

(65) Zheng, B.; Cai, X. L.; Zhou, Y.; Xia, X. H. Pure Pyridinic Nitrogen-Doped Single-Layer Graphene Catalyzes Two-Electron Transfer Process of Oxygen Reduction Reaction. *ChemElectroChem* **2016**, *3* (12), 2036–2042.

(66) Yasuda, S.; Yu, L.; Kim, J.; Murakoshi, K. Selective Nitrogen Doping in Graphene for Oxygen Reduction Reactions. *Chem. Commun.* **2013**, *49* (83), 9627–9629.

(67) Yin, S.; Niu, Z.; Chen, X. Assembly of Graphene Sheets into 3D Macroscopic Structures. *Small* **2012**, *8* (16), 2458–2463.

(68) Chen, W.; Yan, L. In Situ Self-Assembly of Mild Chemical Reduction Graphene for Three-Dimensional Architectures. *Nanoscale* **2011**, *3* (8), 3132–3137.

(69) Sun, H.; Xu, Z.; Gao, C. Multifunctional, Ultra-Flyweight, Synergistically Assembled Carbon Aerogels. *Adv. Mater.* **2013**, *25* (18), 2554–2560.

(70) Worsley, M. A.; Kucheyev, S. O.; Mason, H. E.; Merrill, M. D.; Mayer, B. P.; Lewicki, J.; Valdez, C. A.; Suss, M. E.; Stadermann, M.; Pauzauskie, P. J.; Satcher, J. H.; Biener, J.; Baumann, T. F. Mechanically Robust 3D Graphene Macroassembly with High Surface Area. *Chem. Commun.* **2012**, *48* (67), 8428–8430.

(71) Chen, Z.; Ren, W.; Gao, L.; Liu, B.; Pei, S.; Cheng, H. M. Three-Dimensional Flexible and Conductive Interconnected Graphene Networks Grown by Chemical Vapour Deposition. *Nat. Mater.* **2011**, *10* (6), 424–428.

(72) Sohn, K.; Joo Na, Y.; Chang, H.; Roh, K. M.; Dong Jang, H.; Huang, J. Oil Absorbing Graphene Capsules by Capillary Molding. *Chem. Commun.* **2012**, *48* (48), 5968–5970.

(73) Zangmeister, C. D. Preparation and Evaluation of Graphite Oxide Reduced at 220 °C. *Chem. Mater.* **2010**, *22* (19), 5625–5629.

(74) Wang, W. N.; Jiang, Y.; Biswas, P. Evaporation-Induced Crumpling of Graphene Oxide Nanosheets in Aerosolized Droplets: Confinement Force Relationship. *J. Phys. Chem. Lett.* **2012**, *3* (21), 3228–3233.

(75) Zhu, W.; Low, T.; Perebeinos, V.; Bol, A. A.; Zhu, Y.; Yan, H.; Tersoff, J.; Avouris, P. Structure and Electronic Transport in Graphene Wrinkles. *Nano Lett.* **2012**, *12* (7), 3431–3436.

(76) Mao, S.; Lu, G.; Chen, J. Three-Dimensional Graphene-Based Composites for Energy Applications. *Nanoscale* **2015**, *7* (16), 6924–6943.

(77) Miao, P.; He, J.; Sang, Z.; Zhang, F.; Guo, J.; Su, D.; Yan, X.; Li, X.; Ji, H. Hydrothermal Growth of 3D Graphene on Nickel Foam as a Substrate of Nickel-Cobalt-Sulfur for High-Performance Supercapacitors. *J. Alloys Compd.* **2018**, *732*, 613–623.

(78) Trinsoutrot, P.; Vergnes, H.; Caussat, B. Three Dimensional Graphene Synthesis on Nickel Foam by Chemical Vapor Deposition from Ethylene. *Mater. Sci. Eng. B Solid-State Mater. Adv. Technol.* **2014**, *179* (1), 12–16.

(79) Lee, K.; Lee, J.; Kwon, K. W.; Park, M. S.; Hwang, J. H.; Kim, K. J. 3D Graphene-Ni Foam as an Advanced Electrode for High-Performance Nonaqueous Redox Flow Batteries. *ACS Appl. Mater. Interfaces* **2017**, *9* (27), 22502–22508.

(80) Hu, C.; Zhao, Y.; Cheng, H.; Wang, Y.; Dong, Z.; Jiang, C.; Zhai, X.; Jiang, L.; Qu, L. Graphene Microtubings: Controlled Fabrication and Site-Specific Functionalization. *Nano Lett.* **2012**, *12* (11), 5879–5884.

(81) Yoon, S. M.; Choi, W. M.; Baik, H.; Shin, H. J.; Song, I.; Kwon, M. S.; Bae, J. J.; Kim, H.; Lee, Y. H.; Choi, J. Y. Synthesis of Multilayer Graphene Balls by Carbon Segregation from Nickel Nanoparticles. *ACS Nano* **2012**, *6* (8), 6803–6811.

(82) Schwierz, F. Graphene Transistors. *Nat. Nanotechnol.* **2010**, *5*, 487.

(83) Marconcini, P.; Cresti, A.; Triozon, F.; Fiori, G.; Biel, B.; Niquet, Y. M.; MacUcci, M.; Roche, S. Atomistic Boron-Doped Graphene Field-Effect Transistors: A Route toward Unipolar Characteristics. *ACS Nano* **2012**, *6* (9), 7942–7947.

(84) Boukhvalov, D. W.; Son, Y. W.; Ruoff, R. S. Water Splitting over Graphene-Based Catalysts: Ab Initio Calculations. *ACS Catal.* **2014**, *4* (6), 2016–2021.

(85) Zhang, J.; Dai, L. Nitrogen, Phosphorus, and Fluorine Tri-Doped Graphene as a Multifunctional Catalyst for Self-Powered Electrochemical Water Splitting. *Angew. Chemie - Int. Ed.* **2016**, *55* (42), 13296–13300.

(86) Jia, Y.; Zhang, L.; Du, A.; Gao, G.; Chen, J.; Yan, X.; Brown, C. L.; Yao, X. Defect Graphene as a Trifunctional Catalyst for Electrochemical Reactions. *Adv. Mater.* **2016**, *28* (43), 9532–9538.

(87) Churchill, H. O. H.; Jarillo-Herrero, P. Two-Dimensional Crystals: Phosphorus Joins the Family. *Nat. Nanotechnol.* **2014**, *9* (5), 330–331.

(88) Zhu, J.; Xiao, P.; Li, H.; Carabineiro, S. A. C. Graphitic Carbon Nitride: Synthesis, Properties, and Applications in Catalysis. *ACS Appl. Mater. Interfaces* **2014**, *6* (19), 16449–16465.

(89) Liu, J.; Wang, H.; Antonietti, M. Graphitic Carbon Nitride “Reloaded”: Emerging Applications beyond (Photo)Catalysis. *Chem. Soc. Rev.* **2016**, *45* (8), 2308–2326.

(90) Lin, J.; Pan, Z.; Wang, X. Photochemical Reduction of CO_2 by Graphitic Carbon Nitride Polymers. *ACS Sustain. Chem. Eng.* **2014**, *2* (3), 353–358.

(91) Mao, J.; Peng, T.; Zhang, X.; Li, K.; Ye, L.; Zan, L. Effect of Graphitic Carbon Nitride Microstructures on the Activity and Selectivity of Photocatalytic CO_2 Reduction under Visible Light. *Catal. Sci. Technol.* **2013**, *3* (5), 1253.

(92) Zhao, Y.; Zhang, J.; Qu, L. Graphitic Carbon Nitride/Graphene Hybrids as New Active Materials for Energy Conversion and Storage. *ChemNanoMat* **2015**, *1* (5), 298–318.

(93) Dean, C. R.; Young, A. F.; Meric, I.; Lee, C.; Wang, L.; Sorgenfrei, S.; Watanabe, K.; Taniguchi, T.; Kim, P.; Shepard, K. L.; Hone, J. Boron Nitride Substrates for High-Quality Graphene Electronics. *Nat.*

Nanotechnol. **2010**, *5* (10), 722–726.

(94) Roy, T.; Tosun, M.; Kang, J. S.; Sachid, A. B.; Desai, S. B.; Hettick, M.; Hu, C. C.; Javey, A. Field-Effect Transistors Built from All Two-Dimensional Material Components. *ACS Nano* **2014**, *8* (6), 6259–6264.

(95) Lee, G.-H.; Yu, Y.-J.; Cui, X.; Petrone, N.; Lee, C.-H.; Choi, M. S.; Lee, D.-Y.; Lee, C.; Yoo, W. J.; Watanabe, K.; Taniguchi, T.; Nuckolls, C.; Kim, P.; Hone, J. Flexible and Transparent MoS_2 Field-Effect Transistors on Hexagonal Boron Nitride-Graphene Heterostructures. *ACS Nano* **2013**, *7* (9), 7931–7936.

(96) Ba, K.; Jiang, W.; Cheng, J.; Bao, J.; Xuan, N.; Sun, Y.; Liu, B.; Xie, A.; Wu, S.; Sun, Z. Chemical and Bandgap Engineering in Monolayer Hexagonal Boron Nitride. *Sci. Rep.* **2017**, *7*, 1–8.

(97) Jamieson, J. C. Crystal Structures Adopted by Black Phosphorus at High Pressures. *Science* **1963**, *139*, 1291–1292.

(98) Morita, A. Semiconducting Black Phosphorus. *Appl. Phys. A Solids Surfaces* **1986**, *39* (4), 227–242.

(99) Ren, X.; Zhou, J.; Qi, X.; Liu, Y.; Huang, Z.; Li, Z.; Ge, Y.; Dhanabalan, S. C.; Ponraj, J. S.; Wang, S.; Zhong, J.; Zhang, H. Few-Layer Black Phosphorus Nanosheets as Electrocatalysts for Highly Efficient Oxygen Evolution Reaction. *Adv. Energy Mater.* **2017**, *7* (19), 1–8.

(100) Jiang, Q.; Xu, L.; Chen, N.; Zhang, H.; Dai, L.; Wang, S. Facile Synthesis of Black Phosphorus: An Efficient Electrocatalyst for the Oxygen Evolving Reaction. *Angew. Chemie - Int. Ed.* **2016**, *55* (44), 13849–13853.

(101) He, R.; Hua, J.; Zhang, A.; Wang, C.; Peng, J.; Chen, W.; Zeng, J. Molybdenum Disulfide-Black Phosphorus Hybrid Nanosheets as a Superior Catalyst for Electrochemical Hydrogen Evolution. *Nano Lett.* **2017**, *17* (7), 4311–4316.

(102) Akhtar, M.; Anderson, G.; Zhao, R.; Alruqi, A.; Mroczkowska, J. E.; Sumanasekera, G.; Jasinski, J. B. Recent Advances in Synthesis, Properties, and Applications of Phosphorene. *npj 2D Mater. Appl.* **2017**, *1* (1), 5.

(103) Khandelwal, A.; Mani, K.; Karigerasi, M. H.; Lahiri, I. Phosphorene – The Two-Dimensional Black Phosphorous: Properties, Synthesis and Applications. *Mater. Sci. Eng. B Solid-State Mater. Adv. Technol.* **2017**, *221*, 17–34.

(104) Kitchaev, D. A.; Peng, H.; Liu, Y.; Sun, J.; Perdew, J. P.; Ceder, G. Energetics of MnO_2 Polymorphs in Density Functional Theory. *Phys. Rev. B* **2016**, *93* (4), 1–5.

(105) Pinaud, B. A.; Chen, Z.; Abram, D. N.; Jaramillo, T. F. Thin Films of Sodium Birnessite-Type MnO_2: Optical Properties, Electronic Band Structure, and Solar Photoelectrochemistry. *J. Phys. Chem. C* **2011**, *115* (23), 11830–11838.

(106) Lucht, K. P.; Mendoza-Cortes, J. L. Birnessite: A Layered Manganese Oxide to Capture Sunlight for Water-Splitting Catalysis. *J. Phys. Chem. C* **2015**, *119* (40), 22838–22846.

(107) Zhou, J.; Qin, L.; Xiao, W.; Zeng, C.; Li, N.; Lv, T.; Zhu, H. Oriented Growth of Layered-MnO_2 Nanosheets over α-MnO_2 Nanotubes for Enhanced Room-Temperature HCHO Oxidation. *Appl. Catal. B Environ.* **2017**, *207*, 233–243.

(108) Robinson, D. M.; Go, Y. B.; Mui, M.; Gardner, G.; Zhang, Z.; Mastrogiovanni, D.; Garfunkel, E.; Li, J.; Greenblatt, M.; Dismukes, G. C. Photochemical Water Oxidation by Crystalline Polymorphs of Manganese Oxides: Structural Requirements for Catalysis. *J. Am. Chem. Soc.* **2013**, *135* (9), 3494–3501.

(109) Li, Y. F.; Liu, Z. P. Active Site Revealed for Water Oxidation on Electrochemically Induced δ-MnO_2: Role of Spinel-to-Layer Phase Transition. *J. Am. Chem. Soc.* **2018**, *140* (5), 1783–1792.

(110) Shi, C.; Zang, G. L.; Zhang, Z.; Sheng, G. P.; Huang, Y. X.; Zhao, G. X.; Wang, X. K.; Yu, H. Q. Synthesis of

Layered MnO_2 Nanosheets for Enhanced Oxygen Reduction Reaction Catalytic Activity. *Electrochim. Acta* **2014**, *132*, 239–243.

(111) Wang, H.; Zhang, J.; Hang, X.; Zhang, X.; Xie, J.; Pan, B.; Xie, Y. Half-Metallicity in Single-Layered Manganese Dioxide Nanosheets by Defect Engineering. *Angew. Chemie - Int. Ed.* **2015**, *54* (4), 1195–1199.

(112) Zhao, Y.; Chang, C.; Teng, F.; Zhao, Y.; Chen, G.; Shi, R.; Waterhouse, G. I. N.; Huang, W.; Zhang, T. Defect-Engineered Ultrathin δ-MnO_2 Nanosheet Arrays as Bifunctional Electrodes for Efficient Overall Water Splitting. *Adv. Energy Mater.* **2017**, *7* (18), 1–7.

(113) Feng, Q.; Mao, N.; Wu, J.; Xu, H.; Wang, C.; Zhang, J.; Xie, L. Growth of $MoS_{2(1-x)}Se_{2x}$ (x = 0.41-1.00) Monolayer Alloys with Controlled Morphology by Physical Vapor Deposition. *ACS Nano* **2015**, *9* (7), 7450–7455.

(114) Zhang, W.; Li, X.; Jiang, T.; Song, J.; Lin, Y.; Zhu, L.; Xu, X. CVD Synthesis of $Mo_{(1-x)}W_xS_2$ and $MoS_{2(1-x)}Se_{2x}$ Alloy Monolayers Aimed at Tuning the Bandgap of Molybdenum Disulfide. *Nanoscale* **2015**, *7* (32), 13554–13560.

(115) Zheng, M.; Du, J.; Hou, B.; Xu, C.-L. Few-Layered $Mo_{(1-x)}W_xS_2$ Hollow Nanospheres on Ni_3S_2 Nanorod Heterostructure as Robust Electrocatalysts for Overall Water Splitting. *ACS Appl. Mater. Interfaces* **2017**, *9* (31), 26066–26076.

(116) Kosmala, T.; Coy Diaz, H.; Komsa, H. P.; Ma, Y.; Krasheninnikov, A. V.; Batzill, M.; Agnoli, S. Metallic Twin Boundaries Boost the Hydrogen Evolution Reaction on the Basal Plane of Molybdenum Selenotellurides. *Adv. Energy Mater.* **2018**, *8* (20), 1–8.

(117) Hussain, S.; Akbar, K.; Vikraman, D.; Karuppasamy, K.; Kim, H.-S.; Chun, S.-H.; Jung, J. Synthesis of $MoS_{2(1-x)}Se_{2x}$ and WS2(1-x)Se2x Alloy for Enhanced Hydrogen Evolution Reaction Performance. *Inorg. Chem. Front.* **2017**, 2068–2074.

(118) Gong, Q.; Cheng, L.; Liu, C.; Zhang, M.; Feng, Q.; Ye, H.; Zeng, M.; Xie, L.; Liu, Z.; Li, Y. Ultrathin $MoS_{2(1-x)}Se_{2x}$ Alloy Nanoflakes For Electrocatalytic Hydrogen Evolution Reaction. *ACS Catal.* **2015**, *5* (4), 2213–2219.

(119) Voiry, D.; Salehi, M.; Silva, R.; Fujita, T.; Chen, M.; Asefa, T.; Shenoy, V. B.; Eda, G.; Chhowalla, M. Conducting MoS_2 Nanosheets as Catalysts for Hydrogen Evolution Reaction. *Nano Lett.* **2013**, *13* (12), 6222–6227.

(120) Toh, R. J.; Sofer, Z.; Luxa, J.; Sedmidubský, D.; Pumera, M. 3R Phase of MoS_2 and WS_2 Outperforms the Corresponding 2H Phase for Hydrogen Evolution. *Chem. Commun.* **2017**, *53* (21), 3054–3057.

(121) Coutinho, S. S.; Tavares, M. S.; Barboza, C. A.; Frazão, N. F.; Moreira, E.; Azevedo, D. L. 3R and 2H Polytypes of MoS_2: DFT and DFPT Calculations of Structural, Optoelectronic, Vibrational and Thermodynamic Properties. *J. Phys. Chem. Solids* **2017**, *111*, 25–33.

(122) Shi, J.; Yu, P.; Liu, F.; He, P.; Wang, R.; Qin, L.; Zhou, J.; Li, X.; Zhou, J.; Sui, X.; Zhang, S.; Zhang, Y.; Zhang, Q.; Sum, T. C.; Qiu, X.; Liu, Z.; Liu, X. 3R MoS_2 with Broken Inversion Symmetry: A Promising Ultrathin Nonlinear Optical Device. *Adv. Mater.* **2017**, *29* (30), 1701486.

(123) Weber, T.; Muijsers, J. C.; Niemantsverdriet, J. W. The Structure of Amorphous MoS_3. *Bull. des Sociétés Chim. Belges* **1995**, *104* (4–5), 299–299.

(124) Benck, J. D.; Hellstern, T. R.; Kibsgaard, J.; Chakthranont, P.; Jaramillo, T. F. Catalyzing the Hydrogen Evolution Reaction (HER) with Molybdenum Sulfide Nanomaterials. *ACS Catal.* **2014**, *4* (11), 3957–3971.

(125) Nguyen, D. N.; Nguyen, L. N.; Nguyen, P. D.; Thu, T. V.; Nguyen, A. D.; Tran, P. D. Crystallization of Amorphous Molybdenum Sulfide Induced by Electron or Laser Beam and Its Effect on H_2-Evolving

Activities. *J. Phys. Chem. C* **2016**, *120* (50), 28789–28794.

(126) Yang, L.; Wu, X.; Zhu, X.; He, C.; Meng, M.; Gan, Z.; Chu, P. K. Amorphous Nickel/Cobalt Tungsten Sulfide Electrocatalysts for High-Efficiency Hydrogen Evolution Reaction. *Appl. Surf. Sci.* **2015**, *341*, 149–156.

(127) Yu, W. J.; Liu, Y.; Zhou, H.; Yin, A.; Li, Z.; Huang, Y.; Duan, X. Highly Efficient Gate-Tunable Photocurrent Generation in Vertical Heterostructures of Layered Materials. *Nat. Nanotechnol.* **2013**, *8* (12), 952–958.

(128) Desai, S. B.; Madhvapathy, S. R.; Sachid, A. B.; Llinas, J. P.; Wang, Q.; Ahn, G. H.; Pitner, G.; Kim, M. J.; Bokor, J.; Hu, C.; Wong, H.-S. P.; Javey, A. MoS_2 Transistors with 1-Nanometer Gate Lengths. *Science* **2016**, *354*, 99.

(129) Yu, W. J.; Li, Z.; Zhou, H.; Chen, Y.; Wang, Y.; Huang, Y.; Duan, X. Vertically Stacked Multi-Heterostructures of Layered Materials for Logic Transistors and Complementary Inverters. *Nat. Mater.* **2013**, *12* (3), 246–252.

(130) Bertolazzi, S.; Krasnozhon, D.; Kis, A. Nonvolatile Memory Cells Based on MoS_2/Graphene Heterostructures. *ACS Nano* **2013**, *7* (4), 3246–3252.

(131) Zhang, W.; Chuu, C.-P.; Huang, J.-K.; Chen, C.-H.; Tsai, M.-L.; Chang, Y.-H.; Liang, C.-T.; Chen, Y.-Z.; Chueh, Y.-L.; He, J.-H.; Chou, M.-Y.; Li, L.-J. Ultrahigh-Gain Photodetectors Based on Atomically Thin Graphene-MoS_2 Heterostructures. *Sci. Rep.* **2015**, *4* (1), 3826.

(132) Cao, X.; Shi, Y.; Shi, W.; Rui, X.; Yan, Q.; Kong, J.; Zhang, H. Preparation of MoS_2-Coated Three-Dimensional Graphene Networks for High-Performance Anode Material in Lithium-Ion Batteries. *Small* **2013**, *9* (20), 3433–3438.

(133) Chang, K.; Chen, W. L -Cysteine-Assisted Synthesis of Layered MoS_2/Graphene Composites with Excellent Electrochemical Performances for Lithium Ion Batteries. *ACS Nano* **2011**, *5* (6), 4720–4728.

(134) Feng, C.; Ma, J.; Li, H.; Zeng, R.; Guo, Z.; Liu, H. Synthesis of Molybdenum Disulfide (MoS_2) for Lithium Ion Battery Applications. *Mater. Res. Bull.* **2009**, *44* (9), 1811–1815.

(135) Zhang, H.; Yun, Q.; Lu, Q.; Zhang, X.; Tan, C. Three-Dimensional Architectures Constructed from Transition Metal Dichalcogenide Nanomaterials for Electrochemical Energy Storage and Conversion. *Angew. Chemie* **2018**, *57*, 626–646.

(136) Feng, J.; Sun, X.; Wu, C.; Peng, L.; Lin, C.; Hu, S.; Yang, J.; Xie, Y. Metallic Few-Layered VS_2 Ultrathin Nanosheets: High Two-Dimensional Conductivity for in-Plane Supercapacitors. *J. Am. Chem. Soc.* **2011**, *133* (44), 17832–17838.

(137) Yang, Y.; Fei, H.; Ruan, G.; Xiang, C.; Tour, J. M. Edge-Oriented MoS_2 Nanoporous Films as Flexible Electrodes for Hydrogen Evolution Reactions and Supercapacitor Devices. *Adv. Mater.* **2014**, *26* (48), 8163–8168.

(138) Nam, M. S.; Patil, U.; Park, B.; Sim, H. B.; Jun, S. C. A Binder Free Synthesis of 1D PANI and 2D MoS_2 Nanostructured Hybrid Composite Electrodes by the Electrophoretic Deposition (EPD) Method for Supercapacitor Application. *RSC Adv.* **2016**, *6* (103), 101592–101601.

(139) Zhou, H.; Yu, F.; Huang, Y.; Sun, J.; Zhu, Z.; Nielsen, R. J.; He, R.; Bao, J.; Goddard III, W. A.; Chen, S.; Ren, Z. Efficient Hydrogen Evolution by Ternary Molybdenum Sulfoselenide Particles on Self-Standing Porous Nickel Diselenide Foam. *Nat. Commun.* **2016**, *7*, 12765.

(140) Pesci, F. M.; Sokolikova, M. S.; Grotta, C.; Sherrell, P. C.; Reale, F.; Sharda, K.; Ni, N.; Palczynski, P.; Mattevi, C. MoS_2/WS_2 Heterojunction for Photoelectrochemical Water Oxidation. *ACS Catal.* **2017**, 4990–4998.

(141) Asadi, M.; Kumar, B.; Behranginia, A.; Rosen, B. A.; Baskin, A.; Repnin, N.; Pisasale, D.; Phillips, P.; Zhu, W.; Haasch, R.; Klie, R. F.; Král, P.; Abiade, J.; Salehi-Khojin, A. Robust Carbon Dioxide Reduction on Molybdenum Disulphide Edges. *Nat. Commun.* **2014**, *5*, 1–8.

(142) Asadi, M.; Kim, K.; Liu, C.; Addepalli, A. V.; Abbasi, P.; Yasaei, P.; Phillips, P.; Behranginia, A.; Cerrato, J. M.; Haasch, R.; Zapol, P.; Kumar, B.; Klie, R. F.; Abiade, J.; Curtiss, L. A.; Salehi-Khojin, A. Nanostructured Transition Metal Dichalcogenide Electrocatalysts for CO_2 Reduction in Ionic Liquid. *Science* **2016**, *353* (6298), 467–470.

Chapter Two:

Promotion of the hydrogen evolution kinetics by Ni-doping of 3D-structured MoS_2 in acid and alkaline media

2.1 Introduction

As already mentioned in Section 1.2.1, *hydrogen economy* is one the most promising perspectives in the *Green Economy* area. The most common method to produce large quantities of hydrogen, *i.e.* steam reforming of methane or light alcohols, is neither clean nor sustainable. In addition, the final product contains small amounts of CO that constitutes a poison for the Pt-based catalysts used in FCs, limiting their lifecycles.[1] Electrolysers, based on the electrocatalytic water splitting (WS), are emerging as the best devices to obtain clean hydrogen through hydrogen evolution reaction (HER).[2] However, to be exploitable, WS must be boosted by suitable electrocatalysts. In other words, the role of HER electrocatalysts at the cathode is fundamental: they must be based on cost-effective non-critical raw materials (i.e. noble metals-free) and guarantee efficiency, durability in operating condition and cost-effectiveness. Moreover, the electrocatalyst has to work efficiently also in basic media, where HER is usually hindered, in order to boost the oxygen evolution reaction at the counter electrode.

The influence of the pH on the cathodic half-reaction can be easily described taking into consideration the two accredited mechanisms for HER (i.e. Volmer-Heyrovsky and Volmer-Tafel) that result from the composition of two out of the following reactions steps:[3,4]

Volmer step (Electrochemical Hydrogen Adsorption):

$$Acid\colon\ H_3O^+ + e^- \leftrightarrows H_{ads} + H_2O$$
$$Base\colon H_2O + e^- \leftrightarrows H_{ads} + OH^-$$

Heyrovsky step (Electrochemical Desorption):

$$Acid\colon H_{ads} + \ H_3O^+ + e^- \leftrightarrows H_2 + H_2O$$
$$Base\colon H_{ads} + H_2O + e^- \leftrightarrows H_2 + OH^-$$

Tafel Step (Chemical Desorption):

$$2H_{ads} \leftrightarrows H_2$$

Hence, the electrocatalyst HER performances can be dramatically influenced because different species have to be adsorbed and reduced in steps that are affected by pH change. For instance, Durst *et al.* demonstrated that kinetics parameters of some noble metals (Pt, Ir and Ru) are strongly pH dependent and that a two order of magnitude activity decrease on all these surfaces when going from low to high pH. [3] These issues arise from the extra energy needed for breaking the covalent H-OH bond, which clearly is harder to cleave than the dative $^+$H-OH$_2$ bond.[4] Moreover, hydroxyl anions could poison metal sites, hindering the catalytic activity, even in precious metal-based catalysts.

For these reasons, in literature a relatively low number of papers addressing HER in alkali media are present with respect to the huge amount of catalyst explored for HER in acid. On the other hand, when exploring catalysts in acidic conditions, stability issues of non-noble metals may arise. As an alternative to the unsustainable noble-metal based catalysts, earth-abundant transition metals-based catalyst are currently investigated,[5,6] in the form of metal or alloys, carbides and nitrides,[7] and, above all, transition metals dichalcogenides (TMDCs).[8] TMDCs are 2D-layered materials and, especially MoS_2 has been extensively studied as HER electrocatalyst, mainly in acidic media, whereas few people studied it at different pH. As

elegantly demonstrated by Wiensch and coworkers, MoS_2 has diverse preferential sites for the HER at different pH: [9] Mo-terminated edge sites are active at low pH because of thermoneutral adsorption of hydrogen on Mo site, but in hydroxyl rich environment the formation of Mo-H is inhibited and S-rich terraces become the preferential site for HER.[10] Therefore, in MoS_2-based materials exposing high quantity of edges only HER in acid would be enhanced, while paradoxically HER in alkaline medium would be enhanced by exposing large terraces. Indeed, as proven by calculations, on Mo-edge the prior dissociation of water is the limiting step in alkaline HER, because of the formation of strong Mo-OH bond, slowing down OH^- desorption and consequently tearing down the turnover number of the Volmer step.[11,12] However, the work of Wiensch demonstrated as well that in polycrystalline and defective MoS_2, exposing similar quantity of edge-like and basal plane sites, it is possible to obtain similar performances in acidic and alkaline ambient.

Hence, one actual goal is to design MoS_2 catalysts to obtain pH-independent HER. This can be addressed also by taking advantage of the knowledge about the handling of 2D-layered materials gained in the last few years from the graphene field. In particular, in recent years the attention moved from simple 2D sheets[13–19] to 3D-structured systems,[20–26] that ensure higher surface areas and number of exposed catalytic sites. To improve the intrinsic catalytic activity of MoS_2, also doping with transition metals has been proposed. Theoretical calculations were carried out and a better catalytical performance was predicted because of the doping.[27,28] In 2015 Tsai *et al*. published the results of their calculations, in which they covered the effect of doping of a wide array of 19 transition metals on MoS_2.[29] Nevertheless, the introduction of a different cation in the lattice can cause the modification of the structure, which can also influence the HER.

In this paper, we prepared 3D-structured MoS_2 samples (hereafter 3D-MoS_2) obtained starting from ammonium tetrathiomolybdate (ATM) using a procedure that also allows to introduce the dopant by a simple one-pot. We then studied the effects of Ni doping both on the 3D-MoS_2 structure and the catalytic performances in HER, both in acidic and in basic media.[10,21,30]

2.2 Experimental Section

ATM Synthesis

Ammonium Molybdate $(NH_4)_6Mo_7O_{24} \cdot 4H_2O$ (3 g; 2.43 mmol, from Sigma-Aldrich) was dissolved under stirring in 45 ml of aqueous $(NH_4)_2S$ (20 %wt, from Fluka) in a closed bottle. When a clear solution was obtained, stirring was stopped and the solution was keep at r.t. for 1h. Afterwards, the solution was kept at 4°C overnight to allow the formation of deep red needle-like crystals. ATM crystals were filtered under a gentle Ar flow and washed with cold water and cold ethanol. The product was then dried under nitrogen and stored in inert gas (3.5 g; yield 79.1 %).

3D-MoS_2 Synthesis

ATM (300 mg; 1.15 mmol) and the dopant precursor $NiCl_2 \cdot 6H_2O$ were dissolved in the selected volume of water (milliQ 18.2 MΩ, degassed with N_2 for 1h) by helping with 2h sonication.

ATM concentration (mg/ml):	*Water Volume (ml):*
5	60
10	30
25	12
Dopant %at. (vs Mo):	*$NiCl_2 \cdot 6H_2O$ (mg):*
2% Ni	5.5
5% Ni	13.7
10% Ni	27.4
15% Ni	41.1

Table 2.1. Summary of the samples prepared in the present paper.

After cooling down at r.t., the so-obtained grey powder was collected apart and stored under nitrogen to prevent surface oxidation.

Physico-chemical characterization

X-ray photoemission spectroscopy (XPS) data was acquired by a custom-designed UHV system equipped with an EA 125 Omicron electron analyzer with five channeltrons, working at a base pressure of 10^{-9} mbar. Core level photoemission spectra were taken in normal emission using the Mg Kα line (hv = 1253.6 eV) of a nonmonochromatized dual-anode DAR400 X-ray source. High resolution spectra were acquired using 0.5s dwell time, 0.1 eV energy steps, and 20 eV pass energy. In the case of Ni $2p_{3/2}$ region, the parameters were set to 0.25s dwell time, 0.2 eV energy step and 50 eV pass energy, in order to obtain a better signal-to-noise ratio. In the same conditions, a set of measurement (not shown) of Mo 3d and S 2p core levels was acquired as well to calculate the surface composition. The multipeak analysis of S 2p, Mo 3d and Ni $2p_{3/2}$ photoemission lines was performed by means of Gaussian–Lorentzian functions and subtracting a Shirley background using the *KolXPD* software.

Scanning electron microscopy (SEM) micrographs were acquired using a field emission source equipped with a GEMINI column (Zeiss Supra VP35) with an acceleration voltage of 5 kV using secondary electrons detection.

Raman spectroscopy was carried out with a ThermoFisher DXR Raman microscope. The spectra were recorded using a laser with an excitation wavelength of 532 nm (0.1 mW), focused on the sample with a 50× objective (Olympus).

EDX analysis and mapping were performed by using a FEI Tecnai G2 F20 TWIN TMP with a Schottky emitter operated at 200 kV. The EDX analyses have been acquired using a Bruker XFlash 6|T30 silicon-drift detector (SDD), with 30 mm^2 effective area.

The X-ray diffraction (XRD) characterization was performed with a Philips PW 1729, configured with a glancing angle geometry, operating with Cu K_α radiation (λ = 0.15406 nm) generated at 30 kV and 40 mA. The mean crystallite size was calculated from the MoS_2(002) peak using the Scherrer equation: $L_c = k \cdot \lambda / ß \cdot \cos\theta$, where *k* is the shape factor (k = 0.9), λ is the X-ray wavelength, *ß* is the line broadening at half the maximum intensity of the peak, and θ is the Bragg angle.

Electrochemical Characterization

The electrochemical studies were performed in a conventional three-electrode electrochemical cell, using an Ag/AgCl (3M KCl) electrode (calibrated as +0.218 V vs. the reversible hydrogen electrode, RHE) and a Pt wire as reference and counter electrode, respectively. For the long duration chronopotentiometric measurements, a glassy carbon (GC) rod was used as counter electrode. The working electrode was prepared by depositing 2.5 µl of catalyst ink on a GC electrode (2.8 mm diameter), corresponding to an active material loading of 142 µg cm^{-2}. The catalyst ink consisted of 2 mg of active material and 2 mg of Vulcan XC-72 carbon, grinded in a mortar and subsequently suspended in 0.5 mL of N,N-dimethylformamide and 5 µL of Nafion solution. The measurements were carried out in N_2-saturated 0.5 M H_2SO_4 or 1.0 M KOH at room temperature. Polarization curves were recorded from +0.2 V to -0.5 V vs RHE using a scan rate of 0.005 V s^{-1}. *V-t* curves were recorded at 10 mA/cm^2 for 15 h. Currents presented in the text are normalized by the geometrical area and iR-corrected by using the resistance determined by electrochemical impedance spectroscopy (EIS) measurements. EIS was performed at η = 0.28 V and fitted using a R(RQ) as equivalent circuit.

2.3 Results and Discussion

2.3.1 Preliminary study on 3D-MoS_2 scaffold

It is already reported in literature that using a freeze-drying process ATM can form 3D networks, that are maintained also during the chemical conversion to MoS_2, whose density can be tuned by changing the precursor concentration,[21] because the volume of the final product is related to the volume of the ice formed during the freeze-drying process. Starting from this literature achievement, in the first part of this work we tried to optimize the morphology/stability of the MoS_2 scaffold. We performed the synthesis using ATM solutions with several different concentrations. In order to demonstrate the limit of the mechanical stability of the final material, that is if ATM is too diluted, the 3D-network can collapse during the freeze-drying process. We report here the results achieved with 5, 10 and 25 mg/ml ATM solutions (hereafter named as MoS_2-5, MoS_2-10 and MoS_2-25, respectively). We found that the samples obtained with ATM solutions of 10 and 25 mg/ml concentration maintained their shape both during freeze-drying and during the annealing step, while the material obtained with 5 mg/ml solution underwent to network collapse during the drying step.

To decide the best scaffold, preliminary HER tests on these materials were performed 0.5 M H_2SO_4. In Figure 2.1, polarization curves and Tafel plots for the three samples are reported. From the kinetics point of view, samples MoS_2-10 and MoS_2-25 show a better Tafel slope, which may be due to a higher amount of defects in the scaffold. As expected, the materials behaved similarly at low overpotential: the differences in the onset potential and overpotential at 10 mA/cm^2 were lower than 30 mV among the three samples. However, at higher overpotentials, differences in the current densities were observed, being the MoS_2-10 sample the most active one. Therefore, study on doped materials was based on MoS_2-10 scaffold, hereafter named simply as undoped 3D-MoS_2.

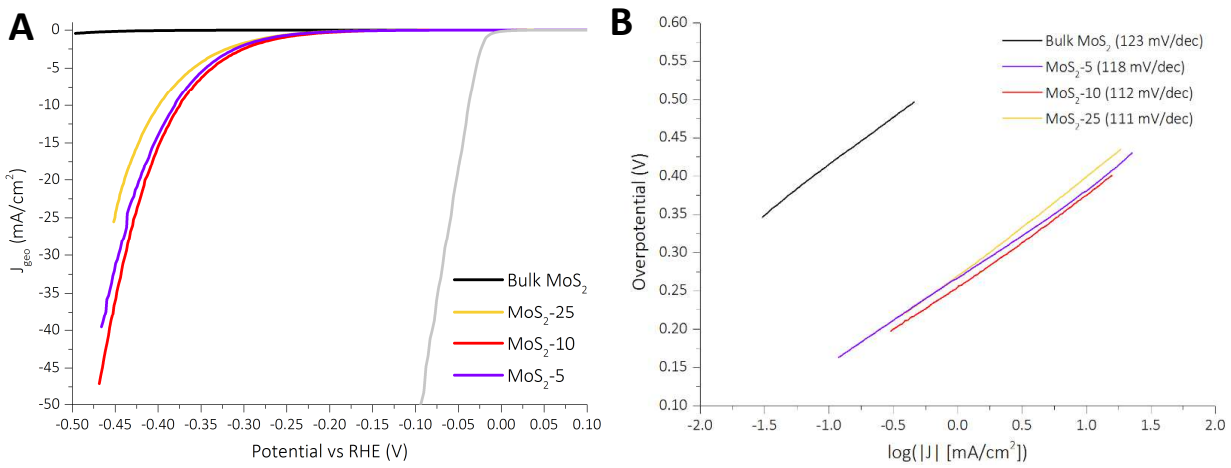

Figure 2.1. Polarization curves (A) and Tafel plot (B) for undoped 3D-MoS_2 materials prepared with different starting solutions.

2.3.2 Synthesis and physico-chemical characterization

In Figure 2.2A, we report SEM image of 3D structure of the designed scaffold in which the typical lamellar structure of MoS_2 is clearly evident. The same lamellar structure is also maintained in all Ni-doped 3D-MoS_2 samples (2, 5, 10 and 15 % at. vs Mo) as can be seen in Figure 2.3. This suggests that the metal doping has not a significant effect on the morphology, although a slightly denser structure can be observed when higher Ni loadings are used. In all cases, as shown *via* TEM and EDX chemical mapping (Figure 1B-Q), we observe a homogeneous distribution of Ni in the 3D-MoS_2 lattice independently of the percentage of the Ni-doping.

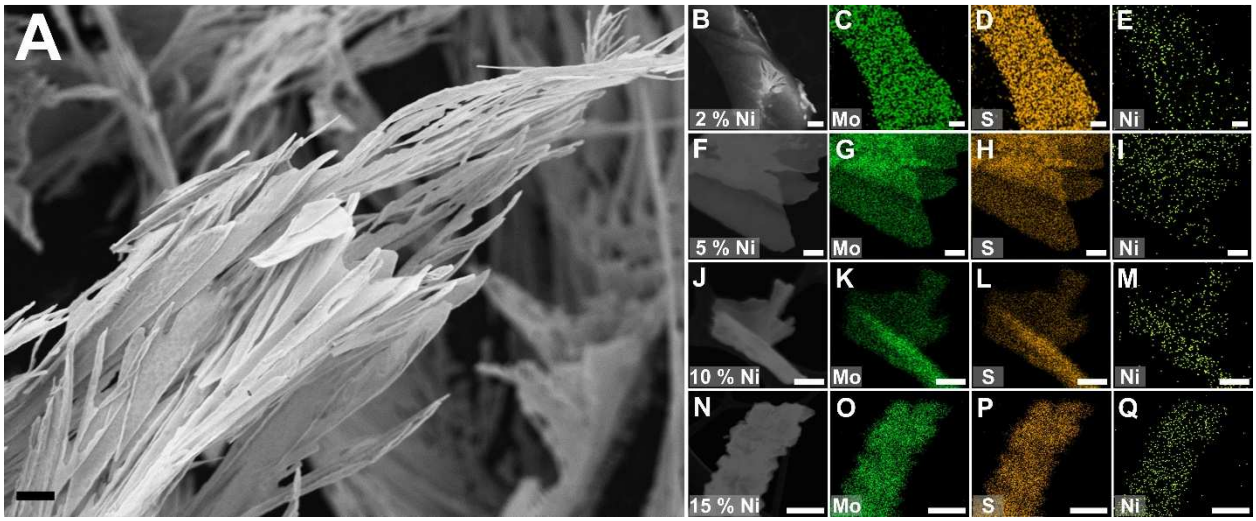

Figure 2.2. *A)* SEM image of undoped 3D-MoS_2-10 undoped sample (scale bar: 2 µm). TEM image with EDX chemical mapping of Mo, S and Ni for the Ni-doped 3D-MoS_2 samples (scale bar: 300 nm) with the Ni-doping of 2 % (B-D), 5 % (F-I), 10 % (J-M) and 15 % (N-Q), respectively.

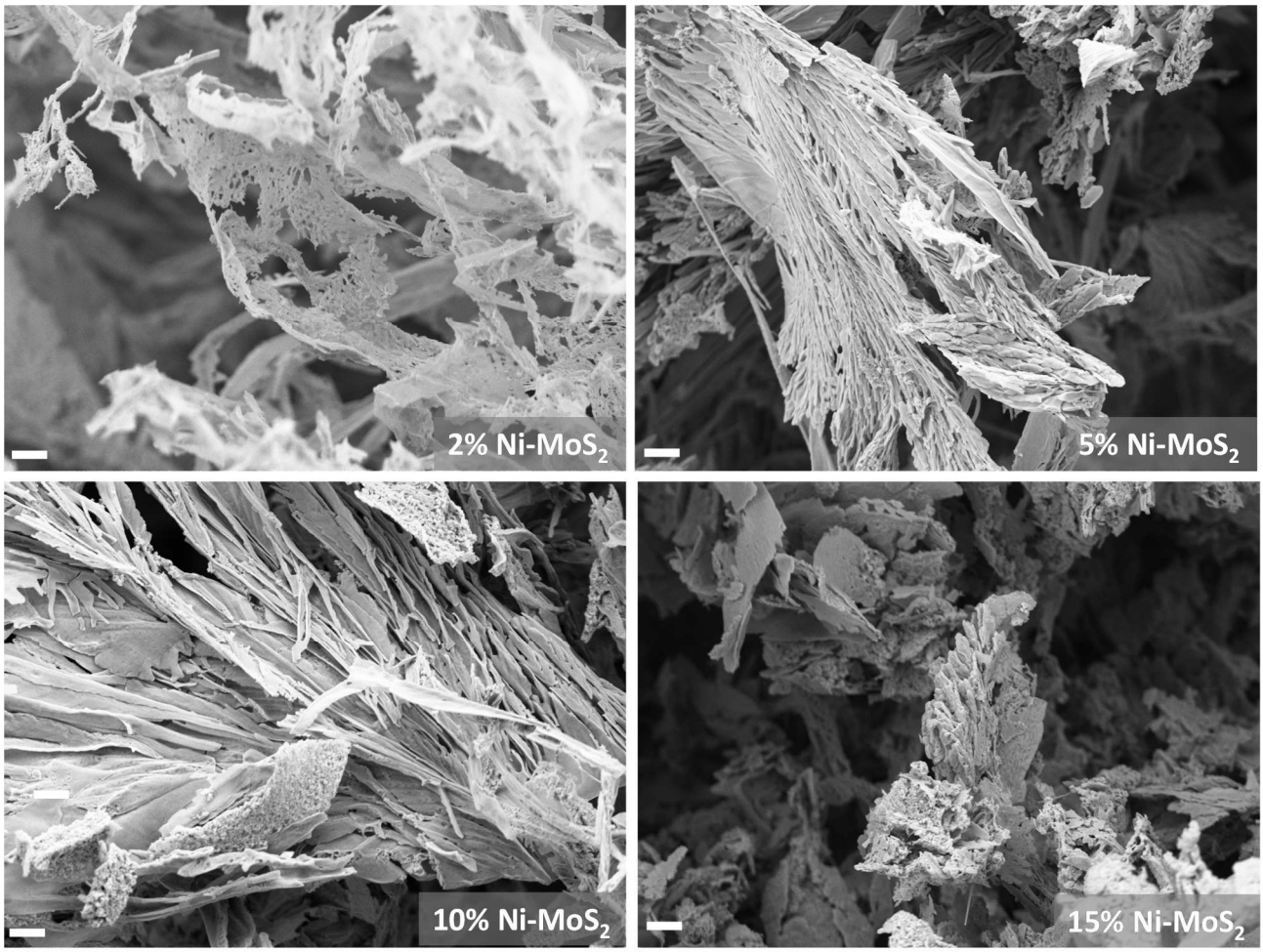

Figure 2.3. SEM images for Ni-doped 3D-MoS_2 (scale bar: 2 µm).

The incorporation of Ni in the MoS_2 lattice was investigated by XRD and Raman spectroscopy and the results are reported in Figure 2.4. Figure 2.4A shows the XRD patterns of the Ni-doped 3D-MoS_2 and as well undoped 3D-MoS_2. All the samples show four main peaks at 2θ values of 13.8°, 33.1°, 39.3° and 58.9° attributed to the (002), (100), (103) and (110) reflections of the hexagonal structure of MoS_2 (see XRD pattern of the commercial MoS_2).[31] The diffraction peaks slightly shift to higher 2θ values when the Ni content increases, suggesting a contraction of the MoS_2 lattice cell due to the incorporation of Ni into the MoS_2 structure. This result is in agreement with the fact that Ni has an atomic radius (1.49 Å) smaller than that of Mo (1.90 Å). In addition, the diffraction peaks become narrower when the Ni doping increases. This indicates that Ni induces the growth of MoS_2 crystallites above a certain amount. No extra-peak clearly associated with Ni sulfides/oxides is observed, further confirming the Ni incorporation into the MoS_2 structure. The crystallite size was calculated from the (002) peak by using the Scherrer equation. The undoped 3D-MoS_2 sample showed a crystallite size of 3.8 nm that remained almost unchanged when a 2-5 at.% of Ni was added (~ 4.0 nm). However, when the Ni content increased up to 10 and 15 at.%, the crystallite size was 5 nm and 9.7 nm, respectively (see Figure 2.4B). This is further confirmed by the appearance of high index reflections of MoS_2 lattice at 38.3° and 44.5°, assigned to (104) and (009) facets. The increase of particles dimensions can be also associated to the formation of $[Ni(MoS_4)_2]^{2-}$ complex in the starting ATM solution, that may induce a different behavior during the synthesis with respect to uncomplexed ATM.[32,33]

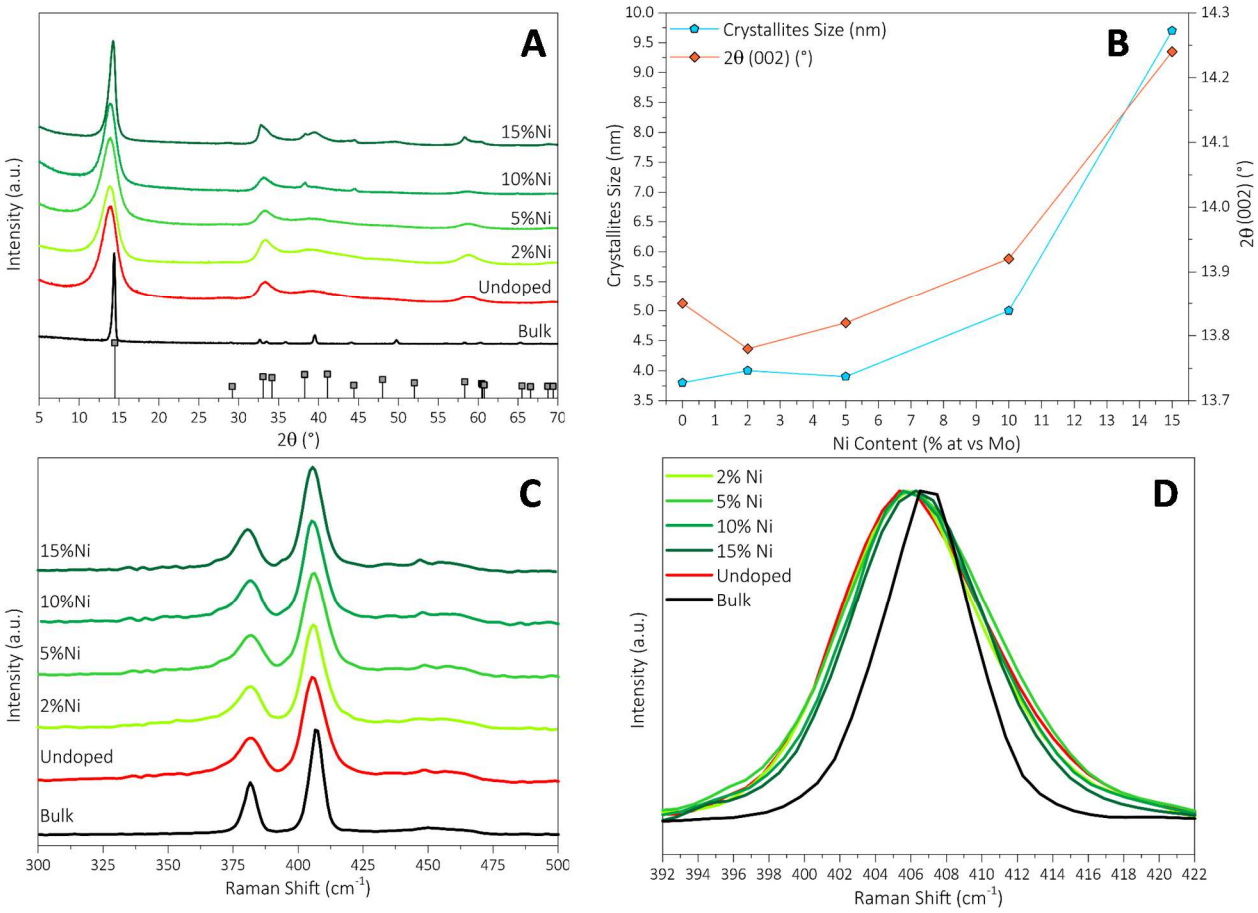

Figure 2.4. XRD and Raman data of the Ni-doped 3D-MoS_2 as a function of Ni loading. (A) XRD patterns, bulk MoS_2 data are reported as a reference; (B), crystallite size and 2θ (002) using the Scherrer equation; (C) Raman spectra and (D) detail of A_{1g} peak for the 3D-MoS_2 samples. Reference XRD data: ICDD Nr. 00-086-2308.

Figure 2.4C shows the Raman spectra for the 3D-MoS_2 samples and the commercial bulk MoS_2 sample (Aldrich). All the samples show two bands at around 380 cm^{-1} and 405 cm^{-1} that correspond to the in-plane E^1_{2g} and out-of-plane A_{1g} vibrational modes, respectively, characteristic of 2H-MoS_2.[34] Compared to the bulk commercial sample, the 3D based samples show a broader A_{1g} band that can be associated with a small number of stacked layers along the *c* axis,[35] confirming the limited growth and smaller size of the 3D-MoS_2 lamellae and the defective nature of 3D materials. As the amount of Ni dopant increased, a slight shift of the A_{1g} band toward higher values was observed (Figure 2.4D). The separation between the E^1_{2g} and A_{1g} bands is usually adopted to calculate the number of stacked layers,[35] indicating that high Ni loadings induce a higher stacking of the MoS_2 layers, in agreement with the XRD results. However, the differences were not significant and all the materials range between 4 and 5 layers.

XPS was used to further investigate the incorporation of Ni in the MoS_2 structure and the relative electronic effect, since it can reveal different chemical environments as well as variations of the electronic structure of the 3D-MoS_2 scaffold.[10] First of all the XPS data allow to obtain the surface composition of the whole series of Ni-doped samples (Table 2.2): in all the cases the Ni surface composition is proportional to the nominal Ni loading values set during the one-pot synthesis.

	% Mo	*% S*	*% Ni*	*S/Mo*	*Ni/Mo*
Bulk MoS_2	32.9	67.1	-	2.0	-
Undoped 3D-MoS_2	33.5	66.5	-	2.0	-
2%Ni 3D-MoS_2	33.0	66.1	0.9	2.0	2.7
5%Ni 3D-MoS_2	33.3	65	1.7	2.0	5.1
10%Ni 3D-MoS_2	32.2	64.4	3.4	2.0	10.6
15%Ni 3D-MoS_2	32.4	62.2	5.4	1.9	16.7

Table 2.2. Surface composition of Bulk MoS_2, undoped and Ni-doped 3D-MoS_2 materials.

Mo 3d and S 2p XPS core levels of the are shown in Figure 2.5, whereas the corresponding regions Ni $2p_{3/2}$ can be found in Figure 2.6. Mo 3d and S 2p XPS regions of the commercial bulk sample are also presented for comparison in order to gauge the effect of the morphology on the electronic structure of the material. Mo 3d peak of the bulk MoS_2 was fitted using two doublets whose larger components are at a binding energy (BE) of 229.1 eV and 232.2 eV, assigned to Mo(IV) in 2H-MoS_2 and to Mo(VI) in MoO_3 surface oxide (due to the oxidation in air, 4 at.% of total Mo), respectively (Figure 2.5). S 2p peak was fitted with a single component at 161.8 eV in agreement with the values reported in the literature.[36] For undoped 3D-MoS_2, the deconvolution of Mo 3d XPS peak revealed one main component at BE of 228.9 eV (2H-MoS_2) and a smaller amount of MoO_3 (232.1 eV) with respect to bulk MoS_2 (1.3 at.%). The analysis of the S 2p region showed the presence of a single component at 161.7 eV, assigned to S^{2-} species. It is worth noting that the absence of components related to a S_2^{2-} dimer (expected at ca. 163.0 eV) is a clear indication that there is no residual precursor in the samples, so that conversion from ATM to MoS_2 was complete.[37,38] The small BE shift of the Mo 3d and S 2p XPS peaks of the bulk MoS_2 with respect to the 3D-MoS_2 is attributed to the higher nanoparticles size of the former.[39]

The same analysis was performed on Ni-doped 3D-MoS_2 samples and similar features were found, i.e. a main component attributed to 2H-MoS_2, as well as a minor component related to MoO_x species (4-6 at.%, slightly higher than undoped 3D-MoS_2). This means that the Ni addition does not induce any restructuring of the MoS_2 layers and that a small number of Mo atoms transforms the Mo-S bonds into Mo-O bonds when Ni atoms are introduced. A 0.1 eV shift toward lower BEs was observed in the MoS_2 component of the Mo 3d peak, compared to the undoped sample. This shift can be attributed to the modification of the electronic environment of Mo due to the incorporation of Ni. This is expected to have an effect on the electrochemical properties of MoS_2, since it indicates an electron-richer surface.[10]

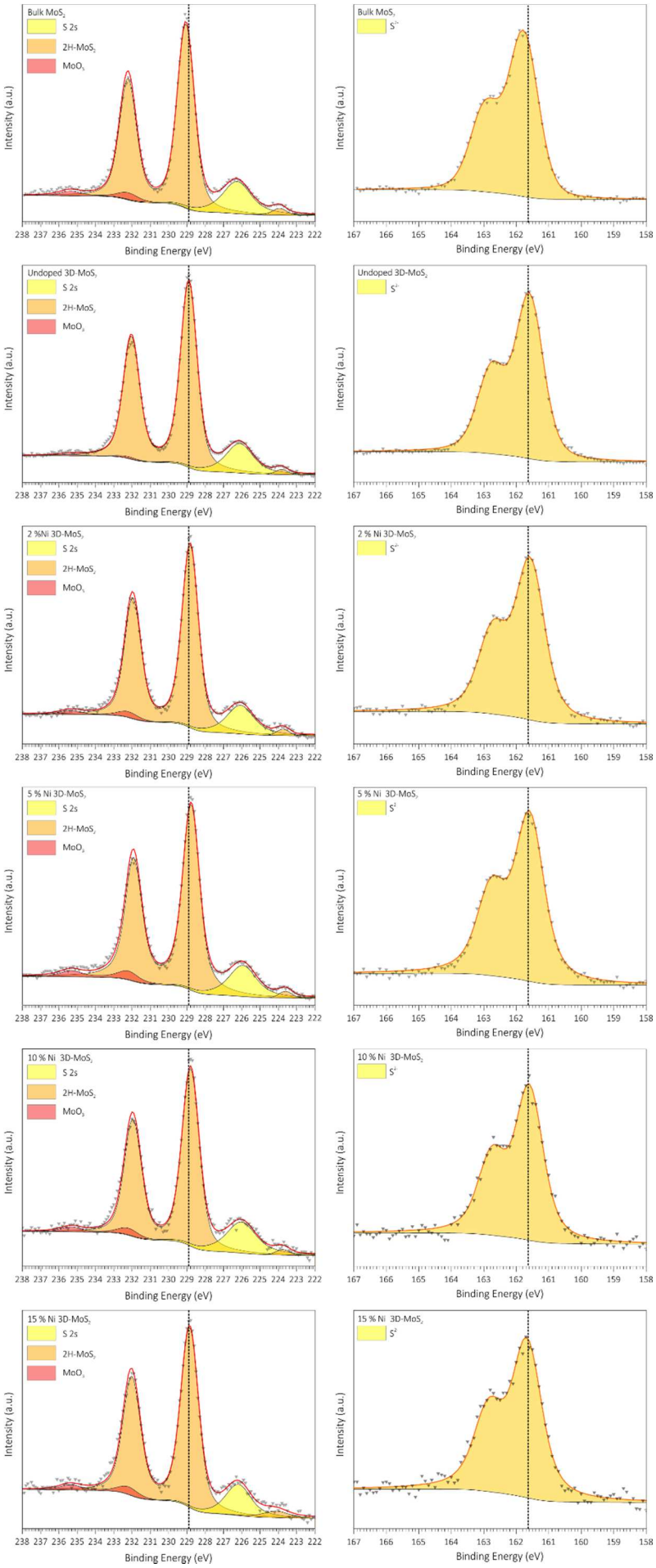

Figure 2.5. Mo 3d and S 2p XPS regions for Bulk MoS_2, undoped and Ni-doped 3D-MoS_2 samples. Dotted lines in graphs refer to BE values found for undoped 3D-MoS_2.

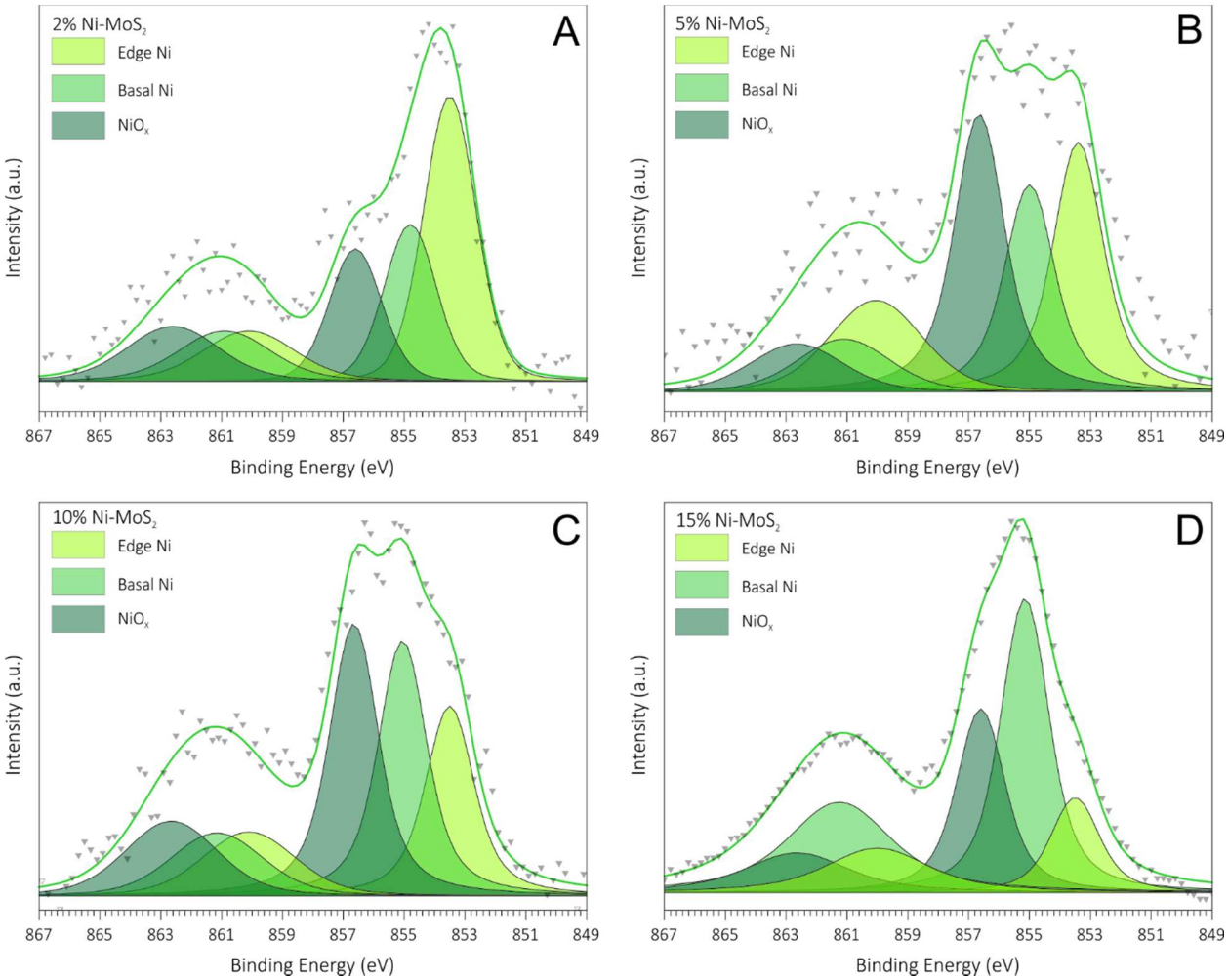

Figure 2.6. Multipeak analysis of Ni $2p_{3/2}$ photoemission region for Ni-doped 3D-MoS_2 samples at different Ni loadings: A) 2%Ni; B) 5%Ni; C) 10%Ni and D) 15%Ni.

According to the literature, the Ni atoms are incorporated in the MoS_2 network by substituting Mo atoms and, according to DFT calculations and other studies reported in the literature, such substitutional doping is believed to start from edges to subsequently pass to basal plane insertion.[29,30,40,41] Let us see if our XPS data can be interpreted following such a picture from the analysis of Ni $2p_{3/2}$ core-level spectra.

The Ni $2p_{3/2}$ peak was separated into chemically shifted components in order to gauge the nature of the Ni species. Three components at BEs of 853.5 eV, 855.0 eV and 856.6 eV were included in the fit, which were tentatively attributed to edge-substitional Ni, basal plane-substitutional Ni and NiO_x species, respectively.[32,33,42,43] Then, we analyzed the evolution of each component as a function of the Ni doping (Table 2.3, Figure 2.7), comparing the results with the existing models for Ni doping. Following such a method, we have found a decrease of the lower BE component with the increase of the Ni amount, while the component at 855.0 eV follows the opposite trend. In other words, our XPS data suggests that the substitution of Mo atoms at the edge is first favored (Ni-edge component), whereas the substitution of Mo atoms in the basal plane is favored for higher amounts of dopant after the substitution of edge Mo atoms (Ni-basal component). This is exactly what is expected on the basis of the DFT predictions and other studies reported in the literature: substitutional doping is believed to begin from edges to subsequently pass to basal plane

insertion.[29,30,32,40–44] This is also in tune with our XRD data that say that Ni is substitutional. When in the basal plane, Ni tends to relax assuming an under-coordinated structure with respect to Mo (4-fold S coordination *vs* 6-fold S for Mo), leaving unbounded S atoms and justifying the BE shift observed between the edge and bulk Ni components of the Ni $2p_{3/2}$ line.[40,45–49] On the other hand, the NiO_x component, seems to be independent on the Ni content, and in all the samples is about a 30 at.% of the total Ni.

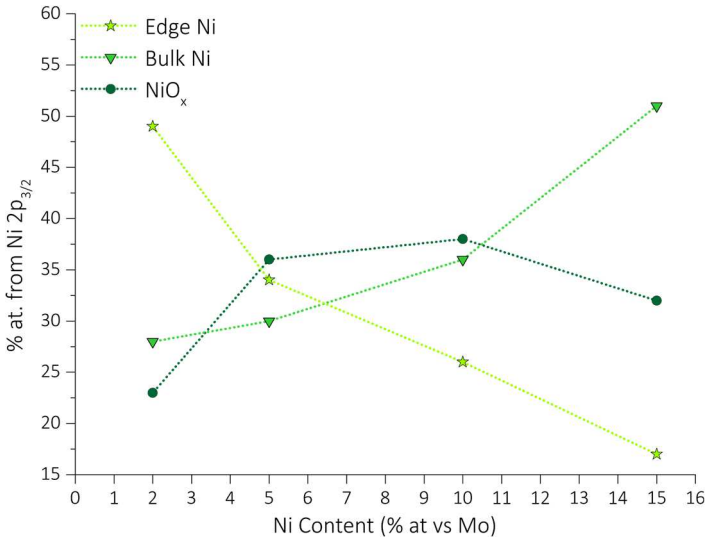

Figure 2.7. Evolution of Ni species as a function of the Ni content determined from the XPS analysis.

	% Ni Edge	***% Ni Basal***	***% NiO_x***
2%Ni 3D-MoS_2	49	27	24
5%Ni 3D-MoS_2	34	30	36
10%Ni 3D-MoS_2	26	36	38
15%Ni 3D-MoS_2	17	51	32

Table 2.3. Composition of Ni $2p_{3/2}$ photoemission line.

2.3.3 Electrochemical Characterization

The electrochemical HER activities of the Ni-doped 3D-MoS_2 materials were tested in alkaline and acid conditions to correlate their performances with the Ni doping (see Figure 2.8). Commercial bulk MoS_2 (Aldrich) and 20 wt.% Pt/C (Johnson Matthey) are also included for comparison. Tafel slopes and overpotentials at 10 mA cm^{-2} ($\eta_{10mA/cm2}$) are reported in Table 2.4.

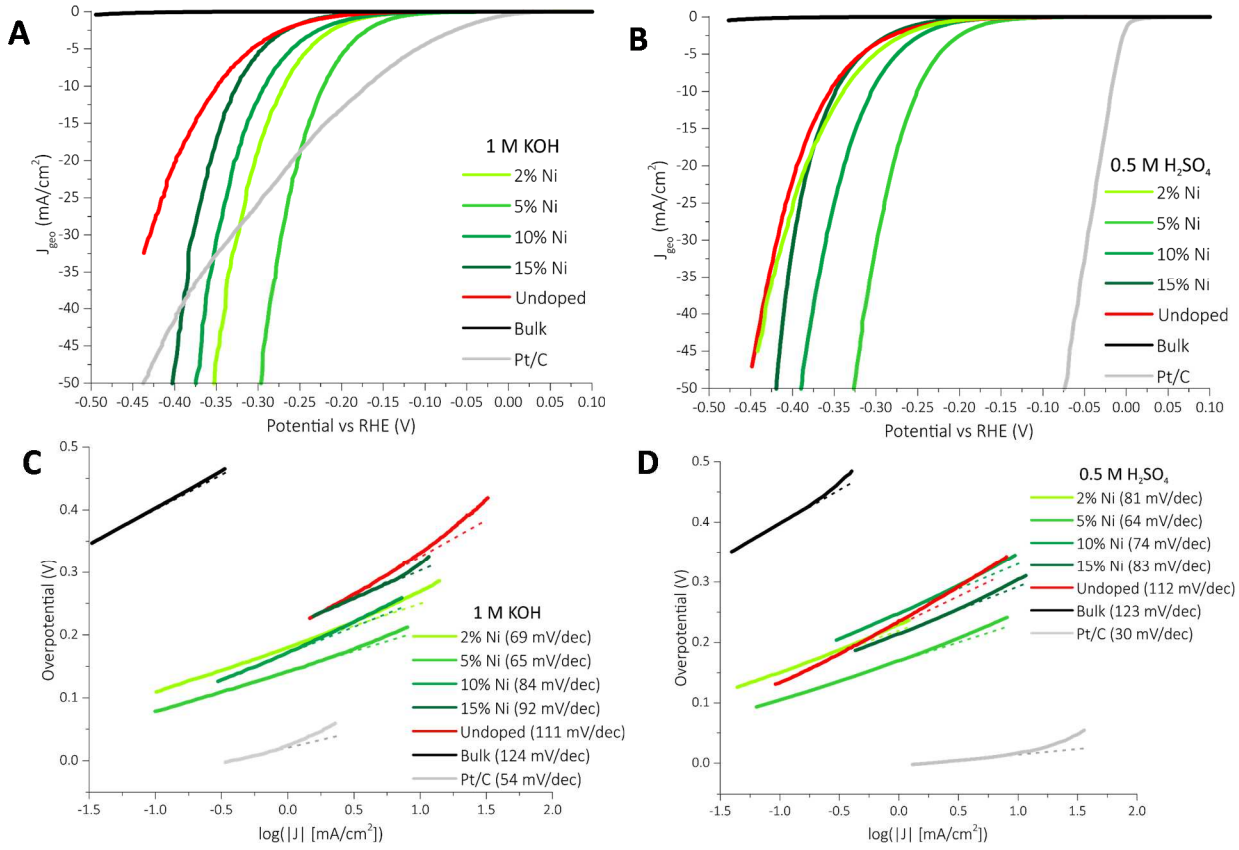

Figure 2.8. Polarization curves and Tafel plots in 1.0M KOH (*A,C*) and in 0.5M H_2SO_4 (*B,D),* respectively, for the 3D-MoS_2 and Ni-doped 3D-MoS_2 materials.

The Ni-doping of 3D-MoS_2 increases the activity in all cases, shifting the onset potential to lower overpotentials and increasing the current density. However, the differences observed among the Ni-doped 3D-MoS_2 samples leads to interesting considerations about the Ni sites and their effect on the HER kinetics in acid and alkaline conditions. It is important to note that the undoped 3D-MoS_2 sample behaves similarly in acid and alkaline solutions. On the contrary, when Ni doping is included, relevant differences are found in the different electrolytes.

In the case of catalytic performance in alkaline conditions an increase of the activity with the amount of Ni is observed up to a 5 at.% doping (Figure 2.8A and Table 2.4), whereas higher Ni loadings result in a decrease of the activity. In the literature, it has been reported that the doping of MoS_2 with Ni accelerates the HER kinetics by lowering the energy barrier for the water dissociation and OH^- desorption steps (see Scheme 1A).[11,12,50] Indeed, late transition metals tends to form weaker bonds with OH^- with respect to Mo, favoring the byproducts desorption. Moreover, as seen by XPS, the introduction of Ni causes a slight electron enrichment of Mo, facilitating desorption of H_{ads} species and hence accelerating the Heyrovsky step.[10,51–53]

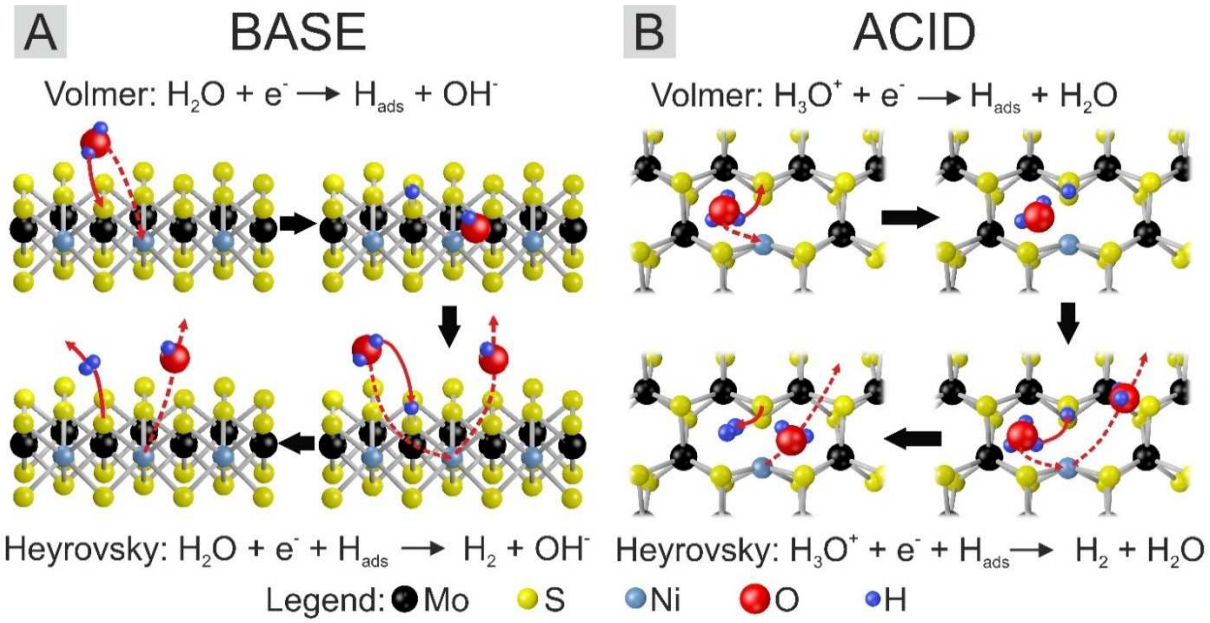

Scheme 1. Schematic representation of different catalytic sites for HER in alkaline (A) and acidic (B) conditions.

From the different Ni species distribution determined from XPS, an interesting correlation between them and the HER activity comes up. The activity increases with the amount of substitutional Ni atoms at the edge (Ni-edge) up to a 5 at.% doping and then starts to decrease due to the promotion of basal plane substitution for high Ni loadings (see Table 2.3). In terms of absolute values, the amount of edge-Ni sites always increases with the Ni content; however, the fact that the HER activity decreases for loadings higher than 10 at.% can be explained taking into account the larger crystallite size and denser morphology of these materials, that results in a lower amount of active sites (edge sites) and as well in higher charge transfer resistance as measured by EIS experiments (see Figure 2.9A and Table 2.5). This result suggests that the Ni-basal species do not promote the HER activity in alkaline medium. This is also confirmed by the analysis of the HER kinetics through the Tafel slope values (Table 2.4). They follow the same trend than the HER activity, that is, the Tafel slope decreases with the amount of Ni up to a 5 at.% Ni-doping and increases for higher Ni loadings. The lowest value (65 mV dec^{-1}) is obtained for the 5 at.% Ni-MoS_2 sample.

	Overpotential at 10 mA/cm² (V)		**Tafel slope (mV/dec)**	
	0.5M H_2SO_4	*1.0M KOH*	*0.5M H_2SO_4*	*1.0M KOH*
Commercial MoS_2	-	-	123	124
Undoped 3D-MoS_2	0.35	0.35	112	111
2%Ni 3D-MoS_2	0.34	0.27	85	69
5%Ni 3D-MoS_2	0.25	0.22	64	65
10%Ni 3D-MoS_2	0.3	0.29	74	84
15%Ni 3D-MoS_2	0.35	0.33	83	92
Pt/C	0.02	0.17	28	47

Table 2.4. Overpotentials at 10 mA cm^{-2} and Tafel slopes for the undoped and Ni-doped 3D-MoS_2, commercial MoS_2 and 20 wt.% Pt/C in 0.5M H_2SO_4 and 1.0M KOH.

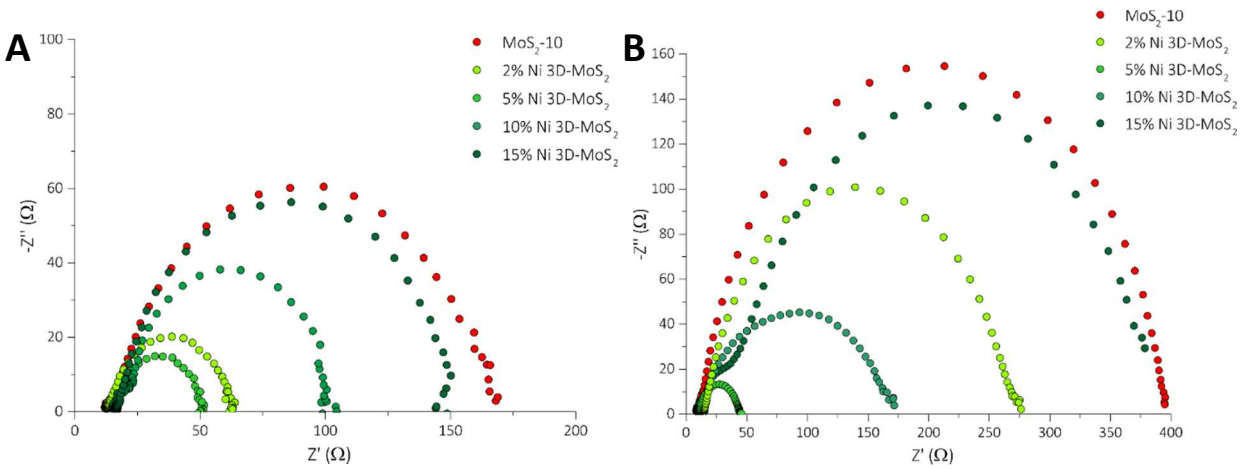

Figure 2.9. Nyquist plot for doped and undoped 3D-MoS_2 recorded at η = 0.28 V in 1.0 M KOH (A) and in 0.5 M H_2SO_4 (B).

	R_{ct} (Ω) 0.5M H2SO4	***R_{ct} (Ω) 1.0M KOH***
Undoped 3D-MoS_2	384	152
2%Ni 3D-MoS_2	260	50
5%Ni 3D-MoS_2	34	34
10%Ni 3D-MoS_2	160	76
15%Ni 3D-MoS_2	370	128

Table 2.5. Charge transfer resistance (R_{ct}) calculated in 0.5 M H_2SO_4 and 1.0 M KOH.

Interestingly, HER activities in acidic conditions show some differences with respect to those observed in alkaline conditions, suggesting variations in the active sites involved. The introduction of 2 at.% Ni does not induce an enhancement of the HER activity in terms of both onset potential and current density respect to the pristine 3D MoS_2, contrary to what happens in alkaline media. This result suggests that the Ni-edge sites, main Ni species in this sample, do not have any role in the HER mechanism. However, a further increase of Ni-doping up to 5 at.% significantly improves the HER activity by decreasing the η_{10mA} by 0.1 V. Taking into account that the relative amount of Ni-basal and Ni-edge species increases and decreases, respectively, compared to the 2% Ni-MoS_2 sample, we could attribute the enhancement of HER activity to the Ni-basal species. When the amount of Ni-basal species increases (10% and 15% Ni samples), the HER is enhanced compared with the pristine and 2% Ni-MoS_2 sample, confirming the key role of these species. However, these materials show a lower activity than the 5 % Ni-MoS_2 sample due to an increase of charge transfer resistance (see Figure 2.9 and Table 2.5) caused by the enlargement of the particle size, as mentioned above.

In order to elucidate the role of the different Ni species, the structural changes caused by the addition of Ni have to be considered. As mentioned above, Ni atoms inserted in the basal plane of MoS_2 network assume a relaxed structure, leaving two unbounded sulfur atoms as shown in Scheme 1B. In agreement with the literature,[10,40,44] the presence of these unsaturated S atoms can favor the proton adsorption step (Volmer step), which is the rate determining step for pure MoS_2, as demonstrated by Tafel analysis. The lowering of the Tafel slope with the addition of Ni confirms the acceleration of the proton adsorption. Moreover, as in the case of HER in alkaline medium, XPS proofed the electron enrichment induced by Ni to the catalyst

surface, hence the adsorption strength of H atom will be weakened, making the following H recombination and release process easier and quickening the overall reaction kinetics.[10,51–53]

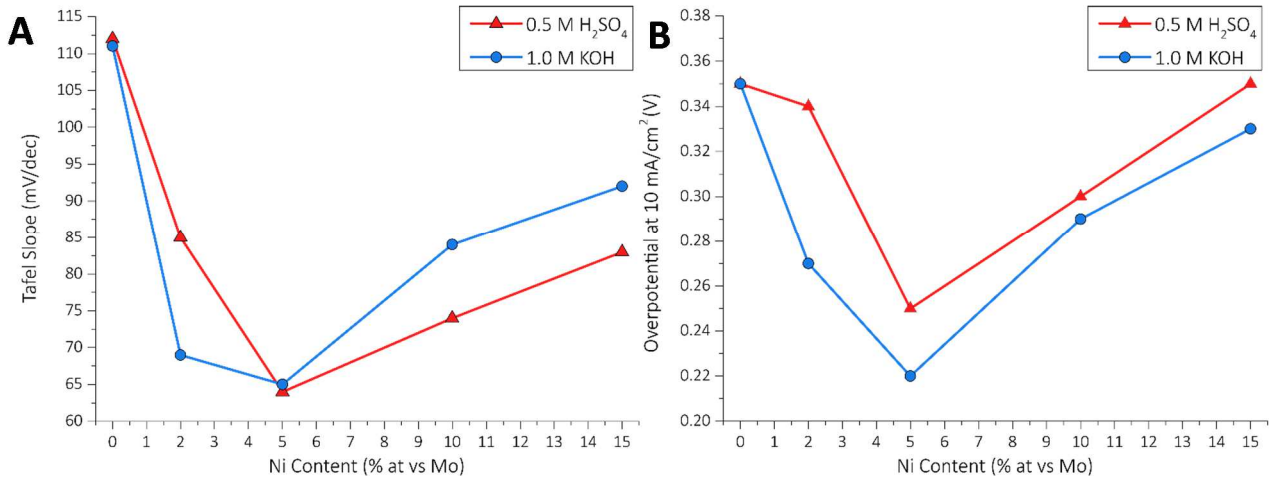

Figure 2.10. Evolution of Tafel slope (A) and Overpotential at 10 mA/cm^2 with the Ni content in both electrolytes.

Interestingly, as shown in Figure 2.10, kinetics in 10 and 15 at.% Ni 3D-MoS_2 slow down in sulfuric acid in less marked way with respect to alkaline environment. This is a clear indication that abundance of Ni-Bulk sites allows a preferential pathway for protons adsorption cleaving H^+-OH_2 molecules, but not for the adsorption and the dissociation of neutral water molecules at higher pH.

2.4 Conclusion

In this Chapter, we studied the effects on the electrocatalytic performances of several amounts of Ni introduced in a 3D-structured MoS_2 scaffold. We observed that introducing large quantities of dopant could strongly influence affect the scaffold structure, by modifying the crystallites growth process and then the crystallinity of the resulting materials and their performances in HER. Moreover, thanks to XPS analysis, we could proof experimentally that Ni atoms tends to preferentially substitute Mo on the edges when the loading is low enough, while the basal plane substitution become preferential for larger amounts of dopant. Finally, we could correlate the electrocatalytic behavior in different environments with the Ni species detected by XPS, observing that Edge Ni species are prone to promote HER in alkaline medium, while the Basal Ni showed preferential activity at low pH.

References

(1) Balasubramanian, B.; Ortiz, A. L.; Kayatakoglu, S.; Harris, D. P. Hydrogen from Methane in a Single-Step. *Process. Chem. Eng. Sci.* **1999**, *54*, 3543.

(2) Faber, M. S.; Jin, S. Earth-Abundant Inorganic Electrocatalysts and Their Nanostructures for Energy Conversion Applications. *Energy Environ. Sci.* **2014**, *7* (11), 3519–3542.

(3) Durst, J.; Siebel, A.; Simon, C.; Hasché, F.; Herranz, J.; Gasteiger, H. A. New Insights into the Electrochemical Hydrogen Oxidation and Evolution Reaction Mechanism. *Energy Environ. Sci.* **2014**, *7* (7), 2255–2260.

(4) Mahmood, N.; Yao, Y.; Zhang, J. W.; Pan, L.; Zhang, X.; Zou, J. J. Electrocatalysts for Hydrogen Evolution in Alkaline Electrolytes: Mechanisms, Challenges, and Prospective Solutions. *Adv. Sci.* **2018**, *5* (2).

(5) Jamesh, M. I. Recent Progress on Earth Abundant Hydrogen Evolution Reaction and Oxygen Evolution Reaction Bifunctional Electrocatalyst for Overall Water Splitting in Alkaline Media. *J. Power Sources* **2016**, *333*, 213–236.

(6) Roger, I.; Shipman, M. A.; Symes, M. D. Earth-Abundant Catalysts for Electrochemical and Photoelectrochemical Water Splitting. *Nat. Rev. Chem.* **2017**, *1*.

(7) Ma, L.; Ting, L. R. L.; Molinari, V.; Giordano, C.; Yeo, B. S. Efficient Hydrogen Evolution Reaction Catalyzed by Molybdenum Carbide and Molybdenum Nitride Nanocatalysts Synthesized via the Urea Glass Route. *J. Mater. Chem. A* **2015**, *3* (16), 8361–8368.

(8) Ding, Q.; Song, B.; Xu, P.; Jin, S. Efficient Electrocatalytic and Photoelectrochemical Hydrogen Generation Using MoS_2 and Related Compounds. *Chem* **2016**, *1* (5), 699–726.

(9) Wiensch, J. D.; John, J.; Velazquez, J. M.; Torelli, D. A.; Pieterick, A. P.; McDowell, M. T.; Sun, K.; Zhao, X.; Brunschwig, B. S.; Lewis, N. S. Comparative Study in Acidic and Alkaline Media of the Effects of PH and Crystallinity on the Hydrogen-Evolution Reaction on MoS_2 and $MoSe_2$. *ACS Energy Lett.* **2017**, 2234–2238.

(10) Shi, Y.; Zhou, Y.; Yang, D.-R.; Xu, W.-X.; Wang, C.; Wang, F.-B.; Xu, J.-J.; Xia, X.-H.; Chen, H.-Y. Energy Level Engineering of MoS_2 by Transition-Metal Doping for Accelerating Hydrogen Evolution Reaction. *J. Am. Chem. Soc.* **2017**, jacs.7b08881.

(11) Staszak-Jirkovský, J.; Malliakas, C. D.; Lopes, P. P.; Danilovic, N.; Kota, S. S.; Chang, K.-C.; Genorio, B.; Strmcnik, D.; Stamenkovic, V. R.; Kanatzidis, M. G.; Markovic, N. M. Design of Active and Stable Co–Mo–S_x Chalcogels as PH-Universal Catalysts for the Hydrogen Evolution Reaction. *Nat. Mater.* **2015**, *15* (2), 197–203.

(12) Zhang, J.; Wang, T.; Liu, P.; Liu, S.; Dong, R.; Zhuang, X.; Chen, M.; Feng, X. Engineering Water Dissociation Sites in MoS_2 Nanosheets for Accelerated Electrocatalytic Hydrogen Production. *Energy Environ. Sci.* **2016**, *9* (9), 2789–2793.

(13) Geng, X.; Sun, W.; Wu, W.; Chen, B.; Al-Hilo, A.; Benamara, M.; Zhu, H.; Watanabe, F.; Cui, J.; Chen, T. Pure and Stable Metallic Phase Molybdenum Disulfide Nanosheets for Hydrogen Evolution Reaction. *Nat. Commun.* **2016**, *7*, 10672.

(14) Chia, X.; Eng, A. Y. S.; Ambrosi, A.; Tan, S. M.; Pumera, M. Electrochemistry of Nanostructured Layered Transition-Metal Dichalcogenides. *Chem. Rev.* **2015**, *115* (21), 11941–11966.

(15) Gao, M.-R.; Chan, M. K. Y.; Sun, Y. Edge-Terminated Molybdenum Disulfide with a 9.4-Å Interlayer Spacing for Electrochemical Hydrogen Production. *Nat. Commun.* **2015**, *6* (May), 7493.

(16) Benck, J. D.; Hellstern, T. R.; Kibsgaard, J.; Chakthranont, P.; Jaramillo, T. F. Catalyzing the Hydrogen Evolution Reaction (HER) with Molybdenum Sulfide Nanomaterials. *ACS Catal.* **2014**, *4* (11), 3957–

3971.

(17) Chang, K.; Hai, X.; Pang, H.; Zhang, H.; Shi, L.; Liu, G.; Liu, H.; Zhao, G.; Li, M.; Ye, J. Targeted Synthesis of 2H- and 1T-Phase MoS_2 Monolayers for Catalytic Hydrogen Evolution. *Adv. Mater.* **2016**, *28* (45), 10033–10041.

(18) Ahn, E.; Kim, B.-S. Multidimensional Thin Film Hybrid Electrodes with MoS_2 Multilayer for Electrocatalytic Hydrogen Evolution Reaction. *ACS Appl. Mater. Interfaces* **2017**, *9* (10), 8688–8695.

(19) Zhang, H.; Yun, Q.; Lu, Q.; Zhang, X.; Tan, C. Three-Dimensional Architectures Constructed from Transition Metal Dichalcogenide Nanomaterials for Electrochemical Energy Storage and Conversion. *Angew. Chemie* **2018**, *57*, 626–646.

(20) Subrahmanyam, K. S.; Sarma, D.; Malliakas, C. D.; Polychronopoulou, K.; Riley, B. J.; Pierce, D. A.; Chun, J.; Kanatzidis, M. G. Chalcogenide Aerogels as Sorbents for Radioactive Iodine. *Chem. Mater.* **2015**, *27* (7), 2619–2626.

(21) Worsley, M. A.; Shin, S. J.; Merrill, M. D.; Lenhardt, J.; Nelson, A. J.; Woo, L. Y.; Gash, A. E.; Baumann, T. F.; Orme, C. A. Ultralow Density, Monolithic WS_2, MoS_2, and MoS_2/Graphene Aerogels. *ACS Nano* **2015**, *9* (5), 4698–4705.

(22) Liao, L.; Zhu, J.; Bian, X.; Zhu, L.; Scanlon, M. D.; Girault, H. H.; Liu, B. MoS_2 Formed on Mesoporous Graphene as a Highly Active Catalyst for Hydrogen Evolution. *Adv. Funct. Mater.* **2013**, *23* (42), 5326–5333.

(23) Lu, X.; Lin, Y.; Dong, H.; Dai, W.; Chen, X.; Qu, X.; Zhang, X. One-Step Hydrothermal Fabrication of Three-Dimensional MoS2 Nanoflower Using Polypyrrole as Template for Efficient Hydrogen Evolution Reaction Xin. *Sci. Rep.* **2017**, *7*, 42309.

(24) Yang, D.; Tayebi, M.; Huang, Y.; Yang, H.; Ai, Y. A Microfluidic DNA Sensor Based on Three-Dimensional (3D) Hierarchical MoS_2/Carbon Nanotube Nanocomposites. *Sensors* **2016**, *16* (11), 1911.

(25) Jia, Y.; Wan, H.; Chen, L.; Zhou, H.; Chen, J. Facile Synthesis of Three Dimensional MoS_2 Porous Film with High Electrochemical Performance. *Mater. Lett.* **2017**, *195*, 147–150.

(26) Cao, X.; Shi, Y.; Shi, W.; Rui, X.; Yan, Q.; Kong, J.; Zhang, H. Preparation of MoS_2-Coated Three-Dimensional Graphene Networks for High-Performance Anode Material in Lithium-Ion Batteries. *Small* **2013**, *9* (20), 3433–3438.

(27) Merki, D.; Vrubel, H.; Rovelli, L.; Fierro, S.; Hu, X. Fe , Co , and Ni Ions Promote the Catalytic Activity of Amorphous Molybdenum Sulfide Films for Hydrogen Evolution Sulfide Films for Hydrogen Evolution. *Chem. Sci.* **2012**, *3*, 2515–2525.

(28) Travert, A.; Nakamura, H.; Santen, R. A. Van; Cristol, S.; Paul, J. F.; Payen, E. Hydrogen Activation on Mo-Based Sulfide Catalysts, a Periodic DFT Study. *J. Am. Chem. Soc.* **2002**, *124* (24), 7084–7095.

(29) Tsai, C.; Chan, K.; Nørskov, K.; Abild-pedersen, F. Rational Design of MoS_2 Catalysts: Tuning the Structure and Activity via Transition Metal Doping. *Catal. Sci. Technol.* **2015**, *5* (1), 246–253.

(30) Tedstone, A. A.; Lewis, D. J.; O'Brien, P. Synthesis, Properties, and Applications of Transition Metal-Doped Layered Transition Metal Dichalcogenides. *Chem. Mater.* **2016**, *28* (7), 1965–1974.

(31) Chung, D. Y.; Park, S.-K.; Chung, Y.-H.; Yu, S.-H.; Lim, D.-H.; Jung, N.; Ham, H. C.; Park, H.-Y.; Piao, Y.; Yoo, S. J.; Sung, Y.-E. Edge-Exposed MoS_2 Nano-Assembled Structures as Efficient Electrocatalysts for Hydrogen Evolution Reaction. *Nanoscale* **2014**, *6* (4), 2131–2136.

(32) Genuit, D.; Afanasiev, P.; Vrinat, M. Solution Syntheses of Unsupported Co(Ni)-Mo-S Hydrotreating Catalysts. *J. Catal.* **2005**, *235* (2), 302–317.

(33) Yang, L.; Wu, X.; Zhu, X.; He, C.; Meng, M.; Gan, Z.; Chu, P. K. Amorphous Nickel/Cobalt Tungsten

Sulfide Electrocatalysts for High-Efficiency Hydrogen Evolution Reaction. *Appl. Surf. Sci.* **2015**, *341*, 149–156.

(34) Li, H.; Zhang, Q.; Yap, C. C. R.; Tay, B. K.; Edwin, T. H. T.; Olivier, A.; Baillargeat, D. From Bulk to Monolayer MoS_2: Evolution of Raman Scattering. *Adv. Funct. Mater.* **2012**, *22* (7), 1385–1390.

(35) Lee, C.; Yan, H.; Brus, L. E.; Heinz, T. F.; Hone, J.; Ryu, S. Anomalous Lattice Vibrations of Single- and Few-Layer MoS_2. *ACS Nano* **2010**, *4* (5), 2695–2700.

(36) Muijsers, J. C.; Weber, T.; Vanhardeveld, R. M.; Zandbergen, H. W.; Niemantsverdriet, J. W. Sulfidation Study of Molybdenum Oxide Using MoO3/SiO2/Si (100) Model Catalysts and Mo-IV3-Sulfur Cluster Compounds. *Journal of Catalysis*. 1995, pp 698–705.

(37) Weber, T.; Muijsers, J. C.; Niemantsverdriet, J. W. The Structure of Amorphous MoS_3. *Bull. des Sociétés Chim. Belges* **1995**, *104* (4–5), 299–299.

(38) Wang, H. W.; Skeldon, P.; Thompson, G. E. XPS Studies on MoS_2 Formation from Ammonium Tetrathiomolybdate Solutions. *Surf. Coatings Technol.* **1997**, *91*, 200–207.

(39) Wang, D.; Zhang, X.; Bao, S.; Zhang, Z.; Fei, H.; Wu, Z. Phase Engineering of a Multiphasic 1T/2H MoS_2 Catalyst for Highly Efficient Hydrogen Evolution. *J. Mater. Chem. A* **2017**, *5* (6), 2681–2688.

(40) Deng, J.; Li, H.; Xiao, J.; Tu, Y.; Deng, D.; Yang, H.; Tian, H.; Li, J.; Ren, P.; Bao, X. Triggering the Electrocatalytic Hydrogen Evolution Activity of the Inert Two-Dimensional MoS_2 Surface via Single-Atom Metal Doping. *Energy Environ. Sci.* **2015**, *8* (5), 1594–1601.

(41) Kibsgaard, J.; Tuxen, A.; Knudsen, K. G.; Brorson, M.; Topsoe, H.; Laegsgaard, E.; Lauritsen, J. V.; Besenbacher, F. Comparative Atomic-Scale Analysis of Promotional Effects by Late 3d-Transition Metals in MoS2 Hydrotreating Catalysts. *J. Catal.* **2010**, *272* (2), 195–203.

(42) Escobar, J.; Barrera, M. C.; Toledo, J. A.; Cortés-Jácome, M. A.; Angeles-Chávez, C.; Núñez, S.; Santes, V.; Gómez, E.; Díaz, L.; Romero, E.; Pacheco, J. G. Effect of Ethyleneglycol Addition on the Properties of P-Doped NiMo/Al_2O_3 HDS Catalysts: Part I. Materials Preparation and Characterization. *Appl. Catal. B Environ.* **2009**, *88* (3–4), 564–575.

(43) Leyral, G.; Ribes, M.; Courthéoux, L.; Uzio, D.; Pradel, A. Synthesis and Structuring of Ni MoS_2 by Using an Ionic Liquid. *Eur. J. Inorg. Chem.* **2012**, No. 31, 4967–4971.

(44) Dai, X.; Du, K.; Li, Z.; Liu, M.; Ma, Y.; Sun, H.; Zhang, X.; Yang, Y. Co-Doped MoS_2 Nanosheets with the Dominant CoMoS Phase Coated on Carbon as an Excellent Electrocatalyst for Hydrogen Evolution. *ACS Appl. Mater. Interfaces* **2015**, *7* (49), 27242–27253.

(45) Hakala, M.; Kronberg, R.; Laasonen, K. Hydrogen Adsorption on Doped MoS_2 Nanostructures. *Sci. Rep.* **2017**, *7* (1), 15243.

(46) Sattayanon, C.; Namuangruk, S.; Kungwan, N.; Kunaseth, M. Reaction and Free-Energy Pathways of Hydrogen Activation on Partially Promoted Metal Edge of CoMoS and NiMoS: A DFT and Thermodynamics Study. *Fuel Process. Technol.* **2017**, *166*, 217–227.

(47) Liu, G.; Robertson, A. W.; Li, M. M. J.; Kuo, W. C. H.; Darby, M. T.; Muhieddine, M. H.; Lin, Y. C.; Suenaga, K.; Stamatakis, M.; Warner, J. H.; Tsang, S. C. E. MoS_2 Monolayer Catalyst Doped with Isolated Co Atoms for the Hydrodeoxygenation Reaction. *Nat. Chem.* **2017**, *9* (8), 810–816.

(48) Lauritsen, J. V.; Kibsgaard, J.; Olesen, G. H.; Moses, P. G.; Hinnemann, B.; Helveg, S.; Nørskov, J. K.; Clausen, B. S.; Topsøe, H.; Lægsgaard, E.; Besenbacher, F. Location and Coordination of Promoter Atoms in Co- and Ni-Promoted MoS_2-Based Hydrotreating Catalysts. *J. Catal.* **2007**, *249* (2), 220–233.

(49) Wang, H.; Tsai, C.; Kong, D.; Chan, K.; Abild-Pedersen, F.; Nørskov, J. K.; Cui, Y. Transition-Metal Doped Edge Sites in Vertically Aligned MoS_2 Catalysts for Enhanced Hydrogen Evolution. *Nano Res.* **2015**, *8*

(2), 566–575.

(50) Wang, M.; Ju, P.; Li, W.; Zhao, Y.; Han, X. Ag_2S Nanoparticle-Decorated MoS_2 for Enhanced Electrocatalytic and Photoelectrocatalytic Activity in Water Splitting. *Dalt. Trans.* **2017**, *46* (2), 483–490.

(51) Maitra, U.; Gupta, U.; De, M.; Datta, R.; Govindaraj, A.; Rao, C. N. R. Highly Effective Visible-Light-Induced H_2 Generation by Single-Layer 1T-MoS_2 and a Nanocomposite of Few-Layer 2H-MoS_2 with Heavily Nitrogenated Graphene. *Angew. Chemie Int. Ed.* **2013**, *52* (49), 13057–13061.

(52) Liu, Q.; Fang, Q.; Chu, W.; Wan, Y.; Li, X.; Xu, W.; Habib, M.; Tao, S.; Zhou, Y.; Liu, D.; Xiang, T.; Khalil, A.; Wu, X.; Chhowalla, M.; Ajayan, P. M.; Song, L. Electron-Doped 1T-MoS_2 via Interface Engineering for Enhanced Electrocatalytic Hydrogen Evolution. *Chem. Mater.* **2017**, *29* (11), 4738–4744.

(53) Lei, Y.; Pakhira, S.; Fujisawa, K.; Wang, X.; Iyiola, O. O.; Perea López, N.; Laura Elías, A.; Pulickal Rajukumar, L.; Zhou, C.; Kabius, B.; Alem, N.; Endo, M.; Lv, R.; Mendoza-Cortes, J. L.; Terrones, M. Low-Temperature Synthesis of Heterostructures of Transition Metal Dichalcogenide Alloys ($W_xMo_{(1-x)}S_2$) and Graphene with Superior Catalytic Performance for Hydrogen Evolution. *ACS Nano* **2017**, *11* (5), 5103–5112.

Chapter Three:

Highly Efficient $MoS_2/Ag_2S/Ag$ Photoelectrocatalyst Obtained from a Recycled DVD Surface

3.1 Introduction

The fabrication of efficient, stable and cheap electrodes for electrochemical[1] and photoelectrochemical[2] production of H_2 is nowadays a very challenging and widespread research topic. Both Ag_2S and MoS_2 have been studied for quite a long time as efficient and convenient electrocatalysts for HER.[3–8] It is now well established that bulk MoS_2 is a poorly active HER electrocatalyst, whereas, when 2D nanosheets are considered, their edge sites show a noticeable HER activity. Therefore, many efforts have been devoted primarily to the preparation of exfoliated MoS_2 materials to exploit their HER catalytic activity.[9,10] However, if we want exploit the Solar energy to increment the efficiency of the HER process, the photo-electrocatalytic (PEC) approach must be pursued and in this case designing a composite catalyst is the main challenge. A current strategy is that of decorating the MoS_2 nanosheets with metal nanoparticles (NPs) that can act as carrier sinks and/or produce more efficient active sites.[3] In fact, noble metals have a large work function, i.e. lower Fermi level, which can easily trap the photoexcited electrons to extend the average lifetime of electron-hole pairs. Among the noble metals, Pt has the lowest Fermi level, and thus possesses the best abilities for trapping electrons and the highest HER activities.

Alternatively, the formation of heterojunctions is a suitable strategy to burst the PEC-HER process, e.g. the MoS_2-CdS p-n junction.[11] In this view, Ag_2S offers the possibility to form an alternative p-n junction: in fact, Ag_2S presents a good solar energy absorption, and has already been applied as an electrocatalyst, photo-electrocatalyst and photocatalyst in HER experiments.[8,12] When considering the Ag_2S/MoS_2 composite material, Ag_2S, according to Pearson absolute electronegativity values, has a favourable position of conduction band (CB) and valence band (VB) edges so that a type-II[13] heterojunction might be formed.[14] In addition, it is important to recall that the combination of MoS_2 with highly conductive materials is also a very important issue to enhance charge transportation and catalytic efficiency.[14] In a recent paper by Tran and co-workers it was shown that the transformation from an amorphous to crystalline MoS_2 material surprisingly did not reveal beneficial with respect to HER: being more defective, the amorphous material possesses a better HER activity and appears to be more tolerant to oxidation stress.[15]

Considering all these evidences and having in mind the goal of sustainability, we decided to pursue an easy and cheap approach to the preparation of a composite Ag_2S/MoS_2 PEC material using as support the nanostructured Ag layer present in a commercial Digital Versatile Disc (DVD), thus turning an abundant waste into an added-value material. Actually, a writable DVD contains a 1µm thick Ag layer sandwiched between two polycarbonate discs containing a 400 nm periodic nanostructure, i.e. the DVD grooves. It is possible to delaminate the sandwich and expose the Ag layer nanostructure after washing with ethanol the dye that coats the Ag surface. This procedure is easy and can be performed in few minutes.[16–18] Therefore, this abundant and cheap substrate is ideal to assemble an electrode taking advantage of a highly conductive substrate (i.e. Ag) that can serve also as a Ag source for the formation of Ag_2S,[16,17] eventually producing the composite Ag_2S/MoS_2 material. By using the Ag DVD surface as an electrode, the following well-known electrochemical reduction of MoS_4^{2-} can be performed:[19,20] $MoS_4^{2-} + 2e^- + 2H_2O \rightarrow MoS_2 + 2SH^- + 2OH^-$ and the sulphide anions produced in solution (depending on the pH), can simultaneously sulphidize the native Ag_2O naturally present on the Ag surface and transform it into Ag_2S. In this Chapter, we describe the preparation and characterization of such an electrode: we obtained a nanocomposite material containing amorphous MoS_2, Ag_2S and, of course, metallic Ag. The final MoS_2/Ag_2S/Ag-DVD electrode can be considered

as a convenient route to recycle the existing large stock of unused/used DVDs. These results have been published[21] and reproduced with the permission of the *American Chemical Society*.

3.2 Experimental Section

Synthesis of MoS_2/Ag_2S/Ag-DVD and Ag_2S/Ag-DVD

The deposition of the composite MoS_2/Ag_2S/Ag-DVD was performed following the recipe reported in reference[19] and consisting in the potentiostatic reduction of $(NH_4)_2MoS_4$ (50*mM* solution) using a standard three electrode equipment. A standard calomel electrode (SCE) and a Pt wire were used as reference and counter electrode, respectively. The deposition was performed in a N_2 purged solution at potentials of -1.0 and -1.1 V vs SCE for 180s.

The deposition of only Ag_2S on the Ag-DVD surface, to be used as control material in XPS and electrochemical experiments, was performed by dipping the Ag-DVD surface in a solution obtained by addition of elemental S to a concentrated NaOH solution. The following reaction occurs: $4S + 6NaOH \xrightarrow{80°C} Na_2S_2O_3 + 2Na_2S + 3H_2O$ (0.04 *M* Na_2S). After several seconds (60-120 s) of immersion a dark brown Ag_2S film appears. Alternatively, the deposition can be performed by applying a potential of 0.02 V vs SCE for 15-20 s with the Ag-DVD electrode immersed in the same solution. The Linear Sweeps Voltammetry (LSV) and XPS spectra reported in the results refer to Ag_2S samples prepared in this way.

Chemical and structural characterization

Samples were characterized by field-emission scanning electron microscopy (SEM, Zeiss Supra 35VP equipment). Energy dispersive X-ray spectroscopy (EDX) elemental maps were acquired with the same instrument. Raman spectra were acquired with a ThermoFisher DXR Raman microscope using a 532 nm laser (0.1 mW), focused on the sample with a 50x objective (Olympus) obtaining a spot size of about 1 µm. Grazing incidence X-ray diffraction (GIXRD) patterns were recorded in the diffraction angular range 10-50° 2ϑ by a Philips X'Pert PRO diffractometer, working in the reflection geometry and equipped with a graphite monochromator on the diffracted beam (CuK_α radiation). The surface chemical composition of the samples was investigated by X-ray photoemission spectroscopy (XPS) using a home developed equipment working at a base pressure of 10^{-10} mbar and adopting an EA 125 Omicron electron analyzer with a five channeltron detector. The XPS data were collected at room temperature using the Mg K_α line (hv = 1253.6 eV) of a non-monochromatized dual-anode DAR400 X-ray source. High resolution spectra were acquired using 0.1 eV energy steps, and 20 eV pass energy. The multipeak analysis of S 2p and Mo 3d photoemission lines was performed by means Voigt function and subtracting a Shirley background using KolXPD software.

Electrochemical characterization

The electrochemical (EC) and photoelectrochemical (PEC) HER measurements were carried out in a custom designed three-electrode configuration cell using an Autolab PGSTAT-204 (Ecochemie) potentiostat. A Pt wire was used as a counter electrode, whereas an $Ag/AgCl_{(3M\ KCl)}$ electrode, calibrated with respect to the reversible hydrogen electrode (RHE), was the reference electrode. All potentials reported in the text and figures are referred to the (RHE) and corrected according to the equation: E(RHE) = E(Ag/AgCl) + 0.225 V + 0.059 pH. The EC and PEC experiments were carried out in Ar-saturated 0.5 M H_2SO_4 solution prepared from

high-purity reagents (Sigma-Aldrich) and ultrapure Milli-Q water with a resistivity of 18.2 MΩ·cm. The area during EC was limited by Teflon tape to 0.07 cm^2. The polarization curves were recorded in in the potential range between + 0.05 and -0.5 V vs RHE at a 5 mV/s scan rate. Curves were iR-corrected using the resistance found in Electrochemical impedance spectroscopy (EIS). EIS were measured at overpotential of η = 0.18 V and superimposing a small sinusoidal voltage of 10 mV over the frequency range 0.1 MHz to 100 mHz. The PEC measurement was conducted by applying constant cathodic potential (-0.18 V vs RHE) to the working electrode and the current respond was measured under chopped light illumination from a white neutral LED (LDCNW, Metrohm, Autolab LED Driver kit), with the light intensity of 97 mW/cm^2. A calibrated photodiode was used to measure the light intensity after the light goes through the glass window of PEC cell. The double-layer capacitance was measured according to the model proposed by McCrory et al..[22]

3.3 Results and Discussion

In Figure 3.1 we report the SEM image acquired from a MoS_2/Ag_2S/Ag-DVD electrode obtained after a potentiostatic deposition from a $(NH_4)_2MoS_4$ solution by applying a potential of -1.1 V vs SCE for 180 s. The image, acquired from a freshly deposited sample, shows that the original morphology of the Ag-DVD layer (400 nm periodic structure) is maintained although the roughness of the surface is much higher than that of a clean DVD (inset in Figure 3.1a). Spherical particles with a dimension between 10 and 25 nm appear as uniformly distributed on the surface. There is also no evident difference between the edges and the bottom of the grooves. The increment in roughness was further confirmed with double-layer capacitance (C_{DL}) measurements:[22] C_{DL} increased from 0.004 mF to 0.114 mF after formation of MoS_2/Ag_2S/Ag-DVD (Figure 3.2), a 2 order-of-magnitude improvement due to hybrid deposition.

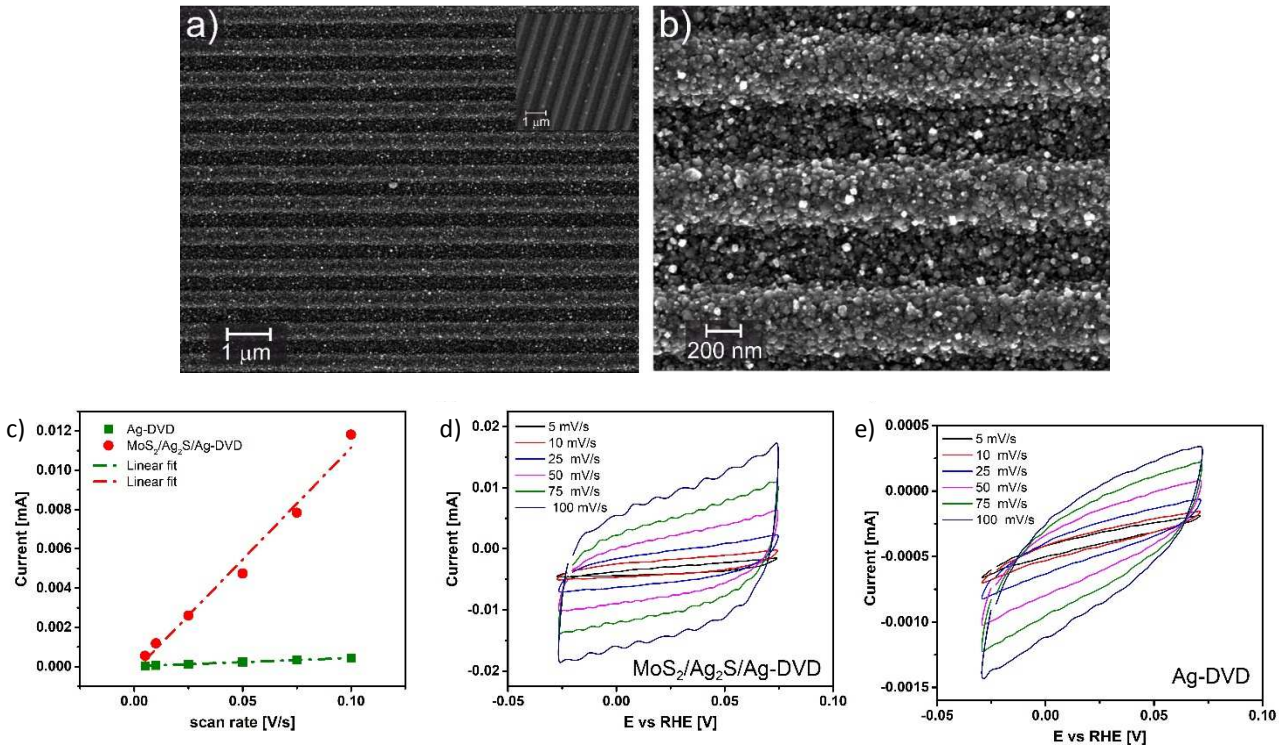

Figure 3.1. a-b) SEM images of as prepared MoS_2/Ag_2S/Ag-DVD, inset in (a) show the morphology of clean Ag-DVD. c) Capacitive current at 0.0125 V vs RHE with scan rate for Ag-DVD and MoS_2/Ag_2S/Ag-DVD. Cyclic voltammetry of (d) MoS_2/Ag_2S/Ag-DVD, (e) Ag-DVD recorded in 0.5 M H_2SO_4 at scan rates of 5, 10, 25, 50, 75, 100 mV/s. Reproduced from Ref. 21.

In order to proof that both MoS_2 and Ag_2S were homogeneously generated on the DVD surface, EDX elemental map, reported in of Figure 3.2, shows the presence of S, Ag, and Mo with a uniform distribution.

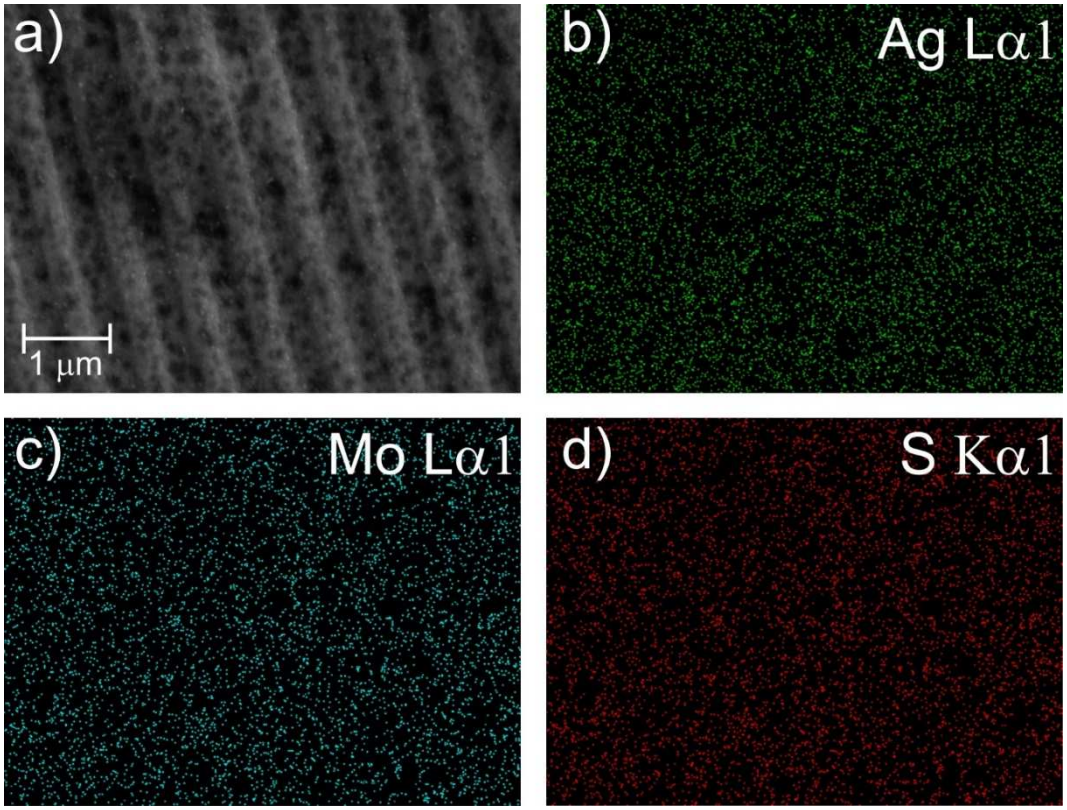

Figure 3.2. a) SEM image of area used for the EDX mapping, (b)-(d) EDX mapping of MoS_2/Ag_2S/Ag-DVD sample showing the uniform distribution of Ag, Mo and S. Reproduced from Ref. 21.

Figure 3.3 reports the XRD analysis of the MoS_2/Ag_2S/Ag-DVD sample, showing a featureless spectrum with a very large amorphous signal between 2θ =14 and 23°. No signals corresponding to crystalline MoS_2, Ag_2S or MoO_x were detectable. The only detectable signals at 2θ = 38.1° (Ag(111)) and 2θ = 44.3° (Ag(200)) correspond to crystalline Ag of the substrate.

More details about the sample composition can be obtained from the Raman and XPS data. The Raman spectra of MoS_2/Ag_2S/Ag-DVD samples are all very similar and apparently independent of the potential applied during the potentiostatic deposition (0.9 – 1.1 V) and whether the deposition is performed under nitrogen or in air. A typical Raman spectrum obtained from a sample deposited at -1.1 V vs SCE for 180 s is reported in Figure 3.3. The low intensity of the bands and the lack of sharp signals is indicating the presence of an amorphous sample or of a partially crystallized sample where the crystallization process is probably induced by the heating of the laser beam (laser power 0.5 mW). Nevertheless, it is possible to distinguish some features that can be attributed to the presence of amorphous MoS_2 (band at 410 cm-1, vibration A1g of crystalline MoS_2[15]), Ag_2S (shoulder at about 190-200 cm^{-1} corresponding to ν Ag-S[23,24]), while the very large and featureless bands at about 350 and 900 cm^{-1} can be due to amorphous MoO_x.[25–27] Other Raman signal, typical of amorphous MoS_2 at 150, 200-250 and about 330 cm^{-1} are most probably overlapping with MoO_x and Ag_2S signals.[28] The lack of Raman signal at 1072 and 1100 cm^{-1} also indicates that the amount of Ag_2O within the detection depth is rather low.[29]

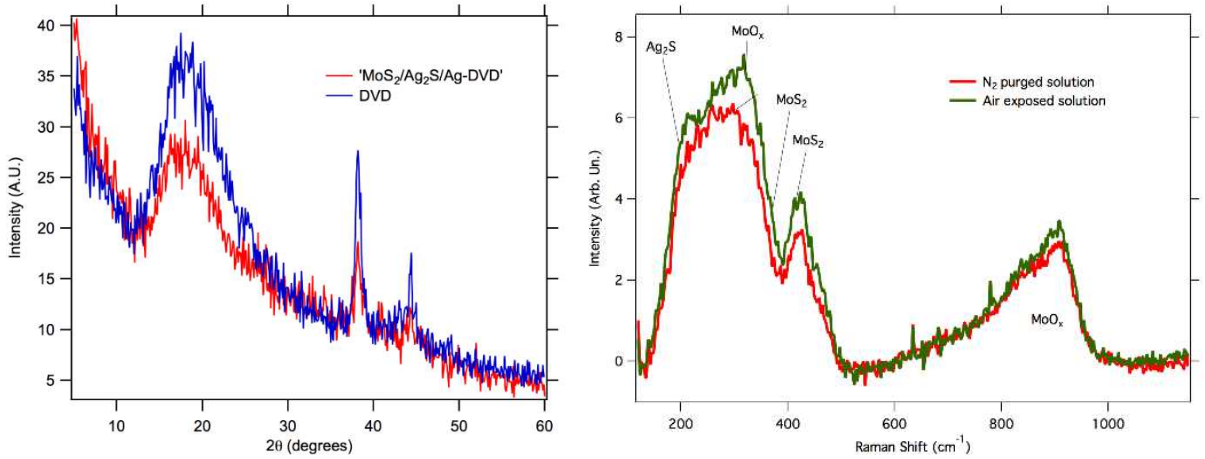

Figure 3.3. *Left*: GIXRD spectra of MoS_2/Ag_2S/Ag-DVD and clean DVD samples. *Right*: Raman spectra of MoS_2/Ag_2S/Ag-DVD samples. The red curve corresponds to the Raman signal obtained from a sample grown in a N_2 purged solution and in a N_2 atmosphere. Reproduced from Ref. 21.

More details on surface composition can be obtained from the XPS data reported in Figure 3.4. We show the S 2p peak recorded for MoS_2/Ag_2S/Ag-DVD and Ag_2S/Ag-DVD obtained after the potentiostatic deposition at 0.02 V vs SCE for 15s in a 0.04 M Na_2S solution. In the first case the S 2p peak can be easily fitted with 2 doublets, corresponding to the S $2p_{3/2}$ and S $2p_{1/2}$ signals, at 160.9 and 161.5 eV (the BE value is the one corresponding to the $2p_{3/2}$ component). It is immediately evident, after comparing the S 2p peak obtained from the Ag_2S/Ag-DVD sample, that the S 2p signal corresponding to Ag_2S is at 160.9 eV, while the one corresponding to MoS_2 is at 161.5 eV. It is therefore straightforward to calculate the ratio between MoS_2 and Ag_2S which is, expressed as atomic %, 44 (MoS_2) and 56 (Ag_2S) (taking in account of the different S:Metal ratio in the compounds). The Mo 3d peak is also rich of information: it can be fitted with 3 doublets at 228.5, 230.1 and 232.0 eV (again the position refers to the $3d_{5/2}$ component of the doublet) corresponding to MoS_2, MoO_x and MoO_3 respectively. As shown in Figure 3.4b the further peak at 225.8 eV corresponds to the S 2s signal. Interestingly, the Mo $3d_{5/2}$ component is shifted to lower binding energy if compared with the pure 2H-MoS_2. This shift can be associated to both amorphous nature of MoS_2 and a quite strong interaction between Ag_2S and MoS_2 corresponding to the formation of a n-p junction (see following paragraphs). The presence of Mo oxides, mostly as MoO_2, is not unexpected. In fact, tetrathiomolybdate may undergo a partial hydrolysis in H_2O ($MoO_4^{2-} + 4H_2S \rightleftharpoons MoS_4^{2-} + 4H_2O$) forming molybdate and H_2S and thermodynamics tells us that, in any case, at a potential of -0.50 vs SHE in a solution containing Ag^+, MoO_4^{2-} and H_2S the predominant species, at pH values between 8 and 11, are Ag(s), Ag_2S(s) and MoS_2(s). If the concentration of sulfide is lower than that of MoO_4^{2-}, the amount of MoO_2 and MoS_2 are comparable. As discussed above, the S 2p peak allows to distinguish between Ag_2S and MoS_2. Therefore, by considering the S 2p intensity of the peak assigned to MoS_2 (161.5 eV) it is possible to obtain a Mo/S atomic ratio of 1/2. Finally, the MoO_x amount (MoO_3 + MoO_x) is about 44% with respect to the total amount of Mo. The calculated Mo/O ratio is 1/2.8 and this number indicates that the amount of Ag_2O is quite low. In fact, supposing that the Mo 3d signal at 230.1 eV corresponds to MoO_2, from the ratio of Mo 3d signals at 232.0 and 230.1 eV it is possible to obtain the molar fraction of MoO_3 (0.2) and MoO_2 (0.8) with respect to the total amount of oxidized Mo. Therefore, the number of O moles is simply given by: $\chi_{MoO_3}\{O\ in\ MoO_3\} + \chi_{MoO_2}\{O\ in\ MoO_2\} = 2.2$. This means that about 20% of the O 1s intensity is due to the presence of Ag_2O. In any case, we think that this small amount

of Ag_2O (highly segregated in at the surface, see the Raman evidence) should not have any effect on the electrochemical properties of this composite material since in the 0.5 M H_2SO_4 solution used to characterize the electrochemical HER activity Ag_2O should be completely soluble.

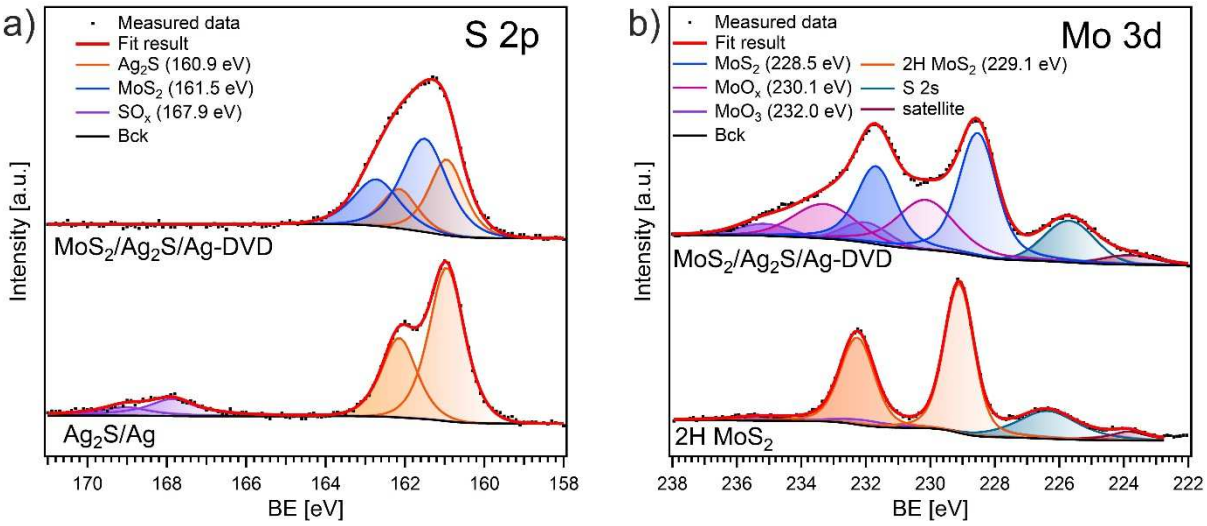

Figure 3.4. High resolution core-level XPS spectra of (a) S 2p of as-prepared MoS_2/Ag_2S/Ag-DVD, Ag_2S/Ag-DVD, and (b) Mo 3d of as-prepared MoS_2/Ag_2S/Ag-DVD and reference 2H MoS_2. Reproduced from Ref. 21.

The electrochemical HER activities of the as prepared catalysts were then investigated using the procedure described in the experimental section. Comparison of the HER activity of clean Ag-DVD, Ag_2S/Ag-DVD, MoO_x/Ag-DVD and MoS_2/Ag_2S/Ag-DVD are reported in Figure 3.5. Overpotential (η) values, Tafel slopes and charge transfer resistances are all reported in Table 3.1. In the inset of Figure 3.5a we also report, for comparison, the polarization curve for Pt/C commercial catalyst (Johnson Matthey, 20 wt%) on GC electrode. The MoS_2/Ag_2S/Ag-DVD presents an enhanced HER activity in comparison to the clean Ag-DVD, MoO_x/Ag-DVD and Ag_2S/Ag-DVD electrodes, with an overpotential for a current density of 10 mA cm^{-2} as low as 0.206 V vs RHE. The same current density, in the case of the clean Ag-DVD, MoO_x/Ag-DVD and Ag_2S/Ag-DVD electrodes can be reached at higher overpotentials of 0.348 V, 0.456 V and 0.266 V, respectively. It is interesting to note that the Ag_2S/Ag-DVD electrode exhibits a lower overpotential (η = 0.056 V vs RHE) in comparison to MoS_2/Ag_2S/Ag-DVD (η = 0.121 V vs RHE) if one considers the onset of H_2 evolution on the electrode surface. The exhibition of better overpotential for Ag_2S/Ag-DVD than MoS_2/Ag_2S/Ag-DVD catalyst, but on the other hand worse overpotential required to reach current density of 10 mA cm^{-2} can be deduced from Tafel slope which is often utilized to validate the efficiency of catalytic reaction. A smaller Tafel slope means a faster increase of the HER rate with the increased overpotential. Therefore, in order to determine the Tafel slope, the polarization curves were fitted into the Tafel equation ($\eta = a + b \log J$, where b is the Tafel slope, a is exchange current density, and J is the current density).[8,30–32]

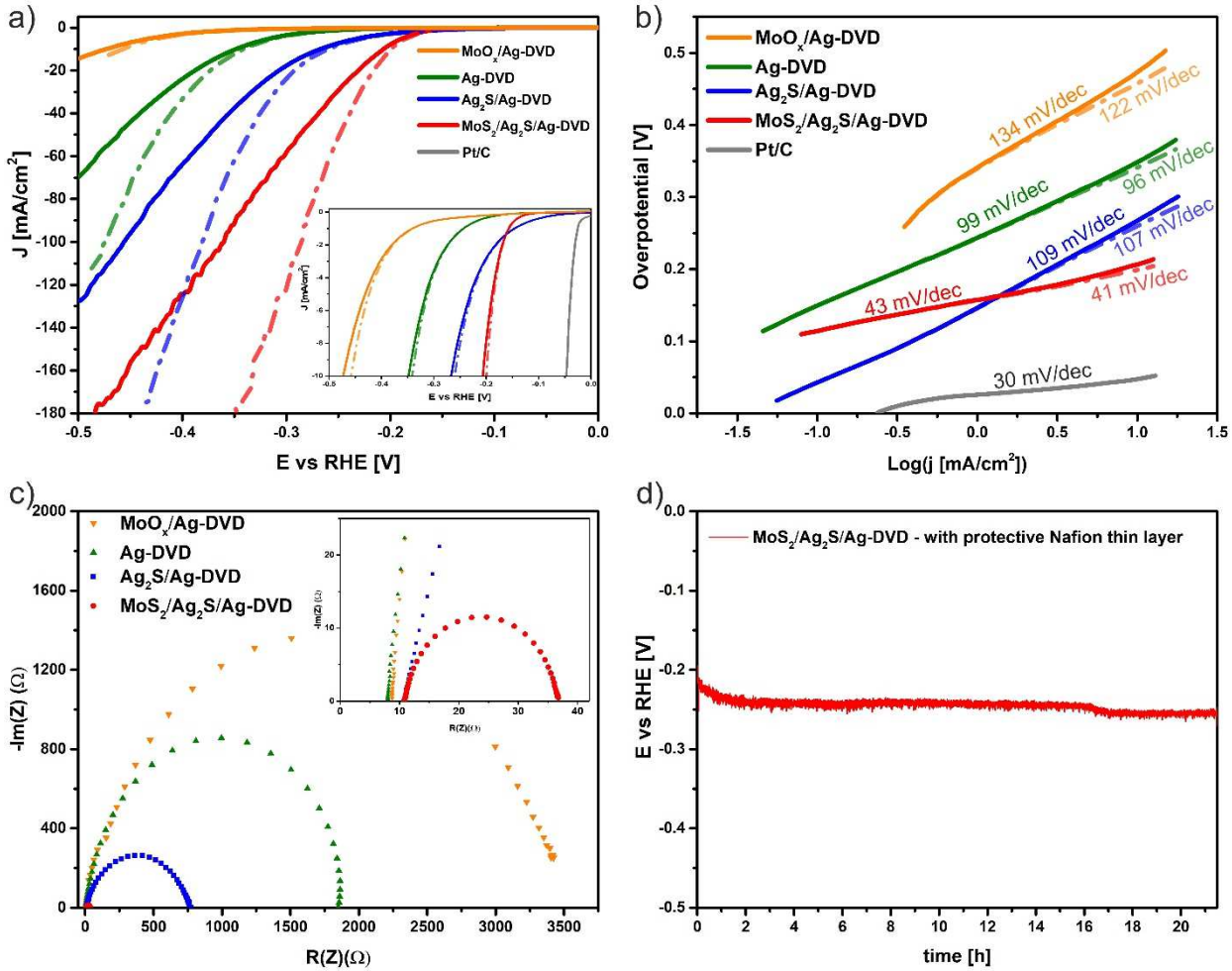

Figure 3.5. (a) HER performance of MoS_2/Ag_2S/Ag-DVD, Ag_2S/Ag-DVD, MoO_x/Ag-DVD, Ag-DVD catalysts and Pt/C as reference. HER polarization curves recorded with scan rate of 5mV/s, 0.5 M H_2SO_4 as electrolyte and purged with Ar. (b) Tafel plot for the HER. ((a) and (b): solid/dashed line before/after iR correction, respectively). (c) EIS Nyquist plots acquired at overpotential of η = 0.18 V. (d) The durability test of MoS_2/Ag_2S/Ag-DVD recorded at 10mA/cm^2. Reproduced from Ref. 21.

As shown in Figure 3.5b, the Tafel slope of the Pt/C catalyst is 30 mV/dec, which is in accordance with the literature.[8] Moreover, the MoS_2/Ag_2S/Ag-DVD also exhibits a very small Tafel slope of 41 mV/dec, which is much smaller in comparison to clean Ag-DVD (96 mV/dec), Ag_2S/Ag-DVD (107 mV/dec) and as well as to MoO_x/Ag-DVD (122 mV/dec), indicating an excellent HER activity.

In the acidic media, the HER reaction proceeds through three principal reaction steps:

Volmer adsorption step:

$$H_3O^+ + e^- \rightarrow H_{ad} + H_2O \qquad \textbf{(1)}$$

Heyrovsky desorption step:

$$H_{ad} + H_3O^+ + e^- \rightarrow H_2 + H_2O \qquad \textbf{(2)}$$

Tafel recombination step:

$$2H_{ad} \rightarrow H_2 \qquad \textbf{(3)}$$

where H_{ad} is the hydrogen adsorption site onto the surface of the catalyst. The Volmer (1) process is called a discharge reaction and is the first step. After that, there are two possibilities that the reaction now may follow an electrochemical desorption reaction called Heyrovsky process (2), or recombination step (3), called the Tafel step. Depending of the rate-determining step of the HER reaction the value of the Tafel slope should be 120 mV/dec for the Volmer step, and for the Heyrovsky process and Tafel process 40 and 30 mV/dec, respectively.[8,30–32] Therefore, the HER reaction for the studied MoS_2/Ag_2S/Ag-DVD sample follows the Volmer-Heyrovsky mechanism, but in the case of Ag-DVD and Ag_2S/Ag-DVD the rate-determining step is the Volmer process.

	Onset η [V]	**η at J = 10 mA cm^{-2} iR Corrected [V]**	**Tafel Slope iR Corrected [mV/dec]**	**Charge-Transfer Resistance [Ω]**
Ag-DVD	0.169	0.341	96	1870
MoO_x/Ag- DVD	0.308	0.456	122	3440
Ag_2S/Ag- DVD	0.056	0.259	107	756
MoS_2/Ag_2S/Ag- DVD	0.121	0.198	41	26
Pt/C	0	-	30	-

Table 3.1. Onset Overpotentials, Overpotentials at J = 10 mA/cm^2, Tafel slopes and Charge Transfer Resistances obtained from Ag-DVD, Ag_2S-/Ag-DVD and MoS_2/Ag_2S/Ag-DVD. All η are referred to RHE.

The enhanced electrocatalytic activity of MoS_2/Ag_2S/Ag-DVD may be attributed to a co-catalyst effect of Ag_2S (usually n-type) on MoS_2 (usually p-type) with formation of many nanoscale n-p junctions uniformly distributed on the electrode surface. If one considers the conduction band (CB) and valence band (VB) edges approximate position, as reported in Figure 3.6a (red lines), obtained from Mott-Schottky plots (MS) of p-type MoS_2[33] on carbon paper and n-type Ag_2S/Ag[34] (Figure 3.6c), it is easy to see that the relative position of (Fermi levels) (E_{Fs}), slightly above the VB for MoS_2 and slightly below the CB for Ag_2S, would require a rearrangement to be aligned. After thermal equilibrium the E_{Fs} alignment is due to an electron flow from Ag/Ag_2S to MoS_2. The result is that the VB for MoS_2 is shifted upward, to a more favorable position for HER. The more favorable position of VB for the HER will of course imply a lower overpotential. We think that a contribution from Ag NPs decorating both Ag_2S and MoS_2 may also be considered. The n-p junction formation is confirmed by the "V" shaped MS plot reported in Figure 3.6b.[33] In the MS plot, the part of the curve characterized by a positive slope is due to the presence of a n-type semiconductor, i.e. Ag_2S, while the curve with a negative slope corresponds to MoS_2. In this case, we do not have a direct indication that MoS_2 is characterized by a p-type conductivity, but a comparison of the Mott-Schottky plot with a similar system[33] led us to safely attribute the part of the curve characterized by a negative slope to the MoS_2 contribution. When the n-p junction forms, there is electrons transfer to MoS_2, confirmed by XPS data, and the corresponding E_F alignment, as recently described by Parida et al. in the case of CeO_2/MoS_2 n-p junction[35]. The approximate position of CB and VB edges, obtained from the MS plot for both Ag_2S and MoS_2, is shown in Figure 5a (solid black lines), assuming in both cases the energy gaps of bulk materials.

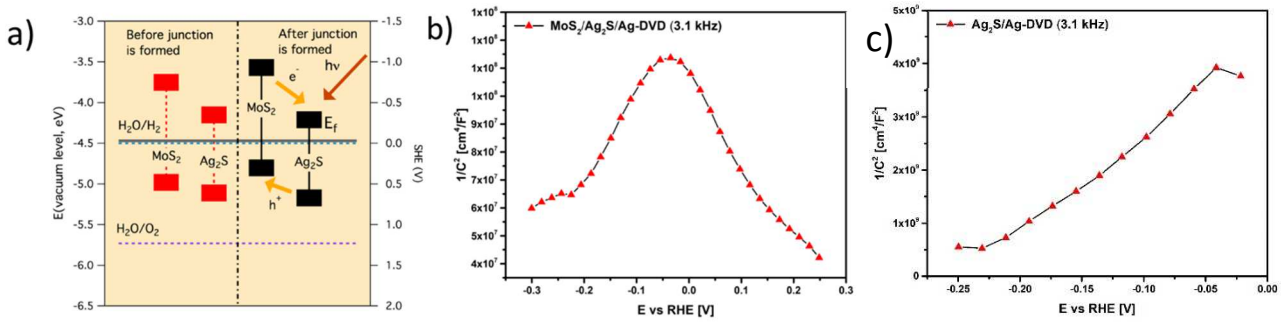

Figure 3.6. a) Approximate position of VB and CB edges of MoS_2 and Ag_2S before and after the n-p junction is formed. Approximate values for CB and VB edges, after E_F alignment, are represented as black rectangles. In both cases, the band gap values are assumed equal to those of bulk materials. Yellow arrows indicate the carriers direction under illumination. (b-c) Mott-Schottky plot obtained from MoS_2/Ag_2S/Ag-DVD (b) and Ag_2S/Ag-DVD (c). The values of the plot were extracted using a simplified Rs-(Rc) circuit. Reproduced from Ref. 21.

Moreover, also the occurrence of a photocurrent, as shown in the chronoamperometry of Figure 3.7, is an indirect information about the formation of the n-p junction. It is clear that after the junction has formed MoS_2 VB edge is in a more favorable position for HER. Photocurrents as high as 0.6 mA/cm^2 can be recorded at η= 0.2 V with about 10% improvement in the total current density. This situation is comparable to what already found in the case of p-type MoS_2/n-type (N-doped)-GO nanocomposites, where similar photocurrent densities were recorded, showing also very similar MS plots as well.[33] Other literature examples are the MoS_2/Ag_2S composites, where the Ag_2S nanoparticles were grown on MoS_2 nanosheets by a simple precipitation method, and CdS/MoS_2 heterostructures recently studied by Fang et al..[14,36,37]

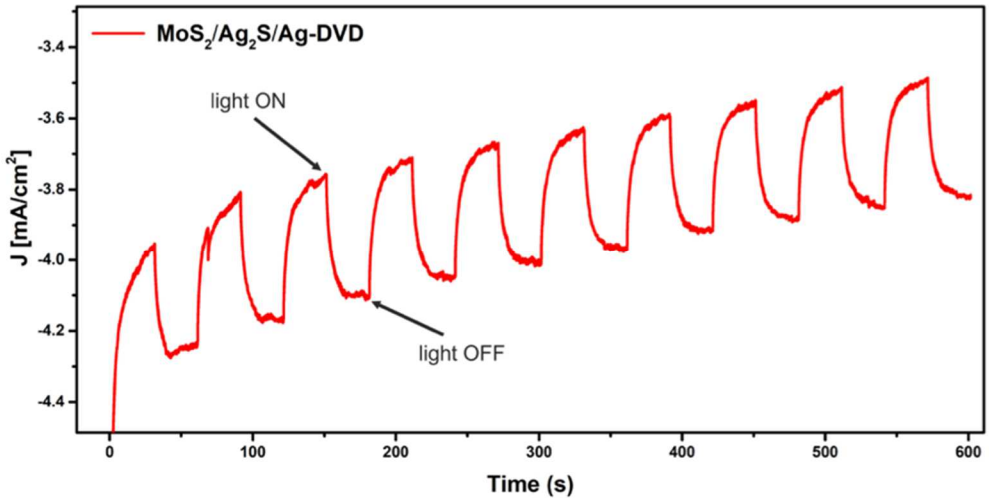

Figure 3.7. J–t curves of MoS_2/Ag_2S/Ag-DVD sample under light (ON) and dark (OFF) conditions at −0.18 V vs RHE. Reproduced from Ref. 21.

A possible contribution of MoO_2 to the electrocatalytic process, as well, may not be excluded considering the fact that in the literature there are several examples where MoO_2 works as an "active" support for MoS_2 or $MoSe_2$ nanostructures[38,39] and that, like Ag_2S, MoO_2 is an n-type oxide[40]. In any case, we have also performed the electrochemical growth of amorphous MoO_x (mixture of MoO_2 and MoO_3) on a clean DVD substrate from

a 50mM $(NH_4)_2MoO_4$ solution and verified that this layer is virtually inactive in the HER process (see Figure 3.5 orange curve). Moreover, the position of E_{Fb}, extrapolated from the MS plot of MoO_x/Ag-DVD plot and corresponding to an n-type semiconductor as shown in Figure 3.8c, is not found at a potential compatible with the V-shaped MS plot of the composite material reported in Figure 3.6b.

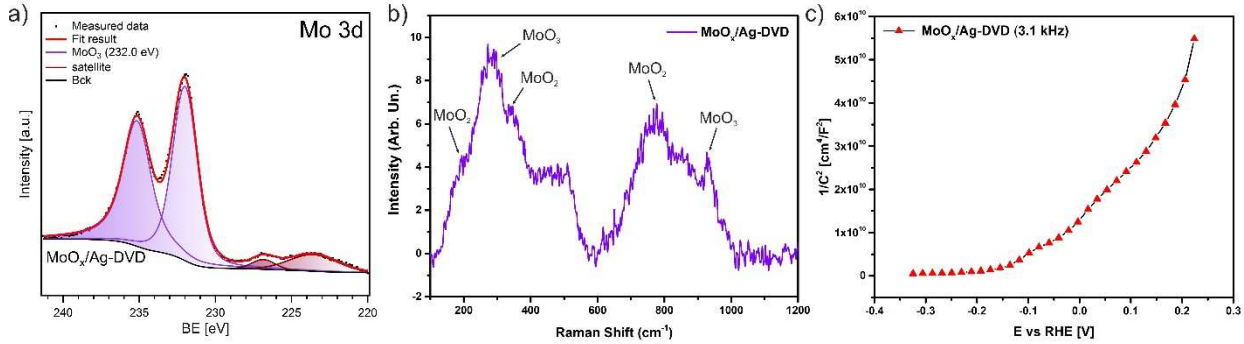

Figure 3.8. (a) High resolution core-level XPS spectrum of Mo 3d of as-prepared MoO_x/Ag-DVD, (b) Raman spectrum of as-prepared MoO_x/Ag-DVD and (c) Mott-Schottky plot obtained from MoO_x/Ag-DVD. Reproduced from Ref. 21.

Finally, the easier charge transfer in the case of the MoS_2/Ag_2S/Ag-DVD system is also confirmed by the EIS data reported in Figure 4c. The much lower semicircle radius in the case of the MoS_2/Ag_2S-Ag-DVD electrode indicates a much smaller charge transfer in the HER process. The EIS data were fitted by a simple Equivalent Circuit where R_s indicates the solution resistance, while the composite layer is represented by a R_c in parallel with a constant phase element (CPE). The calculated values are reported in Table 1.

Durability is another important aspect of an HER electrocatalyst. To assess this, a chronopotentiometry measurement was performed for more than 20h at a cathodic current density of 10 mA/cm^2. In this case, to prevent material loss caused by the small cracks in the Ag film due to the very high turbulence during the H_2 evolution process, as shown in the SEM images in Figure 3.9, it was necessary to add, by drop casting, a Nafion® solution on the electrode surface. The Nafion® solution was prepared by dissolving 10 µL of Nafion® (5 wt.%, Sigma-Aldrich) in 90 µL of ethanol. The Nafion® layer thickness was calculated considering the deposited mass and the surface area of the electrode, assuming the density of dry Nafion® to be 2 g cm^{-3},[41] and resulted to be ~ 0.5 µm. This Nafion® layer greatly increased the stability of the catalyst (see Figure 3.5d). Finally, it is interesting to make a comparison with other MoS_2 based electrocatalysts considering efficiency (Tafel slopes and overpotentials), ease of preparation and starting material costs. For instance, in a recent review on 2D nanomaterials for electrochemical hydrogen evolution,[4] the overpotentials for pure MoS_2 at 10 mA current density are ranging from 0.3 to 0.1 V with the lowest overpotential referring to a porous 1T-MoS_2 phase obtained with a sophisticated liquid-ammonia lithiation route.[42] Instead, the overpotentials at 10 mA current density for composite materials containing MoS_2 in different phases are reported between 0.078 V, for a hierarchical MoS_2 vertical graphene nanosheets structure, to 0.232 V for a MoS_2/r-GO nanosheets.[5] Particularly, comparable composite materials, also based on MoS_2/Ag_2S/Ag nanostructures,[24,14] were showing overpotentials at 10 mA current density of about 0.40 V and lower than 0.20 V respectively, but in both cases the preparation procedure requires several steps and is much more time consuming and expensive with respect to our procedure. Similar considerations could be done also considering other MoS_2-based hybrids, FeS_2 or NiS_2 nanoparticles on MoS_2/rGO scaffold, which required 110 and 123 mV

overpotential to deliver 10 mA cm^{-2}, but the preparation in autoclave limits the application in large scale. Even lower onset potential was obtained on $MoS_{2(1-x)}Se_{2x}/NiSe_{foam}$, but also in this case the need of two high temperature processes hinder the use of this material in everyday systems.[43]

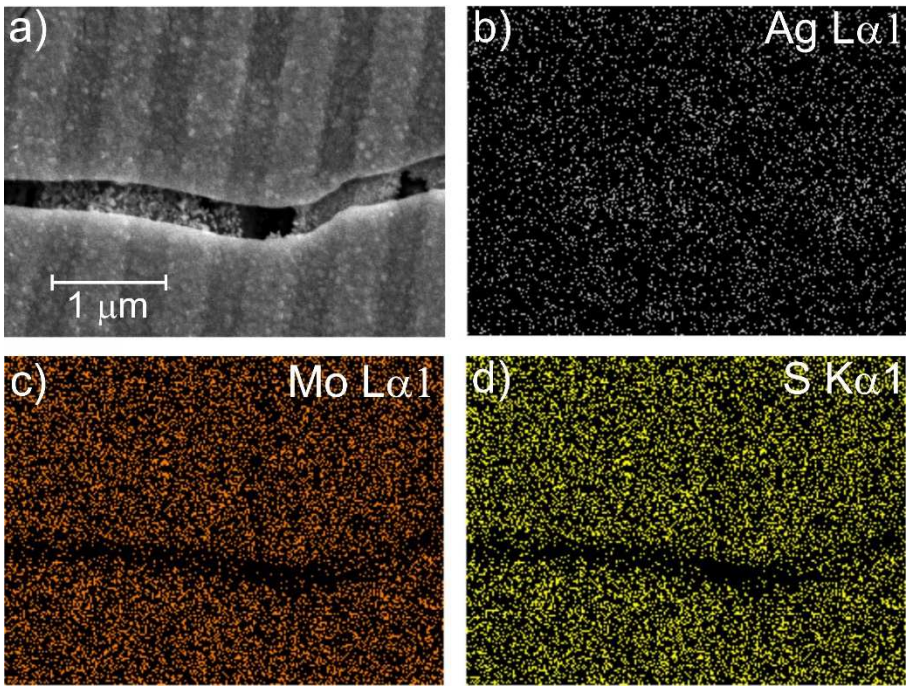

Figure 3.9. a) SEM image of area used for the EDX mapping, (b)-(d) EDX mapping of MoS_2/Ag_2S/Ag-DVD sample after electrochemistry measurements showing the uniform distribution of Ag, Mo and S. Reproduced from Ref. 21.

3.4 Conclusions

We have prepared efficient electrodes for HER from commercial DVDs. The use of the Ag layer as substrate for the electrochemical deposition of MoS_2 leads to the concomitant formation of Ag_2S and MoO_x NPs because of the high concentration of HS^- ions in solution as the result of the MoS_4^{2-} ion reduction and partial hydrolysis.

Figure 3.10. Example of the large area MoS_2/Ag_2S/Ag-DVD electrode. Reproduced from Ref. 21.

The obtained deposit is a composite amorphous layer, characterized by a uniform distribution of nano n-p junctions (between MoS_2-44% and Ag_2S-56%) and Ag NPs that are responsible for the very good electroactivity of this material. Its performances can be further enhanced (≈+10%) exploiting visible light, with a photocurrent as high as 0.6 mA/cm^2 at η=0.2 V. These electrodes also showed a very good durability, with stable currents for more than 20h.

In conclusion, an overpotential of 0.198 V, the ease of preparation, low cost of materials, recycled DVDs, coupled to an added photocatalytic effect make this material very interesting. We would like to stress the fact that these electrodes can be prepared, literally, in minutes using commercial writable DVDs that are becoming quickly obsolete substrates and often are thrown into the garbage can. Moreover, large area electrodes can be obtained easily and quickly by adopting the same deposition procedure on the whole DVD surface as demonstrated in Figure 3.10.

References

(1) Wang, M.; Wang, Z.; Gong, X.; Guo, Z. The Intensification Technologies to Water Electrolysis for Hydrogen Production - A Review. *Renew. Sustain. Energy Rev.* **2014**, *29*, 573–588.

(2) Grewe, T.; Meggouh, M.; Tüysüz, H. Nanocatalysts for Solar Water Splitting and a Perspective on Hydrogen Economy. *Chem. - An Asian J.* **2016**, *11* (1), 22–42.

(3) Chang, K.; Hai, X.; Ye, J. Transition Metal Disulfides as Noble-Metal-Alternative Co-Catalysts for Solar Hydrogen Production. *Adv. Energy Mater.* **2016**, *6* (10), 1–21.

(4) Chen, Y.; Yang, K.; Jiang, B.; Li, J.; Zeng, M.; Fu, L. Emerging Two-Dimensional Nanomaterials for Electrochemical Hydrogen Evolution. *J. Mater. Chem. A* **2017**, *5* (18), 8187–8208.

(5) Lv, Z.; Mahmood, N.; Tahir, M.; Pan, L.; Zhang, X.; Zou, J.-J. Fabrication of Zero to Three Dimensional Nanostructured Molybdenum Sulfides and Their Electrochemical and Photocatalytic Applications. *Nanoscale* **2016**, *8* (43), 18250–18269.

(6) Fan, R.; Mao, J.; Yin, Z.; Jie, J.; Dong, W.; Fang, L.; Zheng, F.; Shen, M. Efficient and Stable Silicon Photocathodes Coated with Vertically Standing Nano-MoS_2 Films for Solar Hydrogen Production. *ACS Appl. Mater. Interfaces* **2017**, *9* (7), 6123–6129.

(7) Lang, B.; Yu, H. K. Novel Ag_2S Nanoparticles on Reduced Graphene Oxide Sheets as a Super-Efficient Catalyst for the Reduction of 4-Nitrophenol. *Chinese Chem. Lett.* **2017**, *28* (2), 417–421.

(8) Basu, M.; Nazir, R.; Mahala, C.; Fageria, P.; Chaudhary, S.; Gangopadhyay, S.; Pande, S. Ag_2S/Ag Heterostructure: A Promising Electrocatalyst for the Hydrogen Evolution Reaction. *Langmuir* **2017**, *33* (13), 3178–3186.

(9) Gupta, A.; Arunachalam, V.; Vasudevan, S. Liquid-Phase Exfoliation of MoS_2 Nanosheets: The Critical Role of Trace Water. *J. Phys. Chem. Lett.* **2016**, *7* (23), 4884–4890.

(10) Lin, H.; Wang, J.; Luo, Q.; Peng, H.; Luo, C.; Qi, R.; Huang, R.; Travas-Sejdic, J.; Duan, C. G. Rapid and Highly Efficient Chemical Exfoliation of Layered MoS_2 and WS_2. *J. Alloys Compd.* **2017**, *699*, 222–229.

(11) Zong, X.; Yan, H.; Wu, G.; Ma, G.; Wen, F.; Wang, L.; Li, C. Enhancement of Photocatalytic H_2 Evolution on CdS by Loading MoS_2 as Cocatalyst under Visible Light Irradiation. *J. Am. Chem. Soc.* **2008**, *130* (23), 7176–7177.

(12) Jiang, W.; Wu, Z.; Yue, X.; Yuan, S.; Lu, H.; Liang, B. Photocatalytic Performance of Ag_2S under Irradiation with Visible and near-Infrared Light and Its Mechanism of Degradation. *RSC Adv.* **2015**, *5* (31), 24064–24071.

(13) Sharma, B. L.; Purohit, R. K. *Semiconductor Heterojunctions*, 1st ed.; Pergamon Press: Oxford: New York, 1974.

(14) Wang, M.; Ju, P.; Li, W.; Zhao, Y.; Han, X. Ag_2S Nanoparticle-Decorated MoS_2 for Enhanced Electrocatalytic and Photoelectrocatalytic Activity in Water Splitting. *Dalt. Trans.* **2017**, *46* (2), 483–490.

(15) Nguyen, D. N.; Nguyen, L. N.; Nguyen, P. D.; Thu, T. V.; Nguyen, A. D.; Tran, P. D. Crystallization of Amorphous Molybdenum Sulfide Induced by Electron or Laser Beam and Its Effect on H_2-Evolving Activities. *J. Phys. Chem. C* **2016**, *120* (50), 28789–28794.

(16) Zanatta, M.; Calvillo, L.; Zheng, J.; Rizzi, G. A.; Durante, C.; Giallongo, G.; Chirkov, D.; Colazzo, L.; Marega, C.; Gennaro, A.; Granozzi, G. Cu_2O/TiO_2 Heterostructures on a DVD as Easy&cheap Photoelectrochemical Sensors. *Thin Solid Films* **2016**, *603*, 193–201.

(17) Zheng, J.; Calvillo, L.; Rizzi, G. A.; Granozzi, G. VO_2/V_2O_5:Ag Nanostructures on a DVD as

Photoelectrochemical Sensors. *Chempluschem* **2016**, *81* (4), 391–398.

(18) Giallongo, G.; Pilot, R.; Durante, C.; Rizzi, G. A.; Signorini, R.; Bozio, R.; Gennaro, A.; Granozzi, G. Silver Nanoparticle Arrays on a DVD-Derived Template: An Easy&cheap SERS Substrate. *Plasmonics* **2011**, *6* (4), 725–733.

(19) Ponomarev, E. A.; Neumann-Spallart, M.; Hodes, G.; Lévy-Clément, C. Electrochemical Deposition of MoS_2 Thin Films by Reduction of Tetrathiomolybdate. *Thin Solid Films* **1996**, *280* (1–2), 86–89.

(20) Ponomarev, E. A. Electrochemical Deposition of Quantized Particle MoS_2 Thin Films. *J. Electrochem. Soc.* **1997**, *144* (10), L277.

(21) Kosmala, T.; Mosconi, D.; Giallongo, G.; Rizzi, G. A.; Granozzi, G. Highly Efficient MoS_2/Ag_2S/Ag Photo-Electrocatalyst Obtained from a Recycled DVD Surface. *ACS Sustain. Chem. Eng.* **2018**, *6*, 7818–7825.

(22) McCrory, C. C. L.; Jung, S.; Peters, J. C.; Jaramillo, T. F. Benchmarking Heterogeneous Electrocatalysts for the Oxygen Evolution Reaction. *J. Am. Chem. Soc.* **2013**, *135* (45), 16977–16987.

(23) Martina, I.; Wiesinger, R.; Schreiner, M. Micro-Raman Investigations of Early Stage Silver Corrosion Products Occurring in Sulfur Containing Atmospheres. *J. Raman Spectrosc.* **2013**, *44* (5), 770–775.

(24) Xia, X.; Zhao, X.; Ye, W.; Wang, C. Highly Porous Ag-Ag_2S/MoS_2 with Additional Active Sites Synthesized by Chemical Etching Method for Enhanced Electrocatalytic Hydrogen Evolution. *Electrochim. Acta* **2014**, *142*, 173–181.

(25) Seguin, L.; Figlarz, M.; Cavagnat, R.; Lassègues, J. C. Infrared and Raman Spectra of MoO_3 Molybdenum Trioxides and $MoO_3 \cdot x\ H_2O$ Molybdenum Trioxide Hydrates. *Spectrochim. Acta Part A Mol. Biomol. Spectrosc.* **1995**, *51* (8), 1323–1344.

(26) Dieterle, M.; Mestl, G. Raman Spectroscopy of Molybdenum Oxides. *Phys. Chem. Chem. Phys.* **2002**, *4* (5), 822–826.

(27) Dieterle, M.; Weinberg, G.; Mestl, G. Raman Spectroscopy of Molybdenum Oxides. *Phys. Chem. Chem. Phys.* **2002**, *4* (5), 812–821.

(28) Fan, X.; Xu, P.; Zhou, D.; Sun, Y.; Li, Y. C.; Nguyen, M. A. T.; Terrones, M.; Mallouk, T. E. Fast and Efficient Preparation of Exfoliated 2H MoS_2 Nanosheets by Sonication-Assisted Lithium Intercalation and Infrared Laser-Induced 1T to 2H Phase Reversion. *Nano Lett.* **2015**, *15* (9), 5956–5960.

(29) Martina, I.; Wiesinger, R.; Schreiner, M. Micro-Raman Characterisation of Silver Corrosion Products : Instrumental Set Up and Reference. *e-Preservation Sci.* **2012**, *9*, 1–8.

(30) Dai, X.; Du, K.; Li, Z.; Liu, M.; Ma, Y.; Sun, H.; Zhang, X.; Yang, Y. Co-Doped MoS_2 Nanosheets with the Dominant CoMoS Phase Coated on Carbon as an Excellent Electrocatalyst for Hydrogen Evolution. *ACS Appl. Mater. Interfaces* **2015**, *7* (49), 27242–27253.

(31) Wang, D. Z.; Zhang, X. Y.; Shen, Y. L.; Wu, Z. Z. Ni-Doped MoS_2 Nanoparticles as Highly Active Hydrogen Evolution Electrocatalysts. *RSC Adv.* **2016**, *6* (20), 16656–16661.

(32) Eng, A. Y. S.; Ambrosi, A.; Sofer, Z.; Šimek, P.; Pumera, M. Electrochemistry of Transition Metal Dichalcogenides: Strong Dependence on the Metal-to-Chalcogen Composition and Exfoliation Method. *ACS Nano* **2014**, *8* (12), 12185–12198.

(33) Carraro, F.; Calvillo, L.; Cattelan, M.; Favaro, M.; Righetto, M.; Nappini, S.; Píš, I.; Celorrio, V.; Fermín, D. J.; Martucci, A.; Agnoli, S.; Granozzi, G. Fast One-Pot Synthesis of MoS_2/Crumpled Graphene p-n Nanonjunctions for Enhanced Photoelectrochemical Hydrogen Production. *ACS Appl. Mater. Interfaces* **2015**, *7* (46), 25685–25692.

(34) Omeiri, S.; Hadjarab, B.; Trari, M. Photoelectrochemical Properties of Anodic Silver Sulphide Thin Films. *Thin Solid Films* **2011**, *519* (13), 4277–4281.

(35) Swain, G.; Sultana, S.; Naik, B.; Parida, K. Coupling of Crumpled-Type Novel MoS_2 with CeO_2 Nanoparticles: A Noble-Metal-Free p-n Heterojunction Composite for Visible Light Photocatalytic H_2 Production. *ACS Omega* **2017**, *2* (7), 3745–3753.

(36) Meng, F.; Li, J.; Cushing, S. K.; Zhi, M.; Wu, N. Solar Hydrogen Generation by Nanoscale P-n Junction of p-Type Molybdenum Disulfide/n-Type Nitrogen-Doped Reduced Graphene Oxide. *J. Am. Chem. Soc.* **2013**, *135* (28), 10286–10289.

(37) Li, C.; Wang, H.; Ming, J.; Liu, M.; Fang, P. Hydrogen Generation by Photocatalytic Reforming of Glucose with Heterostructured CdS/MoS_2 Composites under Visible Light Irradiation. *Int. J. Hydrogen Energy* **2017**, *42* (27), 16968–16978.

(38) Luo, J.; Xu, P.; Zhang, D.; Wei, L.; Zhou, D.; Xu, W.; Li, J.; Yuan, D. Synthesis of 3D-MoO_2 Microsphere Supported $MoSe_2$ as an Efficient Electrocatalyst for Hydrogen Evolution Reaction. *Nanotechnology* **2017**, *28* (46).

(39) Rheem, Y.; Han, Y.; Lee, K. H.; Choi, S.-M.; Myung, N. V. Synthesis of Hierarchical MoO_2/MoS_2 Nanofibers for Electrocatalytic Hydrogen Evolution. *Nanotechnology* **2017**, *28* (10).

(40) Dukštiene, N.; Sinkevičiute, D. Photoelectrochemical Properties of MoO_2 Thin Films. *J. Solid State Electrochem.* **2013**, *17* (4), 1175–1184.

(41) Erikson, H.; Kasikov, A.; Johans, C.; Kontturi, K.; Tammeveski, K.; Sarapuu, A. Oxygen Reduction on Nafion-Coated Thin-Film Palladium Electrodes. *J. Electroanal. Chem.* **2011**, *652* (1–2), 1–7.

(42) Yin, Y.; Han, J.; Zhang, Y.; Zhang, X.; Xu, P.; Yuan, Q.; Samad, L.; Wang, X.; Wang, Y.; Zhang, Z.; Zhang, P.; Cao, X.; Song, B.; Jin, S. Contributions of Phase, Sulfur Vacancies, and Edges to the Hydrogen Evolution Reaction Catalytic Activity of Porous Molybdenum Disulfide Nanosheets. *J. Am. Chem. Soc.* **2016**, *138* (25), 7965–7972.

(43) Zhou, H.; Yu, F.; Huang, Y.; Sun, J.; Zhu, Z.; Nielsen, R. J.; He, R.; Bao, J.; Goddard III, W. A.; Chen, S.; Ren, Z. Efficient Hydrogen Evolution by Ternary Molybdenum Sulfoselenide Particles on Self-Standing Porous Nickel Diselenide Foam. *Nat. Commun.* **2016**, *7*, 12765.

Chapter Four:

One-pot solvothermal synthesis of $MoS_{2(1-x)}Se_{2x}$/N-rGO hybrids for photoenhanced HER

4.1 Introduction

Hydrogen production using photoelectrochemical (PEC) water splitting (WS) has received a great deal of attention as a sustainable and clean way to convert solar to chemical energy. The material requirements of PEC cells (i.e., high visible absorption, slow recombination, and fast carrier transport,...) have some analogies to those of solar cells, but PEC-WS is possibly even more challenging due to side redox reactions that may be triggered by photogenerated carriers. To improve the reaction kinetics, the development of HER cocatalysts with low overpotential is a very important issue. For MoS_2 most research has focused on increasing the number of exposed edges, based on the understanding that these are the primary catalytically active sites for HER in acid environment.[1] In contrast to this point of view, Voiry *et al.* reported that the conductivity of the basal plane is a critical factor in the catalytic performance of MoS_2.[2] Based on this idea, graphene has been used to support MoS_2 support and consequently to enhance the charge transfer properties and to impart a better electrical conductivity with respect to MoS_2 alone.[3,4] However, while graphene itself can improve the electrochemical (EC) performance in the hydrogen production due to the contribution to the raise to the conductivity, being a semimetal gapless material, it cannot participate directly in PEC processes. Indeed, to enhance the PEC properties of MoS_2, usually two main routes are pursued:

- the former is to couple MoS_2 with a suitable material in order to form p-n junctions, which help in enhancing the photogenerated excitons life (as showed in Chapter Three);
- the latter is to tune the optoelectronic properties (i.e. bandgap engineering) aiming to optimize the light absorption and the energy level matching.

As mentioned in Section 1.3.3, a useful way to tailor the optoelectronic properties of TMDCs is the composition alloying, i.e. exploiting ternary compounds by varying the molar fraction of the metal (i.e. $Mo_{(1-x)}W_xS_2$) or of the chalcogenide (i.e. $MoS_{2(1-x)}Se_{2x}$).[5–13] In these studies, a precise control over the nanosheets composition, shape[5], band gap[10] and optical properties[11] has been reached, as demonstrated by several techniques like SEM, TEM, Raman and UV-Vis Spectroscopy, XPS and EDX, giving rise to materials that have been utilized also in hydrogen production with excellent results.[9,12,13] This modification route allows to have a precise control of the chemical composition and physical properties. However, quite often not easily scalable synthetic methods are employed, e.g. Chemical Vapor Deposition (CVD). Moreover, especially when the chalcogenide fraction has to be tuned, generating harmful gases such as H_2Se and H_2S are produced. On the contrary very few works were published about wet chemistry routes for synthesizing $MoS_{2(1-x)}Se_{2x}$.[14] So the design of a safe and scalable synthetic method for TMDCs alloys can pave the way to the utilization of these materials, overcoming the CVD limitations connected to the low throughput.

In this Chapter, we describe a one-pot solvothermal synthetic method to produce $MoS_{2(1-x)}Se_{2x}$ with easy-to-tune Se:S ratio, alternative to the CVD one. Nevertheless, having in mind the goal of hydrogen production *via* PEC-WS, we decided to grow the alloy directly on Nitrogen-doped reduced Graphene Oxide (N-rGO), in order to improve both the electrical conductivity and the photocatalytic properties, thanks to the formation of p-n junction between $MoS_{2(1-x)}Se_{2x}$ (p-type) and N-rGO (n-type). The materials have been extensively characterized by mean of XPS, Raman and UV-Vis spectroscopy techniques and their electrocatalytic and PEC properties have been deeply explored.

4.2 Experimental Section

Synthesis of N-rGO

The GO was synthesized following a modified Hummer's method.[15]

An amount of 3.0 g of graphite was mixed with 75 ml of 9:1 mixture of H_2SO_4 and H_3PO_4. Then an amount of 9.0 g of $KMnO_4$ was slowly added while cooling the mixture in an ice bath. The mixture was stirred for 3 h at 0 °C and then overnight at room temperature. After that, a volume of 150 ml of water was added during heating at 80 °C. After stirring for 1 h, the obtained mixture was sonicated for 1 h at 35 °C. To quench the reaction, 3 mL of 30 %wt. of H_2O_2 was added, stirred for additional 2 h, sonicated for 1 h and finally, diluted with additional water. The supernatant was profusely washed with water, dialyzed 72 h against DI water and 8 h against Milli-Q quality water, and finally lyophilized.

N-doped reduced GO (N-rGO) was synthesized according to literature procedure.[16] First, a 200 mg of GO and 1 g of melamine were grounded in a mortar for 5 minutes and transferred to a combustion boat. Then, the boat was inserted in a tubular furnace with lid and purged with Ar for 10 min at 600 sccm. After that the Ar flow was set at 30 sccm and the temperature was raised to 300 °C (20 min; ramp 5 °C min^{-1}) to allow the adsorption of melamine molecule to GO flakes. Subsequently, the material was annealed at 900 °C (1 h; ramp 5°C min^{-1}) and then cooled down naturally in inert atmosphere.

Synthesis of Ammonium Tetrathiomolybdate (ATM)

The ammonium Molybdate $(NH_4)_6Mo_7O_{24} \cdot 4H_2O$ (3 g; 2.43 mmol, from Sigma-Aldrich) was dissolved under stirring in 45 ml of aqueous $(NH_4)_2S$ (20 %wt, from Sigma-Aldrich) in a closed bottle. When a clear solution was obtained, stirring was stopped and the solution was keep at r.t. for 1h. Afterwards, the solution was kept at 4°C overnight to allow the formation of deep red needle-like crystals. ATM crystals were filtered under a gentle Ar flow and washed with cold water and cold ethanol. The product was then dried under nitrogen and stored in inert gas (3.5 g; yield 79.1 %).

Synthesis of $MoS_{2(1-x)}Se_{2x}$/N-rGO

N-rGO (15 mg) and ammonium tetrathiomolybdate (ATM, 33 mg) were mixed in 15 ml of N,N-dimethyformamide (DMF) in a closed glass vial. Different amounts of Dimethyl Diselenide (DMDSe) (0, 3, 6, 12, 24, 96 µl) were added to the suspension as Se source. The mixture was bath-sonicated for 20 min and then transferred to a Teflon-lined autoclave (23 ml liner). The heating was conducted in two steps in an electric oven: 15h at 180 °C to allow the heterogeneous growth of MoS_x slabs on N-rGO plus additional 5h at 200 °C to activate the selenizing agent. To remove molecular byproducts, materials were centrifuged for 8 min at 10000 rpm (23478-*g*) in DMF and ethanol two times each and then dried in vacuum.

In order to obtain the crystalline product, powders were inserted in a tubular furnace and annealed at 600 °C for 1h (ramp 5 °C min^{-1}) in 95:5 Ar:H_2 atmosphere.

For comparison, two synthesis with 6 µl of DMDSe were conducted with one-step heating (15h at 200°C) and with shorter growth step (10h at 180°C + 5h at 200°C).

Synthesis of $MoSe_2$/N-rGO

To ensure the role of ATM in heterogeneous nucleation and the behaviour of DMDSe at different temperatures, two synthesis with $MoCl_5$ and DMDSe were realized. N-rGO (15 mg) and $MoCl_5$ (34 mg) were poured in a glass vial. 15 ml of DMF and 45 µl of DMDSe were added to the mixture, that was subsequently sonicated for 20 min and transferred to a 23 ml Teflon-lined autoclave. The reaction was carried out for 15h at 180 °C or with stepped heating 15h at 180 °C plus 5h at 200 °C. After natural cooling down, materials were cleaned by centrifugation for 8 min at 10000 rpm (23478-*g*) in DMF and ethanol two times each and then dried in vacuum.

Physico-chemical Characterization

The surface chemical characterization of the hybrids has been carried out using X-ray photoelectron spectroscopy (XPS) in a custom-made UHV system working at a base pressure of 10^{-10} mbar, equipped with an Omicron EA150 electron analyzer and an Omicron DAR 400 X-ray source with a dual Al−Mg anode. Core level photoemission spectra (Mo 3d, S 2p, Se 3p, Se 3d, C 1s, N 1s and O 1s regions) were collected at rt with a non-monochromated Mg Kα X-ray source (1253.6 eV) and using an energy step of 0.1 eV, 0.5 s of integration time, and a 20 eV pass energy. The multipeak analysis of core level photoemission lines was performed by means of Gaussian−Lorentzian functions and subtracting a Shirley background using the *KolXPD* software. The samples were dispersed in 2-propanol and drop casted on an Al support. The nano- and microscale morphology of materials was studied by scanning electron microscopy (SEM) and transmission electron microscopy (TEM). The SEM images were acquired using a field emission source equipped with a GEMINI column (Zeiss Supra VP35) and an Oxford energy-dispersive x-ray spectroscopy (EDX) microprobe, and micrographs were obtained with an acceleration voltage of 5 or 10 kV using in-lens high-resolution detection. The TEM images were acquired using a FEI Tecnai 12 microscope with an acceleration voltage of 100 kV. The Raman spectra were collected using a ThermoFisher DXR Raman microscope using a laser with an excitation wavelength of 532 nm (0.3 mW), focused on the sample with a 50× objective (Olympus). The UV−Vis absorption spectroscopy data were acquired using a Varian Cary 50 Spectrophotometer in the 300-800 nm range. In this case, powder samples were dispersed in DMF, forming a stable colloidal dispersion. All spectra were recorded using 1 cm optical path quartz cells. The concentration and the experimental parameters were optimized to minimize scattering effects.

Electrochemical Characterization

The EC and PEC HER measurements were carried out in a custom designed three-electrode configuration cell using an Autolab PGSTAT-204 (Ecochemie) potentiostat. A Pt wire was used as a counter electrode, whereas an $Ag/AgCl_{(3M\ KCl)}$ electrode, calibrated with respect to the reversible hydrogen electrode (RHE), was the reference electrode. All potentials reported in the text and figures are referred to the (RHE) and corrected according to the equation: E(RHE) = E(Ag/AgCl) + 0.225 V + 0.059 pH. The EC and PEC experiments were carried out in Ar-saturated 0.5 M H_2SO_4 solution prepared from high-purity reagents (Sigma-Aldrich) and ultrapure Milli-Q water with a resistivity of 18.2 MΩ·cm. The working electrode was prepared by depositing 12 µl of catalyst ink on a GC electrode (area delimited to 4.5 mm diameter). The catalyst ink consisted of 5 mg of active material, 1.0 mL of N,N-dimethylformamide and 25 µL of Nafion solution. Polarization curves were

recorded from +0.2 V to -0.35 V vs RHE using a scan rate of 0.005 V s^{-1}. All *V-t* curves were recorded at overpotential (η) equal to 0.18 V. Curves were iR-corrected using the resistance found in Electrochemical impedance spectroscopy (EIS). EIS were measured at overpotential of η = 0.18 V and superimposing a small sinusoidal voltage of 10 mV over the frequency range 0.1 MHz to 100 mHz. The PEC HER enhancement was quantified by measuring polarization curves under light illumination from a white neutral LED (WLED) (LDCNW, Metrohm, Autolab LED Driver kit), with the light intensity of 97 mW/cm^2. Transient current measurement was conducted by applying constant cathodic potential (-0.18 V vs RHE) to the working electrode and the current respond was measured under chopped light from WLED. The same experiments were carried out with different monochromatic LEDs (655 nm, 627 nm, 617 nm, 590 nm, 530 nm, 505 nm and 470 nm) for Incident Photon to Current Efficiency (IPCE) analysis.

4.3 Results and Discussion

4.3.1 N-rGO Structural Characterization

The utilization of N-rGO is fundamental to improve the PEC performances of the final catalysts, since N-rGO can impart two fundamental properties. In particular, the use of a scaffold for $MoS_{2(1-x)}Se_{2x}$ with optimal electrical properties can help in the electron transfer processes and moreover the n-type conductivity of N-rGO allows to form p-n nanojuctions with $MoS_{2(1-x)}Se_{2x,}$ being the latter typically p-type when synthesized *via* bottom-up methods.[17,18] Therefore, we synthesized N-rGO according to the literature in order to obtain a marked N-doping and we used a quite high annealing temperature in order to restore as much as possible a good electronic conduction.[16] N-rGO was characterized by mean of SEM, Raman Spectroscopy and XPS.

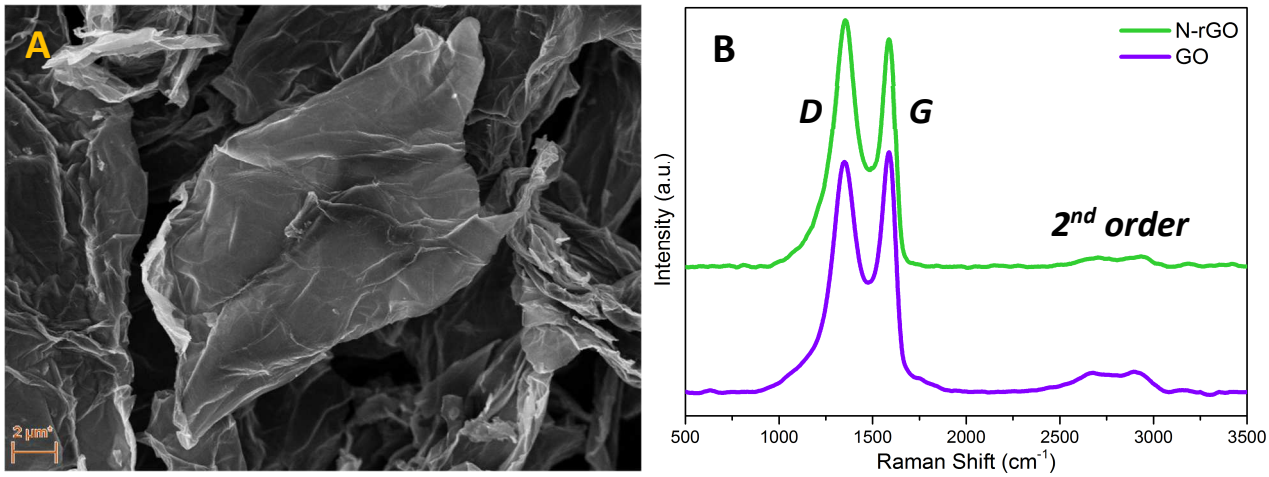

Figure 4.1. (A) SEM image of N-rGO and (B) Raman spectra of pristine GO and N-rGO.

Figure 4.1A reports a SEM micrograph showing the typical N-rGO flake, with lateral size of approximately 20 µm, compatible with the typical values reported for a materials synthesized by the modified Hummer's method. The Raman spectra of pristine GO and N-rGO display the classical graphene-like features, with the D-band at 1350 cm^{-1} and G-band at 1590 cm^{-1}, with the 2nd order spectrum in the 2750 cm^{-1} range. Interestingly, the I_D/I_G ratio increases from 0.96 in the GO to 1.09 in the N-rGO. This increase in disorder may be due to the eventual insertion of nitrogen, since, in several configurations (i.e. pyridinic or pyrrolic), it causes the interruption of the honeycomb lattice.

A more detailed characterization was obtained by XPS. The surface composition (see Table 4.1) highlights the presence of 5.3 %at. of N, indicating the achievement of N-doping.

Material	C (%at.)	O (%at.)	N (%at.)	C/O	N/C
GO	74.1	25.9	-	2.9	-
N-rGO	86.7	8.0	5.3	10.8	0.06

Table 4.1. Surface composition for pristine GO and N-rGO synthesized at 900 °C.

The N/C atomic ratio as well is within the expected range for this kind of procedure[16] and the 4-fold increment on the C/O ratio, proves the reduction of GO. A multipeak analysis of C 1s and N 1s core levels was performed to understand the evolution of the material after the doping procedure (Figure 4.2). Table 4.2 summarizes the components used to fit both photoemission lines, with the associated percentages and binding energies (BEs).

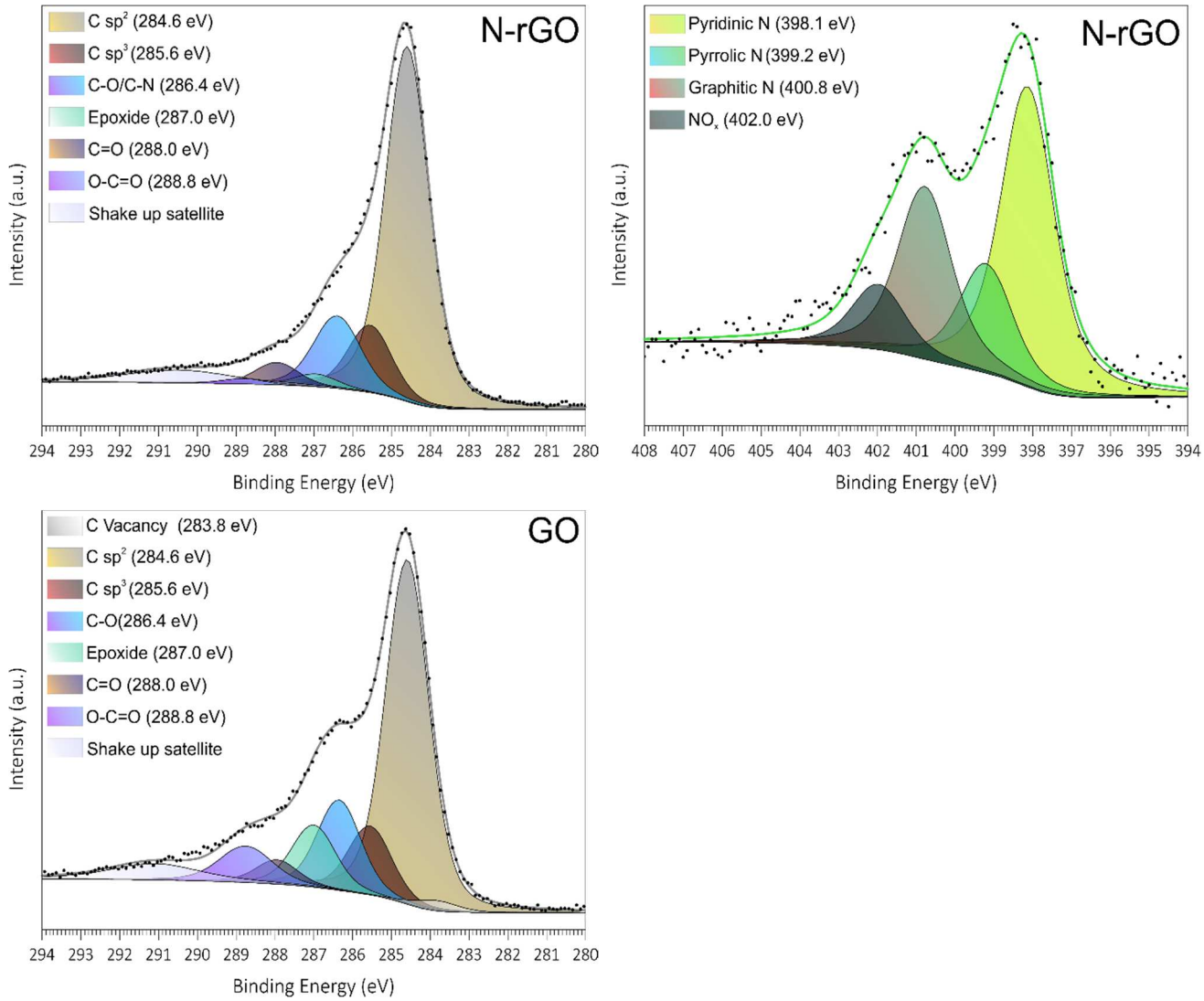

Figure 4.2. High resolution spectra of C 1s (*left*) and of N 1s (*right*) photoemission lines.

C 1s	*C Vacancy*	*C sp²*	*C sp³*	*C-O / C-N*	*Epoxy*	*Carbonyl / Amide*	*Carboxylic Acid*
Binding Energy (eV)	*283.8*	*284.6*	*285.6*	*286.4*	*287.0*	*288.0*	*288.8*
GO	1.6	53.4	10.6	14.0	9.6	3.8	7.0
N-rGO	-	65.5	12.3	14.4	2.3	4.1	1.0
N 1s	*Pyridinic*	*Pyrrolic*	*Graphitic*	*NO_x*			
Binding Energy (eV)	*398.1*	*399.2*	*400.8*	*402.0*			
GO	-	-	-	-			
N-rGO	46.4	16.9	26.6	10.1			

Table 4.2. Summary of components percentages in C 1s (upper part) and N 1s (lower part) core levels.

The C 1s line reveals a remarkable increment in the C sp^2 component at the expenses of the oxygenated moieties, in particular epoxides and carboxylic acids groups, further confirming the achievement of the graphene lattice healing. The band relative to C involved in the bonds with heteroatoms, like N and O, remains substantially constant upon doping procedure, which is not surprising considering the introduction of N in the material.

The multipeak analysis of N 1s core level allows to detect what kind of compounds were formed during the synthesis, considering that there are several ways for N to enter in the graphene lattice.[19] In our material, four components were necessary to achieve a satisfying fitting of the N 1s region, i.e. peaks assignable to Pyridinic N (398.1 eV), Pyrrolic N (399.2 eV), Graphitic N (400.8 eV) and oxidized N (402.0 eV) were found. In particular, the presence of Graphitic Nitrogen (26.6 % of total N signal) is crucial, since this kind of defect imparts the n-type conductivity to N-rGO.[20–22]

4.3.2 Morphological Analysis on $MoS_{2(1-x)}Se_{2x}$/N-rGO hybrids

Having in mind the goal of synthesizing a photoelectrocatalyst, a good electric contact is necessary between the components to take advantage of the formation of p-n nanojunctions. Different synthetic conditions were tested in order to achieve a preferential heterogeneous nucleation of $MoS_{2(1-x)}Se_{2x}$ nanosheets on larger N-rGO flakes, since homogeneous nucleation would form $MoS_{2(1-x)}Se_{2x}$ particles that are only weakly bound to the scaffold. Cleary, a morphological analysis is mandatory in this context to optimize the nucleation-growth conditions. In Figure 4.3, we report the SEM analysis of $MoS_{2(1-x)}Se_{2x}$/N-rGO hybrids prepared with different combinations of reaction times and temperatures, in order to study their effect on the nucleation process. According to the literature, the MoS_4^{2-} should decompose at about 180 °C, nucleating MoS_x slabs on N-rGO.[23] The key role of the ATM in the formation of a hybrid nanostructure was confirmed by performing an additional experiment in which $MoCl_5$ and DMDSe where used as Mo and Se source. In this case a very different structure (nanoparticles) was observed (see Figure 4.3D). Furthermore, it was found that the DMDSe is activated as selenizing agent at higher temperature (200 °C) in comparison to ATM (180 °C). When the synthesis of $MoS_{2(1-x)}Se_{2x}$/N-rGO hybrid is performed directly at 200°C, the homogenous nucleation of $MoS_{2(1-x)}Se_{2x}$ particles can be observed, without any nanosheets grown on N-rGO (see Figure 4.3A). This may be ascribed to two factors: the higher temperature induces a faster decomposition of ATM or/and due to

selenization process which prevent the heterogeneous nucleation as observed in the synthesis of $MoSe_2$/N-rGO (Figure 4.3D). On the other hand, in the low temperature regime, both homogeneous and heterogeneous nucleation are possible but the latter is kinetically favoured by the slower decomposition of ATM (Figure 4.3B). Extending the growth step at 180°C (Figure 4.3C), the density of nanosheets increases, with 40 nm flakes assemblies. In all the cases, no substantial differences were observed before and after the thermal annealing, as proved by TEM images reported for 6µl $MoS_{2(1-x)}Se_{2x}$/N-rGO before (E) and after annealing (F).

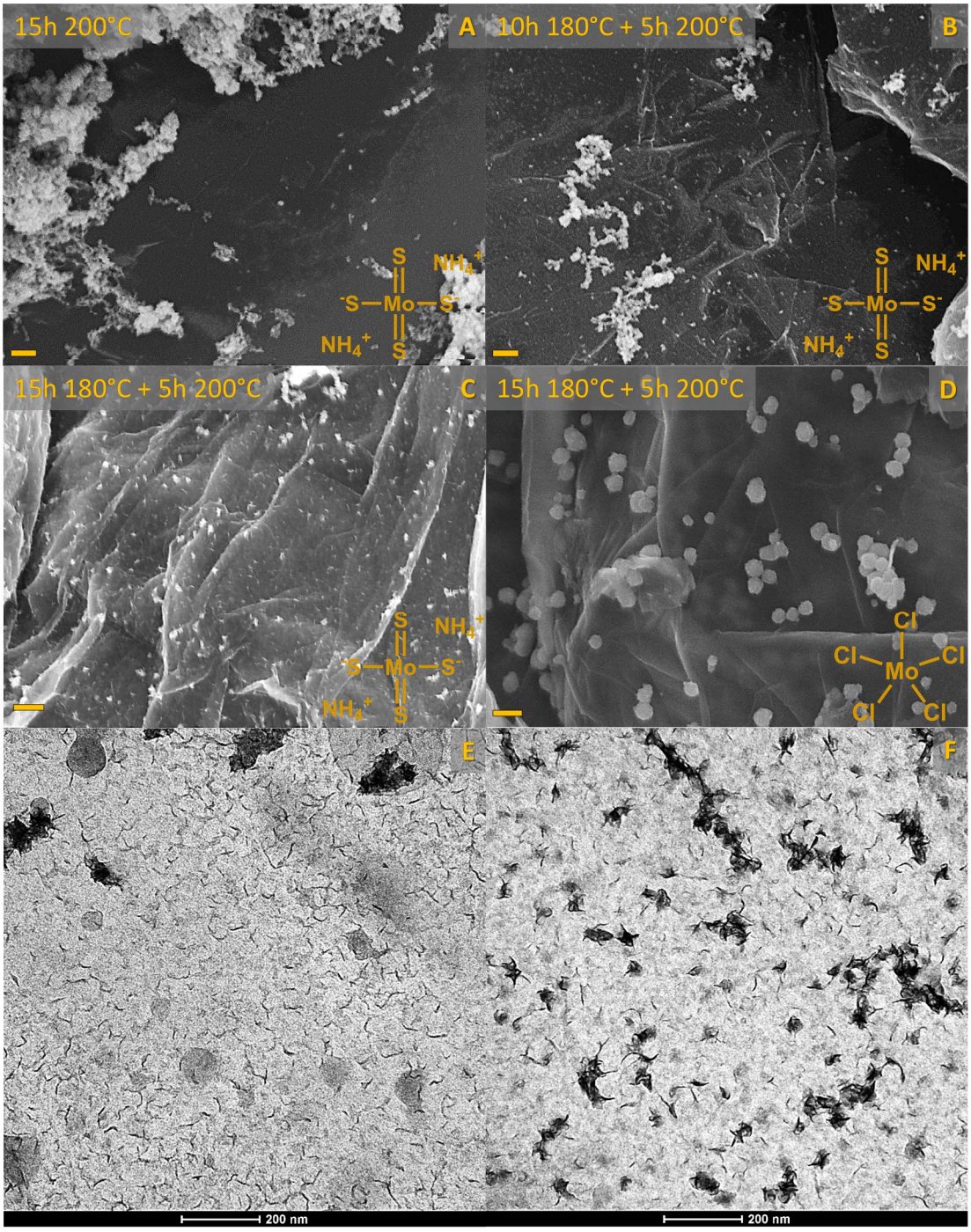

Figure 4.3. (A-D) SEM images of $MoS_{2(1-x)}Se_{2x}$ /N-rGO (see text for more infos): A) without step-temperature heating; B-C) with different growth step dwell time and D) with $MoCl_5$ as Mo source. (scale bar: 200 nm) (E-F) TEM images of the same sample represented in Figure 4.3C, before (E) and after (F) the annealing step.

4.3.3 Structural and chemical characterization

Raman spectroscopy was used, together with X-ray Photoemission Spectroscopy (XPS), to follow the composition of the hybrid material depending on the amount of the DMDSe precursor used in the synthesis.[11] Figure 4.4 shows the Raman spectra of $MoS_{2(1-x)}Se_{2x}$/N-rGO hybrids prepared with different amount of selenizing agent, before and after the annealing at 600 °C .

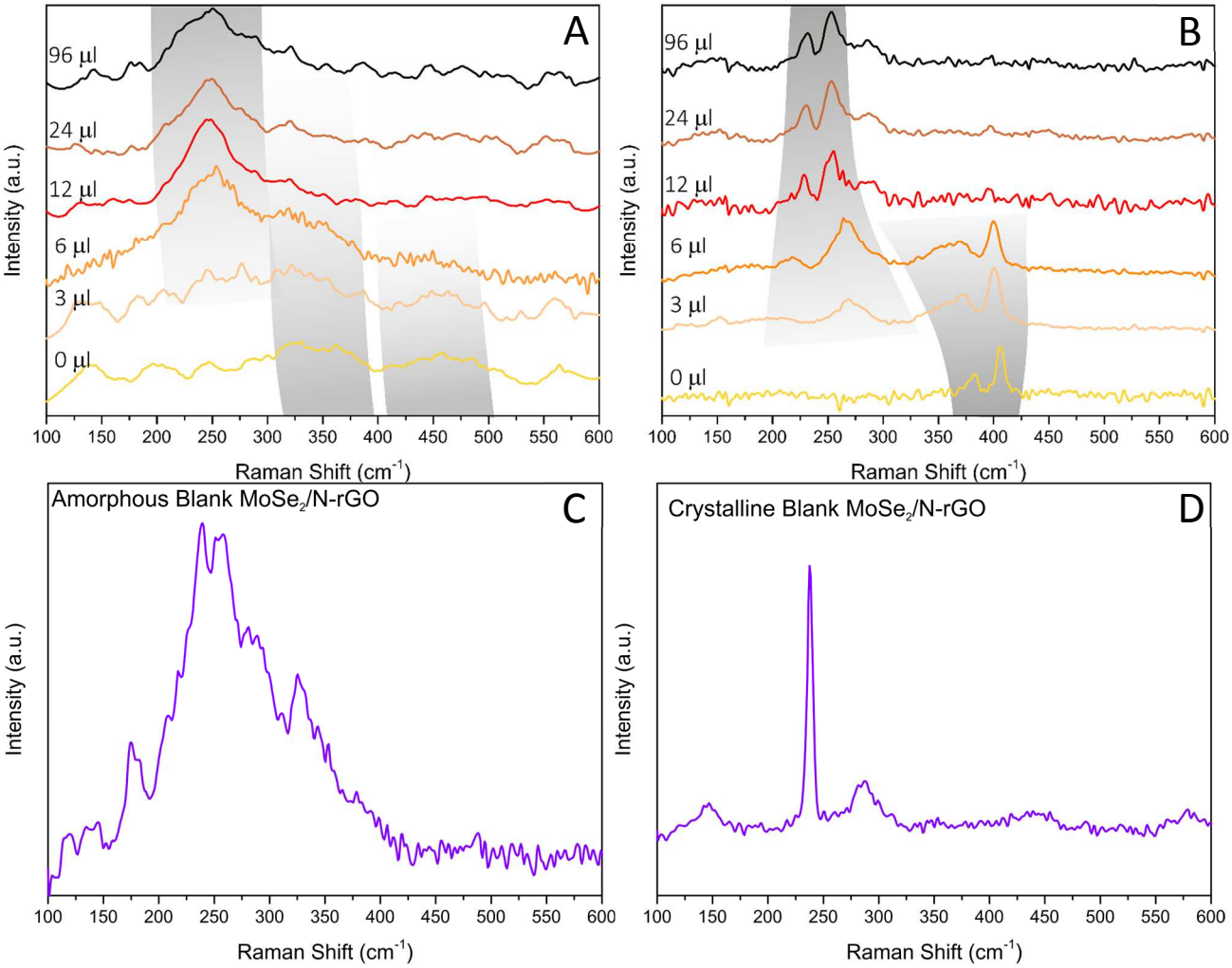

Figure 4.4. Raman spectra for samples with different Se loading before (A) and after annealing at 600°C (B). Raman spectra of blank $MoSe_2$/N-rGO before (C) and after (D) annealing are reported as well.

The samples before annealing show weak and broad peaks, indicating the amorphous nature of the $MoS_{2(1-x)}Se_{2x}$, as often reported in hydro- or solvothermal synthesis of TMDCs.[24–28] However, some trends can be observed: MoS_2/N-rGO (0 µl sample) exhibits two broad bands centred at about 350 and 460 cm^{-1} (defective form of E^1_{2g} and A_{1g} normal modes of MoS_2)[29]. Increasing the DMDSe volume, both these bands tend to downshift to lower wavenumbers, which is a consequence of the substitution of S with the heavier Se anion. Starting from the 3 µl $MoS_{2(1-x)}Se_{2x}$ sample, another weak mode appears at 260 cm^{-1} (A_{1g} of $MoSe_2$) and moving toward low wavenumbers with the increment of Se amount.

The annealing process of the amorphous samples induces a crystallization as it can be deduced by Figure 4.4B, which exhibit spectra with sharper vibrational bands. Moreover, as in the case of amorphous samples, we observe a shift of the bands as a function of the content of Se. The Raman spectrum of MoS_2/N-rGO shows

the typical spectral fingerprint of semiconducting 2H-phase MoS_2, with E^1_{2g} and A_{1g} at 383 and 405 cm^{-1}, respectively. The difference between the centroids of these peaks is a useful tool to estimate the average number of layers in MoS_2 particles and, according to the literature, the measured 22 cm^{-1} separation indicates about 3 layers per stack.[30,31]

In the case of crystalline samples by increasing the Se content, it can be clearly seen a typical "two mode behaviour", which does not entail phase separation.[32–34] The two-mode behaviour occurs when the frequencies of phonon modes in the pure compounds (*e.g.* MoS_2 and $MoSe_2$) differs sufficiently from one another. The phonon features of pure MoS_2 and $MoSe_2$ are separated of about 200 cm^{-1}, which allows for the observation of the two-mode behaviour in $MoS_{2(1-x)}Se_{2x}$/N-rGO hybrid. The consequence is that E^1_{2g} and A_{1g} vibrations of MoS_2 tends to downshift as S is exchanged for Se, with a concomitant broadening of E^1_{2g}. Similarly, $MoSe_2$-like features start appearing at 270 cm^{-1} in 3 µl sample and shifts down to 253 cm^{-1} in 96 µl sample, at the same time getting narrower. It is worthwhile to mention that above 12 µl few changes can be observed in Raman analysis and moreover, the typical Raman spectrum of $MoSe_2$ (single sharp peak at 238 cm^{-1}, see Figure 4.4D) was not observed. This may be due to an equilibrium between S^{x-} and Se^{x-} species during the synthesis, which would not allow reaching the full anion exchange and obtaining pure $MoSe_2$/N-rGO.

These considerations were further confirmed by an extensive XPS study. Mo 3d core levels are shown in Figure 4.5A (amorphous) and B (crystalline), in both cases a clear shift to lower BE of Mo $3d_{5/2}$peak is observed by increasing the amount of Se precursor. Considering crystalline samples, the Mo 3d line of MoS_2/N-rGO (0 µl) has the expected position of the semiconducting 2H-phase of MoS_2 (228.9 eV);[35] increasing the quantity of Se causes the BE to shift continuously toward lower values. The value observed for the 96 µl sample was 228.6 eV (0.3 eV lower than 0 µl) and, even if close, it is not the same BE (228.5 eV) observed for commercial $MoSe_2$ and $MoSe_2$/N-rGO obtained from the blank experiment with $MoCl_5$ (see Figure 4.23A in the appendix). This is an additional indication that using the combination of ATM and DMDSe is not possible to reach full anion exchange, at least within the tested conditions. The deconvolution of Mo 3d region always shows the presence of a main component related to $MoS_{2(1-x)}Se_{2x}$, with a minor component at 232.1 eV ascribed to MoO_x due to surface oxidation. Moreover, the evolution of S 2s (226.0 eV) and Se 3s (229.1 eV) spectra is consistent with the progressive introduction of Se in MoS_2 lattice.

Additionally in the case of amorphous samples, the XPS analysis confirms the hypothesis made from Raman spectroscopy, since the Mo 3d photoemission lines of amorphous $MoS_{2(1-x)}Se_{2x}$/N-rGO show broader peaks with respect to the crystalline counterpart, with an average 24% broadening of Full Width at Half Maximum (FWHM) of Mo $3d_{5/2}$ band. Furthermore, an average BE downshift of 0.5 eV was found comparing amorphous and crystalline samples, which has already been reported phenomenon for amorphous materials.[36]

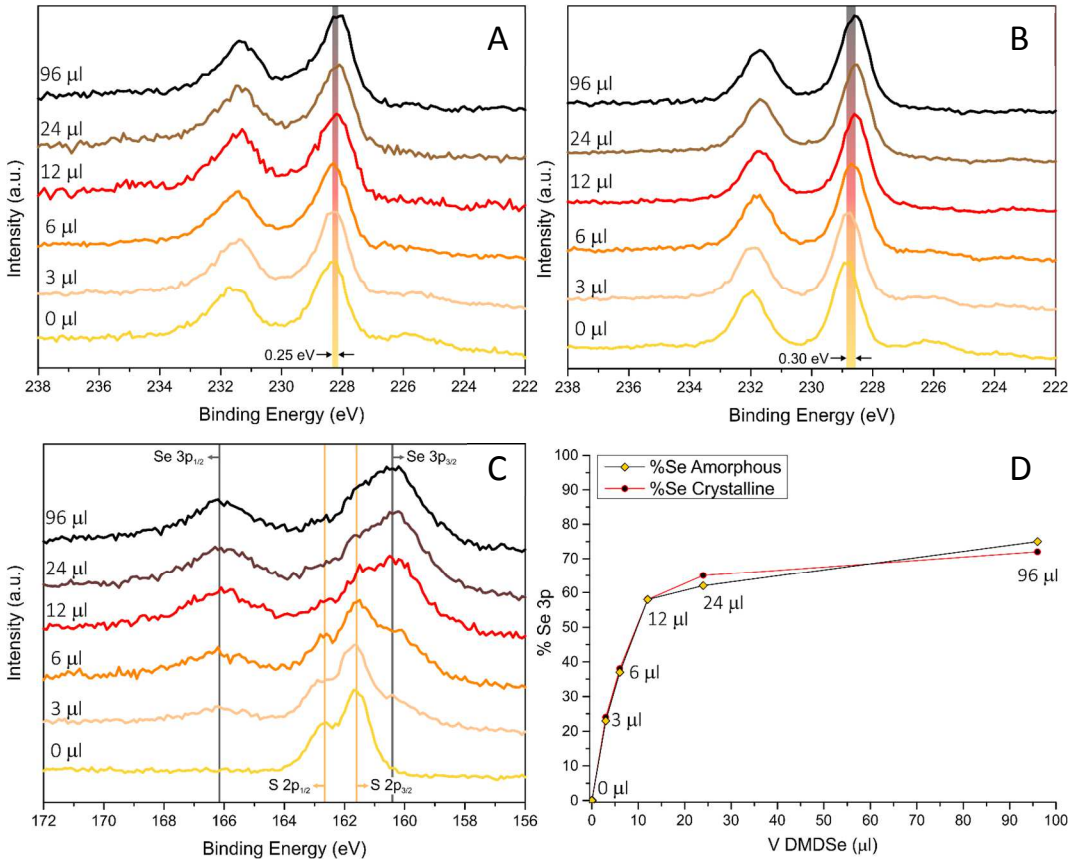

Figure 4.5. High resolution XPS spectra of Mo 3d core levels for amorphous (A) and crystalline (B) $MoS_{2(1-x)}Se_{2x}$/N-rGO samples. Evolution of S 2p and Se 3p regions of crystalline samples (C), with related Se content calculated by multipeak analysis (D).

The XPS study was performed also on chalcogenides core levels: the overlap between S 2p and Se 3p lines makes the fit challenging for high Se contents, but allows a precise quantification at Se percentages lower than 50%. The multipeak analysis was performed both on amorphous and crystalline samples and the obtained spectra are showed in the appendix Sections 4.5.1 and 4.5.2, respectively. The first analysis was made on S 2p photoemission line of 0 µl material (Figure 4.10B), since the presence of S_2^{2-} dimer (163.0 eV) in the pre-annealing sample would indicate a certain amount of MoS_3 present in the amorphous MoS_2 matrix.[37,38] The deconvolution revealed a major component at 161.4 eV, ascribed to monomer S^{2-}, and a small amount of S_2^{2-} at 163.0 eV (<4 %at.), indicating that most of ATM is completely decomposed before the annealing step. After annealing at 600 °C, no S_2^{2-} species were detected, but the crystallization of MoS_2 induced a substantial narrowing of the monomer component and also a shift to 161.6 eV.

With the introduction of Se, a progressive enhancement of the Se 3p band was observed, allowing an estimation of the Se percentage in the $MoS_{2(1-x)}Se_{2x}$/N-rGO. As previously suggested by Raman spectroscopy, the composition tends to saturate at about 70:30 Se:S ratio: indeed, the increment in % of Se from 12 µl to 96 µl sample is just 14%, despite of the 8-fold concentration of DMDSe in the reaction environment. A similar analysis was performed on amorphous samples and, despite the peak broadening, an excellent accord with crystalline samples was found, especially for a low Se loading. Clearly, at higher loading, the error in the determination of the composition is higher because of the gradual disappearance of the S 2p peak.

The Se 3d (see C panels of Figure 4.11-4.15 and 4.18-4.22) peak shows a behaviour similar to other regions: the Se 3d peak in crystalline samples was found at 53.9 eV, only at 0.1 eV higher than the value observed in commercial $MoSe_2$ and $MoSe_2$/N-rGO obtained from the blank experiment with $MoCl_5$ precursor (53.8 eV) (Figure 4.16). Only the 3 µl sample, characterized 24% Se, shows a slight shift to 54.0 eV, suggesting a composition dependent position. As in the previous analysis, the amorphous samples display broadened features, downshifted of about 0.3 eV.

4.3.4 Electrochemical and Photoelectrochemical Characterization

Both amorphous and crystalline materials were tested in typical HER conditions (0.5 M H_2SO_4) in dark and under illumination. In principle, we expect the amorphous samples to be more active than crystalline analogues in dark conditions because of the higher defectivity that should provide a higher number of active sites. On the other hand, the more ordered structure and lack of recombination centres in crystalline samples should help in light-driven experiments with photons light absorption. Moreover, photo-HER should be helped by the formation of p-n junctions between the typically p-type $MoS_{2(1-x)}Se_{2x}$ and n-type N-rGO and it should depend on the composition, being $MoS_{2(1-x)}Se_{2x}$ bandgap tunable by adjusting the Se:S ratio.[10,11,18]

Linear Sweeps Voltammetries (LSVs) in dark conditions, revealed outstanding performances for most of the amorphous samples (Figure 4.6). Surprisingly, the best performance was found for MoS_2/N-rGO (0 µl) sample, that needed only 160 mV to drive 10 mA/cm^2 current density. The insertion of low dosages of Se (3 and 6 µl) cause overpotential at 10 mA/cm^2 ($\eta_{10\ mA/cm2}$) to shift to 190 mV (see Table 4.3). For further Se additions, $\eta_{10\ mA/cm2}$ tends to increase progressively, even if the 12 and 24 µl samples are swapped with respect to the expected trend. Also from the kinetic, point of view amorphous MoS_2/N-rGO exhibits a superior 39 mV/dec Tafel slope, indicating a pure Volmer-Heyrovsky mechanism for HER. As for another figure of merit such as $\eta_{10\ mA/cm2}$ similar trends were observed, with the 3 and 6 µl materials showing intermediate kinetics with respect to MoS_2 and the 12, 24 and 96 µl samples.

	Overpotential at 10 mA/cm^2 (mV)		**Tafel Slope (mV/dec)**	
V DMDSe (µl)	Amorphous	Crystalline	Amorphous	Crystalline
0	160	320	39	102
3	190	330	47	89
6	190	210	52	56
12	220	240	62	72
24	200	250	61	80
96	230	250	63	92

Table 4.3. Overpotential at 10 mA/cm^2 and Tafel slopes for amorphous and crystalline $MoS_{2(1-x)}Se_{2x}$/N-rGO.

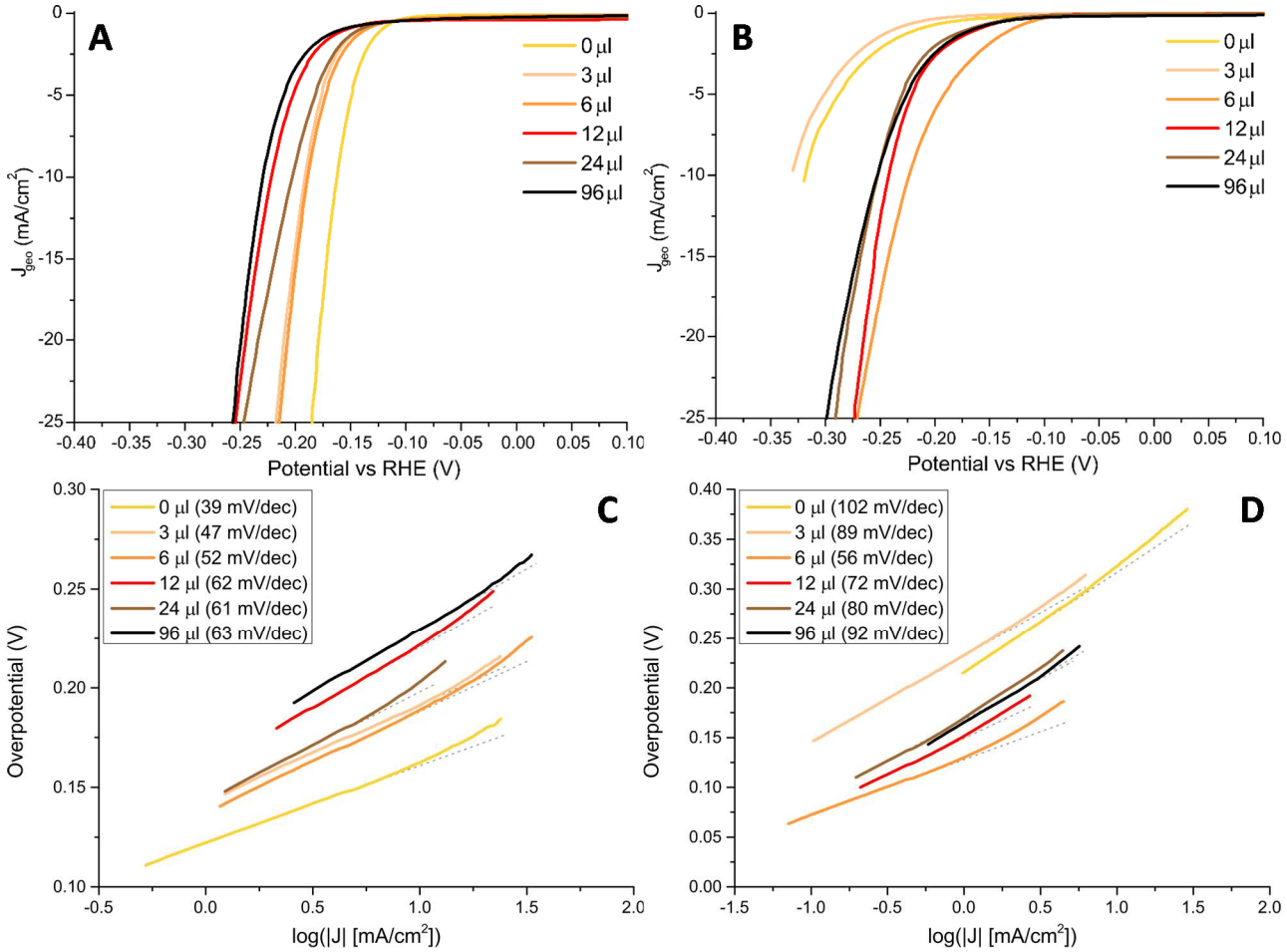

Figure 4.6. Polarization curves for amorphous (A) and crystalline (B) $MoS_{2(1-x)}Se_{2x}$/N-rGO samples. The related Tafel plots are reported as well for amorphous (C) and crystalline (D) samples.

The LSVs of annealed samples reveal completely different trends. The samples containing 0 and 3 µl of DMDSe were, together with 6 µl one, the best performing among amorphous materials, underwent to a dramatic performance drop after the thermal treatment: the overpotential needed to draw 10 mA/cm^2 increased twice in the case of MoS_2, and analogously for $MoS_{2(1-x)}Se_{2x}$ with lowest Se content. In principle, pure $MoSe_2$ has better or equal onset potentials with respect to a MoS_2 sample with same morphology and number of active sites, thanks to improved electrical properties.[39,40] Clearly, after crystallization the MoS_2 structure was re-established, repairing defects and, therefore, lowering the number of active sites, as proven by the change in $\eta_{10\ mA/cm2}$. The outstanding Tafel slope of 39 mV/dec clearly does not come only from the typical edge-site of MoS_2, but most probably from the coexistence of with other lattice defects, such as the presence of residual S_2^{2-} that are known to have low energy barriers for H_2 formation.[41] Evidently, the equivalent defects in amorphous $MoSe_2$ are much less suitable for HER than in sulphide, as also proved by the modest performances reported in the literature.[42] Indeed, no evident changes in the morphology were seen from SEM and TEM after the annealing (*i.e.* no substantial edges loss) and also the Tafel slope is in compatible with the typical literature values, indicating that the Volmer step (i.e. adsorption of H species from H_3O^+) is the rate determining step. In 3 µl sample, despite the presence of 24% of Se, the structure is still very similar to MoS_2, as proven by Raman spectroscopy and by XPS. The latter, in particular, indicates that this amount of Se is not enough to induce a strong modification of the electronic structure, as

demonstrated by the small shift (*ca.* 0.1 eV) in the Mo 3d region. Therefore, only a slight improvement in the activity (Tafel slope from 102 to 89 mV/dec) is determined by the introduction of this amount of Se. On the contrary, the 6 µl sample (about 39% Se) has an intermediate structure and, thanks to its intrinsic defectivity, it maintains an excellent performance even after annealing, requiring only additional 20 mV on $\eta_{10\ mA/cm2}$. This is further validated by Tafel slope, which remains very similar after annealing. So, even if the structure crystallizes (as observed in changing of Raman and XPS spectra) repairing lattice defects, this $MoS_{2(1-x)}Se_{2x}$ outperforms low dosages materials because of its intrinsic defectivity. Increasing the amount of Se confirms that with presence of a medium quantity of Se (40-70 %), the material can preserve the performances after the thermal treatments, even if the overall performance is worse. Moreover, the progressively worsening of Tafel slope for increasing Se percentages demonstrates that optimal Se amount is around 40%.

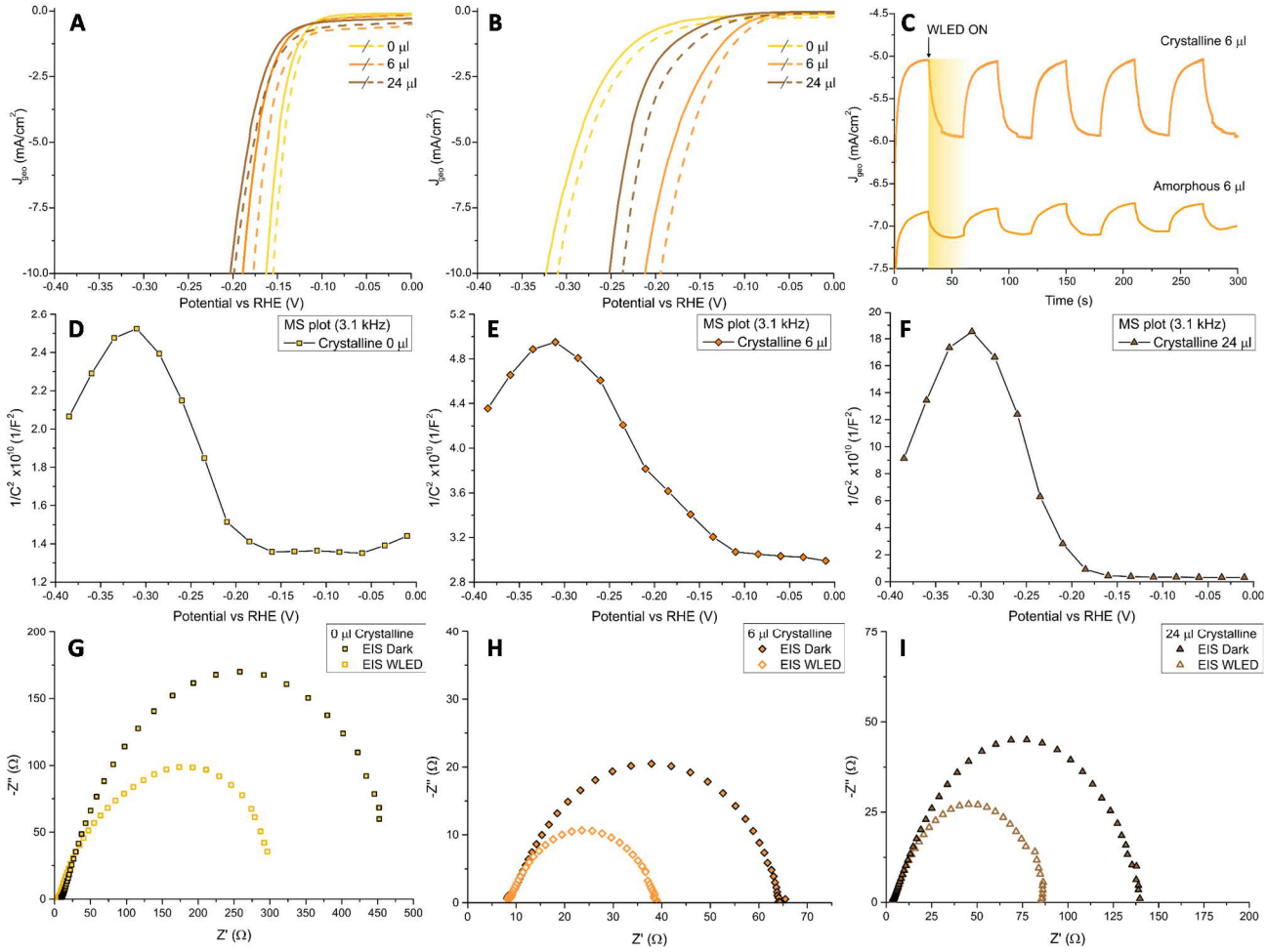

Figure 4.7. Polarization curves in dark (solid line) and under illumination (dashed line) for several amorphous (A) and crystalline (B) $MoS_{2(1-x)}Se_{2x}$/N-rGO samples. In panel (C) the *J-t* curve (η = 180 mV) comparing the light response of amorphous and crystalline 6 µl $MoS_{2(1-x)}Se_{2x}$/N-rGO. (D-F) Mott-Schottky plots for 0, 6 and 24 µl crystalline $MoS_{2(1-x)}Se_{2x}$/N-rGO and (G-I) the related EIS Nyquist plots performed at η = 180 mV in dark and under illumination.

Considering other works in literature about $MoS_{2(1-x)}Se_{2x}$ prepared *via* wet chemistry routes, similar performances were found.[14] Indeed, Gong *et al.* designed an *hot injection* protocol for non-supported $MoS_{2(1-x)}Se_{2x}$ and they found as well that mixed chalcogenides material (in particular sample with x = 1)

exhibited performances better than pure species, with similar proportions to the ones we found. In addition, similar overpotentials (170 mV to drive 10 mA/cm^2) and Tafel slopes (48 mV/dec) were measured in their material. Looking at graphene-TMDCs hybrids,[17,26] if MoS_2 or $MoSe_2$ were used as active material, generally worse HER activity were recorded, with $\eta_{10\ mA/cm2}$ above 0.25 V. However, in other cases $MoS_{2(1-x)}Se_{2x}$-based materials exhibited even better performances, recording $\eta_{10\ mA/cm2}$ even lower than 0.1 V, but in all the cases CVD protocols were required to achieve sulphidization or selenization.[9,12,13,43]

HER performed under illumination with white LED (WLED, Figure 4.7A and 4.7B) confirmed the hypothesis presented above: amorphous samples show a very small improvement at 10 mA/cm^2, especially for MoS_2 and high Se-loaded sample. The highest improvement was found on 6 µl sample, with a gain on $\eta_{10\ mA/cm2}$ of about 5%. On the other hand, the gain on $\eta_{10\ mA/cm2}$ in crystalline samples was found to be doubled, reaching 10% in the case of 6 µl sample. Tafel slope remained the same in dark and under illumination in all the measured samples. Chronoamperometric measurements with chopped WLED light of 6 µl $MoS_{2(1-x)}Se_{2x}$/N-rGO were recorded as example material: as it is possible to see in Figure 4.7C, amorphous material has slow and weak response to light, even if a 0.4 mA/cm^2 enhancement was found when light was turned on. Besides, annealed sample shows a sharper response when irradiated by WLED and in this case the improvement was about 1 mA/cm^2, for a 20% current density gain upon irradiation.

Mott-Schottky analysis (Figure 4.7D-F) and Electrochemical Impedance Spectroscopy (EIS) (Figure 4.7G-I) were performed as well on crystalline samples. Mott-Schottky plot is an electrochemical technique that allows to know the conductivity type of the semiconductor at the working electrode, having the plot a positive (negative) slope when the analyzed material is n-type (p-type). Obviously, when Mott-Schottky analysis is carried out on a multi-component material, the contribution of all the semiconducting constituents will be traced in the plot. Hence, in the case of p-n junctions both p- and n-type contributions have to be observed, resulting in a "V-shaped" plot. This kind of plot was found in all the analysed materials and, considering the works in the literature, we can safely attribute the positive slope contribution to N-rGO and the other to $MoS_{2(1-x)}Se_{2x}$.[8,17,18] EIS experiments are useful to get a plenty of information about a material and its basic use allows to observe the evolution of the charge transfer resistance (R_{ct}) depending on the experiment conditions. We decided to perform EIS at the same overpotential (η = 180 mV) in dark and under WLED illumination, in order to crosscheck both the performances in dark and the enhancement coming up from irradiation. Table 4.4 summarizes the values obtained by fitting the spectra showed in Figure 4.7G-I.

Material	*R_{ct} (Ω) Dark*	*R_{ct} (Ω) WLED*	*Relative R_{ct} variation*
0 µl	443	301	32 %
6 µl	56	29	48 %
24 µl	135	82	39 %

Table 4.4. Charge transfer resistance (R_{ct}) values obtained for 0, 6 and 24 µl crystalline samples at η = 180 mV in dark and under WLED illumination.

R_{ct} values measured for experiments in dark trace the trend observed both in HER activity and kinetics. The introduction of 40% of Se induces an 8-fold reduction of R_{ct} with respect to pure MoS_2, confirming the improvement in the reaction rate. However, as observed also in Tafel analysis, the further increase in Se content cause R_{ct} to double, even if better values compared to 0 µl sample were found. As expected, all the

materials show a reduction of R_{ct} upon WLED illumination, since the photo-induced promotion of electrons in $MoS_{2(1-x)}Se_{2x}$ conduction band grants in all the cases an higher number of carriers ready to be transferred to the electrolyte. Moreover, the presence of p-n junctions helps in stabilizing photo-generated excitons suppressing the recombination. However, different efficiencies in exploiting light harvesting are expected, as already observed in photocurrents and gain in $\eta_{10\ mA/cm2}$: despite the lowest starting R_{ct} value, again 6 µl sample exhibited the best photo-enhancement, halving the resistance under illumination. In 0 and 24 µl $MoS_{2(1-x)}Se_{2x}$/N-rGO, the trend was still the same: a nice 39% reduction of R_{ct} value was observed in high Se-loaded sample, that is mid-way between 6 µl sample and MoS_2/N-rGO (32% reduction).

In order to shed some light on the influence of Se:S ratio on the photoinduced reaction, we recorded UV-Vis spectra of all the crystalline materials to check absorption bands position and then, as above, we analysed the 0, 6 and 24 µl sample.

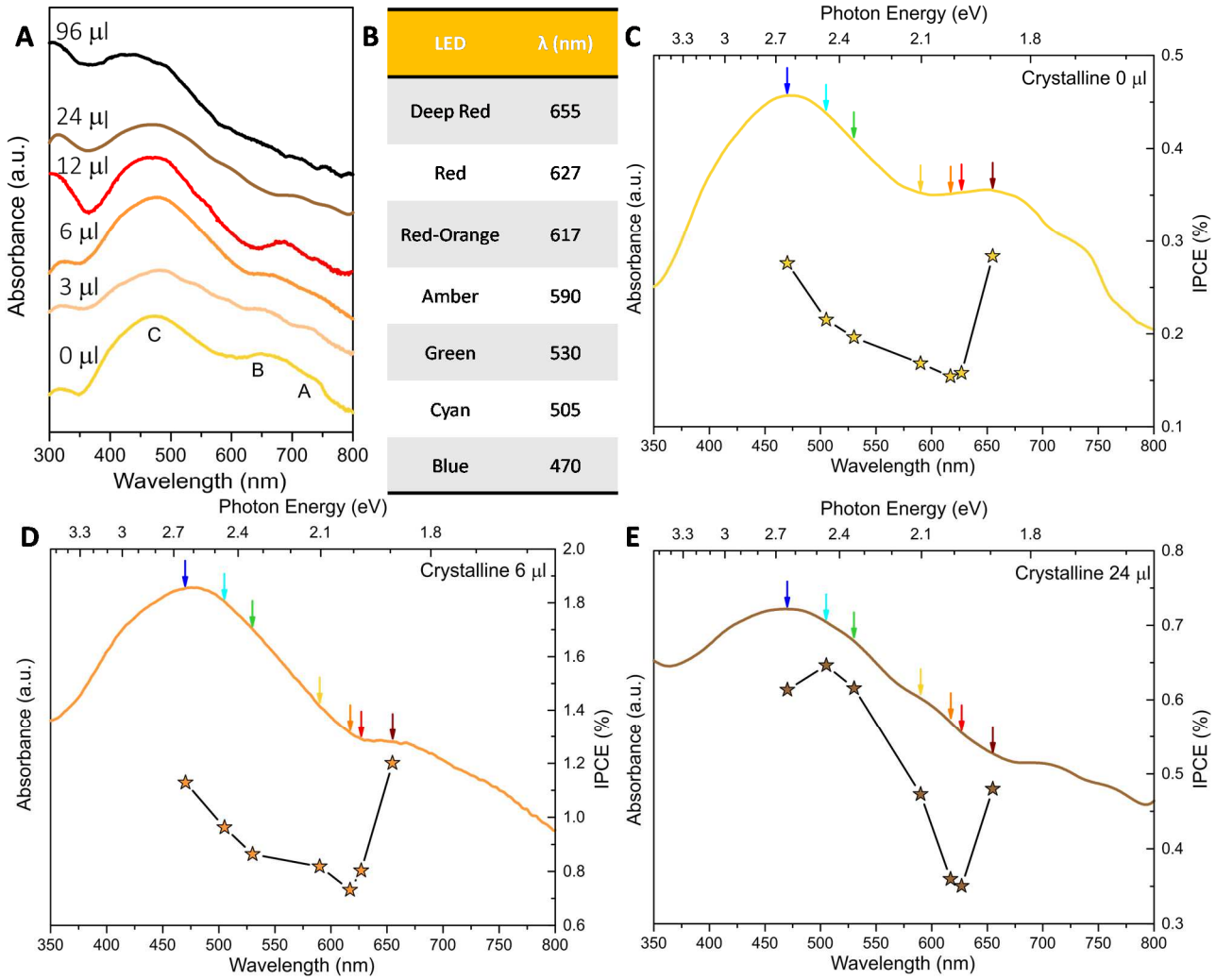

Figure 4.8. A) UV-Vis spectra of crystalline $MoS_{2(1-x)}Se_{2x}$/N-rGO crystalline samples. B) List of monochromatic LEDs used for studying wavelength-dependent performances of $MoS_{2(1-x)}Se_{2x}$/N-rGO materials. C-E) IPCE measurements recorded at η = 180 mV for 0 µl (C), 6 µl (D) and 24 µl (E) samples. Relative absorption spectra are reported as well.

UV-Vis spectroscopy (Figure 4.8A) shows the typical electronic transitions of Mo-based TMDCs, that are three excitonic features named as A, B and C, respectively. The A and B excitonic peaks come from the direct transitions from two valence bands (which are split due to spin–orbit coupling) to the lowest conduction band at the K point, while the C exciton arises from the indirect transition between the valence band maximum located at the Γ point and the conduction band minimum located at the Λ point of the Brillouin zone.[44–46] As it can be seen in Figure 4.8A, the A and B peaks undergo to a 70 nm (0.2 eV) redshift with increasing the Se amount, which is consistent with the band gap narrowing due to the interlayer transition from MoS_2 to $MoSe_2$.[11,47–49] On the contrary, the C-exciton peak remains rather constant (ca. 475 nm, 2.6 eV) across the composition change, even if a broadening of the band can be observed.

In Figure 4.8C-E, Incident Photon to Current Efficiency (IPCE) measurements are reported for several of our materials using seven different monochromatic LEDs in the visible range (see Figure 4.8B). The equation used to calculate IPCE is the following:

$$IPCE\ (\%) = \frac{hc}{e} \cdot \left(\frac{j_{photo}\ (\lambda)}{\lambda \cdot P(\lambda)} \right) \cdot 100 = 1240.6 \cdot \left(\frac{j_{photo}\ (\lambda)}{\lambda \cdot P(\lambda)} \right) \cdot 100$$

$$where\ h = Planck\ constant; c = speed\ of\ light; e = elementary\ charge$$

$$\lambda = wavelength\ (nm);\ j_{photo}\ (\lambda) = photocurrent\ density; P(\lambda) = LED\ power$$

All the $MoS_{2(1-x)}Se_{2x}$/N-rGO show similar trends, according to the relative absorption spectra. All the samples exhibited higher photo-activity when irradiated with wavelengths that match the main electronic transitions, in particular the B exciton in the low energy range of the spectrum. Above the B transition, a substantial photoactivity drop was observed because of the lack of optical transitions around 620 nm, being the absorbance in this region of UV-Vis spectra mainly due to scattering events. When the photon energy is increased, the IPCE slowly rises following the profile and peaking in correspondence of the C band maximum. At this wavelength, the IPCE reaches values close to the those measured in the deep-red range, despite the indirect nature of C transition. Only for the 24 µl sample, higher ICPE values were recorded in the blue region, but this should not mislead since at high Se content, the A and B exciton peaks are beyond the last available LED, so actually we are measuring the decaying tail observed in the previous materials. Therefore, we can imagine that the Se-containing samples would be even more active if irradiated with near-infrared light in the region of A and B excitons, widening the range of wavelengths to absorb for enhancing HER. Moreover, we can qualitatively observe that the increment in IPCE with photon energy is steeper at larger Se content, which may be associated with the broadening of C exciton band highlighted by UV-Vis spectra.

Considering the values of IPCE, 6 µl $MoS_{2(1-x)}Se_{2x}$/N-rGO outperformed the other materials, with values ranging between 0.8% and 1.2%, with an average 4- and 2-fold increment with respect to 0 and 24 µl samples, respectively. These values are rather low compared to others reported in the literature,[50–52] but it has to be considered that no bulk semiconductor was used as support for active material and, consequently, all the light absorption is carried out by the $MoS_{2(1-x)}Se_{2x}$ slabs on the electrode. Indeed, when similar systems are considered, values in the same range have been found.[53,54] Moreover, the intrinsic defectivity of both the constituents of the final material (N-doping of graphene and Se-doping in MoS_2) allow to form p-n junctions, giving photoactivity to the final material, but may induce charge recombination as well.

Since charge recombination phenomena may strongly influence HER, transient photocurrent curves were acquired using WLED to investigate the charge to better understand recombination behaviour (Figure 4.9A). A normalized parameter (D) was derived from the transient photocurrent curve to quantitatively determine the charge recombination behaviour:[17,55]

$$D\ (t) = \frac{J_t(t) - J_{st}}{J_{in} - J_{st}}$$

$$where\ J_i\ are\ current\ densities: J_t(t) = time\ dependent;\ J_{st} = steady\ state;\ J_{in} = initial.$$

Subsequently, the normalized curve of *ln(D)–t* has to be plotted (Figure 4.9B) and the transient time constant (τ) is defined as the time when *ln(D) = -1*.[55]

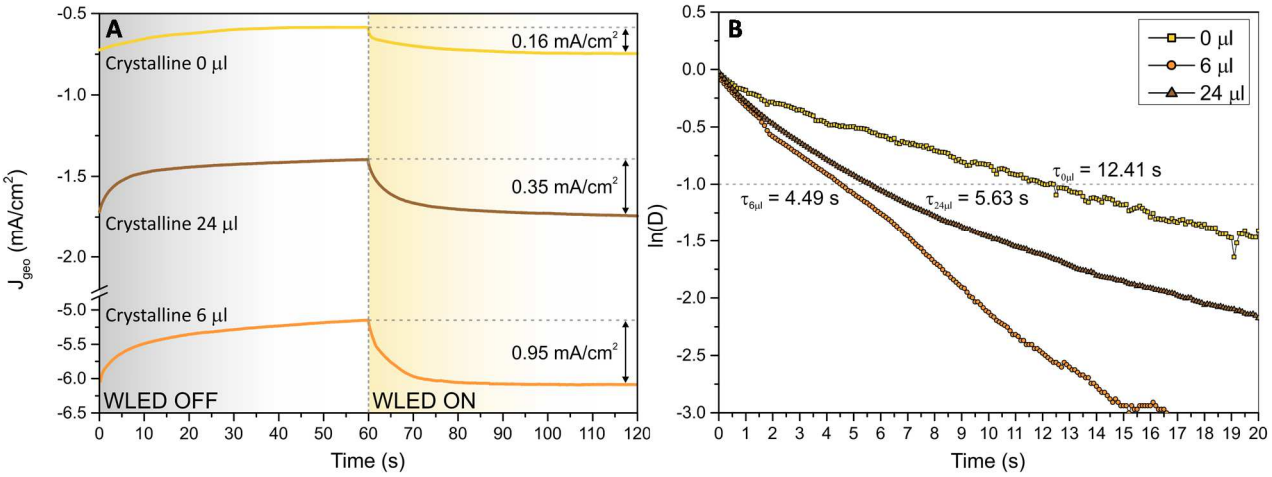

Figure 4.9. A) Transient photocurrent *J-t* curves recorded at η = 180 mV using WLED as light source. B) *ln(D)–t* plot for 0, 6 and 24 µl $MoS_{2(1-x)}Se_{2x}$/N-rGO. Transient time constant (τ) for each material is reported as well.

Transient photocurrent curves clearly confirm that the larger photo-induced enhancement is obtained on the 6µl sample with ~1 mA/cm^2 of photocurrent. However, the analysis of *ln(D)–t* plot reveals an unexpected trend: according to the literature,[17,55] the larger is τ, the longer is the exciton lifetime before recombination, while in our case the best performing material has the shorter time constant. Meng *et al.*[17] show that in their MoS_2/N-rGO hybrid τ is longer compared to simple MoS_2/rGO because of the formation of p-n nanojunctions, not present in the latter, that supresses the charge recombination and allows to reach higher photocurrents. In our $MoS_{2(1-x)}Se_{2x}$/N-rGO samples, the p-n nanojunctions are always present, therefore the different lifetimes should be correlated to other factors. $\tau_{0µl}$ has the same value reported by Meng and coworkers, indicating that morphology or synthesis method does not affect charge recombination behaviour. Moreover, $\tau_{6µl}$ and $\tau_{24µl}$ are much more similar to each other than if compare to $\tau_{0µl,}$ therefore we can affirm that the introduction of structural defects (i.e. Se anions), even if beneficial for the overall performances, may interfere with the photogenerated excitons. However, it has to be considered the reaction kinetics as well: indeed, in the work of Meng *et al.* only MoS_2 was considered as electroactive material, therefore, even if Tafel analysis is not reported, we can expect similar values between MoS_2/N-rGO and MoS_2/rGO, being the HER active sites the same. In our case, the introduction of Se boosts the adsorption of H_{ads} species during the Volmer step (Tafel slope: 56 mV/dec in 6 µl vs 102 in 0 µl), making the HER much faster. Hence, once that exciton is generated upon light absorption, the faster kinetics can increase the probability of using

photogenerated electrons in HER, making this pathway competitive with charge recombination and making the exciton apparently short-living.

4.4 Conclusions

In this Chapter, we designed a novel solvothermal synthesis for the heterogeneous growth of ternary $MoS_{2(1-x)}Se_{2x}$ on a N-rGO scaffold, with the goal of forming p-n nanojunctions to catalyse the photo-enhanced HER. The utilization of ATM and DMDSe as reactants allowed to obtain the desired morphology and to tune easily the fraction *x* in the 0 ÷ 0.71 range, without the formation of harmful gases like H_2S and H_2Se. However, as produced materials were found to be amorphous, therefore an annealing step was necessary to induce the $MoS_{2(1-x)}Se_{2x}$ crystallization. The structure and composition were thoroughly analysed by mean of Raman Spectroscopy and XPS, which were used to follow the evolution of composition-dependent parameters such as peak positions and relative intesities, according to the different amount of DMDSe used in the synthesis. In agreement with XPS analysis, using DMDSe it is possible to precisely tune the Se amount in the final material, but because of an equilibrium between S^{x-} and Se^{x-} species during the synthesis, it is not achievable the full anion exchange to obtain pure $MoSe_2$/N-rGO.

Both amorphous and crystalline materials were tested in typical HER conditions (0.5 M H_2SO_4) in dark and under illumination. Experiments confirmed the expectations: amorphous samples were more active than crystalline analogues in dark conditions because of the higher defectivity that should provide a higher number of active sites; while the more ordered structure of the crystalline samples granted better performances in light-driven experiments. Among amorphous samples, pure MoS_2/N-rGO was found the best performing materials, with a progressive worsening of activity with the increase of Se, proving that the active sites of amorphous MoS_2 have better catalytic performances compared to selenide equivalents. On the contrary, annealed Se-containing samples exhibited better HER activity and kinetics, with the material prepared from 6 µl of DMDSe (about 40% of Se) outperforming the others. When the light was shed on the samples, each material showed a different response upon light irradiation, therefore we chose three of them (0, 6 and 24 µl samples) to study in detail the interaction with light. Experiments with white light and IPCE measurements revealed that 6 µl sample exhibited both the best absolute performance and also the higher enhancement upon light irradiation. Surprisingly, transient photocurrent experiments showed that the introduction of Se in the lattice, even if beneficial for the overall performances, causes a destabilization of the photo-generated exciton, probably with the contribution of the accelerated reaction kinetics observed in these materials.

4.5 Appendix: XPS data of $MoS_{2(1-x)}Se_{2x}$/N-rGO

4.5.1 XPS data of Amorphous $MoS_{2(1-x)}Se_{2x}$/N-rGO samples

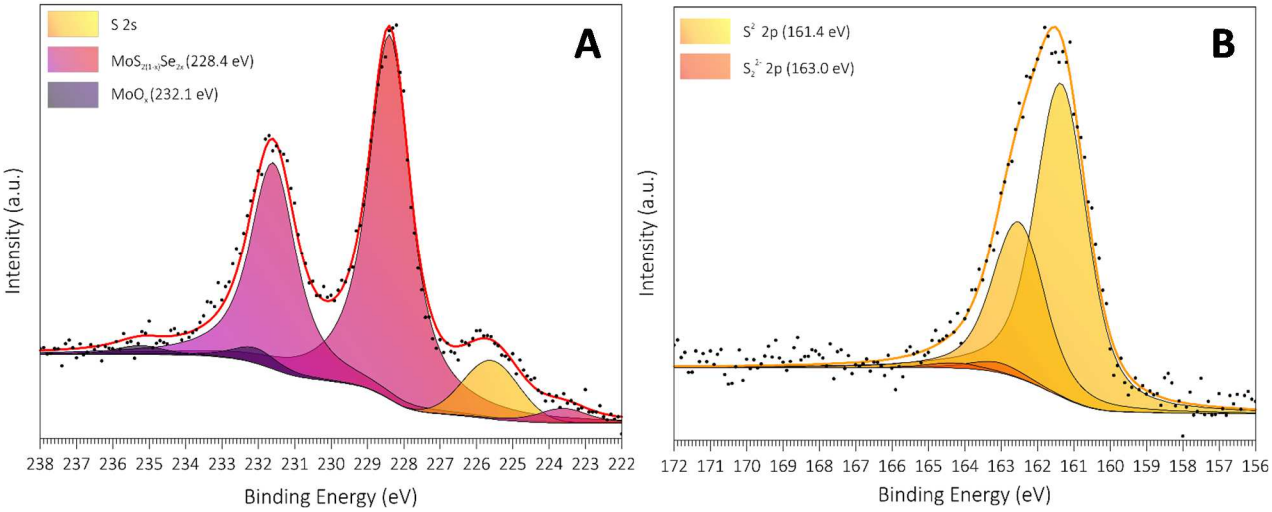

Figure 4.10. XPS multipeak analysis on Mo 3d (A) and S 2p (B) core levels of 0 µl amorphous $MoS_{2(1-x)}Se_{2x}$/N-rGO.

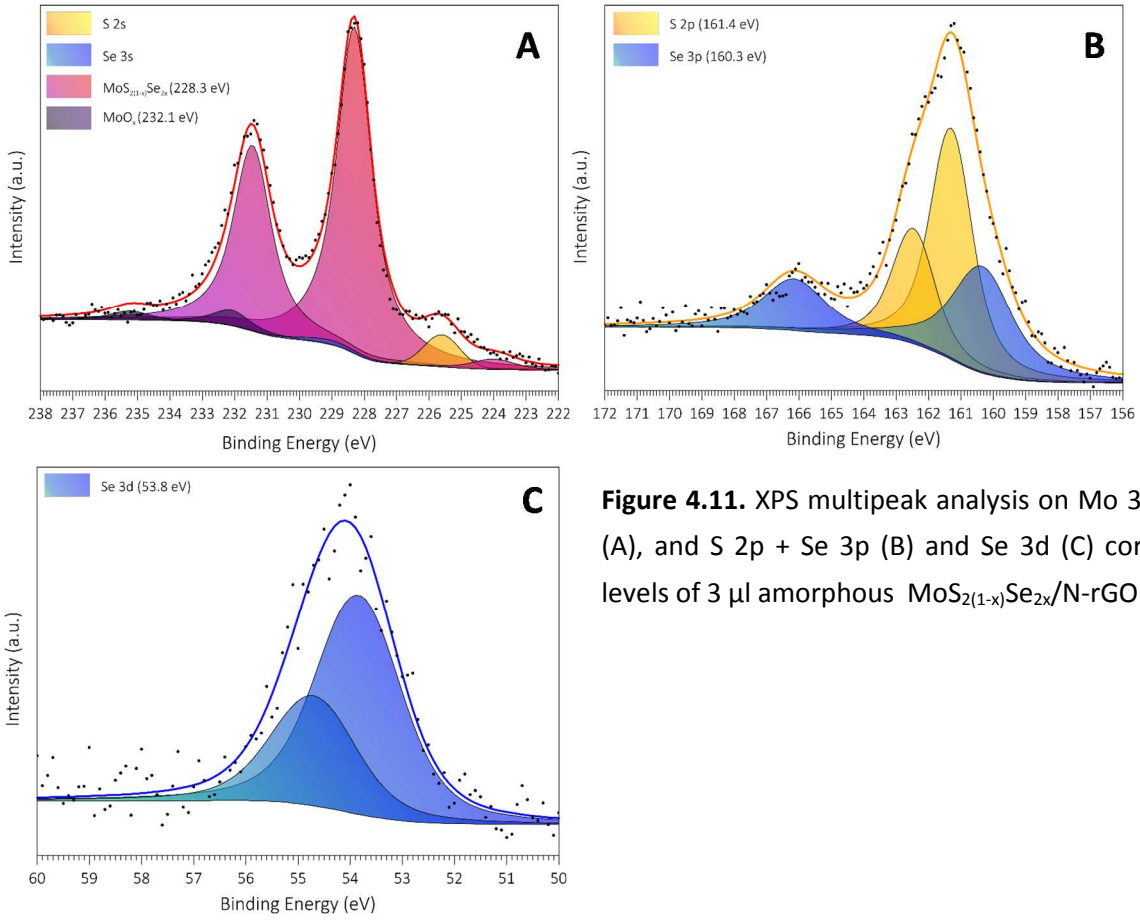

Figure 4.11. XPS multipeak analysis on Mo 3d (A), and S 2p + Se 3p (B) and Se 3d (C) core levels of 3 µl amorphous $MoS_{2(1-x)}Se_{2x}$/N-rGO.

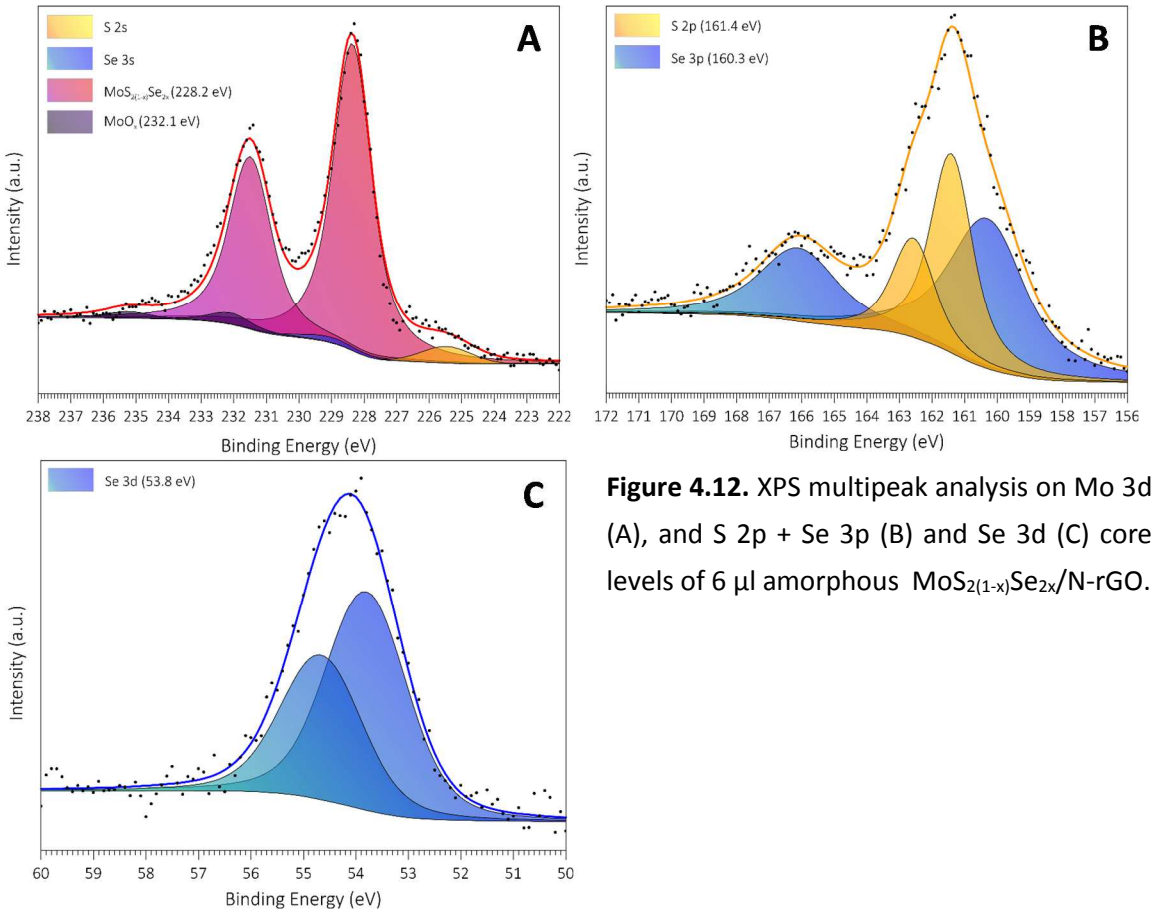

Figure 4.12. XPS multipeak analysis on Mo 3d (A), and S 2p + Se 3p (B) and Se 3d (C) core levels of 6 µl amorphous $MoS_{2(1-x)}Se_{2x}$/N-rGO.

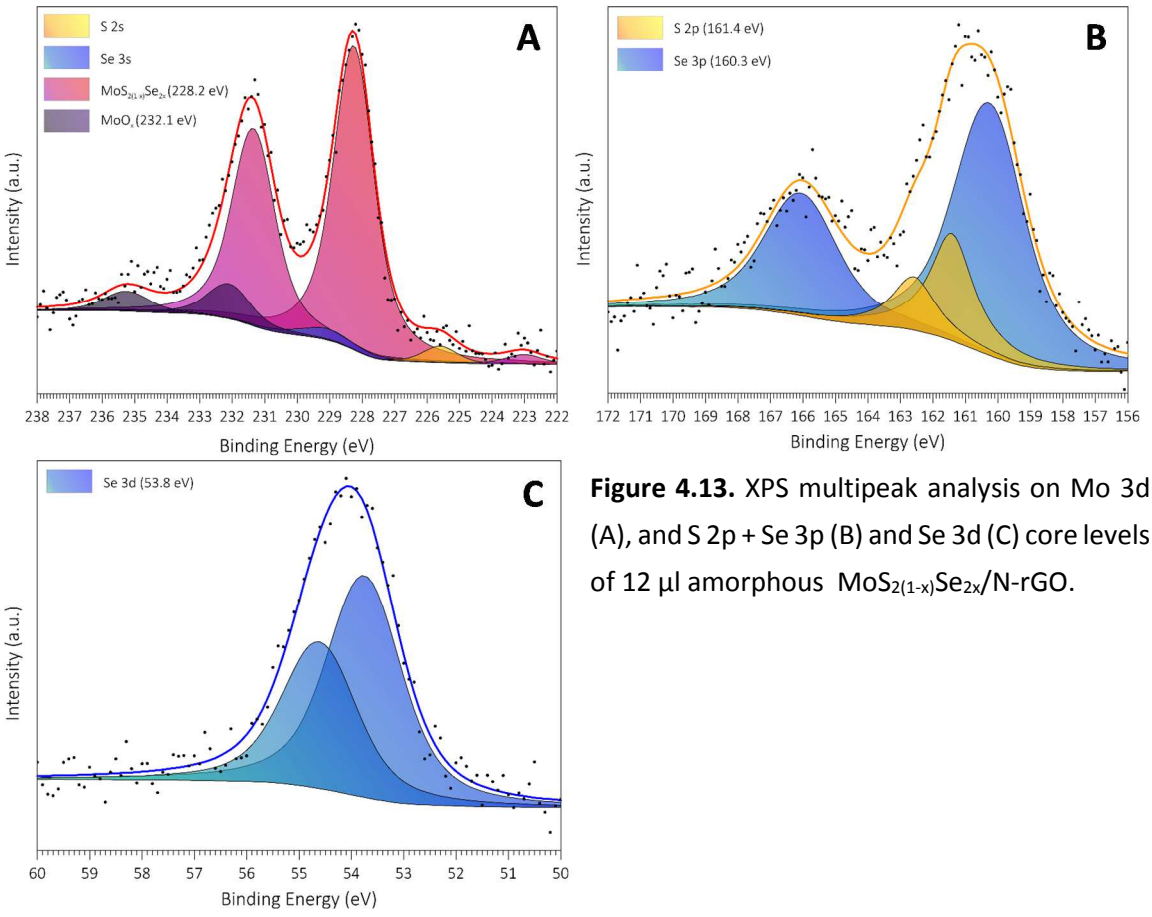

Figure 4.13. XPS multipeak analysis on Mo 3d (A), and S 2p + Se 3p (B) and Se 3d (C) core levels of 12 µl amorphous $MoS_{2(1-x)}Se_{2x}$/N-rGO.

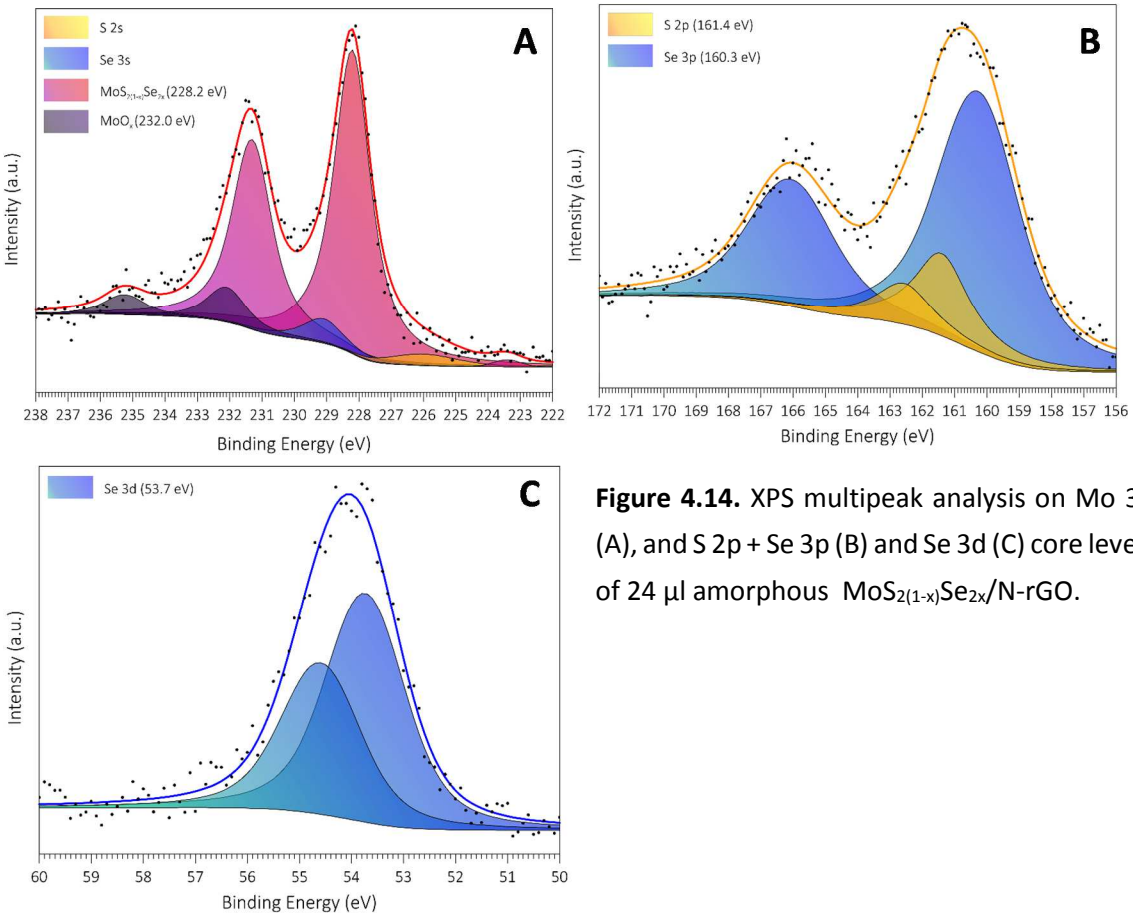

Figure 4.14. XPS multipeak analysis on Mo 3d (A), and S 2p + Se 3p (B) and Se 3d (C) core levels of 24 µl amorphous $MoS_{2(1-x)}Se_{2x}$/N-rGO.

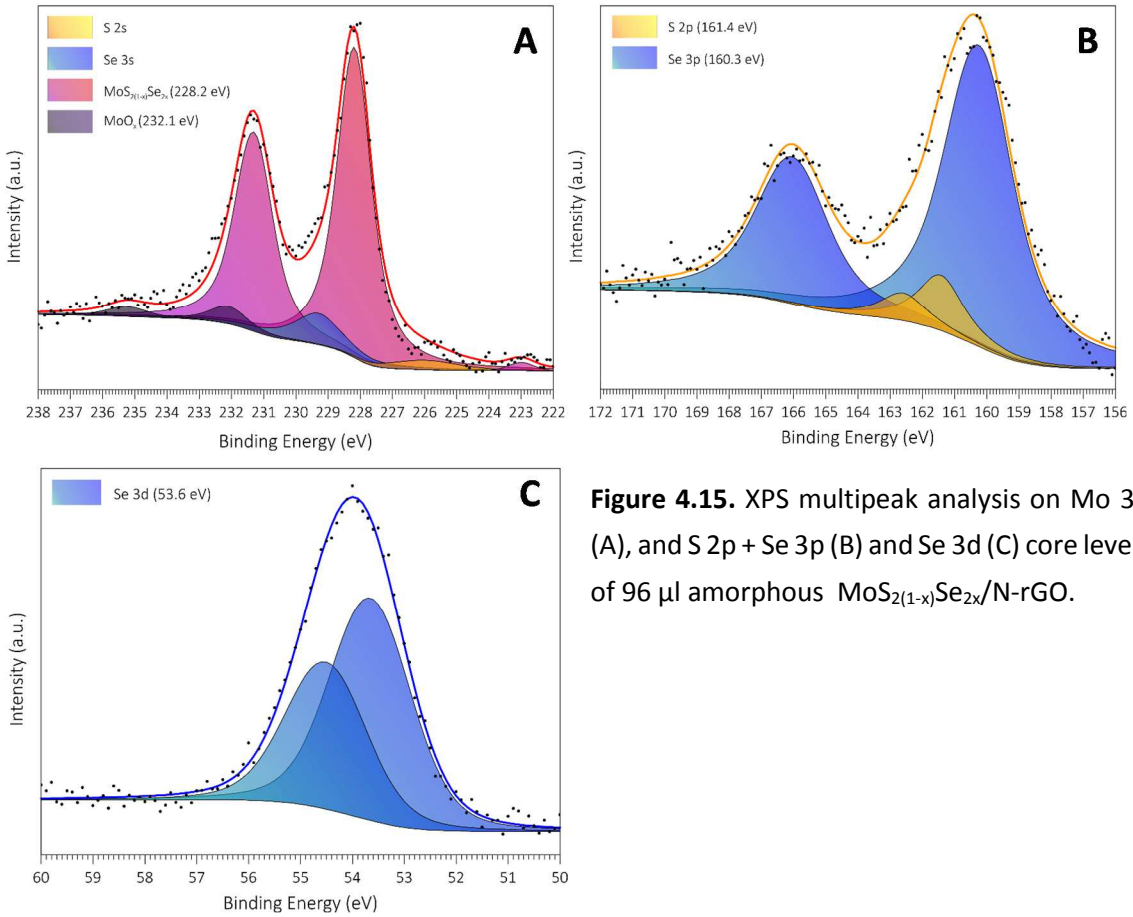

Figure 4.15. XPS multipeak analysis on Mo 3d (A), and S 2p + Se 3p (B) and Se 3d (C) core levels of 96 µl amorphous $MoS_{2(1-x)}Se_{2x}$/N-rGO.

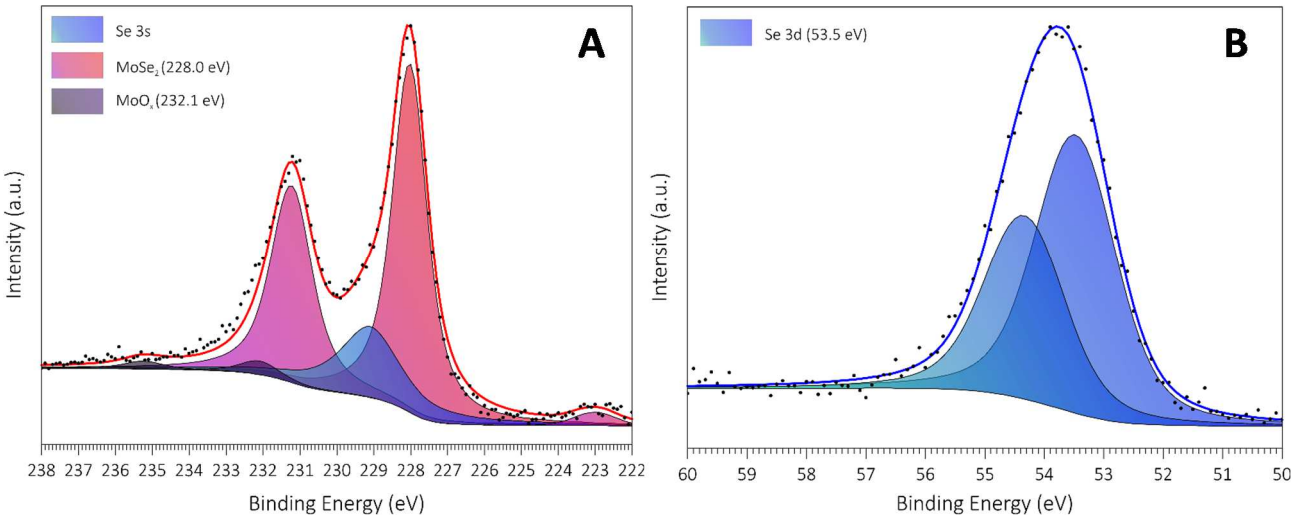

Figure 4.16. XPS multipeak analysis on Mo 3d (A) and Se 3d (B) core levels amorphous $MoSe_2$/N-rGO control material.

4.5.2 XPS data of Crystalline $MoS_{2(1-x)}Se_{2x}$/N-rGO samples

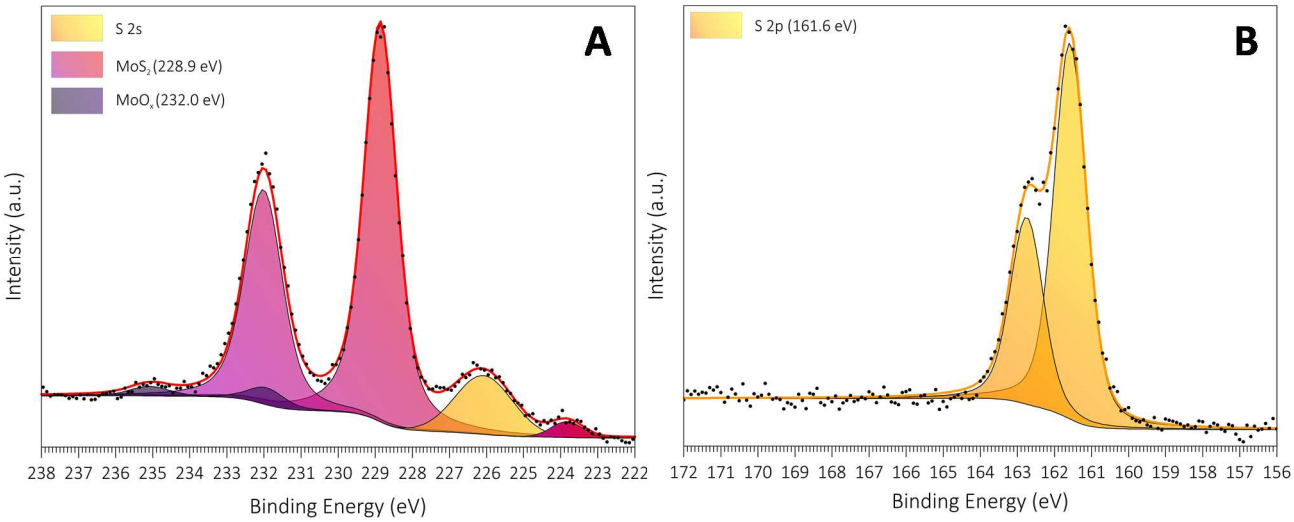

Figure 4.17. XPS multipeak analysis on Mo 3d (A) and S 2p (B) core levels of 0 µl crystalline $MoS_{2(1-x)}Se_{2x}$/N-rGO.

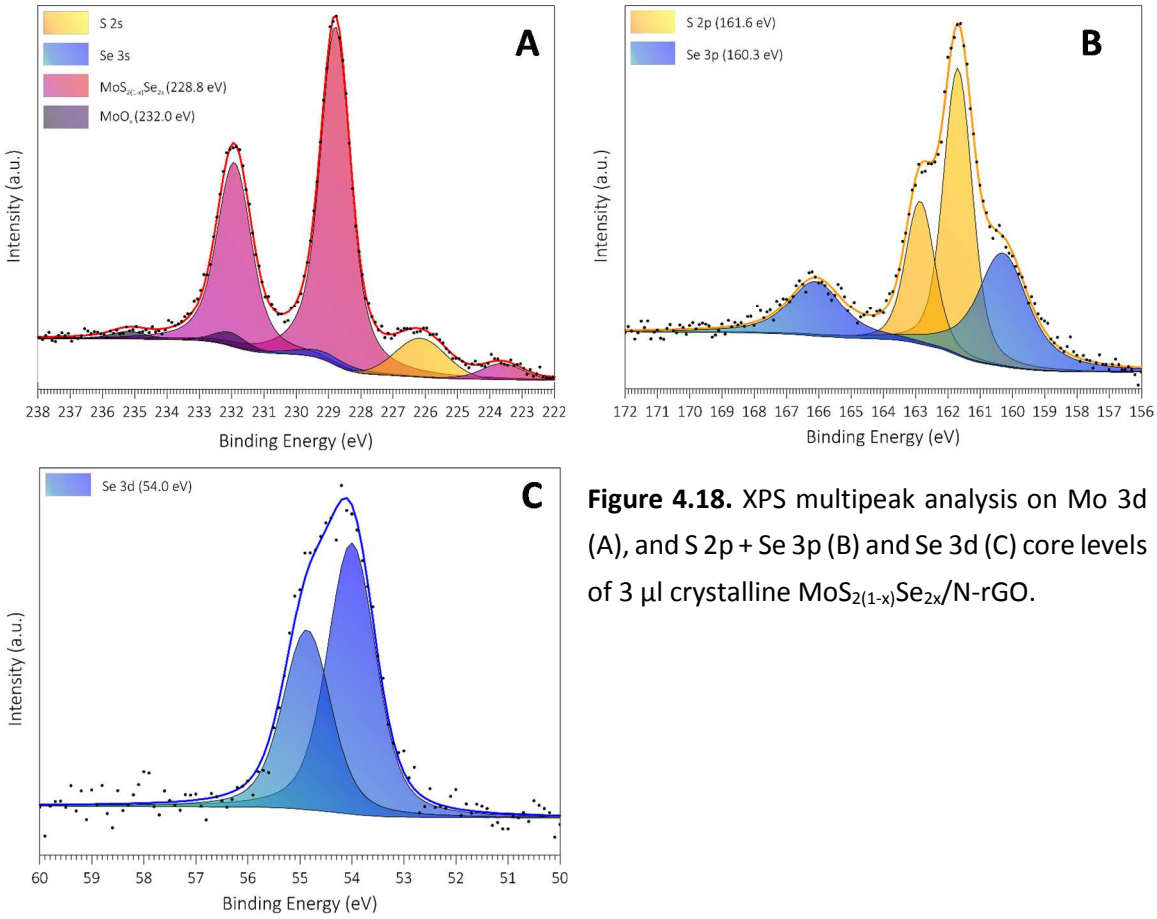

Figure 4.18. XPS multipeak analysis on Mo 3d (A), and S 2p + Se 3p (B) and Se 3d (C) core levels of 3 µl crystalline $MoS_{2(1-x)}Se_{2x}$/N-rGO.

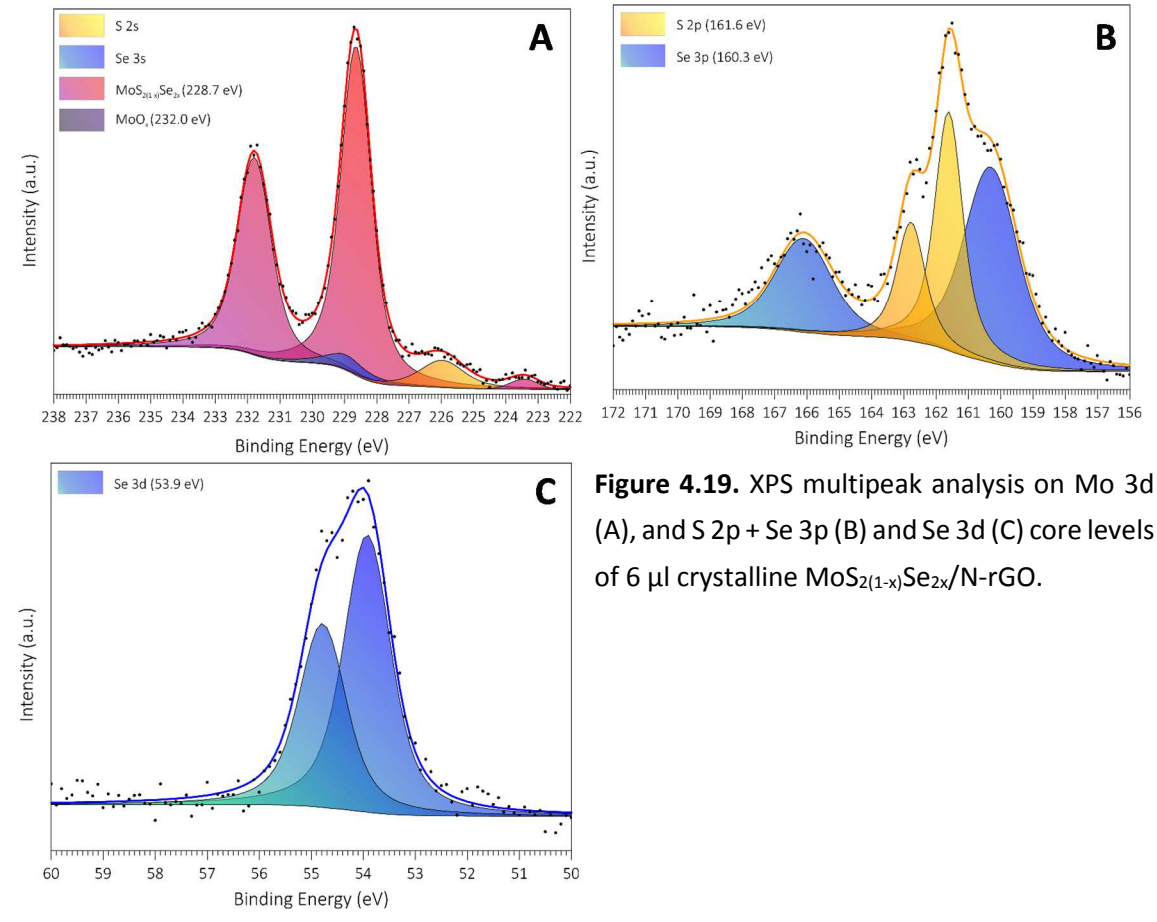

Figure 4.19. XPS multipeak analysis on Mo 3d (A), and S 2p + Se 3p (B) and Se 3d (C) core levels of 6 µl crystalline $MoS_{2(1-x)}Se_{2x}$/N-rGO.

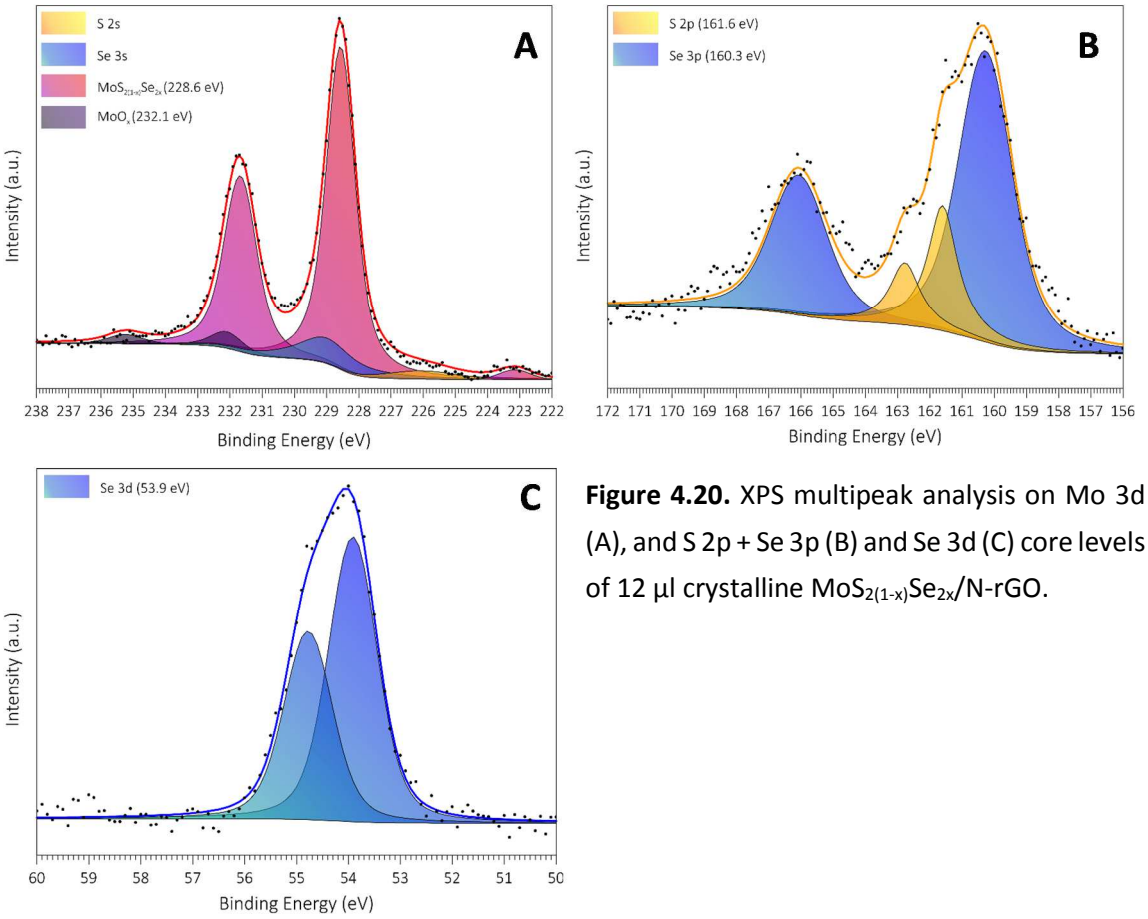

Figure 4.20. XPS multipeak analysis on Mo 3d (A), and S 2p + Se 3p (B) and Se 3d (C) core levels of 12 µl crystalline $MoS_{2(1-x)}Se_{2x}$/N-rGO.

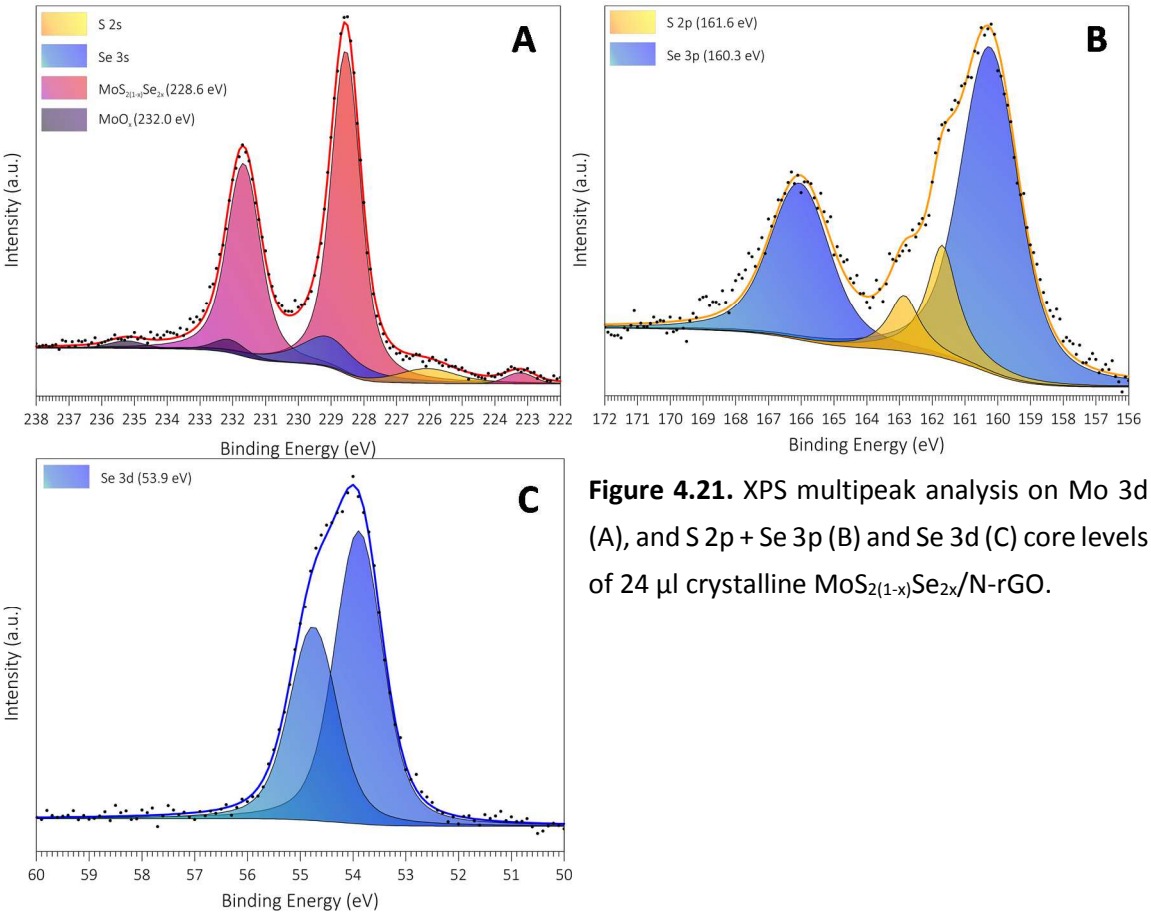

Figure 4.21. XPS multipeak analysis on Mo 3d (A), and S 2p + Se 3p (B) and Se 3d (C) core levels of 24 µl crystalline $MoS_{2(1-x)}Se_{2x}$/N-rGO.

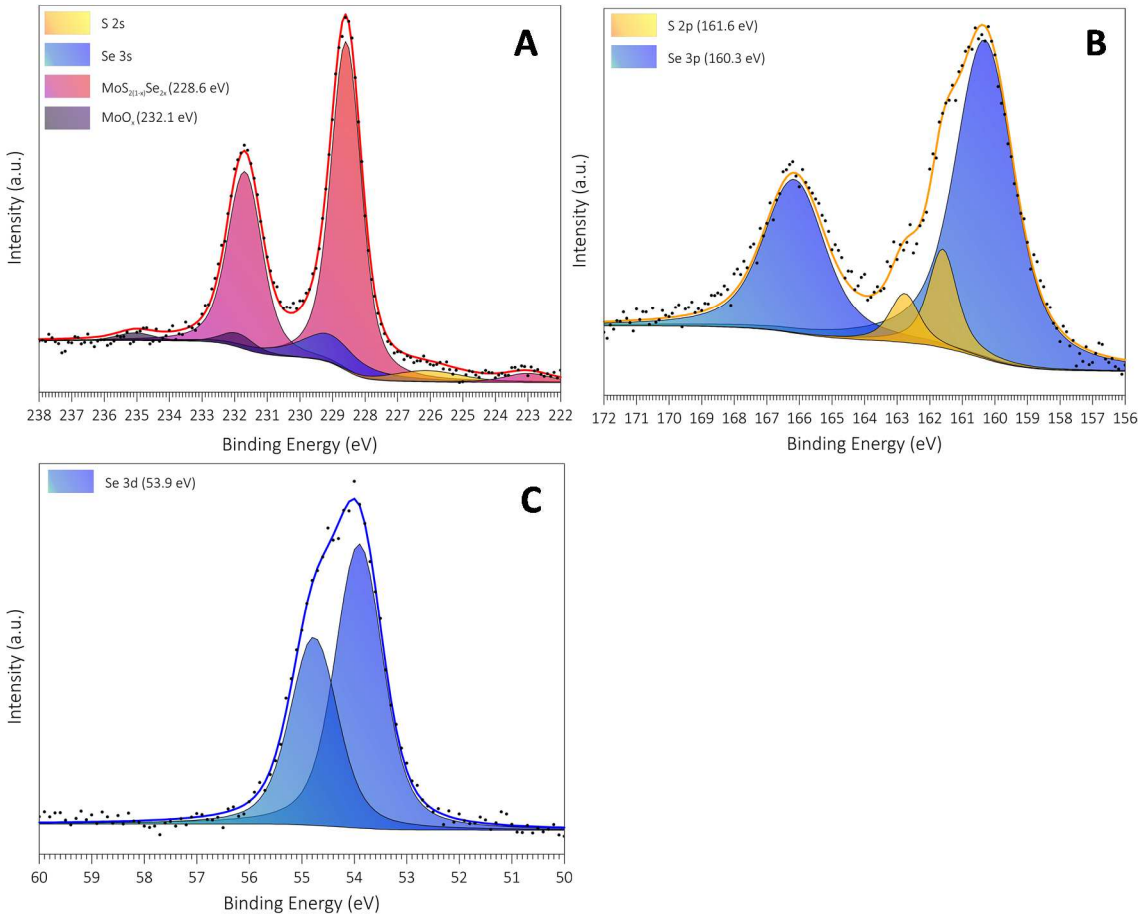

Figure 4.22. XPS multipeak analysis on Mo 3d (A), and S 2p + Se 3p (B) and Se 3d (C) core levels of 96 µl crystalline $MoS_{2(1-x)}Se_{2x}$/N-rGO.

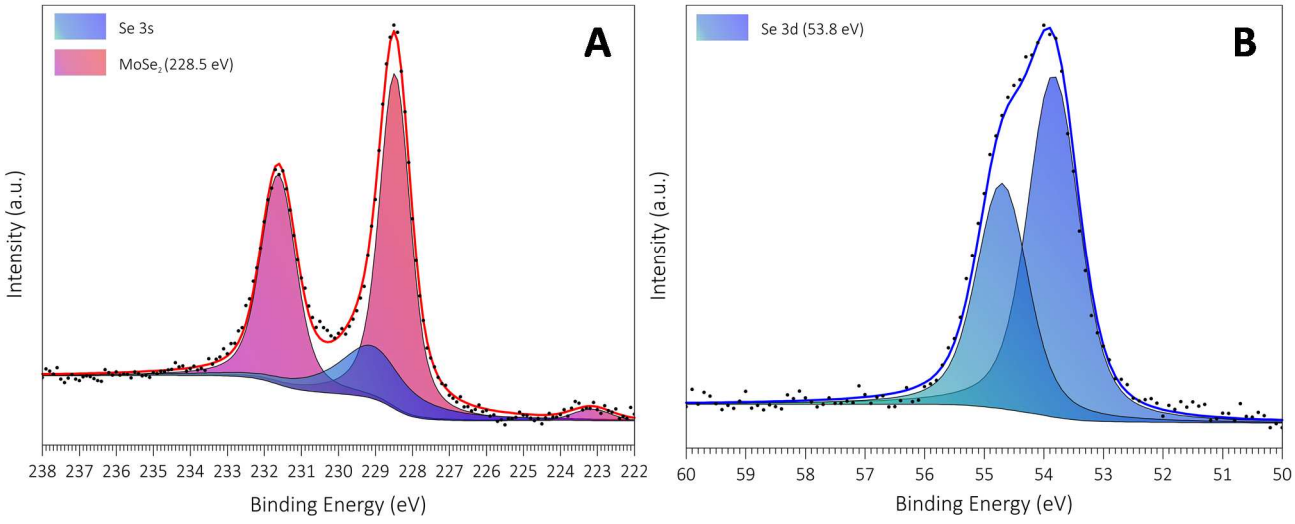

Figure 4.23. XPS multipeak analysis on Mo 3d (A) and Se 3d (B) core levels crystalline $MoSe_2$/N-rGO control material.

References

(1) Jaramillo, T. F.; Jorgensen, K. P.; Bonde, J.; Nielsen, J. H.; Horch, S.; Chorkendorff, I. Identification of Active Edge Sites for Electrochemical H_2 Evolution from MoS_2 Nanocatalysts. *Science (80-.).* **2007**, *317* (5834), 100–102.

(2) Voiry, D.; Salehi, M.; Silva, R.; Fujita, T.; Chen, M.; Asefa, T.; Shenoy, V. B.; Eda, G.; Chhowalla, M. Conducting MoS_2 Nanosheets as Catalysts for Hydrogen Evolution Reaction. *Nano Lett.* **2013**, *13* (12), 6222–6227.

(3) Li, Y.; Wang, H.; Xie, L.; Liang, Y.; Hong, G.; Dai, H. MoS_2 Nanoparticles Grown on Graphene: An Advanced Catalyst for the Hydrogen Evolution Reaction. *J. Am. Chem. Soc.* **2011**, *133* (19), 7296–7299.

(4) Zheng, X.; Xu, J.; Yan, K.; Wang, H.; Wang, Z.; Yang, S. Space-Confined Growth of MoS_2 Nanosheets within Graphite: The Layered Hybrid of MoS_2 and Graphene as an Active Catalyst for Hydrogen Evolution Reaction. *Chem. Mater.* **2014**, *26* (7), 2344–2353.

(5) Feng, Q.; Mao, N.; Wu, J.; Xu, H.; Wang, C.; Zhang, J.; Xie, L. Growth of $MoS_{2(1-x)}Se_{2x}$ (x = 0.41-1.00) Monolayer Alloys with Controlled Morphology by Physical Vapor Deposition. *ACS Nano* **2015**, *9* (7), 7450–7455.

(6) Zhang, W.; Li, X.; Jiang, T.; Song, J.; Lin, Y.; Zhu, L.; Xu, X. CVD Synthesis of $Mo_{(1-x)}W_xS_2$ and $MoS_{2(1-x)}Se_{2x}$ Alloy Monolayers Aimed at Tuning the Bandgap of Molybdenum Disulfide. *Nanoscale* **2015**, *7* (32), 13554–13560.

(7) Zheng, M.; Du, J.; Hou, B.; Xu, C.-L. Few-Layered $Mo_{(1-x)}W_xS_2$ Hollow Nanospheres on Ni_3S_2 Nanorod Heterostructure as Robust Electrocatalysts for Overall Water Splitting. *ACS Appl. Mater. Interfaces* **2017**, *9* (31), 26066–26076.

(8) Kosmala, T.; Coy Diaz, H.; Komsa, H. P.; Ma, Y.; Krasheninnikov, A. V.; Batzill, M.; Agnoli, S. Metallic Twin Boundaries Boost the Hydrogen Evolution Reaction on the Basal Plane of Molybdenum Selenotellurides. *Adv. Energy Mater.* **2018**, *8* (20), 1–8.

(9) Zhou, H.; Yu, F.; Huang, Y.; Sun, J.; Zhu, Z.; Nielsen, R. J.; He, R.; Bao, J.; Goddard III, W. A.; Chen, S.; Ren, Z. Efficient Hydrogen Evolution by Ternary Molybdenum Sulfoselenide Particles on Self-Standing Porous Nickel Diselenide Foam. *Nat. Commun.* **2016**, *7*, 12765.

(10) Su, S. H.; Hsu, Y. Te; Chang, Y. H.; Chiu, M. H.; Hsu, C. L.; Hsu, W. T.; Chang, W. H.; He, J. H.; Li, L. J. Band Gap-Tunable Molybdenum Sulfide Selenide Monolayer Alloy. *Small* **2014**, *10* (13), 2589–2594.

(11) Mann, J.; Ma, Q.; Odenthal, P. M.; Isarraraz, M.; Le, D.; Preciado, E.; Barroso, D.; Yamaguchi, K.; Von Son Palacio, G.; Nguyen, A.; Tran, T.; Wurch, M.; Nguyen, A.; Klee, V.; Bobek, S.; Sun, D.; Heinz, T. F.; Rahman, T. S.; Kawakami, R.; Bartels, L. 2-Dimensional Transition Metal Dichalcogenides with Tunable Direct Band Gaps: $MoS_{2(1-x)}Se_{2x}$ Monolayers. *Adv. Mater.* **2014**, *26* (9), 1399–1404.

(12) Yang, H.; Zhang, T.; Zhu, H.; Zhang, M.; Wu, W. W.; Du, M. L. Synthesis of a $MoS_{2(1-x)}Se_{2x}$ Ternary Alloy on Carbon Nanofibers as the High Efficient Water Splitting Electrocatalyst. *Int. J. Hydrogen Energy* **2017**, *42* (4), 1912–1918.

(13) Hussain, S.; Akbar, K.; Vikraman, D.; Karuppasamy, K.; Kim, H.-S.; Chun, S.-H.; Jung, J. Synthesis of $MoS_{2(1-x)}Se_{2x}$ and WS2(1-x)Se2x Alloy for Enhanced Hydrogen Evolution Reaction Performance. *Inorg. Chem. Front.* **2017**, 2068–2074.

(14) Gong, Q.; Cheng, L.; Liu, C.; Zhang, M.; Feng, Q.; Ye, H.; Zeng, M.; Xie, L.; Liu, Z.; Li, Y. Ultrathin $MoS_{2(1-x)}Se_{2x}$ Alloy Nanoflakes For Electrocatalytic Hydrogen Evolution Reaction. *ACS Catal.* **2015**, *5* (4), 2213–2219.

(15) Marcano, D. C. D.; Kosynkin, D. D. V.; Berlin, J. M. J.; Sinitskii, A.; Sun, Z.; Slesarev, A.; Alemany, L. B.;

Lu, W.; Tour, J. M. Improved Synthesis of Graphene Oxide. *ACS Nano* **2010**, *4* (8), 4806–4814.

(16) Sheng, Z.-H.; Shao, L.; Chen, J.-J.; Bao, W.-J.; Wang, F.-B.; Xia, X.-H. Catalyst-Free Synthesis of Nitrogen-Doped Graphene via Thermal Annealing Graphite Oxide with Melamine and Its Excellent Electrocatalysis. *ACS Nano* **2011**, *5* (6), 4350–4358.

(17) Meng, F.; Li, J.; Cushing, S. K.; Zhi, M.; Wu, N. Solar Hydrogen Generation by Nanoscale P-n Junction of p-Type Molybdenum Disulfide/n-Type Nitrogen-Doped Reduced Graphene Oxide. *J. Am. Chem. Soc.* **2013**, *135* (28), 10286–10289.

(18) Carraro, F.; Calvillo, L.; Cattelan, M.; Favaro, M.; Righetto, M.; Nappini, S.; Píš, I.; Celorrio, V.; Fermín, D. J.; Martucci, A.; Agnoli, S.; Granozzi, G. Fast One-Pot Synthesis of MoS_2/Crumpled Graphene p-n Nanonjunctions for Enhanced Photoelectrochemical Hydrogen Production. *ACS Appl. Mater. Interfaces* **2015**, *7* (46), 25685–25692.

(19) Agnoli, S.; Granozzi, G. Second Generation Graphene : Opportunities and Challenges for Surface Science. *Surf. Sci.* **2013**, *609*, 1–5.

(20) Li, J.; Lin, L.; Rui, D.; Li, Q.; Zhang, J.; Kang, N.; Zhang, Y.; Peng, H.; Liu, Z.; Xu, H. Q. Electron-Hole Symmetry Breaking in Charge Transport in Nitrogen-Doped Graphene. *ACS Nano* **2017**, *11* (5), 4641–4650.

(21) Joucken, F.; Tison, Y.; Le Fèvre, P.; Tejeda, A.; Taleb-Ibrahimi, A.; Conrad, E.; Repain, V.; Chacon, C.; Bellec, A.; Girard, Y.; Rousset, S.; Ghijsen, J.; Sporken, R.; Amara, H.; Ducastelle, F.; Lagoute, J. Charge Transfer and Electronic Doping in Nitrogen-Doped Graphene. *Sci. Rep.* **2015**, *5*, 1–10.

(22) Wang, N.; Lu, B.; Li, L.; Niu, W.; Tang, Z.; Kang, X.; Chen, S. Graphitic Nitrogen Is Responsible for Oxygen Electroreduction on Nitrogen-Doped Carbons in Alkaline Electrolytes: Insights from Activity Attenuation Studies and Theoretical Calculations. *ACS Catal.* **2018**, *8* (8), 6827–6836.

(23) Prasad, T. P.; Diemann, E.; Müller, A. Thermal Decomposition of $(NH_4)_2MoO_2S_2$, $(NH_4)_2MoS_4$, $(NH_4)_2WO_2S_2$ and $(NH_4)_2WS_4$. *J. Inorg. Nucl. Chem.* **1973**, *35* (6), 1895–1904.

(24) Dai, C.; Qing, E.; Li, Y.; Zhou, Z.; Yang, C.; Tian, X.; Wang, Y. Novel $MoSe_2$ Hierarchical Microspheres for Applications in Visible-Light-Driven Advanced Oxidation Processes. *Nanoscale* **2015**, *7* (47), 19970–19976.

(25) Yang, D.; Tayebi, M.; Huang, Y.; Yang, H.; Ai, Y. A Microfluidic DNA Sensor Based on Three-Dimensional (3D) Hierarchical MoS_2/Carbon Nanotube Nanocomposites. *Sensors* **2016**, *16* (11), 1911.

(26) Xu, S.; Lei, Z.; Wu, P. Facile Preparation of 3D MoS_2/$MoSe_2$ Nanosheet-Graphene Networks as Efficient Electrocatalysts for the Hydrogen Evolution Reaction. *J. Mater. Chem. A* **2015**, *3* (31), 16337–16347.

(27) Jia, Y.; Wan, H.; Chen, L.; Zhou, H.; Chen, J. Facile Synthesis of Three Dimensional MoS_2 Porous Film with High Electrochemical Performance. *Mater. Lett.* **2017**, *195*, 147–150.

(28) Tran, X. T.; Poorahong, S.; Siaj, M. One-Pot Hydrothermal Synthesis and Selective Etching Method of a Porous $MoSe_2$ Sand Rose-like Structure for Electrocatalytic Hydrogen Evolution Reaction. *RSC Adv.* **2017**, *7* (82), 52345–52351.

(29) Kosmala, T.; Mosconi, D.; Giallongo, G.; Rizzi, G. A.; Granozzi, G. *Highly Efficient MoS_2/Ag_2S/Ag Photo-Electrocatalyst Obtained from a Recycled DVD Surface*; 2018.

(30) Li, H.; Zhang, Q.; Yap, C. C. R.; Tay, B. K.; Edwin, T. H. T.; Olivier, A.; Baillargeat, D. From Bulk to Monolayer MoS_2: Evolution of Raman Scattering. *Adv. Funct. Mater.* **2012**, *22* (7), 1385–1390.

(31) Lee, C.; Yan, H.; Brus, L. E.; Heinz, T. F.; Hone, J.; Ryu, S. Anomalous Lattice Vibrations of Single- and Few-Layer MoS_2. *ACS Nano* **2010**, *4* (5), 2695–2700.

(32) Weber, W. H.; Merlin, R. E. *Raman Scattering in Materials Science*; 2000.

(33) Pagliara, S.; Sangaletti, L.; Depero, L. E.; Capozzi, V.; Perna, G. Effect of Disorder on the Raman Scattering of $CdS_xSe_{(1-x)}$ Films Deposited by Laser Ablation. **2000**, *116*, 115–119.

(34) Liang, Y.; Zhai, L.; Zhao, X.; Xu, D. Band-Gap Engineering of Semiconductor Nanowires through Composition Modulation. *J. Phys. Chem. B* **2005**, *109* (15), 7120–7123.

(35) Muijsers, J. C.; Weber, T.; Vanhardeveld, R. M.; Zandbergen, H. W.; Niemantsverdriet, J. W. Sulfidation Study of Molybdenum Oxide Using MoO3/SiO2/Si (100) Model Catalysts and Mo-IV3-Sulfur Cluster Compounds. *Journal of Catalysis*. 1995, pp 698–705.

(36) Kosmala, T.; Mosconi, D.; Giallongo, G.; Rizzi, G. A.; Granozzi, G. Highly Efficient MoS_2/Ag_2S/Ag Photo-Electrocatalyst Obtained from a Recycled DVD Surface. *ACS Sustain. Chem. Eng.* **2018**, *6*, 7818–7825.

(37) Weber, T.; Muijsers, J. C.; Niemantsverdriet, J. W. The Structure of Amorphous MoS_3. *Bull. des Sociétés Chim. Belges* **1995**, *104* (4–5), 299–299.

(38) Wang, H. W.; Skeldon, P.; Thompson, G. E. XPS Studies on MoS_2 Formation from Ammonium Tetrathiomolybdate Solutions. *Surf. Coatings Technol.* **1997**, *91*, 200–207.

(39) Eftekhari, A. Molybdenum Diselenide ($MoSe_2$) for Energy Storage, Catalysis, and Optoelectronics. *Appl. Mater. Today* **2017**, *8*, 1–17.

(40) Wiensch, J. D.; John, J.; Velazquez, J. M.; Torelli, D. A.; Pieterick, A. P.; McDowell, M. T.; Sun, K.; Zhao, X.; Brunschwig, B. S.; Lewis, N. S. Comparative Study in Acidic and Alkaline Media of the Effects of PH and Crystallinity on the Hydrogen-Evolution Reaction on MoS_2 and $MoSe_2$. *ACS Energy Lett.* **2017**, 2234–2238.

(41) Dai, X.; Du, K.; Li, Z.; Liu, M.; Ma, Y.; Sun, H.; Zhang, X.; Yang, Y. Co-Doped MoS_2 Nanosheets with the Dominant CoMoS Phase Coated on Carbon as an Excellent Electrocatalyst for Hydrogen Evolution. *ACS Appl. Mater. Interfaces* **2015**, *7* (49), 27242–27253.

(42) Nguyen, Q. T.; Nguyen, P. D.; Nguyen, D.; Truong, Q. D.; Kim Chi, T. T.; Ung, T. T. D.; Honma, I.; Liem, N. Q.; Tran, P. D. Novel Amorphous Molybdenum Selenide as an Efficient Catalyst for Hydrogen Evolution Reaction. *ACS Appl. Mater. Interfaces* **2018**, *10* (10), 8659–8665.

(43) Yang, L.; Wang, W.; Fu, Q.; Zhang, J.; Xiang, B. $MoS_{2(1-x)}Se_{2x}$ Nanobelts for Enhanced Hydrogen Evolution. *Electrochim. Acta* **2015**, *185*, 236–241.

(44) Mak, K. F.; Lee, C.; Hone, J.; Shan, J.; Heinz, T. F. Atomically Thin MoS_2: A New Direct-Gap Semiconductor. *Phys. Rev. Lett.* **2010**, *105* (13), 2–5.

(45) Pagona, G.; Bittencourt, C.; Arenal, R.; Tagmatarchis, N. Exfoliated Semiconducting Pure 2H-MoS_2 and 2H-WS_2 Assisted by Chlorosulfonic Acid. *Chem. Commun.* **2015**, *51* (65), 12950–12953.

(46) Jia, G. Y.; Liu, Y.; Gong, J. Y.; Lei, D. Y.; Wang, D. L.; Huang, Z. X. Excitonic Quantum Confinement Modified Optical Conductivity of Monolayer and Few-Layered MoS_2. *J. Mater. Chem. C* **2016**, *4* (37), 8822–8828.

(47) Ramasubramaniam, A. Large Excitonic Effects in Monolayers of Molybdenum and Tungsten Dichalcogenides. *Phys. Rev. B - Condens. Matter Mater. Phys.* **2012**, *86* (11), 1–6.

(48) Yang, L.; Wu, X.; Zhu, X.; He, C.; Meng, M.; Gan, Z.; Chu, P. K. Amorphous Nickel/Cobalt Tungsten Sulfide Electrocatalysts for High-Efficiency Hydrogen Evolution Reaction. *Appl. Surf. Sci.* **2015**, *341*, 149–156.

(49) Velický, M.; Toth, P. S. From Two-Dimensional Materials to Their Heterostructures: An Electrochemist's Perspective. *Appl. Mater. Today* **2017**, *8*, 68–103.

(50) Zhang, L.; Liu, C.; Wong, A. B.; Resasco, J.; Yang, P. MoS_2-Wrapped Silicon Nanowires for Photoelectrochemical Water Reduction. *Nano Res.* **2014**, *8* (1), 281–287.

(51) Zong, X.; Yan, H.; Wu, G.; Ma, G.; Wen, F.; Wang, L.; Li, C. Enhancement of Photocatalytic H_2 Evolution on CdS by Loading MoS_2 as Cocatalyst under Visible Light Irradiation. *J. Am. Chem. Soc.* **2008**, *130* (23), 7176–7177.

(52) Kwon, K. C.; Choi, S.; Hong, K.; Moon, C. W.; Shim, Y. S.; Kim, D. H.; Kim, T.; Sohn, W.; Jeon, J. M.; Lee, C. H.; Nam, K. T.; Han, S.; Kim, S. Y.; Jang, H. W. Wafer-Scale Transferable Molybdenum Disulfide Thin-Film Catalysts for Photoelectrochemical Hydrogen Production. *Energy Environ. Sci.* **2016**, *9* (7), 2240–2248.

(53) Pesci, F. M.; Sokolikova, M. S.; Grotta, C.; Sherrell, P. C.; Reale, F.; Sharda, K.; Ni, N.; Palczynski, P.; Mattevi, C. MoS_2/WS_2 Heterojunction for Photoelectrochemical Water Oxidation. *ACS Catal.* **2017**, 4990–4998.

(54) Xiao, J.; Zhang, Y.; Chen, H.; Xu, N.; Deng, S. Enhanced Performance of a Monolayer MoS_2/WSe_2 Heterojunction as a Photoelectrochemical Cathode. *Nano-Micro Lett.* **2018**, *10* (4), 60.

(55) Tafalla, D.; Salvador, P.; Benito, R. M. Kinetic Approach to the Photocurrent Transients in Water Photoelectrolysis at N-TiO_2 Electrodes. *J. Electrochem. Soc.* **1990**, *137* (6), 1810–1815.

Chapter Five:

Arene C-H Insertion Catalyzed by Ferrocene Covalently Heterogenized on Graphene Acid

5.1 Introduction

Homogeneous molecular catalysts are considered very attractive systems for chemical synthesis and catalysis because they display high activity and selectivity, and do not have problems associated with diffusion and mass transport.[1] From classic acid-base systems[2] to elaborated chiral organometallic active molecules, to cite some examples,[3] a large library of highly active homogeneous catalysts is accessible to researchers. However, homogeneous catalysts suffer from some drawbacks, such as high price, elaborated synthetic protocols, lack of stability and difficulty to recover and recycle.[4] To overcome these limits, researchers are trying to combine the intrinsic potential of homogeneous catalysts with the advantages of heterogeneous catalysis by anchoring molecular active centers on solid supports. In this way, the activity and selectivity of the homogeneous catalysts is preserved, but also recyclability and stability can be imparted to the final catalytic system.[5]

In order to heterogenize a molecular catalyst, the surface chemistry of the support materials needs to be precisely controlled, providing specific reaction centers poised for the subsequent functionalization. Two different strategies are possible, one exploiting physical and dispersion interactions, the other true covalent bonds. While the former is considered a non-invasive method that merely fixes the active species on the surface of the material,[6] the latter creates a strong covalent interaction between the material and the catalyst precursor, which might promote synergic effects.[7] Several studies can be found in the literature where metal-organic frameworks,[8] activated carbons,[9] zeolites and related inorganic architectures,[10–12] polymers[13] and carbon based nanomaterials (e.g. carbon nanotubes and graphene[14]) have been surface-modified with the aim of anchoring a molecular catalyst.

The well-known properties of graphene (one-atom-thick C-C layer) and related materials, such as high electron[15] and thermal conductivity,[16] tunable porosity and chemical inertness in most reaction media,[17] make these materials suitable for anchoring molecular catalysts. Interestingly, a large variety of graphene derivatives has been developed recently, offering a large gamut of materials characterized by an extremely rich surface chemistry that can be exploited for advanced functionalization protocols. Among these, graphene oxide (GO) is the most widely used support, given its easy and scalable synthesis.[18] However, the oxygen surface groups of GO (i.e. a complex mix of tertiary alcohols, epoxide, carboxyl and carbonyl groups) are very hard to control.[19] In a previous work, some of us developed the graphene acid (GA), which can be considered a graphene layer with the basal plane densely and homogeneously decorated by carboxylic groups.[20] This graphene derivative is quite interesting given its simple synthesis, easy scalability, high surface area and electronic conductivity. Moreover, the precise control on the type of surface groups, while maintaining the high content of the sp^2 network of pristine graphene, makes this material a very attractive platform for chemical functionalization.

Among the possible molecular catalysts that could be heterogenized on the graphene-related materials, ferrocene (Fc) is an organometallic complex with very interesting properties in a variety of applications. It is widely used as an electrochemical probe due to its fully reversible oxidation/reduction properties and stability in aqueous media,[21] and when heterogenized, it can act as an electron transfer mediator.[22] Recently, molecular Fc has shown chemical activity as peroxide scavenger[23] and catalyst in the C-H insertion of diazonium aryl salts to arene substrates,[24] a reaction of pivotal importance for organic chemistry since it

activates a rather inert system, opening new reaction pathways in the synthetic research. This calls for heterogenization of Fc onto suitable solid surfaces for preparing efficient and recyclable catalysts for this valuable reaction. Some of us previously succeeded to anchor a molecular catalyst on the surface of some carbon nanomaterials,[25] in which the substrate-molecule interaction enhanced the properties of the final system adding also stability and cyclability to the catalyst. This second reason encouraged us to heterogenize the Fc on an unconventional graphene support.

In this Chapter, we report on the covalent functionalization of GA nanosheets with a Fc complex. For comparative purposes, GO has been also functionalized under the same experimental conditions (see Figure 5.1). The resulting Fc-modified graphene derivatives have been tested as heterogeneous catalysts for the C-H insertion of aryl diazonium salts into several arene substrates. The heterogenized catalyst resulted to be extremely active and selective, with a much better performance compared to molecular Fc in the case of highly condensed arenes. Moreover, the hybrid Fc functionalized GA catalysts could be easily recovered after the reaction and used for a new catalytic cycle without any loss of activity. Interestingly, a better catalytic performance was observed for the GA-based with respect to the GO-based material, which can be related to the different structural and electronic properties between the two graphenic supports.

5.2 Experimental Section

Graphenic materials synthesis

GA was synthetized by our collaborators in Otyepka research group, following the procedure described in reference and reported below.[20]

To obtain the intermediate Cyanographene (G-CN), Fluorinated graphite (120 mg, ~4 mmol of C-F units) was added to 15 mL of DMF and sonicated (Bandelin Sonorex, DT 255H type, frequency 35 kHz, power 640 W, effective power 160 W) for 4 h under nitrogen atmosphere in a 25 mL round-bottom glass flask. Then 800 mg of NaCN (~16 mmol) was added and the mixture was heated at 130 °C with a condenser under stirring (500 rpm). Sample aliquots were withdrawn from the flask at different time points to monitor the reaction progress. Further experiments were performed on the product treated for 24 h. Intermediates and final product were left to cool to room temperature, after which an equal amount of acetone was added.

The materials were then separated by centrifugation and further purified by successive washing steps using DMF, dichloromethane, acetone, ethanol and water (all 4×). Hot (80 °C) DMF and water was also used. More washing steps using DMF and water were applied if the conductivity of the supernatant aqueous fraction was higher than 200 μS cm^{-1}. During the final centrifugation steps with water, it was necessary to apply centrifugal forces of up to 25000*g* RCF to isolate the product. To obtain Na-free products, G-CN was washed with acidified water (pH = 4) to exchange sodium cations with H_3O^+ (the ζ-potential of G-CN was determined to be in the range of −30 mV, therefore contained Na^+ as counterions).

GA was synthesized *via* acidic hydrolysis of –CN moieties. HNO_3 (65%) was slowly added at RT under stirring to a suspension of G-CN in water in a round-bottom glass flask, until the final concentration of HNO_3 in the mixture reached 20%. The mixture was then heated at 100 °C under reflux with stirring (350 rpm) for 24 h. Various concentrations of HNO_3 and treatment durations were tested to identify optimal conditions, and

samples were periodically withdrawn to monitor the reaction's progress. Intermediates and final products were left to cool to room temperature and then purified by washing with water through centrifugation. After a few washings, the product (GA) stopped precipitating upon centrifugation. Therefore, acidic water (pH = 4) was used to protonate the material and reduce its dispersibility, inducing precipitation. Stable aqueous suspensions of G-COOH were prepared by adjusting the pH of the purified suspension to ~8.

GO was synthesized according to a modified Hummers procedure.[26]

An amount of 3.0 g of graphite was mixed with 75 ml of 9:1 mixture of H_2SO_4 and H_3PO_4. Then an amount of 9.0 g of $KMnO_4$ was slowly added while cooling the mixture in an ice bath. The mixture was stirred for 3 h at 0 °C and then overnight at room temperature. After that, a volume of 150 ml of water was added heating at 80 °C. After stirring for 1 h, the obtained mixture was sonicated for 1 h at 35 °C. To quench the reaction, 3 mL of 30 %wt. of H_2O_2 was added, stirred for additional 2 h, sonicated for 1 h and finally, diluted with additional water. The supernatant was profusely washed with water, dialyzed 72 h against DI water and 8 h against Milli-Q quality water, and finally lyophilized.

Functionalization procedure

The introduction of the Fc moieties in both graphene derivatives was performed through a two-step procedure:

1. functionalization of the graphenic materials with amino groups;
2. coupling of amino-functionalized materials with a Fc molecule having a side carboxyl group (ferrocenecarboxyl acid, hereafter referred to as Fc for the sake of simplicity).

First, an amount of 40 mg of GA (or GO) was dispersed in 2 mL of *N,N*-dimethylformamide (DMF), and then mixed with 20 mL of pure 1,3-diaminopropane (PDA) and 40 mg of dicyclohexylcarbodiimide (DCC). The reaction mixture was stirred at room temperature (rt) for 72 h. After that, the solid fraction was separated by centrifugation and rinsed thoroughly with isopropanol for 4 times. Moreover, before each of these cycles, the sample suspension was sonicated for 5 minutes. The dried samples were labelled as GA-PDA and GO-PDA according to the starting material.

In the second step, an amount of 0.8 mmol of ferrocenecarboxyl acid was dissolved in 5 mL of DMF in an ice bath. The -COOH groups were activated by adding immediately 1.2 mmol of hydroxybenzotriazole (HOBt) and 1.2 mmol of triethylamine. After 45 min of activation at 0 °C, the ice bath was removed, and 1.2 mmol of DCC and 40 mg of the amino-functionalized material previously dispersed in 20 mL of DMF were added. The reaction mixture was stirred at rt for 72 h. The resulting solid was separated and purified by centrifugation and rinse cycles as in the previous step, yielding GO-PDA-Fc and GA-PDA-Fc samples according to the starting precursor.

Synthesis of the diazonium salts for the catalytic tests

The general procedure for the synthesis of the benzenediazonium tetrafluoroborate (BDT) salt followed the standard nitrite methods.[27] Typically, 10 mmol of the corresponding aniline was dissolved in a mixture of 3.6 mL of HBF_4 and 3 mL of H_2O in an ice bath. Then, 10 mmol of $NaNO_2$ dissolved in 1.5 mL of water were slowly

added to this mixture, and the reaction was kept at 0 °C for 45 min. After that, the precipitate was filtered and dissolved in the minimum amount possible of acetone. With the help of diethyl ether, a precipitate was obtained, which was washed with more diethyl ether and dried under vacuum.

Catalytic tests

In a typical experiment, the diazonium salt (1 mmol), arene (0.33 mmol), solvent (3 mL, typically acetone after optimization) and the catalyst (1.6 mol% of active phase vs arene, 1.8 mg of GA-PDA-Fc and 9.2 mg of GO-PDA-Fc, according to XPS and EDX determination) were introduced into a 25 mL round-bottomed flask. The reaction was held at rt for the desired time. Aliquots (100 µl) were taken at regular intervals and analyzed by NMR spectroscopy in order to follow the progress of the reaction. Once the reaction was saturated, the reaction crude was centrifuged to remove the catalyst. Homogeneous experiments were performed following the general procedure employing as catalyst 1.6 mol% of molecular ferrocene, molecular ferrocenium tetrafluoroborate or different molar mixtures of both organometallic complexes. Adsorption experiments were performed under the general conditions without diazonium salt and with parent GA or GO as graphenic materials. For obtaining the C-H insertion product, the solvent was removed under reduced pressure, the residue dissolved in dichloromethane and washed three times with water, dried over anhydrous $MgSO_4$ and concentrated under reduced pressure; purification by column chromatography in silica (hexane:ethyl acetate 4:1) yielded the final product. On the other hand, the recovery of the solid catalysts was obtained by 3 additional centrifugation cycles with fresh acetone, sonicating for 5 min just before each centrifugation cycle. The materials were dried in vacuum, and successively submitted to a new catalytic cycle without adding any catalyst precursor. The whole procedure was repeated 8 times.

Physico-chemical Characterization

The surface chemical characterization of the catalyst has been carried out using X-ray photoelectron spectroscopy (XPS) in a custom-made UHV system working at a base pressure of 10^{-10} mbar, equipped with an Omicron EA150 electron analyzer and an Omicron DAR 400 X-ray source with a dual Al−Mg anode. Core level photoemission spectra (C 1s, N 1s, O 1s and Fe 2p regions) were collected at rt with a non-monochromated Al Kα X-ray source (1486.7 eV) and using an energy step of 0.1 eV, 0.5 s of integration time, and a 20 eV pass energy. The samples were dispersed in 2-propanol and drop casted on an Al support. The nano- and microscale morphology of materials was studied by scanning electron microscopy (SEM) and transmission electron microscopy (TEM). The SEM images were acquired using a field emission source equipped with a GEMINI column (Zeiss Supra VP35) and an Oxford energy-dispersive x-ray spectroscopy (EDX) microprobe, and micrographs were obtained with an acceleration voltage of 5 or 10 kV using in-lens high-resolution detection. The TEM images were acquired using a FEI Tecnai 12 microscope with an acceleration voltage of 100 kV. The Raman spectra were collected using a ThermoFisher DXR Raman microscope using a laser with an excitation wavelength of 532 nm (5 mW), focused on the sample with a 50× objective (Olympus). The UV−visible−NIR absorption spectroscopy data were acquired using a Cary 5000 spectrometer (Varian), in the 200−1000 nm range. In this case, powder samples were dispersed in DMF, forming a stable colloidal dispersion. All spectra were recorded using 1 cm optical path quartz cells. The concentration and the experimental parameters were optimized to minimize scattering effects. The NMR spectra were recorded on a Bruker Avance 300 MHz (300.1 MHz for ^{1}H, 298 K); chemical shifts (δ) are

reported in units of parts per million (ppm) relative to the residual solvent signals and coupling constants (*J*) are expressed in Hz.

Electrochemical Characterization

The electrochemical measurements were performed in a conventional three-electrode cell, using an $Ag/AgCl_{3M\ KCl}$ (calibrated as +0.225 V vs RHE) and a Pt wire as reference and counter electrodes, respectively. The working electrode consisted of 2 µL of catalyst ink deposited on a glassy carbon disk (0.071 cm^2) and dried in vacuum for 1 h. The catalyst ink was prepared by dispersing 2 mg of sample and 15 µL of Nafion solution (5 wt.% in alcohol/water, Sigma-Aldrich) in 0.5 mL of DMF and bath sonicated for 30 min. 50 ml of Ar-saturated 0.1 M tetraethylammonium tetrafluoroborate (NEt_4BF_4) in dry acetonitrile solution was employed as electrolyte for the electrochemical tests. The electrodes were first cycled for 10 times at 0.1 V s^{-1} between +0.1 V and +1.05 V vs Ag/AgCl. Then, cyclic voltammetries (CVs) were recorded at different scan rates (υ = 25, 50, 75, 100, 125, 150, 175, 200, 225 and 250 mV s^{-1}) in the same potential range. The linear proportionality between the peak current (i_p) and υ^x (x = 1 for species immobilized on the surface; x = 0.5 for species in solution) was used to confirm the permanent attachment of Fc to the graphene support. The electrochemical measurements on GO and GA electrodes with molecular Fc in the electrolyte were used as blank experiments. For these measurements, 9.3 mg of Fc (1 mM) were added to the electrolyte and the electrodes were cycled between -0.1 V and +0.9 V vs Ag/AgCl.

5.3 Result and Discussion

5.3.1 Functionalization and characterization of the graphenic materials

We selected GA and GO as 2D-platforms for the heterogenization of the Fc-based catalyst. The chemical and structural characterization of pristine GA and GO presented here is in agreement with previously reported data.[20,26] The highly controlled surface functionalization of GA, mainly based on –COOH groups, was used for creating a novel hybrid material bearing organometallic units; while GO, being the most used graphene derivative in chemical applications, was used as a reference benchmark. The functionalization strategy consisted of two steps. The carbodiimide chemistry[28] was exploited for attaching covalently the Fc moiety on the surface of the different graphene supports (see Figure 5.1). Very briefly, each graphene derivative was firstly modified through a DCC catalyzed coupling reaction between the amine group of 1,3-diaminopropane and the carboxylic groups of the graphene support. In this way, the -NH_2 terminating linkers were grafted on both GA and GO, producing the samples GA-PDA and GO-PDA.[29] Then, the ferrocenecarboxyl acid was introduced using the DCC-HOBt method[30] to yield the final GA-PDA-Fc and GO-PDA-Fc products.

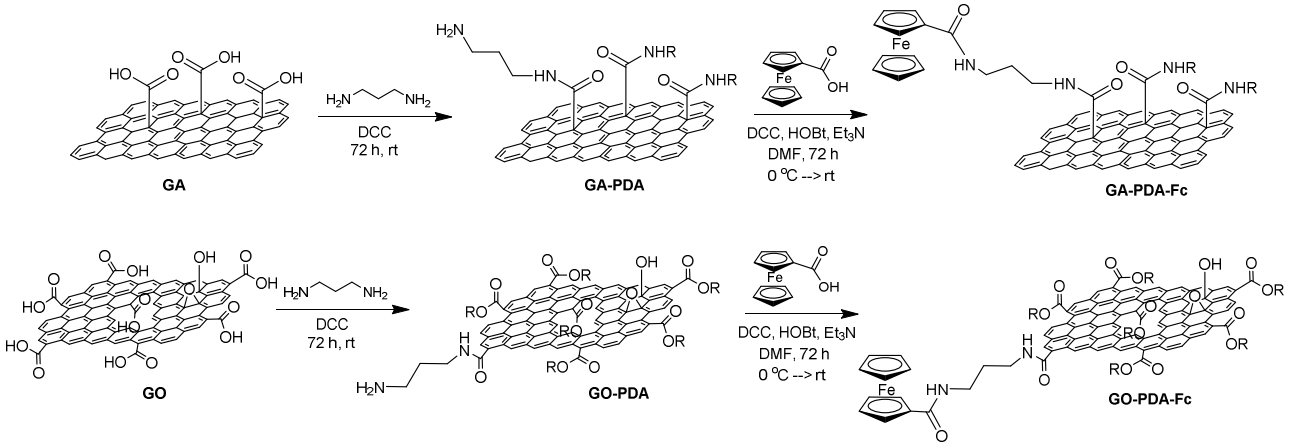

Figure 5.1. Functionalization route of both GA (upper) and GO (lower) derivatives.

The surface modification of GA and GO during the functionalization process was monitored by XPS. Figure 5.2 shows the C 1s photoemission line measured after each step of the functionalization procedure with the corresponding separation into chemically shifted components (see Table 5.1 for more detailed data).[31] The pristine GA has a large fraction of C-sp^2 atoms (61.5 %) and comprises mainly COOH groups since the peak centered at 289 eV is the most intense among the C-O related components (9.7 % of the total signal). On the other hand, the pristine GO shows a more complex chemical composition: the C sp^2 component is reduced to 53.4% of the whole C 1s intensity, whereas the two components at 286.6 eV (13.5 %) and 286.9 eV (9.6 %) corresponding to alcohol and epoxy groups, respectively are about twice more intense than in GA. Finally, in the case of GO, the carboxyl groups accounts only for the 7.0 % of the whole C 1s intensity. After the introduction of the amino linker, the amount of sp^3 C-C bonds slightly increases for both samples as a consequence of the aliphatic carbons present in the diamine chain (see Table 5.1 for more details). The component centred at 286.6 eV, which now can be associated with C-N sp^3 bonds, gains intensity, whereas the intensity of the peak corresponding to carboxyl groups strongly decreases (2.8% and 5.4% of the whole C 1s intensity for GA and GO, respectively). The attachment of amino species was also confirmed by the appearance of the N 1s peak (see Table 5.2). In both materials the component at 288.0 eV, which is associated with amide groups that are also formed by the reaction with the PDA, increases.

After the second functionalization step (i.e. reaction with Fc), in the C 1s photoemission spectra, the reduction in the C-N amino groups and the corresponding increase of the amide components (about 12% for both graphene derivatives) are observed, suggesting that the carboxyl groups of the Fc have reacted with the amino functionalized supports. However, also the intensity of the carboxyl group component increases (8% and 11% of the whole intensity for GA and GO, respectively). This can be understood assuming that this signal stems from the Fc unit physisorbed on the C sp^2 domains of the graphenic support as a consequence of the Fc excess employed. In addition, the amount of nitrogen stays almost constant when passing from the free amine in the PDA samples to the immobilized Fc sample for both materials (Table 5.2). Therefore, the body of photoemission data allows following each step of the covalent functionalization procedure and suggests that the resulting materials contained both Fc units covalently attached through the amide bond and strongly physisorbed species, which cannot be removed even by thorough rinsing.

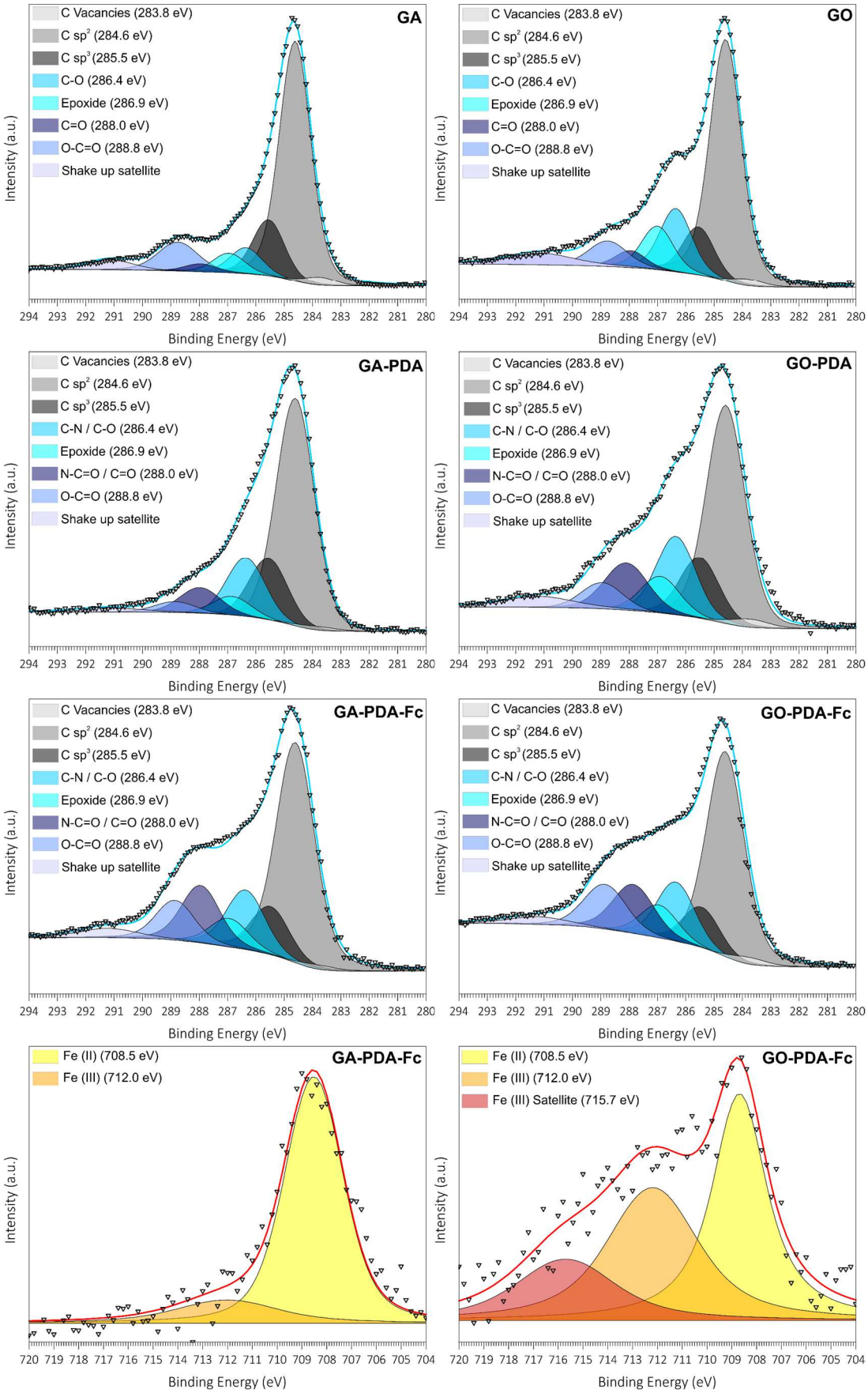

Figure 5.2. C 1s XPS region for GA- (left) and GO-based (right) materials. *Low:* Fe $2p_{3/2}$ line for ferrocene functionalized materials.

We also analyzed the XPS Fe $2p_{3/2}$ region of the final materials (see Figure 5.2 low panels). Two components appear in the spectra, whose intensity maxima are located at a binding energy of approximately 708.5 and 712 eV, which can be assigned to Fe(II) and Fe(III), respectively. A very small amount of Fe(III) was detected in the GA-PDA-Fc sample (15 % of the total signal) whereas a larger amount (38 %) in the GO-PDA-Fc material.[32] It has been already reported in the literature that covalently bound Fc units can undergo a substrate promoted oxidation to ferrocenium ion in aerobic conditions.[32–34] In this case, the larger chemical heterogeneity of GO comprising several types of oxygen species such as epoxides and carbonyls, could promote to a larger extent the oxidation of the Fe centers with respect to the more homogeneous GA surface.[35,36] Overall the surface composition of the samples as determined by XPS measurements indicate a higher presence of iron on the GA (3.6%) with respect to GO (1.0%, see Table 5.2).

	C Vacancy	*C sp²*	*C sp³*	*C-O – C-N*	*Epoxy*	*Carbonyl / Amide*	*Carboxylic*	*C sp³/C sp²*	*(C-O – C-N) /C sp²*
GA	1.2	61.5	14.4	7.1	4.4	1.7	9.7	0.2	0.1
GA-PDA	0.9	55.7	15.0	14.5	4.5	6.6	2.8	0.3	0.3
GA-PDA-Fc	1	48.1	10.6	13.0	6.2	12.5	8.6	0.2	0.3
GO	1.6	53.4	10.6	14.0	9.6	3.8	7.0	0.2	0.3
GO-PDA	1.7	45.3	12.7	16.4	7.6	10.9	5.4	0.3	0.4
GO-PDA-Fc	1.6	45.7	9.1	13.2	7.3	12.1	11	0.2	0.3

Table 5.1. C 1s photoemission line deconvolution data for the pristine and functionalized GA and GO materials. Ratios between C sp^3 and heteroatom bonded C against C sp^2 are reported in order to monitor functionalization procedure.

	C (at.%)	*O (at.%)*	*N (at.%)*	*Fe (at.%)*	*I_D/I_G*
GA	81.0	14.5	4.5	-	1.046
GA-PDA	81.4	10.0	8.6	-	1.126
GA-PDA-Fc	72.4	16.0	8.0	3.6	1.080
GO	74.1	25.9	-	-	0.924
GO-PDA	79.2	14.8	6.0	-	1.059
GO-PDA-Fc	77.6	15.9	5.5	1.0	1.040

Table 5.2. Surface composition (at.%) determined from XPS as well as Raman data for the pristine and functionalized GA and GO materials.

Raman data are in line with the XPS results. Figure 5.3 reports the Raman spectra for the pristine GO and GA and after each functionalization step. The I_D/I_G ratio in both types of scaffold slightly increases after the reaction with the PDA, indicating the formation of defects in the carbon support during this step. The increase of defects after the functionalization treatment with organometallic compounds has been reported previously as a positive confirmation of covalent functionalization.[37] In addition, the grafting of the aromatic structures present in the Fc units (the Fc peaks can also be observed[38]) results in a decrease of the I_D/I_G ratio for the GA-PDA-Fc and GO-PDA-Fc materials, although the final value is higher than that of both pristine materials. This can be explained because the Fc units, such as other aromatic moieties, can “hide” defects in graphene based materials, acting as a sort of patch.[39]

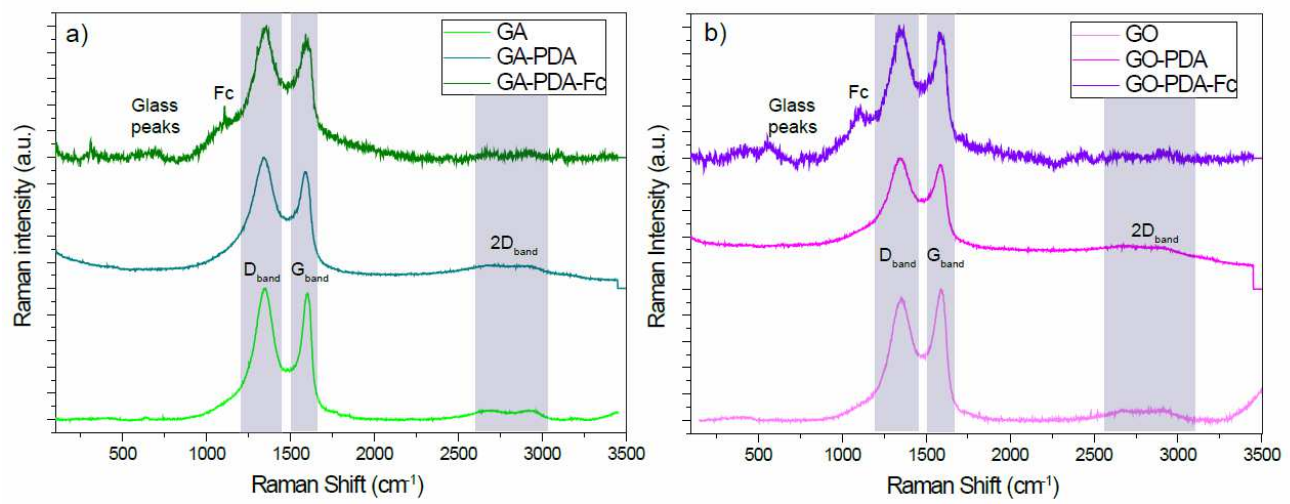

Figure 5.3. Raman spectra of a) GA-based and b) GO-based materials.

The presence of Fc can also be determined by means of UV-Vis-NIR absorption spectroscopy (see Figure 5.4). While the molecular Fc shows a prominent absorption peak at ca. 441 nm, the GA-PDA-Fc sample exhibits an absorption band at 423 nm, i.e. 18 nm blue-shifted with respect to the molecular Fc.[39,40] On the other hand, in the GO-PDA-Fc sample a mixed contribution due to Fe(II) and Fe(III) species was detected. In fact, the material presents the ferrocene absorption band at 438 nm, but also additional peaks due to the ferrocenium ion are visible at 363 nm and 580 nm.[41,42] Therefore, the different optical behavior of the samples nicely matches the XPS data discussed above.

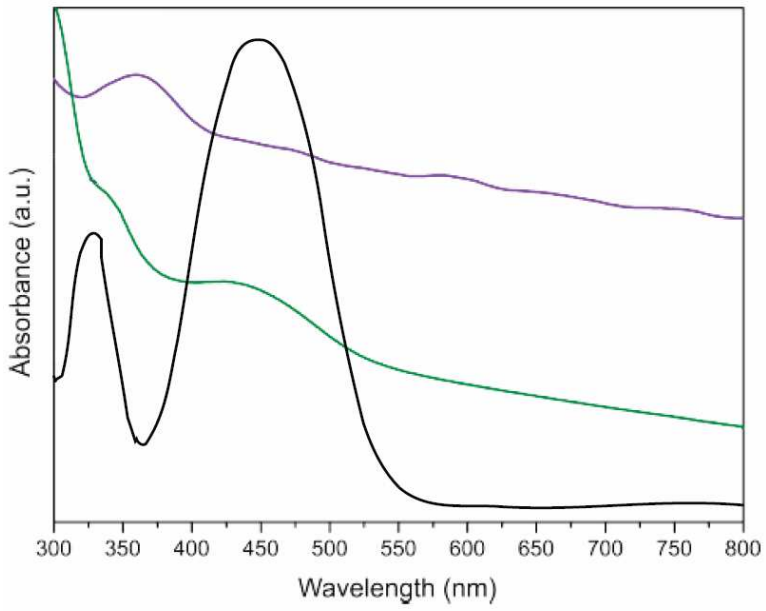

Figure 5.4. UV-Vis-NIR spectra of GA-PDA-Fc (green), GO-PDA-Fc (violet) and molecular Fc (black).

In order to shed some light on the functionalization of the graphene derivatives, electrochemical tests were performed on GA-PDA-Fc and GO-PDA-Fc. It is known that the scan rate (υ) has a different effect on the current (i) for the systems where the electrochemically active species is immobilized on the surface or in solution.[43,44] In the case of systems with the species immobilized on the surface, i is proportional to υ, as

described by equation 1, whereas in the case of systems with the species in solution, *i* is proportional to $\upsilon^{1/2}$, as described by the Randles-Sevcik equation (Eq.2).[43,44]

$$i_p^{rev} = \frac{n^2 \mathrm{F}^2 \Gamma \mathrm{A}}{4\mathrm{RT}} \upsilon \qquad \text{(Eq. 1)}$$

$$i_p^{rev} = 0.446 n \mathrm{FAC} \left(\frac{n\mathrm{FD}}{\mathrm{RT}}\right)^{1/2} \upsilon^{1/2} \qquad \text{(Eq. 2)}$$

Figure 5.5 shows the cyclic voltammetries (CVs) recorded at different scan rates for both GA-PDA-Fc and GO-PDA-Fc systems showing an oxidation and a reduction peak at around 0.68 V and 0.60 V, respectively, related to the Fe^{+3}/Fe^{+2} redox couple of Fe ions in Fc. The redox peaks are symmetrical and bell-shaped, which are features associated with a reversible process where diffusion does not play any role. This suggests that the Fe ions involved in the electrochemical reactions are strongly attached to the electrode surface. The current increases with the scan rate, but the peak potentials are independent of the scan rate, further confirming the reversibility of the process. The decisive evidence of a permanent attachment of Fc to the graphenic substrates however is the linear dependence of the peak current on the scan rate, as seen in Figures 5.5c-d.

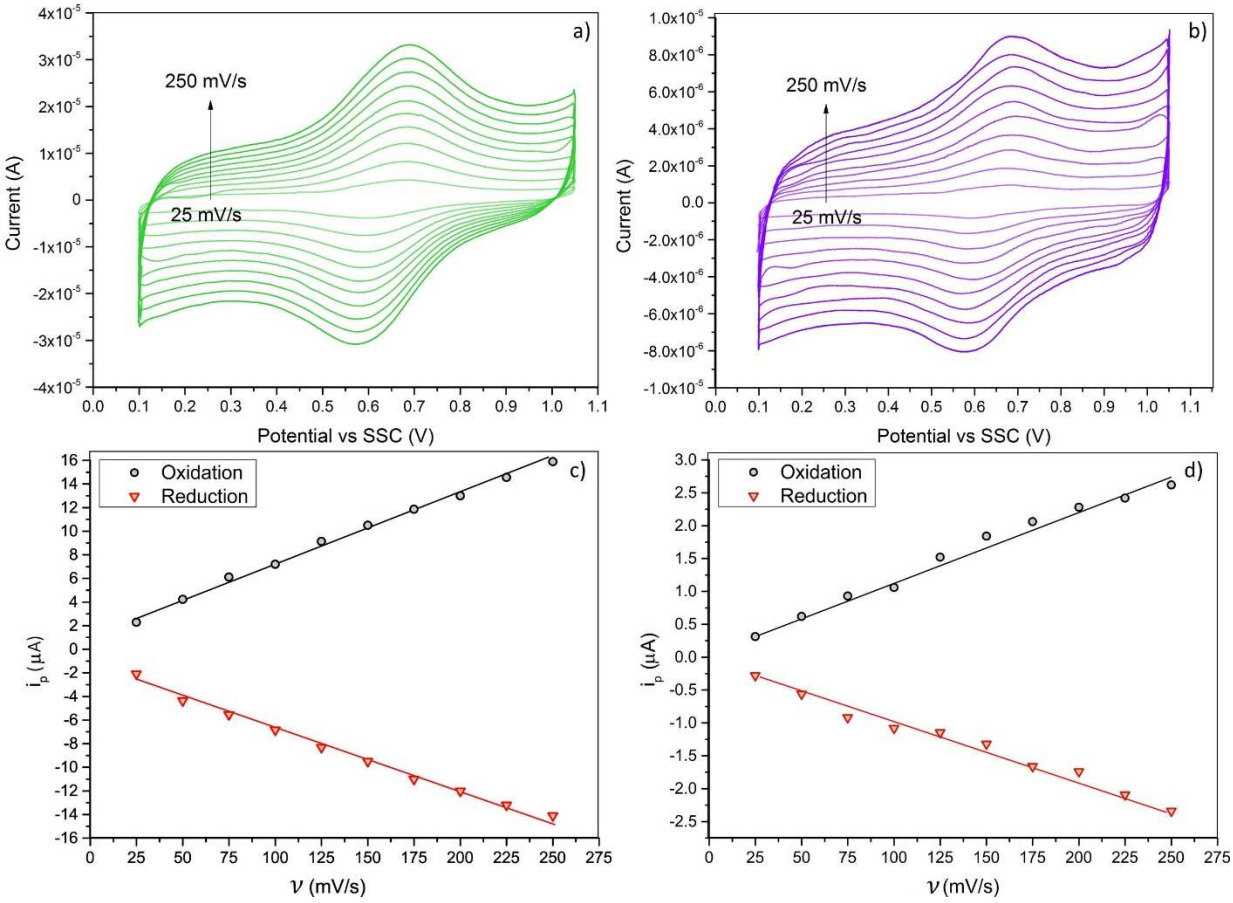

Figure 5.5. CVs in Ar-saturated 0.1 M NEt_4BF_4 in acetonitrile solution for GA-PDA-Fc (a) and GO-PDA-Fc (b) at different scan rates. Figure 3c and 3d show the i_p vs υ plots. i_p-υ plots are determined with the assumption that the double layer capacitance is independent of the applied potential.

To compare these results with those of a system where the active species are in solution, the same electrochemical measurements were performed with the bare GA and GO electrodes by adding Fc to the electrolyte. Figure 5.6 shows the results obtained for these systems. The oxidation and reduction peaks characteristic of the Fe^{+3}/Fe^{+2} redox couple are also observed, but in this case the peaks do not present a bell-shape. Moreover, the current increases with the scan rate and a good linear dependence of i with $\upsilon^{1/2}$ is found (see Figure 5.6 c-d) as expected for a diffusion controlled process. In addition, from these data, it is possible to compare the electronic conductivity of both graphenic materials. GA shows a peak separation of 70 mV, confirming that this material has a high electronic conductivity. On the other hand, GO shows a peak separation of 110 mV, indicating a lower conductivity of GO than GA (see Figure 5.7). This is not surprising since it has been demonstrated by DFT calculations that a COOH-strongly-functionalized graphene sheet owns an electrical conductivity comparable to pristine graphene which could be explained by the higher amount of sp^2 C-C bonds and the lower content of oxygen groups in the GA material, as demonstrated by XPS.[20]

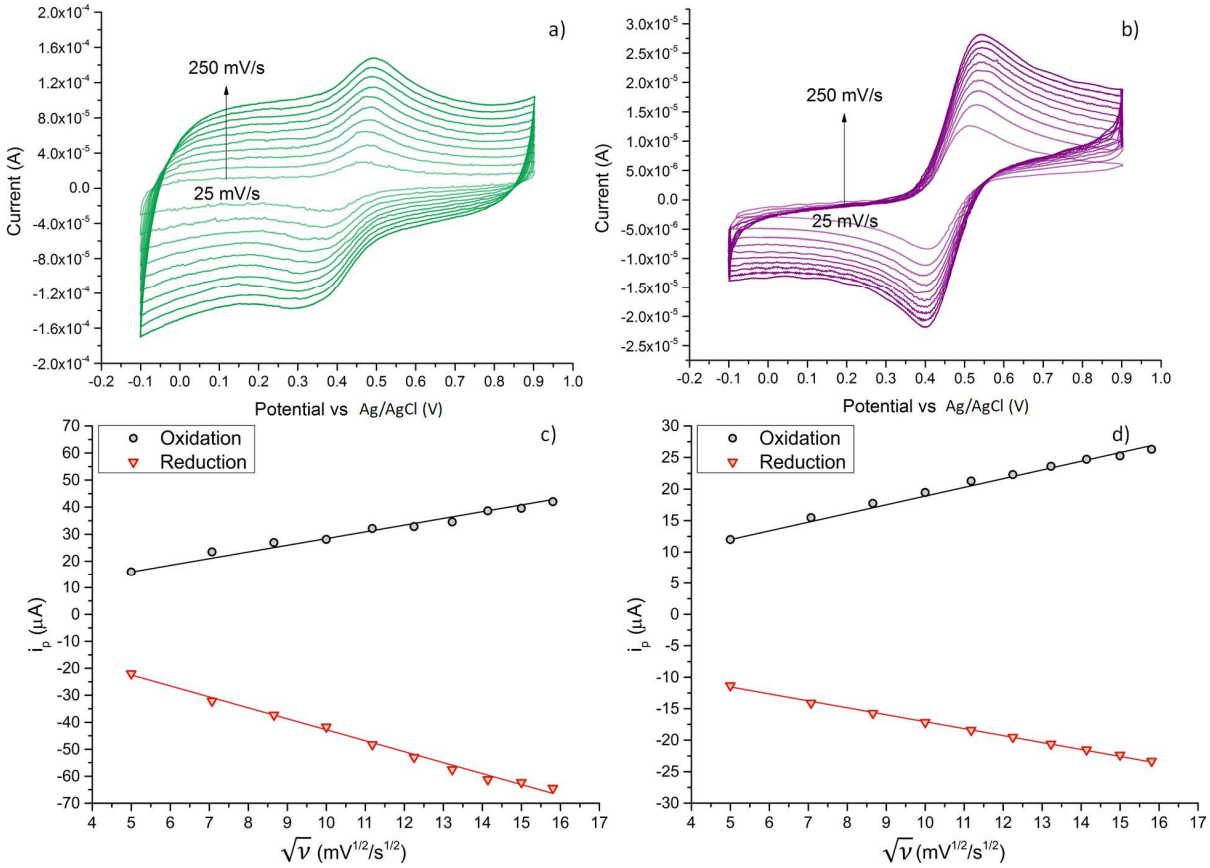

Figure 5.6. CVs in Ar-saturated 1 mM $Fe(C_5H_5)_2$ + 0.1 M NEt_4BF_4 in acetonitrile solution for GA (a) and GO (b) at different scan rates. (c) and (d) show the linear dependence of the current on the square root of the scan rate, as described by the Randles-Sevcik equation for ideally reversible systems with solution phase species. i_p-υ plots are determined with the assumption that the double layer capacitance is independent of the applied potential.

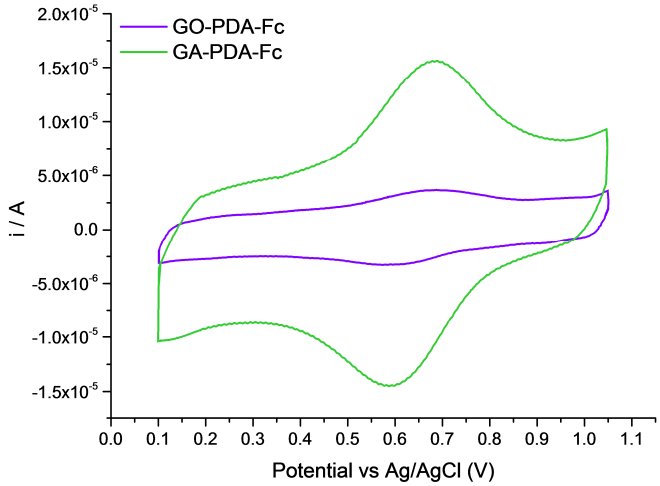

Figure 5.7. CVs in Ar-saturated 0.1 M NEt_4BF_4 in dry acetonitrile on GA-PDA-Fc and GO-PDA-Fc at 50 mV s^{-1}.

The morphology of the samples as well as the possible changes induced by the functionalization treatments were studied by SEM and TEM. Figure 5.8 shows the complete microscopy analysis we carried out: (a-f) are the SEM images of GA- (left panels) and GO-based (right panels) materials along the whole functionalization procedure. (g) and (h) are TEM photographs of the final materials and finally (i) and (j) the size dispersion calculated for pristine materials in SEM analysis. SEM micrographs show flake-like structures for both materials, with lateral sizes in the range of hundreds of nm for pristine GA (250-500 nm), whereas a few µm for pristine GO (1-10 µm). Overall, the morphological features were maintained unaltered throughout the whole functionalization procedure. In addition, it is important to note that the quality of the images is maintained during all the stages of the functionalization, which is not always present in the literature data. This is a proof of clean functionalization steps. In addition, we carried out an EDX analysis of the different materials confirming the detection of iron , which resulted to be 3.9 at % and 0.8 at % in the GA-PDA-Fc and GO-PDA-Fc samples, respectively, which is in good agreement with the surface determination obtained by XPS. The complete composition analysis provided by the EDX measurements is reported in Table 5.3. TEM images of a selected-area of both GA-PDA-Fc and GO-PDA-Fc are also in agreement with the SEM data, showing mainly aggregates comprising few flakes.

	C + N (at.%)[a]	*O (at.%)*	*Fe (at.%)*
GA-PDA-Fc	83.6±6	12.5±1	3.9±0.5
GA-PDA-Fc (a.c.)	82.1±6	14.7±1	3.2±0.5
GO-PDA-Fc	82.7±6	16.5±1	0.8±0.4
GO-PDA-Fc (a.c.)	80.1±6	19.4±1	0.5±0.4

[a] Due to proximity of C and N signal, they are reported together.

Table 5.3. Elemental composition (at. %) from EDX analysis before and after catalysis (a.c.).

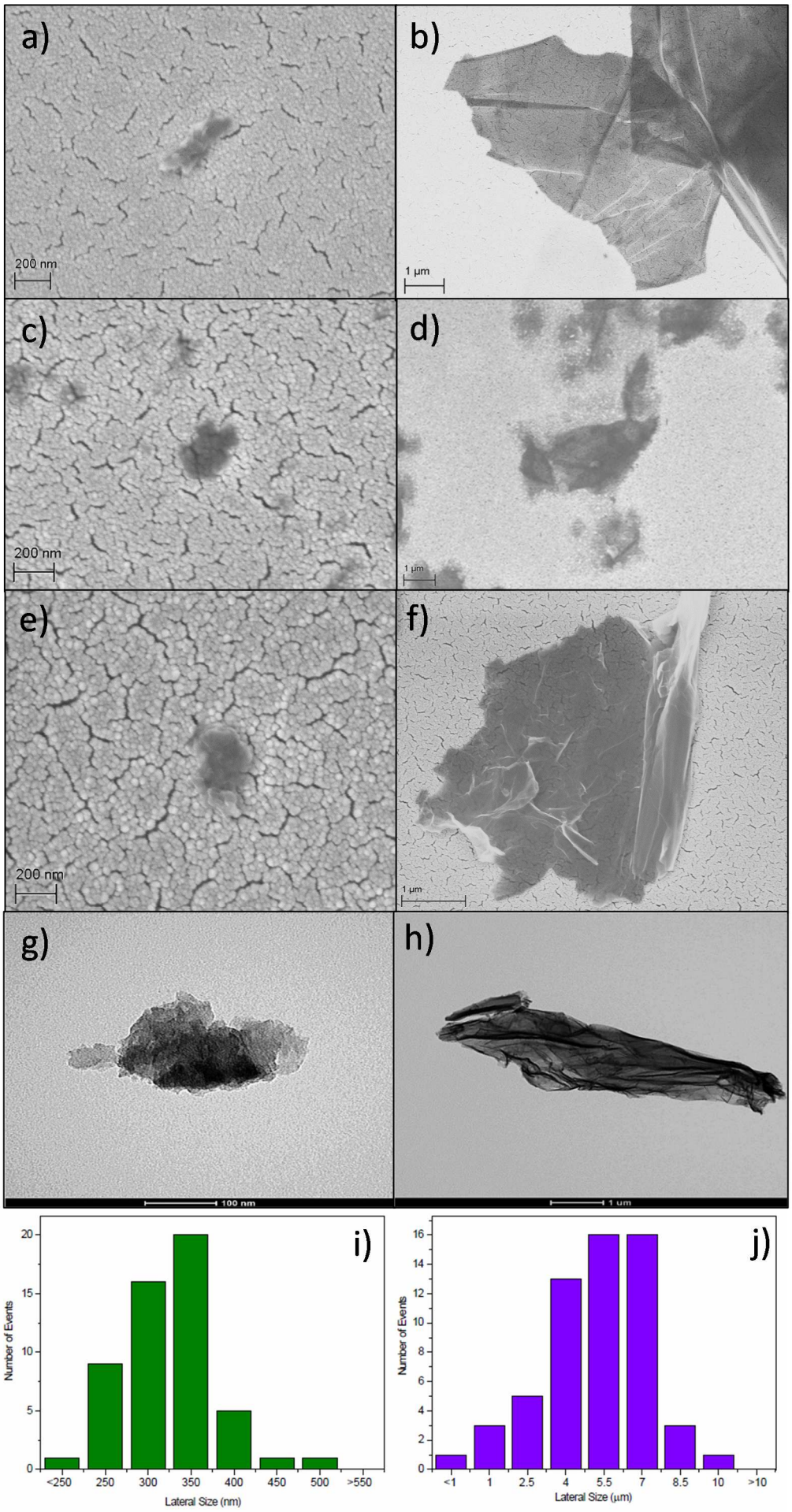

Figure 5.8. SEM analysis of samples (*left* GA; *right* GO): (a-b) Pristine; (c-d) –NH2 capped; (e-f) Fc terminated.

TEM images of GA-PDA-Fc (g) and GO-PDA-Fc (h).

Size dispersion for GA (i) and GO (j) calculated from SEM images.

5.3.2 Catalytic Experiments

Once the successful functionalization of the GA and GO supports with Fc was demonstrated, and considering that molecular Fc shows a good catalytic activity in the C-H insertion of diazonium salts into arene substrates reaction,[24,45–47] the GA-PDA-Fc and GO-PDA-Fc materials were tested as heterogeneous catalysts for the same reaction. With this aim, we first prepared BDT, starting from the corresponding aniline, by the standard nitrite–tetrafluoroboric acid method.[27] The detailed experimental procedure and the full NMR characterization of the salt can be found in the experimental section (5.2) and in the appendix with NMR data of all the isolated compounds (Section 5.3.3).

The C-H insertion of BDT in naphthalene was investigated as a model reaction (Figure 5.9).[48]

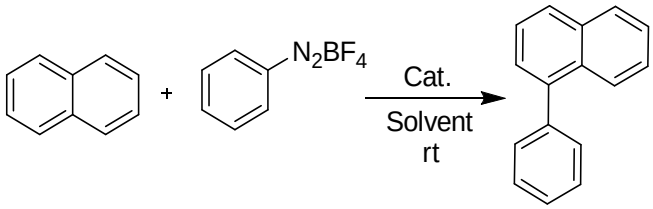

Figure 5.9. Scheme of model reaction studied in this Chapter.

Very briefly, 1 mmol of the freshly synthetized diazonium salt was mixed with 0.33 mmol of the arene in acetone in the presence of the graphene-based catalyst (GO-PDA-Fc or GA-PDA-Fc). Since the efficiency of Fc grafting on the two graphene supports is different, the amount of catalyst to be employed was based according to the EDX measurements. In this way, the same amount of the molecular species was present in the reaction ambient (1.6 mol%) and, therefore, the comparison of the catalytic activity can provide information about the role of the graphene support during the reaction and the chemical and structural differences detected during the characterization steps. The catalytic tests were carried out at rt without protecting atmosphere. The selected experimental conditions, such as the solvent or the diazonium/arene ratio were previously optimized to achieve the highest coupling yield, as showed in in Figure 5.10.[49]

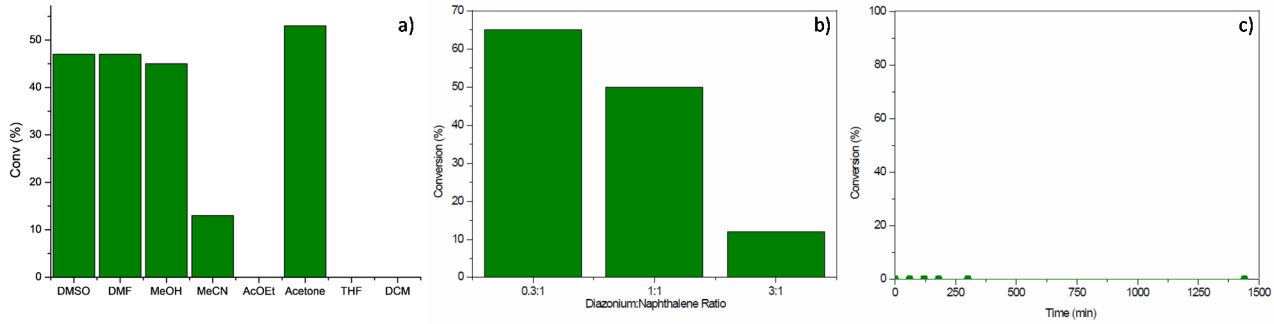

Figure 5.10. a) Solvent optimization in 16 h reaction runs catalyzed by GA-PDA-Fc. b) Diazonium salt:Naphthalene ratio optimization and c) temporal evolution of benzenediazonium salt in the presence of GA-PDA-Fc.

In addition, blank tests with the diazonium salt and the catalyst were carried out. No evolution of the diazonium salt was observed without the arene substrate in the reaction medium while running these blank experiments. To monitor the progress of the reaction, small aliquots of the reaction solution were sampled

at regular intervals and analyzed by NMR spectroscopy. The reaction proceeds smoothly for both GO-PDA-Fc and GA-PDA-Fc heterogenized catalysts, without any induction period, yielding the C-H insertion product, 1-phenylnaphtalene, with high selectivity (no byproducts were detected during the whole duration of the reaction). This chemical conversion can be easily followed through NMR spectroscopy, by monitoring the disappearance of the up-shielded naphthalene multiplets at ~ δ 7.8-7.6 ppm (see Figure 5.11) and the increase of the down-shielded signals at ~ δ 6.8–6.6 ppm, which correspond to the condensed product in the reaction crude.

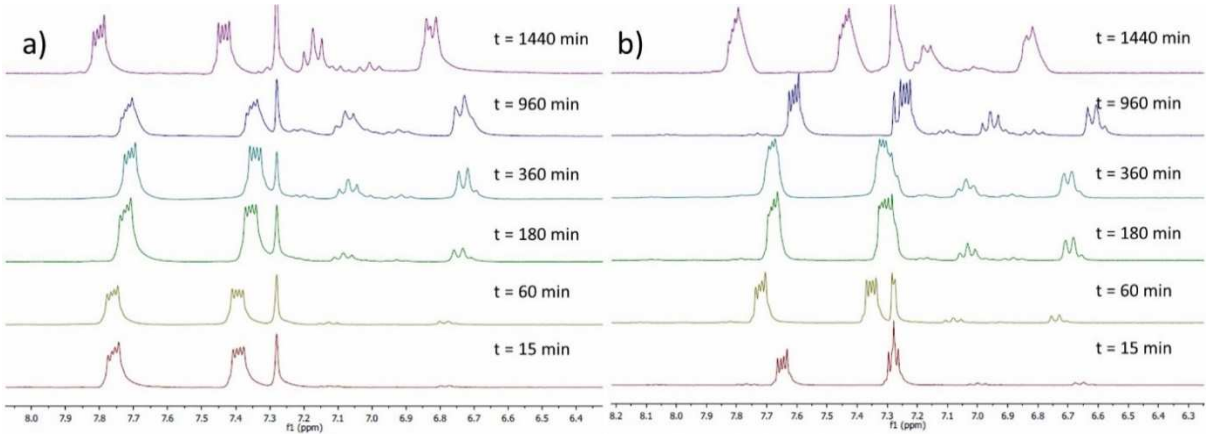

Figure 5.11. Selection of region of interest in the ^{1}H-NMR ($CDCl_3$, 298 K) spectra used for monitoring the C-H insertion catalysed by a) GA-PDA-Fc and b) GO-PDA-Fc.

By using the NMR spectra taken at regular intervals to monitor the progress of the reaction, we were able to construct kinetic profiles for analyzing and comparing the catalytic performance for different catalysts (see Figure 5.12). While a non-Fc-containing sample (i.e. kinetic blank experiment), based on pristine GA, did not show any catalytic activity as expected, the Fc-derivatized graphene materials were found to be good catalysts. In fact, a remarkable production of 210 µmol of 1-phenylnaphthalene in approximately 30 h was achieved by GA-PDA-Fc following a second order kinetic model with respect to the arene substrate (Figure 5.12 inset), with a productivity in terms of turnover number (TON) and turnover frequency at the beginning of the reaction (TOF_0) of 42 and 506.1 h^{-1}, respectively (see Table 5.4). In contrast, its GO-PDA-Fc counterpart can produce only 150 µmol in the same time (with TON = 32 and TOF = 134.0 h^{-1}, also following a second order kinetics with respect to the arene substrate). Increasing the reaction time up to 48 h did not result in any increase of conversion for both materials.

	µmol[a]	***Time[b]***	***TON***	***TOF_0[c]***	***k[d]***
GA-PDA-Fc	211	30	42	506.1	11.2
GO-PDA-Fc	150	30	33	134.0	6.5
Fc	214	30	43	519.8	10.1

a) 1-phenylnaphthalene production (µmol), determined by NMR spectroscopy; b) h; c) h^{-1}, calculated after 15 min of reaction; d) kinetic constant (10^{-3} M^{-1} min^{-1})

Table 5.4. Catalytic parameters for arene insertion reaction.

The comparison of the activity of the heterogenized catalyst with molecular Fc under the same experimental conditions shows that all materials have a very similar performance and kinetics. In fact, molecular Fc produces 215 µmol of 1-phenylnaphthalene in 30 h (TON = 43 and TOF_0 = 519.8 h^{-1}), and saturation is reached already after about 30 h. Therefore, all the covalently-grafted Fc moieties on GA act as catalytic active centers due to the very similar behavior observed when comparing the homogeneous and heterogeneous materials.

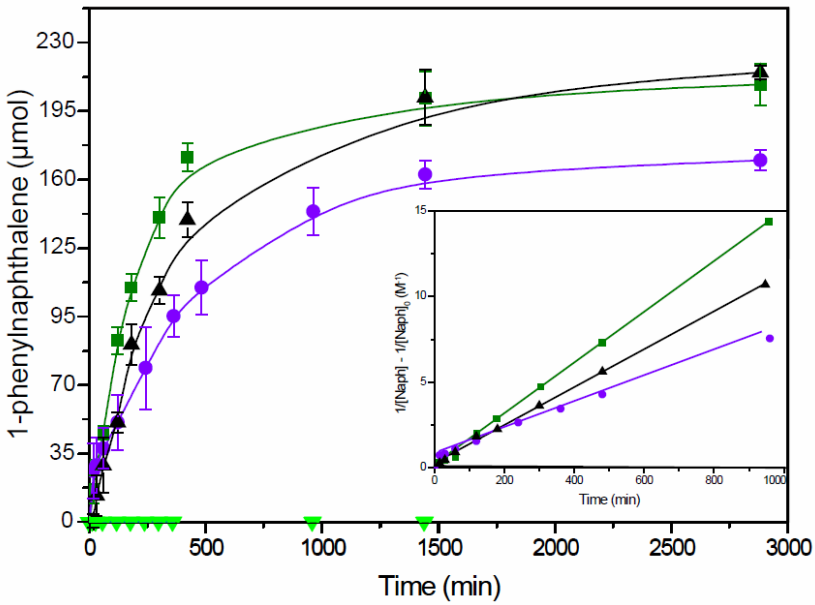

Figure 5.12. Kinetic profiles for the C-H insertion reaction catalyzed by GA-PDA-Fc (green), GO-PDA-Fc (violet), molecular Fc (black) and pristine GA (light green). Inset: kinetics analysis showing the second order dependence on the concentration of the arene substrate.

However, to shed more light on the nature of the active sites, another set of control experiments was performed (see Figure 5.13). Since small amounts of physisorbed Fc on both the graphenic scaffolds were detected, the physical mixture of ferrocene and graphenic materials was also tested as catalyst of the C-H insertion. The results indicate a difference compared with the covalently functionalized samples, since 192 µmol of 1-phenylnaphthalene were produced indistinctly by GA+Fc or GO+Fc catalysts after 24 h of reaction. Therefore, the physical mixture behaves identically to the molecular ferrocene (see Figure 5.12). This observation suggests that the physisorbed molecules do not have any positive or detrimental effect on the catalytic activity, indicating that there might not be any specific interactions between the bare Fc molecules and the support. This result is, however, in contrast with the previously discussed data, highlighting the importance of anchoring the homogeneous catalysts in a specific environment for controlling the activity. On the other hand, different Fe(II)/Fe(III) ratios were detected by XPS on both GO-PDA-Fc and GA-PDA-Fc. Thus, the C-H insertion was attempted with mixtures of Fc/Fc^+ in solution under the same standard reaction conditions. It is known that both members of these redox couple are capable of independently promote radical reactions;[50] therefore, it is not surprising to obtain the same conversion result employing different molar ratios of Fc/Fc^+ but working with the same overall 1.6 mol% iron concentration. Furthermore, molecular oxygen is not involved in the radical activation since no differences were observed between catalytic tests performed in inert or air atmosphere. Thus, the Fe(III) units present at our catalysts surfaces may also act as active centers in analogy to the homogeneous catalytic tests.

Therefore, the differences observed between the performances of GA and GO must be ascribed to their peculiar structural properties, and in particular to some subtle differences in the local environment that the immobilized Fc species experience on the support surface. The mechanism of the C-H insertion reaction consists of an electron transfer from the Fc unit to the diazonium salt, followed by the formation of the radical that allows the coupling reaction with the arene. In the final step, the Fc unit is eventually restored by a H-abstraction from the coupling product.[24] However, different trends were observed in the early stages of the reaction, when higher conversion rates were observed for the GA-PDA-Fc comparing to the other systems, for example. According to the characterization data presented above, especially the XPS measurements, the amount of sp^2 C-C bonds is higher in the GA compared to the GO. In addition, GO owns the carboxylic acids, which are the anchoring points for the Fc units, mostly on the nanosheet edges, while in the GA they can be found on the basal plane amid C sp^2 domains. Therefore, the adsorption of the aromatic substrates on the GA-based catalyst surface might be strongly favored, which means that the immobilized Fc units have a larger availability of reagents, thus accelerating the reaction in terms of TON, TOF and kinetic values at the first steps of the reaction (see Table 5.4). Furthermore, both theoretical[51] and electrochemical data suggest that electron transfer processes, which are also critical elementary steps of the C-H insertion reaction, are highly facilitated on GA compared to GO. Finally, the higher amount of oxidized iron species in the GO sample could also decrease the catalytic activity compared to GA.

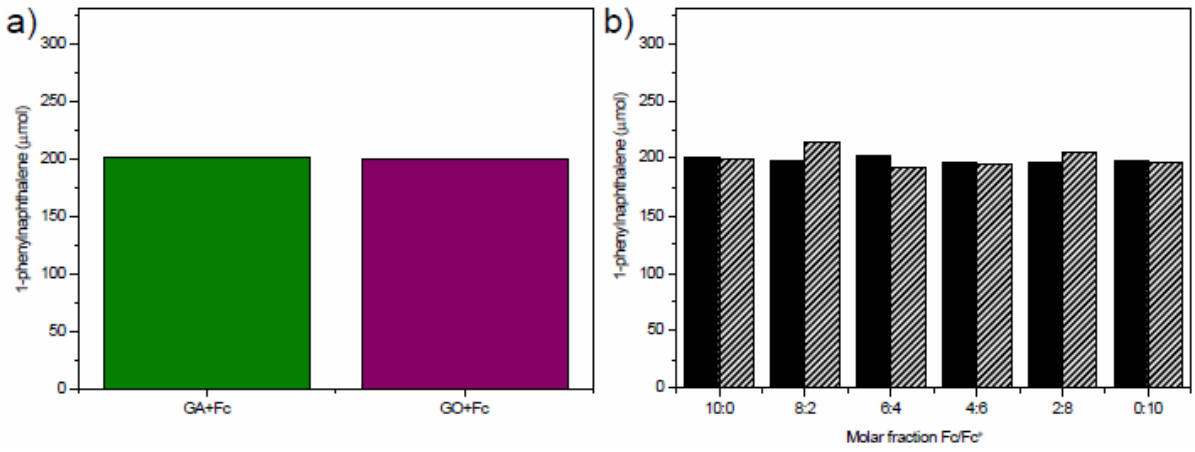

Figure 5.13. a) Catalytic activity of the physical mixture of GX and Fc on the C-H insertion (green: GA, purple: GO), b) Catalytic activity of the Fc/Fc^+ mixtures on the C-H insertion under air (solid) and inert (dashed) atmosphere. All tests have 24 h duration.

We have also evaluated the general activity of the catalysts in the C-H insertion by employing different substrates, in particular testing arenes with an increasing number of condensed rings, such as anthracene and pyrene. In this case, the reaction time was 24 h and the catalytic activity was monitored as previously. The main figures of the catalytic activity in the C-H insertion reaction are summarized in Figure 5.14. Remarkably, compared to the previous model reaction involving naphthalene, the GA-PDA-Fc clearly stands out among other materials as a superior catalyst. In fact, when anthracene is used as substrate (330 µmol), full conversion to 1-phenylantracene is reached in 24 h, whereas starting with pyrene, 270 µmol of 1-phenylpyrene (82% conversion) are produced in about 24 h. In contrast, GO-PDA-Fc shows a poorer performance confirming the trend of the model reaction. In fact, only 209 µmol of 1-phenylanthracene and

131 µmol of 1-phenylpyrene were produced in 24 h. In both cases, the reaction was fully selective to the insertion in the position 1 of the arene substrate, as determined by NMR analysis (see section 5.3.3). Surprisingly, the results for molecular Fc were worse than those for the heterogenized catalysts. The molecular catalyst was able to yield 208 µmol of 1-phenylanthracene and 109 µmol of 1-phenylpyrene in 24 hours, as determined by NMR spectroscopy. The worse performance of Fc with the increasing number of condensed rings in the substrate was also noted in the literature: Dixit *et al.* reported 56 % conversion employing naphthalene, 42 % with anthracene and 21 % with pyrene in C-H insertions catalyzed by 10 mol% of molecular Fc.[24] These values confirm our trend and highlights the superior catalytic performance when the Fc is heterogenized on both types of graphenic supports. The better performance of GO and especially of GA with respect to molecular Fc is likely ascribed to the easy absorption of the catalytic substrate on the graphenic supports (especially GA), as also demonstrated by the adsorption experiments (see Figure 5.15).

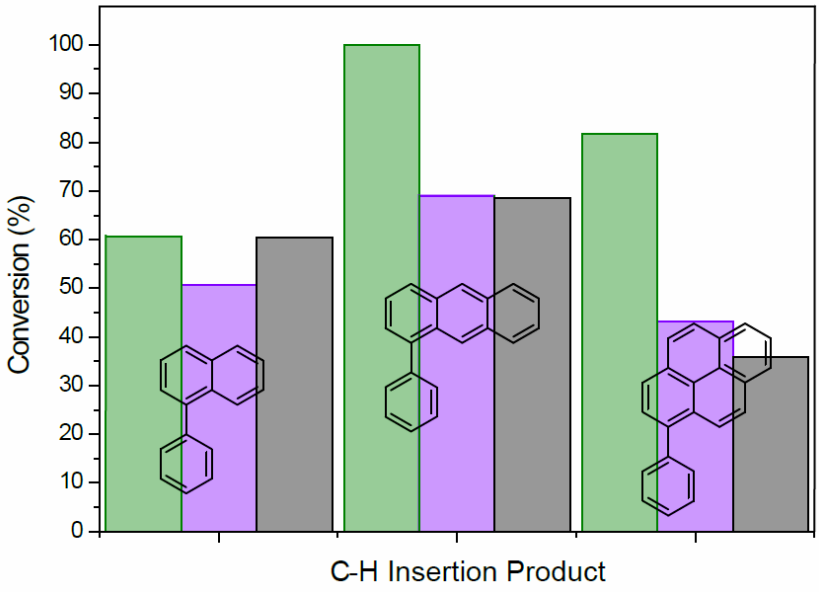

Figure 5.14. Scope studies in the C-H insertion catalysed by GA-PDA-Fc (green), GO-PDA-Fc (violet) and molecular Fc (black).

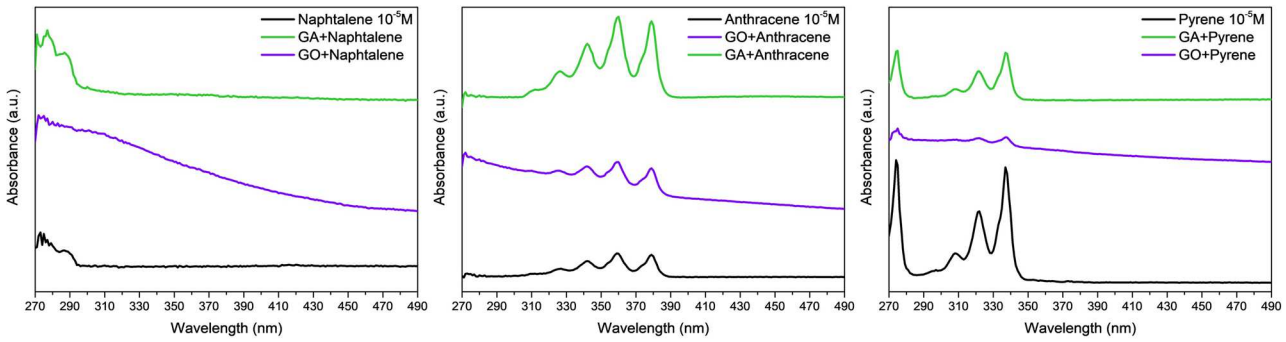

Figure 5.15. Arene adsorption experiments by UV-Vis. Left: naphthalene, middle: anthracene, right: pyrene. For all curves: black: arene, green: GA, purple: GO; absorbance is not normalized.

Finally, we tested the recyclability on the heterogenized systems. After saturation conversion, we recovered the samples by several cycles of centrifugation and rinse with acetone. Then, the catalysts were submitted to a new working cycle in the BDT insertion. This procedure was repeated 8 times using naphthalene as reaction substrate, and the results are depicted in Figure 5.16.

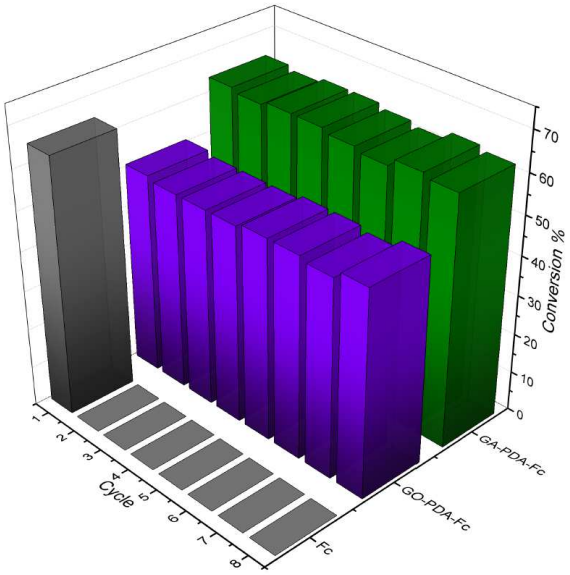

Figure 5.16. Study of the catalytic performance of the Fc-based catalysts (green: GA-PDA-Fc, violet: GO-PDA-Fc, black: molecular Fc) during increasing catalytic and recovery cycles

For the heterogeneous materials, we detected the same conversion value as a function of time for each reaction cycle, while the molecular Fc catalyst was obviously impossible to recover, thus emphasizing the manifest recyclability and durable catalytic performance of the covalently-modified graphene materials. In addition, another UV-Vis analysis was performed on the recovered materials (see Figure 5.17a) showing no modification in the optical behavior of both GA-PDA-Fc and GO-PDA-Fc with respect to the materials before the catalytic work, while negligible leaching of iron was detected by EDX (see Table 5.3). However, any modification in the materials structure could be detected by Raman Spectroscopy (see Figure 5.17b) since for both GA-PDA-Fc and GO-PDA-Fc the same Raman features were observed before and after the catalytic tests.

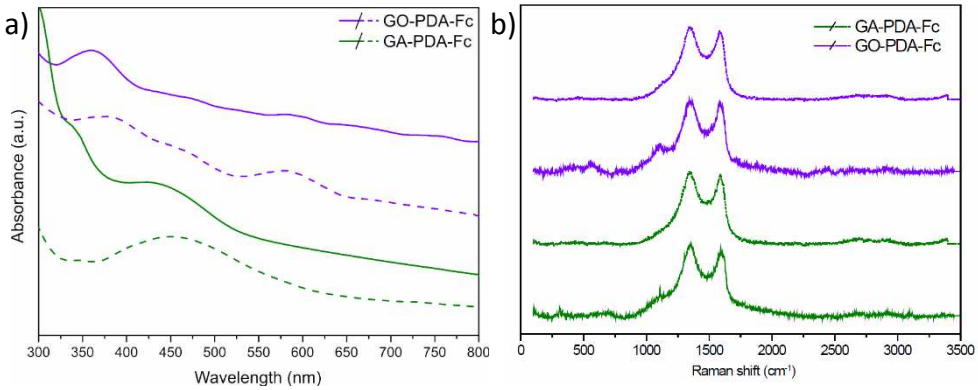

Figure 5.17. UV-Vis (a) and Raman (b) spectra after the catalytic work (dashed lines), compared to the fresh samples (continuous lines) (green: GA-PDA-Fc, violet: GO-PDA-Fc).

5.3.3 NMR data for isolated organic compounds

Benzenediazonium tetrafluoroborate: Prepared according to the general procedure.

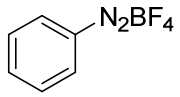

^{1}H NMR (300.1 MHz, DMSO-d_6, δ ppm): 8.67 (d, J = 8.0 Hz, 2H), 8.26 (t, J = 7.7 Hz, 1H), 7.99 (t, J = 7.4 Hz, 2H).

1-phenylnaphthalene: Prepared according to the general procedure.

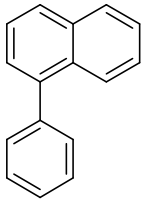

^{1}H NMR (300.1 MHz, DMSO-d_6, δ ppm): 8.95 (d, J = 8.4 Hz, 1H), 8.50 (d, J = 8.1 Hz, 1H), 8.20 (t, J = 8.3 Hz, 1H), 8.09 (t, J = 8.1 Hz, 1H), 7.78 (m, 3H), 7.49 (m, 3H), 7.40 (m, 2H).

1-phenylanthracene: Prepared according to the general procedure.

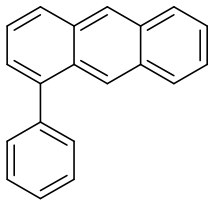

^{1}H NMR (300.1 MHz, DMSO-d_6, δ ppm): 8.61 (m, 1H), 8.31 (d, J = 8.1 Hz, 1H), 8.12 (t, J = 8.3 Hz, 1H), 8.09 (t, J = 8.1 Hz, 1H), 7.95 (m, 1H), 7.79 (t, J = 8.1 Hz, 2H), 7.55 (m, 3H), 7.43 (m, 4H).

1-phenylpyrene: Prepared according to the general procedure.

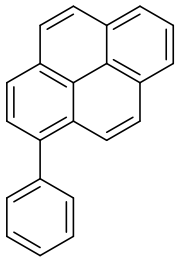

^{1}H NMR (300.1 MHz, DMSO-d_6, δ ppm): 8.51 (d, J = 8.4 Hz, 1H), 8.29 (d, J = 8.1 Hz, 1H), 8.14 (m, 1H), 8.06 (m, 4H), 7.94 (d, J = 8.2 Hz, 1H), 7.74 (m, 3H), 7.43 (m, 3H).

5.4 Conclusions

The covalent functionalization of graphene acid with Fc has been accomplished employing the carbodiimide chemistry. Graphene oxide was also tested in the same experimental conditions as standard oxidized graphenic benchmark for comparison. While the functionalization was confirmed by several independent techniques, the quite precise surface chemistry of the GA, which selectively exposes a high density of carboxylic groups on the basal plane, yielded a higher functionalization degree (3.9 at.% of Fe) of mainly pure Fe(II) ferrocene. On the contrary, the functionalization efficiency on standard graphene oxide was poorer, (0.8 at.% of Fe), probably because of the presence of a wide gamut of surface oxygen species with a variable chemical reactivity, thus limiting the control over functionalization.

Both Fc-modified materials were found to be active and easily recyclable catalysts in the C-H insertion reaction of benzenediazonium tetrafluoroborate on naphthalene. Notably, GA-PDA-Fc sample catalyzed the production of the same amount of 1-phenylnaphthalene as compared to molecular ferrocene, which means that all the iron centers covalently attached on the GA surface behave as active sites. Furthermore, both heterogenized catalysts presented an extended scope, being able to catalyze the C-H insertion using anthracene and pyrene as substrates. In every reaction, the GA-based catalyst achieved a higher production of the insertion product compared to the GO-based sample. The well-defined structure of GA with precise functionalities and higher aromatic content, allowing efficient adsorption of the reagents close to the active centers combined with superior electron conductivity, are likely responsible for the higher catalytic activity than that of the GO analogue.

References

(1) Cole-Hamilton, D. J. Homogeneous Catalysis—New Approaches to Catalyst Separation, Recovery, and Recycling. *Science* **2003**, *223*, 1702–1706.

(2) Peng Peng; Schmidt, R. R. Acid–Base Catalysis in Glycosidations: A Nature Derived Alternative to the Generally Employed Methodology. *Acc. Chem. Res.* **2017**, *50*, 1171–1183.

(3) Morris, R. H. Exploiting Metal–Ligand Bifunctional Reactions in the Design of Iron Asymmetric Hydrogenation Catalysts. *Acc. Chem. Res.* **2015**, *48*, 1494–1502.

(4) Rouhi, A. M. Suzuki-Coupling Chemistry Takes Hold in Commercial Practice, from Small-Scale Synthesis of Screening Compounds to Industrial Production of Active Ingredients. *Chem. Eng. News* **2004**, *82*, 49–58.

(5) Coperet, C.; Comas-Vives, A.; Conley, M. P.; Estes, D. P.; Fedorov, A.; Mougel, V.; Nagae, H.; Nunez-Zarur, F.; Zhizhko, P. A. Surface Organometallic and Coordination Chemistry toward Single Site Heterogeneous Catalysts: Strategies, Methods, Structures, and Activities. *Chem. Rev.* **2016**, *116*, 323–421.

(6) Yan-Li Zhao; Stoddart, J. F. Noncovalent Functionalization of Single-Walled Carbon Nanotubes. *Acc. Chem. Res.* **2009**, *42*, 1161–1171.

(7) Tasis, D.; Tagmatarchis, N.; Bianco, A.; Prato, M. Chemistry of Carbon Nanotubes. *Chem. Rev.* **2006**, *106*, 1105–1136.

(8) Lee, J.-Y.; Farha, O. K.; Roberts, J.; Scheidt, K. A.; Nguyen, S.-B. T.; Hupp, J. T. Metal-Organic Framework Materials as Catalysts. *Chem. soc. Rev.* **2009**, *38*, 1450–1459.

(9) Antolini, E. Carbon Supports for Low-Temperature Fuel Cell Catalysts. *Appl. Catal. B Enviromental* **2009**, *88*, 1–24.

(10) Mandal, S.; Roy, D.; Chaudhari, R. V.; Sastry, M. Pt and Pd Nanoparticles Immobilized on Amine-Functionalized Zeolite: Excellent Catalysts for Hydrogenation and Heck Reactions. *Chem. Mater.* **2004**, *16*, 3714–3724.

(11) Chen, C.; Yeh, Y.-H.; Cargnello, M.; Murray, C. B.; Fornasiero, P.; Gorte, R. J. Methane Oxidation on $Pd@ZrO_2/Si{-}Al_2O_3$ Is Enhanced by Surface Reduction of ZrO_2. *ACS Catal.* **2014**, *4*, 3902–3909.

(12) D. Carta; T. Montini; M. F. Casula; M. Monai; S. Bullita; P. Fornasiero; Corrias, A. The Water Gas Shift Reaction over Pt–CeO2 Nanoparticles Confined within Mesoporous SBA-16. *J. Mater. Chem. A* **2017**, *5*, 20024–20034.

(13) E. Rangel Rangel; E. M. Maya; F. Sánchez; J. G. de la Campa; Iglesias, M. Palladium-Heterogenized Porous Polyimide Materials as Effective and Recyclable Catalysts for Reactions in Water. *Green Chem.* **2015**, *17*, 466–473.

(14) M. Blanco; P. Álvarez; C. Blanco; M.V. Jiménez; J. Fernández-Tornos; J.J. Pérez-Torrente; L.A. Oro; J. Blasco; G. Subías; V. Cuartero; Menéndez, R. Effect of Structural Differences of Carbon Nanotubes and Graphene Based Iridium-NHC Materials on the Hydrogen Transfer Catalytic Activity. *Carbon N. Y.* **2016**, *96*, 66–74.

(15) A. H. Castro Neto; F. Guinea; N. M. R. Peres; K. S. Novoselov; Geim, A. K. The Electronic Properties of Graphene. *Rev. Mod. Phys.* **2009**, *81*, 109–162.

(16) Balandin, A. A. Thermal Properties of Graphene and Nanostructured Carbon Materials. *Nat. Mater.* **2011**, *10*, 569–581.

(17) Akhavan, O.; Ghaderi, E. Toxicity of Graphene and Graphene Oxide Nanowalls against Bacteria. *ACS*

Nano **2010**, *4* (10), 5731–5736.

(18) Chen, D.; Feng, H.; Li, J. Graphene Oxide: Preparation, Functionalization, and Electrochemical Applications. *Chem. Rev.* **2012**, *112* (11), 6027–6053.

(19) Marcano, D. C. D.; Kosynkin, D. D. V.; Berlin, J. M. J.; Sinitskii, A.; Sun, Z.; Slesarev, A.; Alemany, L. B.; Lu, W.; Tour, J. M. Improved Synthesis of Graphene Oxide. *ACS Nano* **2010**, *4* (8), 4806–4814.

(20) Bakandritsos, A.; Pykal, M.; Boński, P.; Jakubec, P.; Chronopoulos, D. D.; Poláková, K.; Georgakilas, V.; Čépe, K.; Tomanec, O.; Ranc, V.; Bourlinos, A. B.; Zbořil, R.; Otyepka, M. Cyanographene and Graphene Acid: Emerging Derivatives Enabling High-Yield and Selective Functionalization of Graphene. *ACS Nano* **2017**, *11* (3), 2982–2991.

(21) S. Martic P.O. Shipman, H.B. Kraatz, M. L. Ferrocene-Peptido Conjugates: From Synthesis to Sensory Applications. *Dalt. Trans.* **2011**, *40*, 7264–7290.

(22) Fan, L.; Zhang, Q.; Wang, K.; Li, F.; Niu, L. Ferrocene Functionalized Graphene: Preparation, Characterization and Efficient Electron Transfer toward Sensors of H_2O_2. *J. Mater. Chem.* **2012**, *22*, 6165–6170.

(23) Wu, S.; Chen, Y.; Zeng, F.; Gong, S.; Tong, Z. Electron Transfer in Ferrocene-Containing Functionalized Chitosan and Its Electrocatalytic Decomposition of Peroxide. *Macromolecules* **2006**, *39*, 6796–6799.

(24) Dixit, S.; Siddiqui, Q. T.; Muneer, M.; Agarwal, N. Ferrocene Catalysed C–H Arylation of Arenes and Reaction Mechanism Study Using Cyclic Voltammetry. *Tetrahedron Lett.* **2016**, *57*, 4228–4231.

(25) Blanco, M.; Álvarez, P.; Blanco, C.; Jiménez, M. V.; Fernández-Tornos, J.; Pérez-Torrente, J. J.; Oro, L. A.; Menéndez, R. Enhanced Hydrogen-Transfer Catalytic Activity of Iridium N-Heterocyclic Carbenes by Covalent Attachment on Carbon Nanotubes. *ACS Catal.* **2013**, *3*, 1307–1317.

(26) Carraro, F.; Calvillo, L.; Cattelan, M.; Favaro, M.; Righetto, M.; Nappini, S.; Píš, I.; Celorrio, V.; Fermín, D. J.; Martucci, A.; Agnoli, S.; Granozzi, G. Fast One-Pot Synthesis of MoS_2/Crumpled Graphene p-n Nanonjunctions for Enhanced Photoelectrochemical Hydrogen Production. *ACS Appl. Mater. Interfaces* **2015**, *7* (46), 25685–25692.

(27) Hanson, P.; Jones, J. R.; Taylor, A. B.; Walton, P. H.; Timms, A. W. Sandmeyer Reactions. Part 7. An Investigation into the Reduction Steps of Sandmeyer Hydroxylation and Chlorination Reactions. *J. Chem. Soc., Perkin Trans* **2002**, *2*, 1135–1150.

(28) Sahoo, N. G.; Bao, H.; Pan, Y.; Pal, M.; Mitali Kakran, M.; Feng Cheng, H. K.; Li, L.; Tan, L. P. Functionalized Carbon Nanomaterials as Nanocarriers for Loading and Delivery of a Poorly Water-Soluble Anticancer Drug: A Comparative Study. *Chem. Commun.* **2011**, *47*, 5235–5237.

(29) Yan, L.; Gu, Z.; Zheng, X.; Zhang, C.; Li, X.; Zhao, L.; Zhao, Y. Elemental Bismuth–Graphene Heterostructures for Photocatalysis from Ultraviolet to Infrared Light. *ACS Catal.* **2017**, *7* (10), 7043–7050.

(30) Paira, T. K.; Saha, A.; Banerjee, S.; Das, T.; Das, P.; Jana, N. R.; Mandal, T. K. Fluorescent Amphiphilic PEG-Peptide-PEG Triblock Conjugate Micelles for Cell Imaging. *Macromol. Biosci. Banner* **2014**, *14* (7), 929–935.

(31) Favaro, M.; Agnoli, S.; Di Valentin, C.; Mattevi, C.; Cattelan, M.; Artiglia, L.; Magnano, E.; Bondino, F.; Nappini, S.; Granozzi, G. TiO_2/Graphene Nanocomposites from the Direct Reduction of Graphene Oxide by Metal Evaporation. *Carbon N. Y.* **2014**, *68*, 319–329.

(32) R. Zanoni; F. Cattaruzza; C. Coluzza; E. A. Dalchiele; F. Decker; G. Di Santo; A. Flamini; L. Funari; Marrani, A. G. An AFM, XPS and Electrochemical Study of Molecular Electroactive Monolayers Formed by Wet Chemistry Functionalization of H-Terminated Si (100) with Vinylferrocene. *Surf. Sci.* **2005**, *575*, 260–272.

(33) Cattaruzza, F.; Llanes-Pallas, A.; Andrea G. Marrani, A. G.; Dalchiele, E. A.; Decker, F.; Zanoni, R.; Prato, M.; Bonifazi, D. Redox-Active Si(100) Surfaces Covalently Functionalised with [60]Fullerene Conjugates: New Hybrid Materials for Molecular-Based Devices. *J. Mater. Chem.* **2008**, *18*, 1570–1581.

(34) Fortgang, P.; Tite, T.; Barnier, V.; Zehani, N.; Maddi, C.; Lagarde, F.; Loir, A.-S.; Jaffrezic-Renault, N.; Donnet, C.; Garrelie, F.; Chaix, C. Robust Electrografting on Self-Organized 3D Graphene Electrodes. *ACS Appl. Mater. Interfaces* **2016**, *8*, 1424–1433.

(35) Dey, R. S.; Raj, C. R. Redox-Functionalized Graphene Oxide Architecture for the Development of Amperometric Biosensing Platform. *ACS Appl. Mater. Interfaces* **2013**, *5*, 4791–4798.

(36) Rabti, A.; Mayorga-Martinez, C. C.; Baptista-Pires, L.; Raouafi, N.; Merkoçi, A. Ferrocene-Functionalized Graphene Electrode for Biosensing Applications. *Anal. Chim. Acta* **2016**, *929*, 28–35.

(37) Fernández-García, L.; Blanco, M.; Blanco, C.; Álvarez, P.; Granda, M.; Santamaría, R.; Menéndez, R. Graphene Anchored Palladium Complex as Efficient and Recyclable Catalyst in the Heck Cross-Coupling Reaction. *J. Mol. Cat. A* **2016**, *416*, 140–146.

(38) Gao, Y.; Hu, G.; Zhang, W.; Ma, D.; Bao, X. P–p Interaction Intercalation of Layered Carbon Materials with Metallocene. *Dalt. Trans.* **2011**, *40*, 4542–4547.

(39) Gatti, T.; Manfredi, N.; Boldrini, C.; Lamberti, F.; Abbotto, A.; Menna, E. A D-π-A Organic Dye – Reduced Graphene Oxide Covalent Dyad as a New Concept Photosensitizer for Light Harvesting Applications. *Carbon N. Y.* **2017**, *115*, 746–753.

(40) Guarracino, P.; Gatti, T.; Canever, N.; Abdu-Aguye, M.; Loi, M. A.; Menna, E.; Franco, L. Probing Photoinduced Electron-Transfer in Graphene–dye Hybrid Materials for DSSC. *Phys. Chem. Chem. Phys* **2017**, *19*, 27716–27724.

(41) Sixt, T.; Fiedler, J.; Kaim, W. Iron versus Ruthenium Oxidation in 1,19-Bis(Diphenylphosphino)Ferrocene–ruthenium(II) Complexes: EPR and Spectroelectrochemical Evidence. *Inorg. Chem. Commun.* **2000**, *3*, 80–82.

(42) Cowan, D. O.; Kaufman, F. The Organic Solid State. Electron Transfer in a Mixed Valence Salt of Biferrocene. *J. Am. Chem. Soc.* **1976**, *92*, 219–220.

(43) Bard, A. J.; Faulkner, L. R.; Harris, D.; Robey, C.; Aiello, E.; Swain, E. *Electrochemical Methods: Fundamentals and Applications*, 2nd ed.; Ed. John Wiley & Sons, Inc, 2001.

(44) Kohmoto, M.; Ozawa, H.; Yang, L.; Hagio, T.; Matsunaga, M.; Haga, M. Controlling the Adsorption of Ruthenium Complexes on Carbon Surfaces through Noncovalent Bonding with Pyrene Anchors: An Electrochemical Study. *Langmuir* **2016**, *32*, 4141–4152.

(45) Verbelen, B.; Boodts, S.; Hofkens, J.; Boens, N.; Dehaen, W. Radical C-H Arylation of the BODIPY Core with Aryldiazonium Salts: Synthesis of Highly Fluorescent Red-Shifted Dyes. *Angew. Chem. Int. Ed.* **2015**, *127*, 4695–4699.

(46) Verbelen, B.; Valckenborgh, M.; Inclán, M.; Nebot, A.; Dehaen, W. Efficient Two-Step Synthesis of Water Soluble BODIPY–TREN Chemosensors for Copper(II) Ions. *RSC Adv.* **2017**, *7*, 3066–3071.

(47) Sirbu, D.; Benniston, A. C.; Harriman, A. One-Pot Synthesis of a Mono-O,B,N-Strapped BODIPY Derivative Displaying Bright Fluorescence in the Solid State. *Org. Lett.* **2017**, *19*, 1626–1629.

(48) Mo, F.; Dong, G.; Zhang, Y.; Wang, J. Recent Applications of Arene Diazonium Salts in Organic Synthesis. *Org. Biomol. Chem.* **2013**, *11*, 1582–1593.

(49) Hari, D. .; Schroll, P.; König, B. Metal-Free, Visible-Light-Mediated Direct C–H Arylation of Heteroarenes with Aryl Diazonium Salts. *J. Am. Chem. Soc.* **2012**, *134*, 2958–2961.

(50) Rossi, R. A.; Pierini, A. B.; Peñéñory, A. B. Nucleophilic Substitution Reactions by Electron Transfer.

Chem. Rev. **2003**, *103* (1), 71–167.

(51) Robinson, J. T.; Burgess, J. S.; Junkermeier, C. E.; Badescu C., S.; Reinecke, T. L.; Perkins, F. K.; Zalalutdniov, M. K.; Baldwin, J. W.; Culbertson, J. C.; Sheehan, P. E.; Snow, E. S. Properties of Fluorinated Graphene Films. *Nano Lett.* **2010**, *10*, 3001–3005.

Chapter Six:

Homo- and cross-coupling palladium nanoparticles – graphene acid system as stable and recyclable bifunctional green catalyst

6.1 Introduction

According to the Green Chemistry principles,[1] the design of heterogeneous multifunctional and selective catalysts is considered as a crucial step for developing sustainable and efficient processes. Thus, a rational knowledge-based approach has to be undertaken in order to avoid the empirical *trial & error* strategy, which has so far dominated the scene of catalysis research.

Especially when Platinum Group Metal (PGMs)-based homogeneous catalysts have to be heterogenized on a support, great efforts on the optimization of metal loading are necessary in order to reduce as much as possible the wasting of precious resources and the release of toxic byproducts. In this respect, it is crucial the right choice of the support where to graft the catalytic site, which is obviously dictated by the chemical properties of both the catalyst and the support.[2]

One much explored support for heterogenized catalysts suitable for innovative chemical processes is graphene: its outstanding properties in terms of electric/electronic conductivity, mechanical strength and chemical stability[3–5] can be combined with the catalytic properties of PGMs derivatives. Among them, Palladium, with its different chemical states,[6] represents a really appealing system to couple with graphenic supports. In such a way, the polluting problems associated with palladium residues[7] can be avoided when supported on an eco-friendly material.[8] The literature is full of reports where researchers explore the combination of graphene-based supports and Pd, in form of atomic[9] or molecular moieties,[10] thin-film depositions[11] or even metallic dots, with diameters ranging from big clusters (less than 2 nm)[12] to big nanoparticles (80-100 nm).[13] However, to the best of our knowledge, details regarding the growth mechanisms of Pd on graphene based supports are still lacking. It is highly probable that surface oxygen groups present in graphene oxide (GO) or partially reduced GO might play a role. In order to shed light about this fundamental question, we have studied graphene acid (GA), i.e., a graphene sheet strongly decorated with COOH in the basal plane,[14] to follow the evolution of Pd nanosystems on a well characterized support. Actually, the well uniform surface composition of GA can contribute to understand the chemical interactions involved during the nucleation and growing stages of the supported Pd nanosystems.

Among the large set of transformations that Pd is able to catalyse, the Suzuki-Miyaura reaction is one of the most exploited by synthetic chemists: it is generally defined as the transition-metal-catalyzed cross-coupling between an organo-boron compound and an organic halide and has become one of the most attractive approach since its discovery in 1979. Such reaction can produce the C-C coupling in a large set of experimental conditions, including reactions in water.[15] In this case such a quite unique economical and environmental-friendly solvent can also enhance the activity and selectivity of the catalyst by solvation effects, providing a suitable green route.[16,17] Actually, graphene-Pd hybrid systems have already been reported to have activity on the cross-coupling of boronic acids with different halides, demonstrating good catalytic performance with high stability, cyclability and versatility, even working under green conditions.[18] Other authors, however, reported the synthesis of homo-coupling catalysts of boronic acids instead of the cross-coupling ones.[19] Thus, the employment of graphene-Pd hybrids has been considered a valid strategy for preventing the utilization of the classical Pd complex ($[Pd(PPh_3)_4]$, $[Pd(PPh_3)_2Cl_2]$ or $Pd(OAc)_2$ among other examples[20]).
Herein, we present a preliminary and not yet finalized work on the use of GA as a possible platform to heterogenize a classical Pd precursor (i.e. $Pd(OAc)_2$) in form of narrow distribution of metallic Pd

nanoparticles. We show that the controlled surface of GA (rich of –COOH groups) participates actively in the nucleation-growth process of Pd nanoparticles and some hints on the mechanism for this process can be advanced. Furthermore, we find that our GA-Pd system is able to perform the aforementioned reactions in environmentally friendly conditions (in water without phosphines and organic bases) with a simple control of the reagents involved. As a result of this study, a high selectivity and an activity comparable to the literature values are obtained with a good recyclability of the heterogenized catalyst as well. Moreover, Pd leaching is not observed. Thus this preliminary study suggests that the GA-Pd is promising as a multifunctional, sustainable and efficient homo-coupling and cross-coupling catalyst.

6.2 Experimental Section

Graphenic materials synthesis

GA was synthetized by our collaborators in Otyepka research group, following the procedure described in reference and reported below.[14]

To obtain the intermediate Cyanographene (G-CN), Fluorinated graphite (120 mg, ~4 mmol of C-F units) was added to 15 mL of DMF and sonicated (Bandelin Sonorex, DT 255H type, frequency 35 kHz, power 640 W, effective power 160 W) for 4 h under nitrogen atmosphere in a 25 mL round-bottom glass flask. Then 800 mg of NaCN (~16 mmol) was added and the mixture was heated at 130 °C with a condenser under stirring (500 rpm). Sample aliquots were withdrawn from the flask at different time points to monitor the reaction progress. Further experiments were performed on the product treated for 24 h. Intermediates and final product were left to cool to room temperature, after which an equal amount of acetone was added.

The materials were then separated by centrifugation and further purified by successive washing steps using DMF, dichloromethane, acetone, ethanol and water (all 4×). Hot (80 °C) DMF and water was also used. More washing steps using DMF and water were applied if the conductivity of the supernatant aqueous fraction was higher than 200 µS cm^{-1}. During the final centrifugation steps with water, it was necessary to apply centrifugal forces of up to 25000*g* RCF to isolate the product. To obtain Na-free products, G-CN was washed with acidified water (pH = 4) to exchange sodium cations with H_3O^+ (the ζ-potential of G-CN was determined to be in the range of −30 mV, therefore contained Na^+ as counterions).

GA was synthesized *via* acidic hydrolysis of –CN moieties. HNO_3 (65%) was slowly added at RT under stirring to a suspension of G-CN in water in a round-bottom glass flask, until the final concentration of HNO_3 in the mixture reached 20%. The mixture was then heated at 100 °C under reflux with stirring (350 rpm) for 24 h. Various concentrations of HNO_3 and treatment durations were tested to identify optimal conditions, and samples were periodically withdrawn to monitor the reaction's progress. Intermediates and final products were left to cool to room temperature and then purified by washing with water through centrifugation. After a few washings, the product (GA) stopped precipitating upon centrifugation. Therefore, acidic water (pH = 4) was used to protonate the material and reduce its dispersibility, inducing precipitation. Stable aqueous suspensions of G-COOH were prepared by adjusting the pH of the purified suspension to ~8.

GO was also prepared to have a reference material to compare the results obtained with GA. It was synthesized according to a modified Hummers procedure.[21]

An amount of 3.0 g of graphite was mixed with 75 ml of 9:1 mixture of H_2SO_4 and H_3PO_4. Then an amount of 9.0 g of $KMnO_4$ was slowly added while cooling the mixture in an ice bath. The mixture was stirred for 3 h at 0 ˚C and then overnight at room temperature. After that, a volume of 150 ml of water was added heating at 80 ˚C. After stirring for 1 h, the obtained mixture was sonicated for 1 h at 35 ˚C. To quench the reaction, 3 mL of 30 %wt. of H_2O_2 was added, stirred for additional 2 h, sonicated for 1 h and finally, diluted with additional water. The supernatant was profusely washed with water, dialyzed 72 h against DI water and 8 h against Milli-Q quality water, and finally lyophilized.

Reaction with $Pd(OAc)_2$

The amount of $Pd(OAc)_2$ to be reacted with the pristine graphenic material (hereafter referred as impregnation step) was precisely determined taking as a reference the amount of COOH groups present at the carbonaceous backbone (see discussion below). Thus, 40 mg of pristine GA was mixed with 0.0245 g (0.11 mmol) of $Pd(OAc)_2$ in 40 mL of MeCN. Reaction was maintained at reflux conditions with magnetic stirring for 6 h (see Figure 6.1). After cooling down, the solids were washed 3 times with 50 mL of fresh acetonitrile and 3 times with 50 mL of 2-propanol by centrifugation methods, sonicating 5 min between each centrifugation cycle. Then, the black solids were dried under vacuum to yield the GA-Pd-100 sample. Using the same conditions, GA-Pd-25, GA-Pd-50 and GA-Pd-200 samples were synthetized employing 40 mg of pristine GA with 0.0065 g (0.028 mmol), 0.0127 g (0.056 mmol) and 0.049 g (0.22 mmol) of $Pd(OAc)_2$, respectively. The synthesis of GO-based hybrid material was performed under the same protocol, recalibrating the quantity of $Pd(OAc)_2$ in order to match the amount of –COOH calculated by XPS. So the synthesis was performed by mixing 40 mg of pristine GO with 0.015 g (0.06 mmol) of $Pd(OAc)_2$ to yield GO-Pd-100 sample as benchmark material.

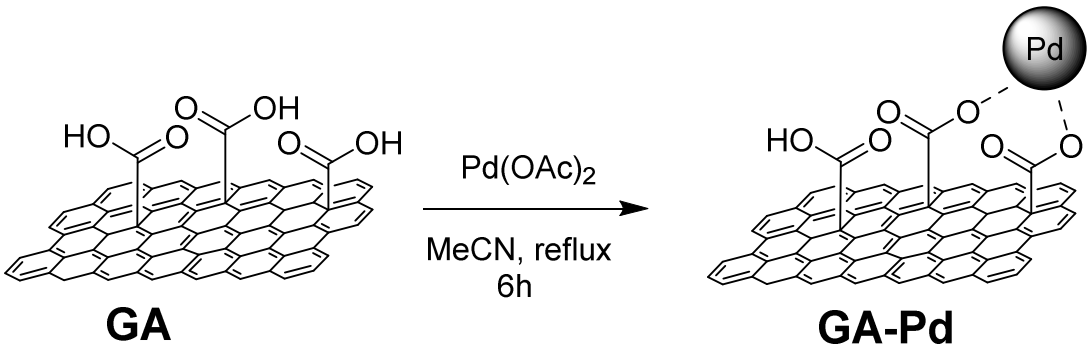

Figure 6.1. Procedure for the growing of Pd nanosystems at the GA surface.

Physico-chemical Characterization

The surface chemical characterization of the catalyst has been carried out using X-ray photoelectron spectroscopy (XPS) in a custom-made UHV system working at a base pressure of 10^{-10} mbar, equipped with an Omicron EA150 electron analyzer and an Omicron DAR 400 X-ray source with a dual Al–Mg anode. Core level photoemission spectra (C 1s, N 1s, O 1s and Pd 3d regions) were collected at rt with a non-monochromated Mg Kα X-ray source (1253.6 eV) and using an energy step of 0.1 eV, 0.5 s of integration time, and a 20 eV pass energy. The samples were dispersed in 2-propanol and drop casted on an Al support. The

nano- and microscale morphology of the materials was studied by scanning electron microscopy (SEM) and transmission electron microscopy (TEM). The SEM images were acquired using a field emission source equipped with a GEMINI column (Zeiss Supra VP35) and an Oxford energy-dispersive x-ray spectroscopy (EDX) microprobe, and micrographs were obtained with an acceleration voltage of 5 or 10 kV using in-lens high-resolution detection. The TEM images were acquired using a FEI Tecnai 12 microscope with an acceleration voltage of 100 kV. High-resolution images were obtained in a FEI Tecnai G2 20 instrument working in the STEM/HAADF mode. Inductive coupled plasma spectroscopy (ICP) measurements were performed in an Agilent Technologies 7700x ICP-MS, equipped with an octupolar collision cell operating in kinetic energy discrimination mode for the removal of polyatomic and argon-based interferences.

The Raman spectra were collected using a ThermoFisher DXR Raman microscope using a laser with an excitation wavelength of 532 nm (5 mW), focused on the sample with a 50× objective (Olympus). The UV-Vis spectra were recorded on a Varian Cary-50 spectrophotometer in the range 225 – 800 nm, employing 2-propanol as solvent. All spectra were recorded using 1 cm optical path quartz cells. The concentration and the experimental parameters were optimized to minimize scattering effects. The NMR spectra were recorded on a Bruker Avance 300 MHz (300.1 MHz for ^{1}H, 298 K); chemical shifts (δ) are reported in units of parts per million (ppm) relative to the residual solvent signals and coupling constants (J) are expressed in Hz.

General Catalytic test

In a typical Suzuki experiment, 1.2 mmol of boronic acid, 1.0 mmol of aryl halide and NaOH as base (typically 4.0 mmol) were dissolved in 10 mL of water with magnetic stirring. 0.1 mol % of Pd-based catalyst material was added, and the mixture was heated for a target temperature, typically 100 ˚C. Reaction was allowed to cool down, extracted 3 times with 10 mL of ethyl acetate, organic fractions were combined, dried and concentrated to submit it to the NMR analysis. On the other hand, catalyst was recovered by centrifugation, profusely washed with water and acetone and submitted to a new catalytic cycle without adding new catalyst precursor. Purification was performed with column chromatography employing a 3:1 mixture of ethyl acetate/hexanes when necessary. Homo-coupling tests were performed under the general protocol but without the halide.

6.3 Results and discussion

6.3.1 Pd nanosystems growth on Graphene Acid

The synthetic design of GA yields a graphenic surface fully covered by COOH groups. From the separation into chemically shifted components of the C 1s photoemission line of the X-ray photoemission spectroscopy (XPS), it results that the pristine GA shows a large amount of C-C sp^2 bonds (61.5 %) together with a large fraction of COOH groups as deduced from the peak centered at 288.8 eV (9.7 % of the total C 1s intensity), which is the most intense component among all C-O species (see Figure 6.2). On the other hand, GO showed less intense components for both C-C sp^2 (53.4 %) and COOH (7.0 %), proving the heterogeneous nature of this derivative. Keeping these values in mind, the amount of $Pd(OAc)_2$ to be reacted with the material was determined. We hypothesize that the surface COOH groups can react with the $Pd(OAc)_2$ in a counter-ion metathesis based reaction, displacing out the acetate groups and grafting the single Pd atom on the surface.

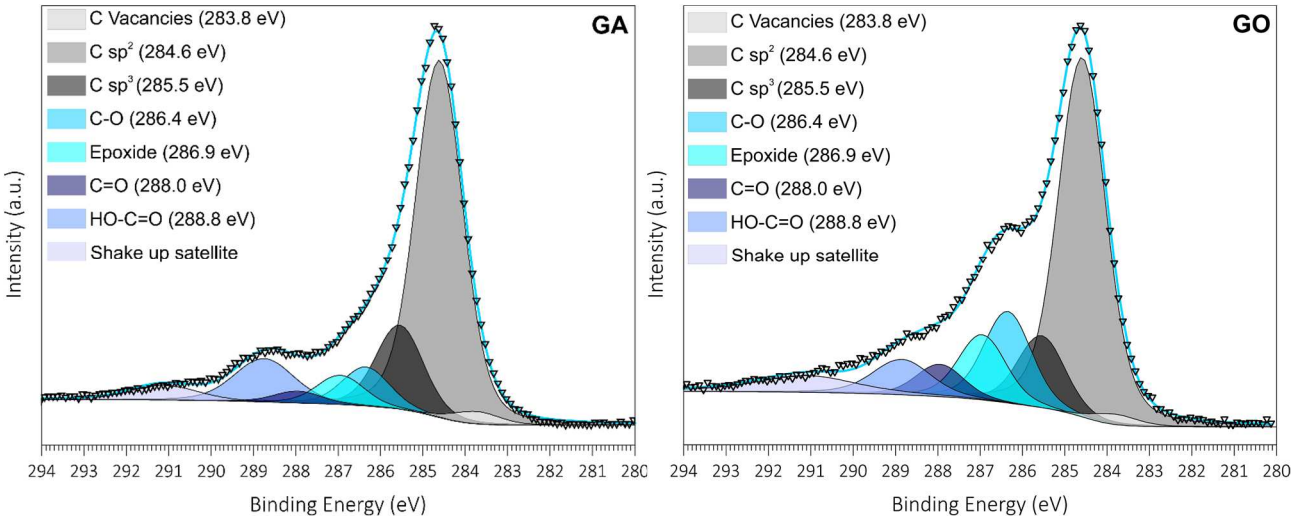

Figure 6.2. C 1s photoemission lines of pristine GA (left) and GO (right) materials.

Figure 6.3 shows the Pd 3d line of the GA-Pd samples with an increasing amount of Pd deposited on the surface, starting from an added amount of 25 % of $Pd(OAc)_2$ vs the COOH groups up to 200 %. The fitting of the XPS spectra afforded three different components. In the case of GA-Pd-25, the first one owns the maximum at binding energy (BE) value at 336.4 eV, which can be assigned to the metallic component. A second maximum appeared at 337.3 eV, corresponding to the Pd(II) species such as PdO.[22] The last component was detected at 338.5 eV and it is compatible with Pd-NCMe bonds, due to acetonitrile molecules coordinated to the Pd atoms (capping the Pd nanosystem),[23] or residual $Pd(OAc)_2$ as well, especially at the low loading values.[24] If we take such XPS evidence, it seems that $Pd(OAc)_2$ aggregates as clusters or nanoparticles on the support surface in which are composed by a metallic palladium core, passivated with a layer of oxides and capping acetonitrile molecules. When the amount of $Pd(OAc)_2$ is increased, *i.e.*, passing from 25% to 200%, the metallic component grows while the oxide one decreases, being the capping component approximately constant. The shift in the metallic Pd(0) component, due to capacitive effects derived from size confinement, can suggest an estimated size for the nanosystem at the surface (See Table 6.1).[25] As expected, with the lowest amount of Pd precursor (GA-Pd-25) the maximum shift (1.4 eV) to higher BE with respect to the bulk palladium (BE 335.0 eV) is observed,[26] which may indicate an approximated size of the nanoparticle of about 1 nm.

Sample	*BE (eV)*	*Size (nm)*	*[Pd] (at.%)*
GA-Pd-25	336.4	1	1.7
GA-Pd-50	336.2	2	2.7
GA-Pd-100	335.9	4-6	4.3
GA-Pd-200	335.6	8-10	4.0

Table 6.1. Pd 3d XPS parameters of the GA-Pd samples

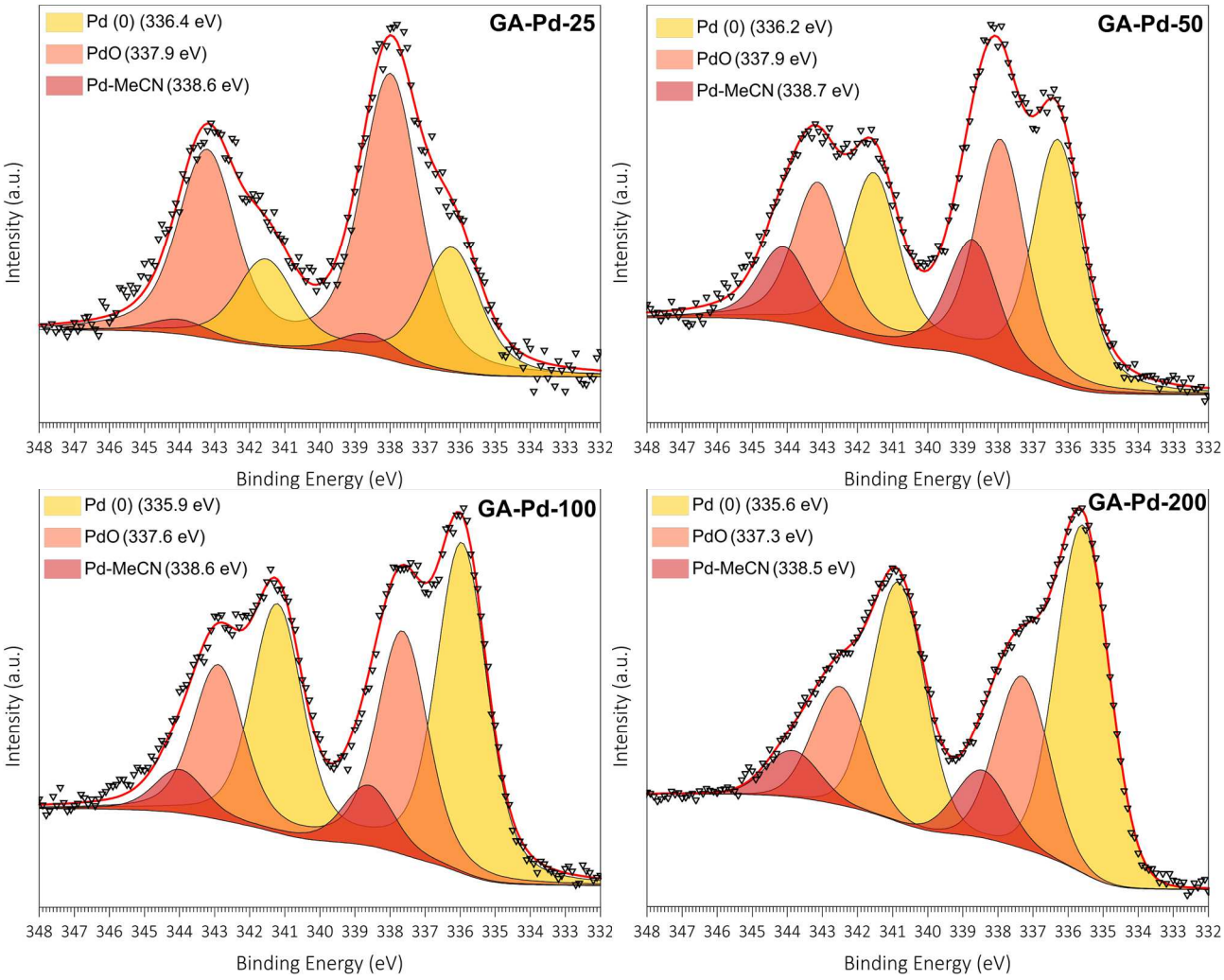

Figure 6.3. Pd 3d photoemission spectra of the different GA-Pd samples.

A clear trend appears when the amount of precursor is increased, since the shift of the metallic Pd(0) component with respect to bulk palladium is 1.2 eV for GA-Pd-50 (nanoparticles ranging 2 nm), 0.9 eV for GA-Pd-100 (nanoparticles of 4-6 nm) and 0.6 eV for GA-Pd-200 (nanoparticles of 8-10 nm). Regarding the total amount of metal grafted into the support, the loading level respected the amount of precursor employed in the impregnation step (see Table 6.1 and 6.2) until saturation was reached when 200% of precursor was employed.

XPS	*C (% at.)*	*N (% at.)*	*O (% at.)*	*Pd (% at.)*
GA	81.0	4.5	14.5	-
GA-Pd-25	68.6	4.5	25.3	1.6
GA-Pd-50	71.1	3.8	22.4	2.7
GA-Pd-100	70.4	4.6	20.7	4.3
GA-Pd-200	72.2	3.0	20.8	4.0
GO	74.1	-	25.9	-
GO-Pd-100	63.5	3.1	31.1	2.3

Table 6.2. Surface composition of the studied samples as determined by XPS.

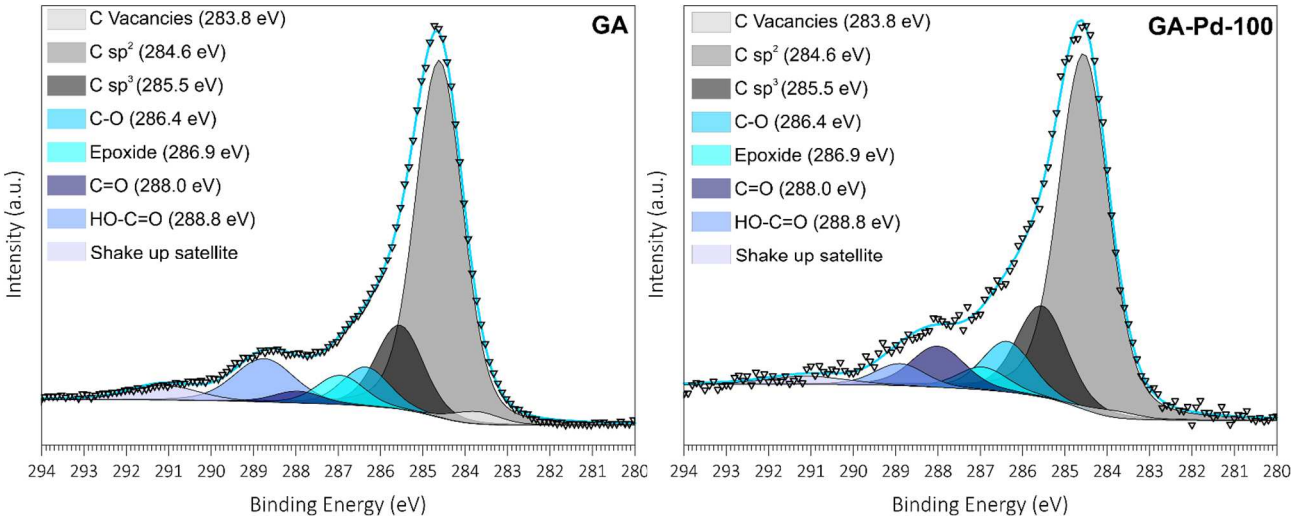

Figure 6.4. C 1s photoemission lines of pristine GA (left) and GA-Pd-100 (right) materials.

Several changes were also observed in the C 1s core level after Pd impregnation. As can be observed in GA-Pd-100, as an example (see Figure 6.4), a simultaneous lowering of –COOH band (288.9 eV) and increment of the band at 288.0 eV clearly indicates the formation of $–COO^-$ moieties as anchoring points for Pd. Therefore, the hypothesis of the counter-ion metathesis mechanism for displacing the acetates from the $Pd(OAc)_2$ precursor seems plausible. Moreover, higher percentage of C sp^3 and C bonded to heteroatoms were found, that may arise from the presence of capping species on Pd. These species can be identified as the acetonitrile molecules, already detected in the Pd 3d photoemission line showed in Figure 6.3. In addition, the formation of nanoparticles seems clear since the COOH band does not vanish as a consequence of Pd aggregation to form nanoparticles: if quantitative counter-ion metathesis would have taken place to fix Pd atoms at surface, all the COOH moieties would be converted to COO^-.

UV-Vis spectroscopy data also agree with XPS, since it is known that the size of the Pd nanoparticle can affect the optical properties regarding the corresponding maximum of the plasmonic effect, centred raging the 270 nm.[27] Analysis of alcoholic suspensions of the graphenic materials revealed the same trend discussed for the XPS analysis (see Figure 6.5). The position of the Pd plasmon is progressively red shifted when the amount of $Pd(OAc)_2$ was increased in the impregnation step, passing from no appreciable optical feature in the GA-Pd-25 sample to clear peaks different from the characteristic GA absorption in the highly impregnated samples.

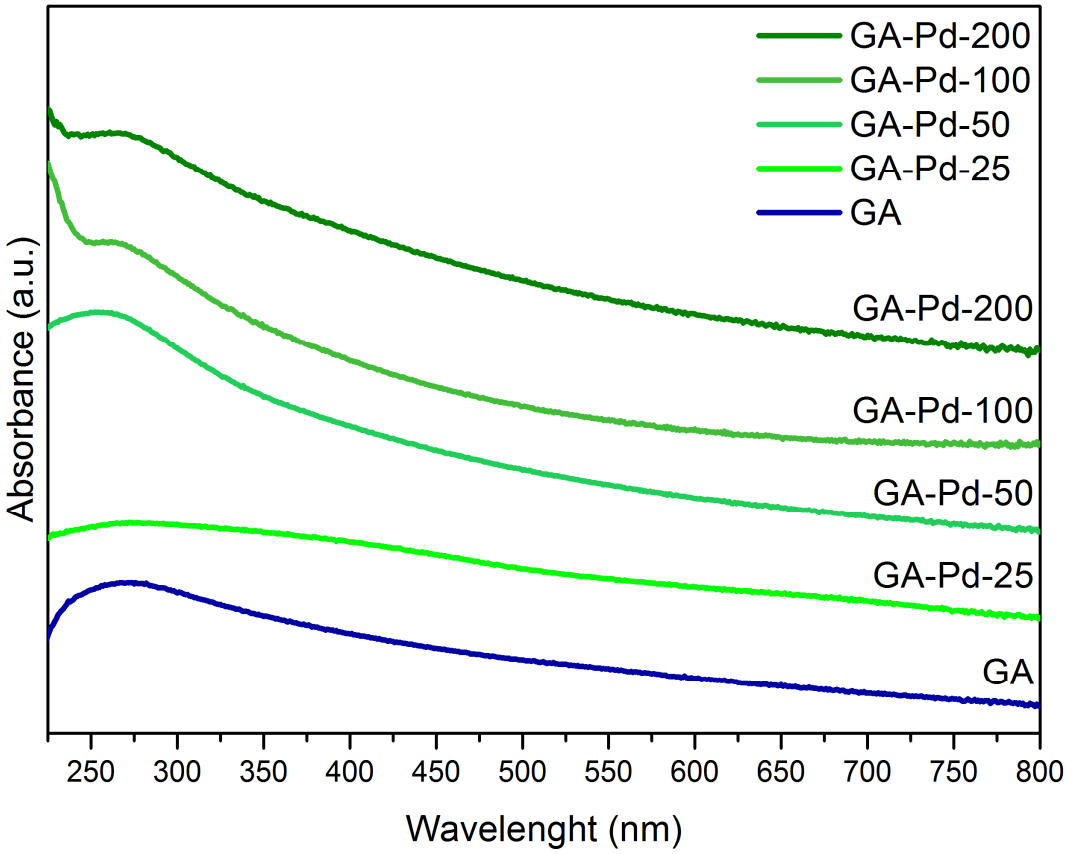

Figure 6.5. UV-Vis spectra of the different GA-Pd materials.

Clear evidences of the size of the nanoparticles were also spotted out by Transmission Electron Microscopy (TEM) observations. After the palladium impregnation, the presence of homogeneously distributed nanoparticles along the material basal plane is apparent (see Figure 6.6), whereas the sheet structure seems to not be modified. In Figure 6.7 the histograms of the sizes of the palladium nanoparticles is reported for the different samples. The GA-Pd-25 sample shows small dots ranging 0.7-0.8 nm. Increasing the Pd loading to 50% rises the size of the nanoparticles to 1.8-1.9 nm. When the amount of Pd reaches the stoichiometric maximum (GA-Pd-100), the maximum size is around 3.3 nm, but the distribution starts to become asymmetric. Doubling again the amount of precursor, i.e., GA-Pd-200, resulted in big Pd aggregations (maximum at 8.3 nm) with a broad distribution compared to the other hybrid materials and completely asymmetric. The evolution and even the absolute values obtained by TEM are in sharp agreement with XPS-based evaluation (Table 6.1) and confirm the trend of the UV-Vis plasmonic resonance data.

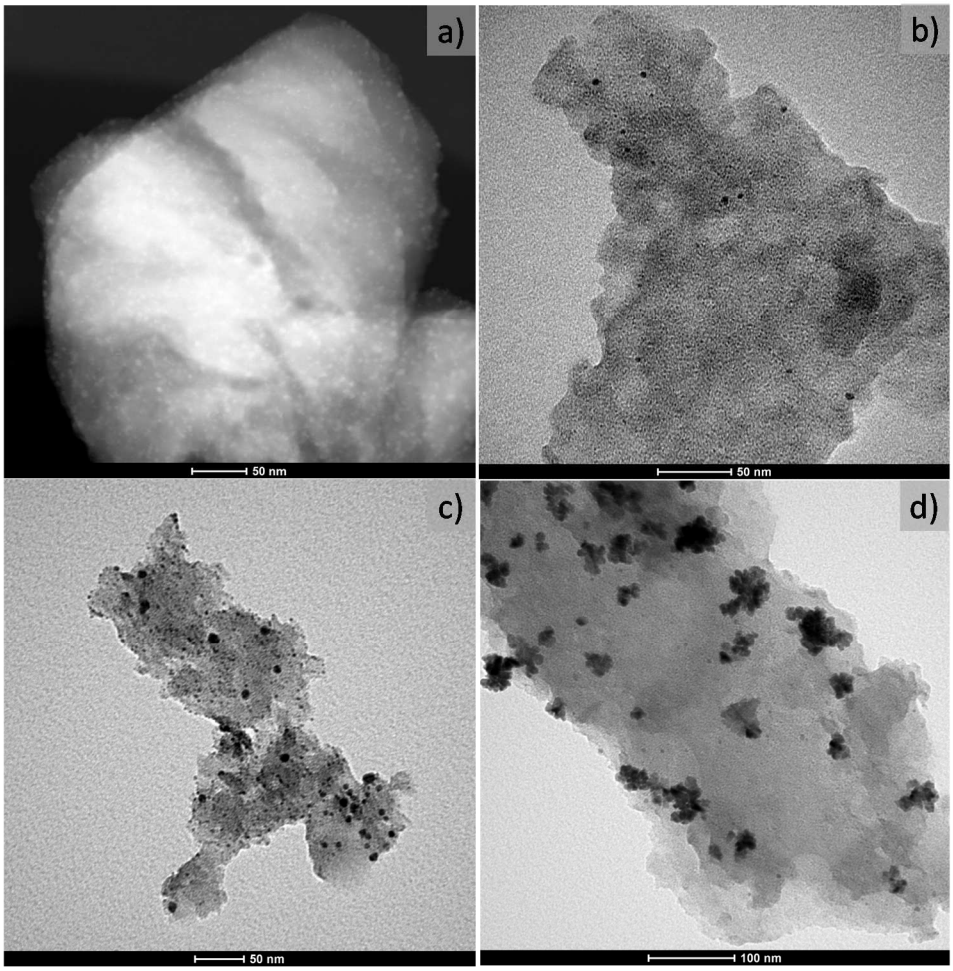

Figure 6.6. TEM images of a) GA-Pd-25, b) GA-Pd-50, c) GA-Pd-100 and d) GA-Pd-200.

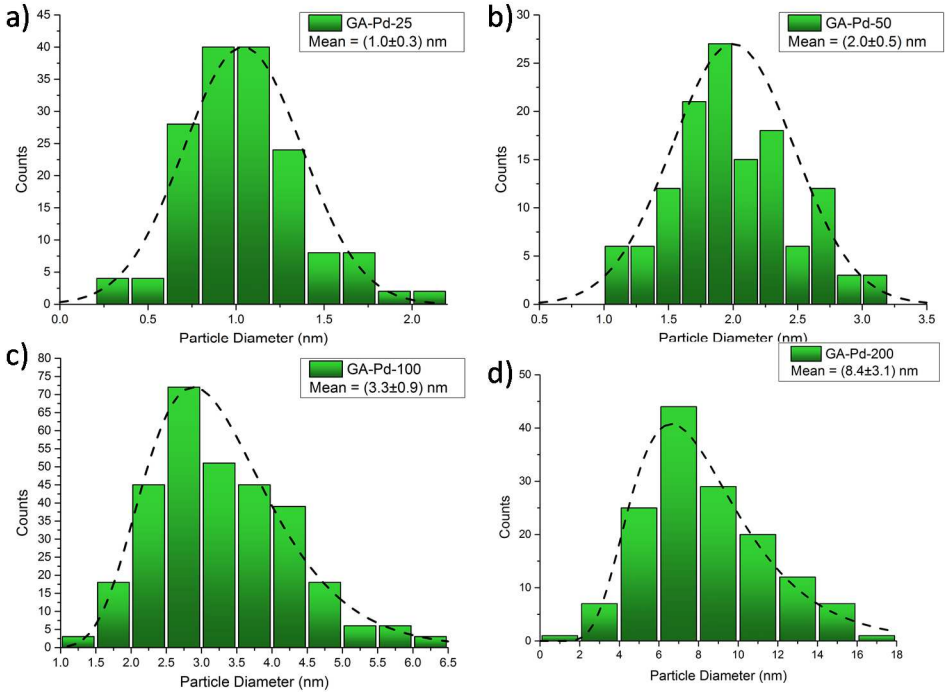

Figure 6.7. Size distribution calculated from TEM images for a) GA-Pd-25, b) GA-Pd-50, c) GA-Pd-100 and d) GA-Pd-200.

Finally, Pd determination was crosschecked by EDX (Table 6.3) and ICP analysis (Table 6.4), reporting a good agreement with the XPS surface composition, as expected when dealing with small nanoparticles.

As a whole, our physico-chemical data suggest that the well controlled surface chemistry of GA offers a suitable environment to effectively graft the impregnated palladium with a correct proportional trend. Indeed, a high loading of small nanoparticles with sharp size-distributions was obtained when the Pd loading is low. This is in stark contrast with the benchmark GO, where the uncontrolled and heterogeneous distribution of oxygen groups forces the Pd atoms to aggregate in larger nanoparticles (around 23 nm for a GO-Pd-100 loading), thus reducing the effectiveness of the grafting.

EDX	***C + N (% at.)[a]***	***O (% at.)***	***Pd (% at.)***
GA-Pd-25	79.4	19.2	1.4
GA-Pd-50	71.1	25.6	3.3
GA-Pd-100	75.0	20.6	4.4
GA-Pd-200	72.4	23.4	4.2
GO-Pd-100	70.3	27.4	2.3

a) Due to the proximity of C and N signals, they have been reported as sum of the contributions.

Table 6.3. Elemental composition from EDX analysis.

Entry	*Sample*	*[Pd][a]*
1	GA-Pd-25	9.8
2	GA-Pd-50	12.9
3	GA-Pd-100	24.0
4	GA-Pd-200	22.8
5	GO-Pd-100	11.2

a) %wt.

Table 6.4. Pd determination by ICP-MS analysis.

A kinetic analysis of the Pd growth have been attempted using the combined data of the different characterization techniques. To do that, aliquots of the GA-Pd-100 impregnation reaction were withdrawn at regular intervals and analysed by TEM and XPS methods. Interestingly, the position of the XPS Pd 3d line was found to be the same in the sample withdrawn at 20 min (see Figure 6.8g) compared to the final material after 6h of reaction (Figure 6.8h). It resulted that the component corresponding to the highest BE component, i.e., Pd-NCMe and/or $Pd(OAc)_2$ aggregates, is larger at 20 min, that is quite reasonable for the first moments of the impregnation. Analysing the TEM images after 20 min (Figure 6.8a), small clusters (0.5-1 nm) coexisted with large aggregates (15-20 nm), which can be assigned to $Pd(OAc)_2$. However, after continuing the reaction (see Figure 6.8b-f), the frequent big spots started to vanish and to decrease their mean diameters (from 15-20 nm to 5-10 nm), while the small dots become predominant. Therefore, this could be taken as an evidence for the transformation of Pd from precursor to nucleated nanoparticle. It is interesting to mention that the number of nanoparticle nuclei is mainly constant from the first aliquot to the final one (around 2.2 x 10^{13} nuclei cm^{-2}).

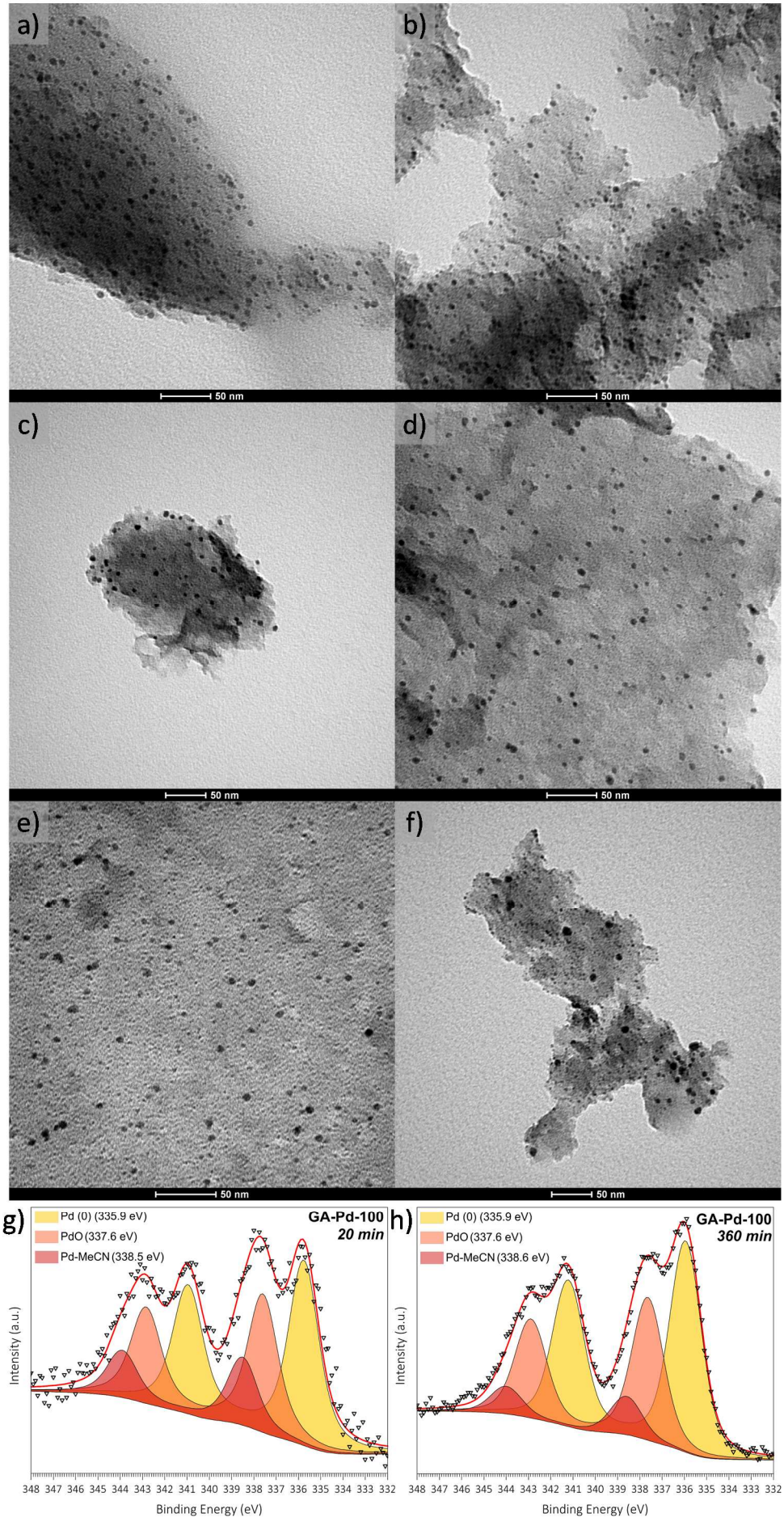

Figure 6.8. TEM images of the GA-Pd-100 sample at different times:
a) 20 min,
b) 40 min,
c) 60 min,
d) 120 min,
e) 180 min
f) 360 min.

XPS Pd 3d core levels for samples GA-Pd-100 at g) 20 min and h) 360 min are reported as well.

In addition, the small dots were detected to progressively grow, passing from 0.5-1 nm to 2-3 nm, in stark agreement with the data discussed before, following a cubic fitting with time that satisfies the Avrami theory (see Figure 6.9).[28] Finally, a very homogeneous and sharp distribution of nanoparticles was obtained at 180 min, reaching therefore the growing saturation in a moment between 4.5 and 6 h of impregnation.

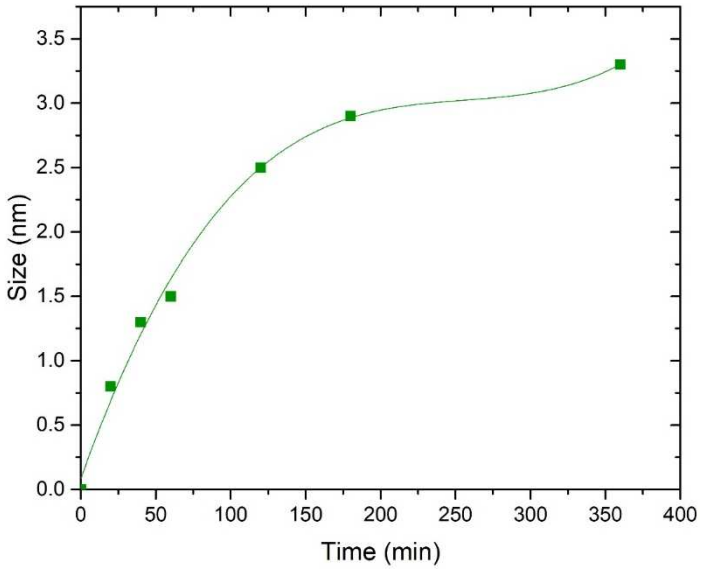

Figure 6.9. Temporal evolution of the mean size of the nanoparticle extracted from the TEM analysis. A cubic fitting with time that satisfies the Avrami theory has been reported (see text).

Gathering all the data, we can speculate on a possible growing mechanism, as depicted in Figure 6.10. The first probable and faster reaction is the counter-ion metathesis step, in which the COOH groups of the support displace out one of the acetates and fix the Pd ion at the surface. The generated acetate molecule (or acetic acid molecule) then promotes the reduction of Pd (II) to metallic Pd in a second fast process.[29] Thus, the fixed Pd can act as a nucleation point for the successive growth. The surface-bound Pd therefore attracts more Pd ions following autocatalytic and slower events to grow the nanoparticle, whose final size strongly depends on the amount of precursor. Similar steps have been proposed for the growth of Au nanoparticles on graphene.[30] Since the process proceeds in air and because of the oxidative environment due to the oxygenated graphenic surface, a passivating layer of PdO is therefore created, which remains mainly constant for the different sizes of the nanoparticles studied. Also, the high conductivity of GA, demonstrated before theoretically and experimentally, could strongly assist the reduction step.[14] Therefore, a parallel growth might be favoured in the conductive platform that GA offers, resulting in a homogenous distribution of small nanoparticles.

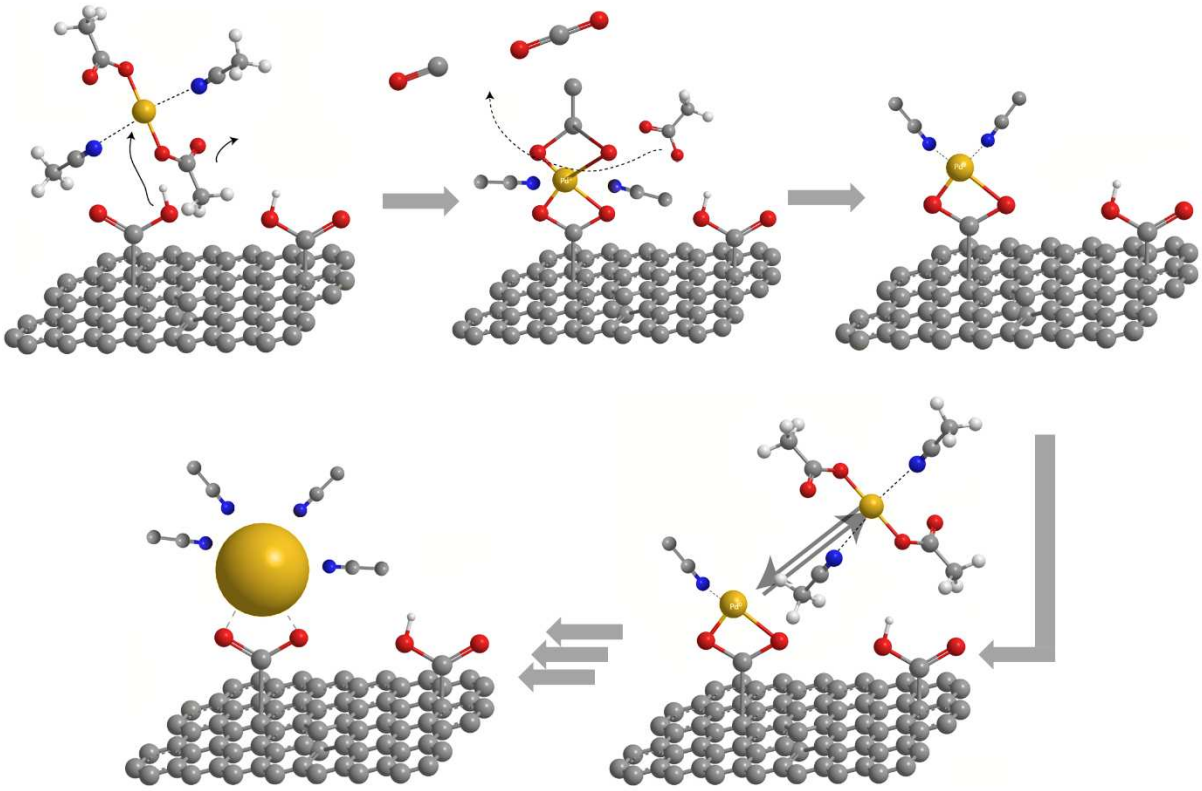

Figure 6.10. Proposed mechanism for the Pd nanoparticle growth on GA. Blue ball=N, red ball=oxygen, grey ball= carbon, yellow ball= palladium atom or nanoparticle.

6.3.2 Catalytic Activity

After unveiling the actual nature of the palladium nanostructures attached to GA, the different GA-Pd samples were tested as catalysts in the Suzuki-Miyaura cross-coupling C-C bond formation reaction. In order to test preliminarily the catalytic behaviour, the coupling between phenyl boronic acid and bromobenzene was chosen as model reaction (it is known that bromoarenes own an intermediate reactivity toward the Suzuki coupling), as depicted in Figure 6.11. Very briefly, 1.2 mmol of boronic acid and 1.0 mmol of bromobenzene were suspended in 10 mL of water, where 4 mmol of NaOH[31] and 0.1 mol% of catalyst were added. The reaction mixture was stirred at 100 °C for a desired time, and after work-up (see Section 6.2), reaction crudes were analysed by NMR spectroscopy. The transformation can be easily followed up tracking the disappearance of the upshifted boronic protons at δ 8.21 ppm while the biphenyl protons appeared downshifted, i.e, δ 7.67 ppm (see section 6.3.3 for full NMR data).

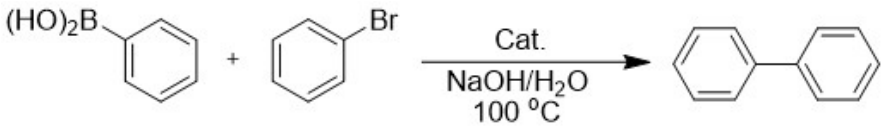

Figure 6.11. Model Suzuki-Miyaura cross-coupling reaction as case study.

The NMR data (see Figure 6.12 for the case of the GA-Pd-100 sample) allowed us to build kinetic profiles to analyse the performance of the hybrid systems.

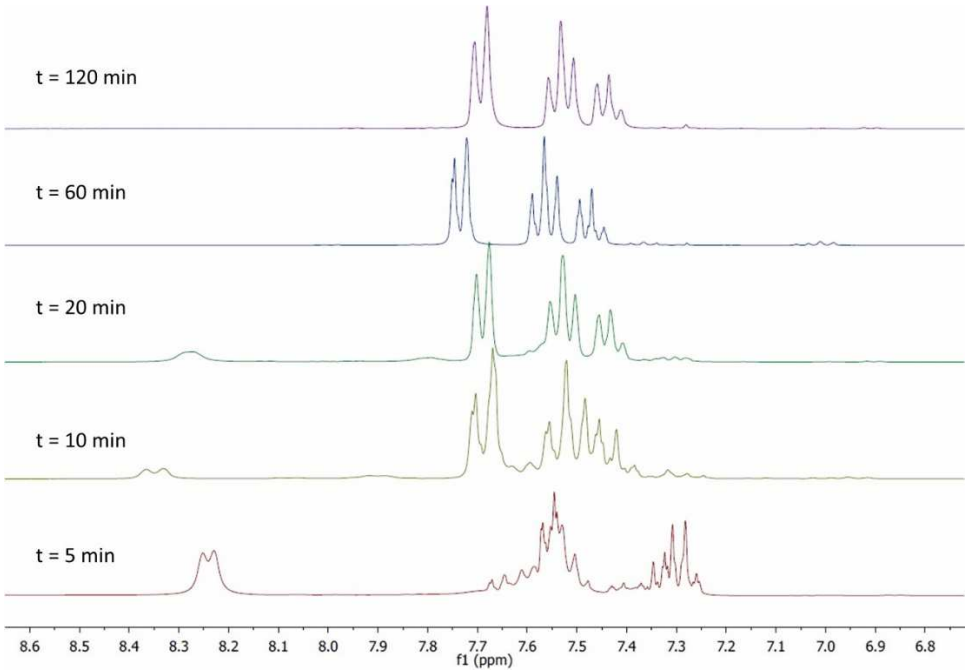

Figure 6.12. NMR tracking ($CDCl_3$, 300.1 MHz, 298 K) of the Suzuki coupling (standard conditions, see text) catalysed by GA-Pd-100.

To compare the performance of the heterogenized Pd catalysts with a reference homogeneous catalysts, we have investigated the activity of molecular $Pd(OAc)_2$, as well, under the same experimental conditions. While a non-catalysed blank experiment showed negligible activity, the homogenous palladium-based catalysts showed high activity toward the formation of biphenyl.

It is important to mention that the Suzuki coupling undertaken in this work is only performed following an environmentally friendly strategy, *i.e.*, water as solvent, without any phosphine sources to stabilize and enhance the palladium activity, and also without any other organic substance added besides both boronic and halide reagents. In addition, the reaction was performed under air atmosphere (no difference was detected under N_2), which may be beneficial from the economical point of view. From the analysis of the kinetic profiles, no induction period is apparent, and the different systems were able to reach high conversion values. However, some differences must be pointed out (see Table 6.5). On the one hand, GA-based materials were able to fully complete the reaction with high selectivity to the coupling product. However, we observed a size-dependent activity (Figure 6.13). Indeed, catalysts showed a progressively better performance following a trend according to the size of the nanoparticle due to the highest specific surface area exposed in the smallest particles.[32] In this way, GA-Pd-25 resulted to be the most active material, reaching a conversion above 99 % after only 2 min of thermal equilibration, with turnover frequency (TOF_0) as high as 30030 h^{-1}. GA-Pd-50 completed the reaction in 10 min, followed by GA-Pd-100 that needed almost 60 min. Finally, GA-Pd-200, where the Pd is more aggregated, fully completed the reaction in a 1 h run, but the selectivity was lower compared to the small nanoparticles present in the other

materials. However, in all cases the performance was superior to that of the benchmark GO-Pd-100, which showed 98% conversion with poorer activity, and also superior to the homogeneous $Pd(OAc)_2$ catalyst. Regarding the byproducts, only small traces of phenol could be detected in the NMR spectra of the different reactions, which is probably due to the hydrolysis of the boronic acid in the reaction medium.[33]

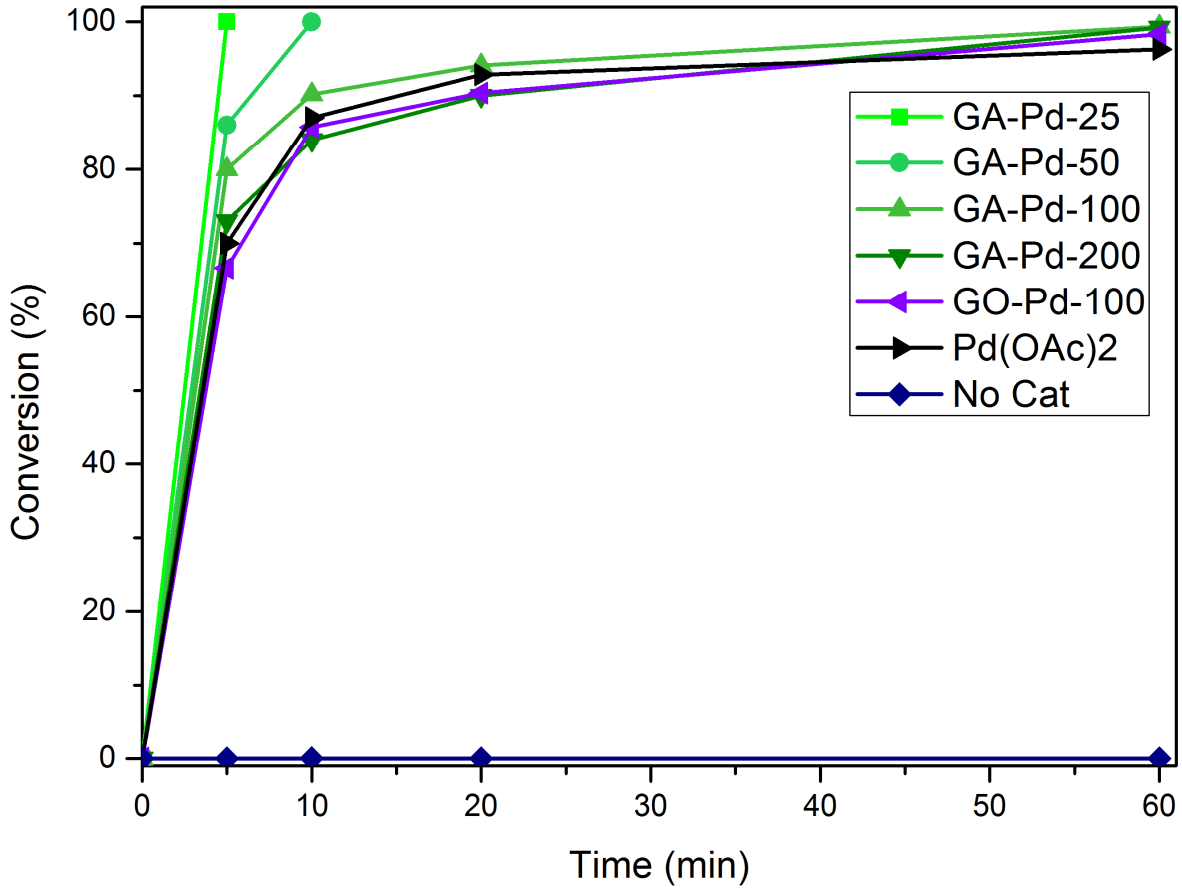

Figure 6.13. Kinetic profiles of the Suzuki-Miyaura cross-coupling reaction of different GA-Pd samples carried out at 100°C.

In addition, using the GA-Pd-100 catalyst as reference material (intermediate behaviour for simplicity reasons), reaction parameters such as temperature and base amount were optimized in order to obtain even milder conditions (see Figure 6.14). Thus, it was found that only 1 equivalent of NaOH is needed to achieve the same level of performance reported in Table 6.5. In addition, a remarkable 82% conversion after 1h-reaction was obtained even at a lower temperature (70 °C). The situation is rather different when the GO-Pd-100 catalyst is used (Figure 6.14)

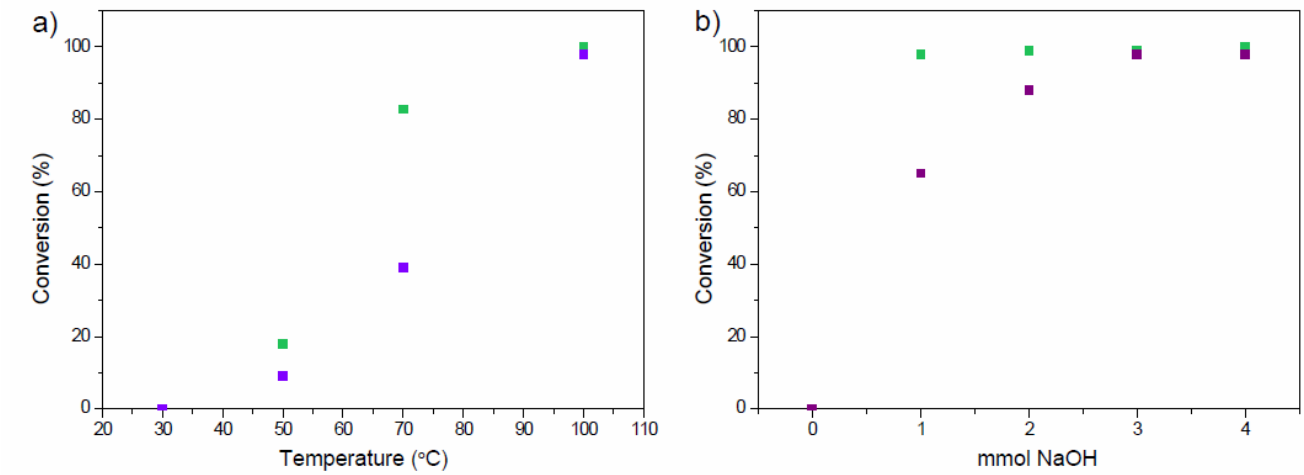

Figure 6.14. Optimization in a) temperature and b) base amount of the Suzuki-Miyaura cross-coupling reaction for GA-Pd-100 (green) and GO-Pd-100 (purple).

Catalyst	*Time*[b]	*Conv.*[c]	*Yield*[d]	*TON*[e]	*TOF*$_0$[f]
No cat.	120	-	-	-	-
GA-Pd-200	60	>99	86	1000	9800
GA-Pd-100	60	>99	98	1000	11520
GA-Pd-50	10	>99	98	1000	12000
GA-Pd-25	2	>99	98.5	1000	30030[g]
GO-Pd-100	60	98	76	980	9590
Pd(OAc)$_2$	60	96	90	960	10800

a) Reactions performed under the standard conditions (T=100°C), b) min, c) %, determined by ^{1}H-NMR, d) % to the coupling product, determined by ^{1}H-NMR, e) Turnover number, f) Turnover frequency (h^{-1}), calculated after 5 min, g) calculated in saturation time.

Table 6.5. Catalytic parameters for model Suzuki-Miyaura cross-coupling reaction carried out with different catalysts.

In order to understand how the coupling is achieved, additional tests were performed without any halide added in the reaction vessel. For the sake of comparison, we employed the standard conditions in order to discern the effects coming from the different reactants. (see Table 6.6). We observed that all the GA-Pd materials were also able to yield, with good selectivity, the biphenyl coupling product under boronic acid homo-coupling conditions. It is well known that reductive solvents are known to promote homocoupling reactions.[34] However, when the reaction was performed under inert conditions (no air), no homo-coupling product was detected . A notable difference with the Suzuki cross-coupling reaction is therefore observed, where just a proper tuning of the atmosphere conditions can trigger the reactivity.

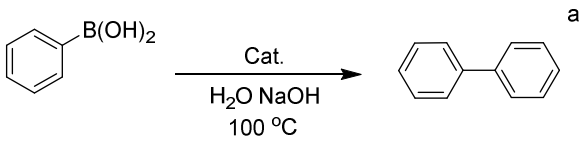

Catalyst	Time[b]	Conversion[c]	Yield[d]
Pd(OAc)₂	960	88	37
GA-Pd-200	960	>99	69
GA-Pd-100	960	>99	72
GA-Pd-100[e]	960	22	-
GA-Pd-50	960	>99	69
GA-Pd-25	960	>99	75
GO-Pd-100	960	80	-

a) Reactions performed under the standard conditions (T=100°C) without halide, b) min, c) %, determined by ^{1}H-NMR, d) % to the coupling product, determined by ^{1}H-NMR, e) performed under inert conditions.

Table 6.6. Results of homo-coupling reaction tests.

Interestingly, we could not detect biphenyl molecules when GO-Pd-100 was used for the homo-coupling test under the same experimental conditions. Hence, the smaller Pd nanoparticles present on the GA-Pd samples are able to overcome, under aerobic conditions, the homo-coupling activation energy, forming the intermediates with the assistance of molecular oxygen. On the contrary, the larger Pd nanoparticles present in GO-Pd-100 cannot sustain this reaction path under the same experimental conditions. It has been reported previously that gold nanoclusters smaller than 2 nm are able to catalyse the homo-coupling reaction, while nanoparticles bigger than 9 nm showed no activity.[35] Our observations confirm such previously reported results. In addition, the molecular $Pd(OAc)_2$ catalyst is not able to accomplish the full conversion and presents a poor selectivity to the coupling product (see Table 6.6). Therefore, the specific surface chemistry of GA is able to deploy Pd nanoparticles suitable for two different reaction pathways (homo- and cross-coupling) with enhanced activity compared to the GO-Pd-100 benchmark and $Pd(OAc)_2$ homogeneous catalysts. Moreover, the efficiency and the atom economy of the GA-Pd catalyst is also improved since it can reach the target product even without a halide source.

However, to further investigate the cross-coupling mechanism of the GA-Pd catalysts, the synthesis of asymmetric biphenyls was also tested. For ease reasons, only GA-Pd-100 was tested in the optimized 1h - run reactions (see Table 6.7). The first cross-coupling test was performed with 4-bromotoluene. The NMR analysis of the reaction crude revealed that the reaction proceeds smoothly, with a conversion above 99% and high selectivity (98 %), to the asymmetric biphenyl. In addition, the sharp singlet corresponding to the methyl group (δ = 2.5 ppm) was coupled to the aromatic signals.

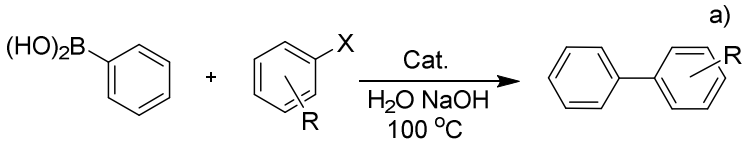

Entry	R	X	Time[b]	Conv.[c]	Yield[d]
1	4-Me	Br	60	>99	98
2	4-OH	Br	60	77	96
3	4-OMe	Br	60	81	>99
4	4-COMe	Br	60	>99	95
5	4-NO_2	Br	60	>99	>99
6	3-Py	Br	60	>99	95
7	H	Cl	960	>99	94
8	H	I	15	>99	>99

a) Reactions performed under the optimized conditions, b) min, c) %, determined by ^{1}H-NMR, d) % to the coupling product, determined by ^{1}H-NMR.

Table 6.7. Tests of different halides for asymmetric Suzuki cross-coupling using GA-Pd-100 as catalyst.

Then, the electronic properties of the halide were modified employing R groups with different donor or withdrawing properties to expand the scope of the GA-based catalysts. For instance, electronic-rich substrates, e.g. *p*-bromophenol or *p*-bromoanisole, yielded lower conversions compared to the standard run (Table 6.7 entries 2 and 3), as a consequence of the higher electron density in the reactive carbon, which hinders the oxidative addition step. On the other hand, electron-withdrawing substituents such as ketones or nitro groups (Table 6.7 entries 4 and 5) afforded high conversions and selectivity values. Interestingly, bromopyridine was also converted with high selectivity to the coupling product (Table 6.7 entries 6). The final step of the screening was done changing the halide atom, i.e., using the less reactive chloride and the more reactive iodide. In the first case, GA-Pd-100 needed 16 h (Table 6.7 entry 7) to produce with full conversion the biphenyl molecule with high selectivity. On the other hand, it tooks only 15 min to reach full conversion employing the iodide (Table 6.7 entry 8), which opens the gate to speed up the reaction rates when aiming to industrial uses.

Another important feature for the green attitude of a catalyst is its ability to be recovered after reaction without being modified. Thus, the cyclability of the heterogenized catalyst was deeply examined by recovering (by centrifugation) the catalyst when the reaction reached the saturation, washing it profusely with a 1:1 mixture of water and acetone five times, and using the materials for a new catalytic cycle without adding any new catalyst. The procedure was repeated for 5 consecutive cycles. We observed that GA-Pd-100 was able to maintain its activity with very close conversion values (always surpassing 97%) throughout the cycling study. On the contrary $Pd(OAc)_2$ was impossible to recover. Interestingly, after the whole procedure, really low leaching levels of Pd (ranging the ppb) were detected in the supernatant liquid, as determined by ICP methods (see Table 6.8 entries 1 and 2), highlighting, together with the cyclability, the outstanding stability of our green family of catalysts.

Entry	*Sample*	*[Pd]*[a]
1	GA-Pd-100[b]	0.6
2	GO-Pd-100[b]	0.6
3	GA-Pd-100[c]	0.3
4	GA-Pd-100[d]	0.7

a) ppm. b) Leaching test of the supernatant of the Suzuki reaction. c-d) Leaching test of the hot-filtration experiment in points 1 (c) and 2 (d).

Table 6.8. Leaching tests determinations on GA-Pd catalysts by ICP-MS.

Furthermore, the TEM images after cycling did not show any significant modification, neither on the sheets morphology nor in the size distribution of the Pd nanoparticles immobilized on the of GA-Pd-100 surface (Figure 6.15 left). No significant leaching was detected by TEM (also the TEM grid is quite clean), and the same 3.5-4 nm mean values in the diameter of the non-agglomerated particles can be clearly distinguished in the images of GA-Pd-100 (see inset in Fig. 6.15), thus discarding ripening effects.

In addition, the possible Pd dynamic exchange from the nanoparticle to the solvent under reactions conditions was also checked by hot filtration experiments (Figure 6.15 right): a Suzuki coupling was attempted at 70 ˚C, and the reaction was hot-filtered after 5 min (point 1) and 60 min (point 2). For both scenarios, the evolution of the biphenyl was retained constant after removing the catalyst out by filtration, as the NMR analysis determined. Moreover, both supernatants were analysed by ICP too, and similar levels of Pd compared to the previous leaching test were found (see Table 6.8 entries 3 and 4).

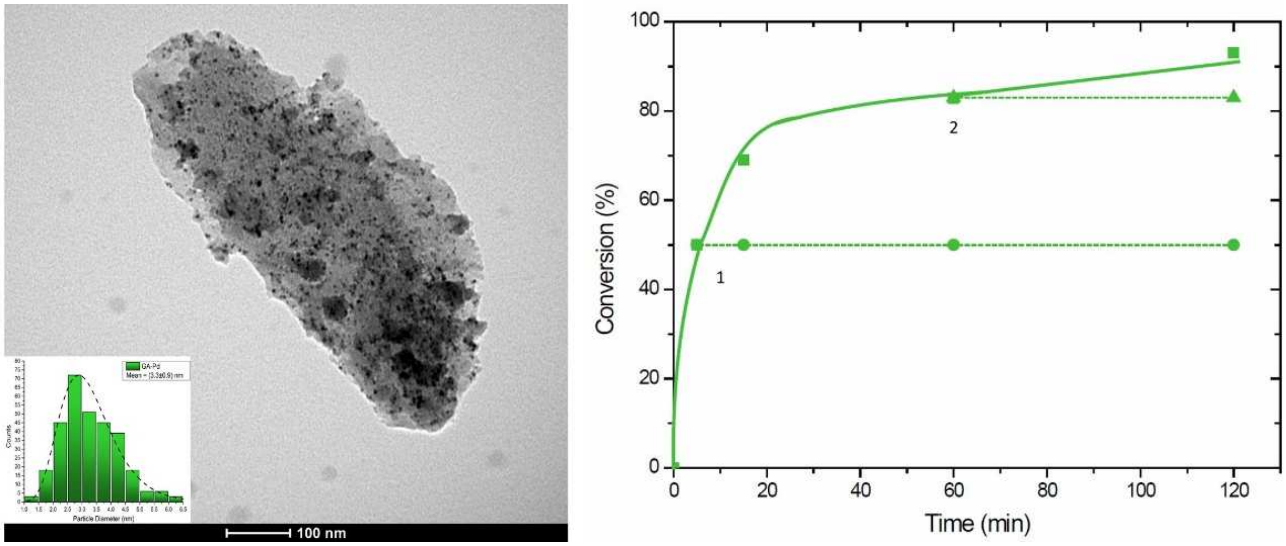

Figure 6.15. Hot-filtration experiments catalysed by GA-Pd-100 (green) at 5 min and 60 min at 70 °C reaction and TEM image of the sample GA-Pd-100 after recovering (inset: particle size distribution).

6.3.3 NMR data for isolated organic compounds

Biphenyl: Prepared according to the general procedure to yield a white solid.

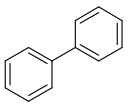

^{1}H-NMR (300.1 MHz, $CDCl_3$, δ ppm): 7.73 (d, *J* = 8.0 Hz, 4 H), 7.55 (t, *J* = 7.5 Hz, 4H), 7.46 (d, *J* = 8.3, 2H).

4-methyl-1,1'-biphenyl: prepared according to the general procedure to yield a white solid.

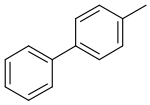

^{1}H-NMR (300.1 MHz, CDCl3, δ ppm): 7.72 (m, 2H), 7.63 (d, *J* = 8.1 Hz, 2H), 7.55 (t, J = 7.9 Hz, 2H), 7.46 (d, J = 7.6 Hz, 1H), 7.38 (d, J = 8.2 Hz, 2H), 2.52 (s, 3H).

[1,1'-biphenyl]-4-ol: Prepared according to the general procedure to yield a white solid.

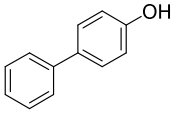

^{1}H-NMR (300.1 MHz, CDCl3, δ ppm): 7.75 (d, *J* = 8.2 Hz, 2 H), 7.55-7.38 (m, 5H), 6.83 (d, *J* = 8.3, 2H), 5.0 (bs, 1H).

4-methoxy-1,1'-biphenyl: Prepared according to the general procedure to yield a white solid.

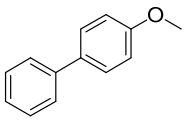

^{1}H-NMR (300.1 MHz, CDCl3, δ ppm): 7.77 (d, *J* = 8.2 Hz, 2 H), 7.55-7.38 (m, 5H), 7.07 (d, *J* = 8.1, 2H), 3.91 (s, 3H).

4-phenylacetophenone: prepared according to the general procedure to yield a white solid.

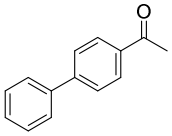

^{1}H-NMR (300.1 MHz, CDCl3, δ ppm): 8.05 (d, *J* = 8.3 Hz, 2H), 7.70 (d, *J* = 8.3 Hz, 2H), 7.61 (t, *J* = 8.3 Hz, 2H), 7.46 (m, 3H), 2.65 (s, 3H).

4-nitro-1,1'-biphenyl: prepared according to the general procedure to yield a yellow solid.

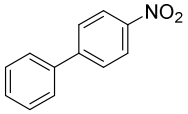

^{1}H-NMR (300.1 MHz, CDCl3, δ ppm): 8.10 (d, *J* = 8.1 Hz, 1H), 7.68 (d, *J* = 8.1 Hz 2H), 7.56 – 7.25 (m, 5H).

3-phenylpyridine: prepared according to the general procedure to yield a pale-yellow oil.

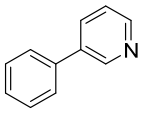

^{1}H-NMR (300.1 MHz, CDCl3, δ ppm): 8.87 (d, *J* = 2.0 Hz, 1H), 8.72 (dd, *J* = 5.1, 1.2 Hz, 1H), 8.13 (m, 2H), 7.92 (ddd, *J* = 8.2, 2.1, 1.4 Hz, 1H), 7.43 (m, 4H), 7.30 (dt, *J* = 13.7, 6.7 Hz, 1H).

Phenol: found as byproduct applying the general procedure.

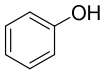

^{1}H-NMR (300.1 MHz, CDCl3, δ ppm): 7.28 (t, *J* = 7.9 Hz, 2H), 6.98 (t, *J* = 7.4 Hz, 1H), 6.89 (d, *J* = 7.9 Hz, 2H).

6.4 Conclusions

Graphene acid is a convenient platform for the surface anchoring of metallic palladium nanoparticles. By a simple and mild impregnation step, GA is able to stabilize a narrow and sharp distribution of tiny Pd nanoparticles that decorates the basal plane of the nanosheet. This is clearly a consequence of the homogeneous distribution of the anchoring carboxyl groups present in GA. In addition, the intrinsic simple structure of the GA support allowed us to figure out, with the help of spectroscopic and microscopic techniques, the actual steps of the nanoparticle growth. Thus, a possible growing mechanism has been proposed, based on the counter-ion metathesis and fast metal reduction and nucleation steps, yielding a constant number of nucleation sites. Then, slow autocatalytic events assure the growing of the nanoparticles, where the size strongly depends on the amount of Pd precursor added.

In addition, the GA-Pd materials have been tested for an green version of the Suzuki-Miyaura coupling. The family of catalysts we are presenting in this work are able to sustain the reaction in water, without any type of organic substance besides the reagents and under air atmosphere, with high yield in short reaction times, selectivity to the coupling product, versatility to different substrates, cyclability and stability without leak out the metal. Moreover, GA-Pd family is also able to perform the homo-coupling reaction of boronic acids to yield the same product in a more atom economical independently bi-functional approach. Thus a highlight of these new catalysts is also their high versatility.

References

(1) Anastas, P. T.; Warner, J. C. *Green Chemistry: Theory and Practice*.; Oxford University Press: New York, 1998.

(2) Coperet, C.; Comas-Vives, A.; Conley, M. P.; Estes, D. P.; Fedorov, A.; Mougel, V.; Nagae, H.; Nunez-Zarur, F.; Zhizhko, P. A. Surface Organometallic and Coordination Chemistry toward Single Site Heterogeneous Catalysts: Strategies, Methods, Structures, and Activities. *Chem. Rev.* **2016**, *116*, 323–421.

(3) A. H. Castro Neto; F. Guinea; N. M. R. Peres; K. S. Novoselov; Geim, A. K. The Electronic Properties of Graphene. *Rev. Mod. Phys.* **2009**, *81*, 109–162.

(4) Balandin, A. A. Thermal Properties of Graphene and Nanostructured Carbon Materials. *Nat. Mater.* **2011**, *10*, 569–581.

(5) Akhavan, O.; Ghaderi, E. Toxicity of Graphene and Graphene Oxide Nanowalls against Bacteria. *ACS Nano* **2010**, *4* (10), 5731–5736.

(6) Bonney, K. J.; Schoenebeck, F. Experiment and Computation: A Combined Approach to Study the Reactivity of Palladium Complexes in Oxidation States 0 to IV. *Chem. Soc. Rev.* **2014**, *43*, 6609–6638.

(7) Yin, L.; Liebscher, J. Carbon−Carbon Coupling Reactions Catalyzed by Heterogeneous Palladium Catalysts. *Chem. Rev.* **2007**, *107*, 133–173.

(8) Chen, J.; Yao, B.; Li, C.; Yi, G. An Improved Hummers Method for Eco-Friendly Synthesis of Graphene Oxide. *Carbon N. Y.* **2013**, *64*, 225–229.

(9) Thapa, R.; Sen, D.; Mitra, M. K.; Chatoopadhyay, K. K. Palladium Atoms and Its Dimers Adsorbed on Graphene: First-Principles Study. *Phys. B Cond. Matt.* **2011**, *406*, 368–373.

(10) Fernández-García, L.; Blanco, M.; Blanco, C.; Álvarez, P.; Granda, M.; Santamaría, R.; Menéndez, R. Graphene Anchored Palladium Complex as Efficient and Recyclable Catalyst in the Heck Cross-Coupling Reaction. *J. Mol. Cat. A* **2016**, *416*, 140–146.

(11) Hoseini, S. J.; Khozestan, H. G.; Fath, R. H. Covalent Attachment of 3-(Aminomethyl)Pyridine to Graphene Oxide: A New Stabilizer for the Synthesis of a Palladium Thin Film at the Oil–water Interface as an Effective Catalyst for the Suzuki–Miyaura Reaction. *RSC Adv.* **2015**, *5*, 47701–47708.

(12) Cabria, I.; López, M. J.; Fraile, S.; Alonso, J. A. Adsorption and Dissociation of Molecular Hydrogen on Palladium Clusters Supported on Graphene. *J. Phys. Chem. C* **2012**, *116*, 21179–21189.

(13) Yang, J.; Tian, C.; Wang, L.; Fu, H. An Effective Strategy for Small-Sized and Highly-Dispersed Palladium Nanoparticles Supported on Graphene with Excellent Performance for Formic Acid Oxidation. *J. Mater. Chem.* **2011**, *21*, 3384–3390.

(14) Bakandritsos, A.; Pykal, M.; Boński, P.; Jakubec, P.; Chronopoulos, D. D.; Poláková, K.; Georgakilas, V.; Čépe, K.; Tomanec, O.; Ranc, V.; Bourlinos, A. B.; Zbořil, R.; Otyepka, M. Cyanographene and Graphene Acid: Emerging Derivatives Enabling High-Yield and Selective Functionalization of Graphene. *ACS Nano* **2017**, *11* (3), 2982–2991.

(15) Li, B.; Dixneuf, P. H. Sp^2 C–H Bond Activation in Water and Catalytic Cross-Coupling Reactions. *Chem. Soc. Rev.* **2013**, *42*, 5744–5767.

(16) Nassar-Hardy, L.; Hierso, J.; Fouquet, E.; Felpin, F. Recyclable Heterogeneous Palladium Catalysts in Pure Water: Sustainable Developments in Suzuki, Heck, Sonogashira and Tsuji–Trost Reactions. *Adv. Synth. Cat.* **2010**, *352*, 33–79.

(17) Simon, M.-O.; Li, C.-J. Green Chemistry Oriented Organic Synthesis in Water. *Chem. Soc. Rev.* **2012**,

41, 1415–1427.

(18) Qiu, B.; Xing, M.; Zhang, J. Recent Advances in Three-Dimensional Graphene Based Materials for Catalysis Applications. *Chem. Soc. Rev.* **2018**, *47*, 2165–2216.

(19) Wang, S.; Hu, D.; Hua, W.; Jiangjiang Gu; Zhang, Q.; Jia, X.; Xi, K. Palladium Salt and Functional Reduced Graphene Oxide Complex: In Situ Preparation of a Generally Applicable Catalyst for C–C Coupling Reactions. *RSC Adv.* **2015**, *5*, 53935–53939.

(20) Suzuki, A.; Miyaura, N. Palladium-Catalyzed Cross-Coupling Reactions of Organoboron Compounds. **2001**, 1–27.

(21) Marcano, D. C. D.; Kosynkin, D. D. V.; Berlin, J. M. J.; Sinitskii, A.; Sun, Z.; Slesarev, A.; Alemany, L. B.; Lu, W.; Tour, J. M. Improved Synthesis of Graphene Oxide. *ACS Nano* **2010**, *4* (8), 4806–4814.

(22) Movahed, S. K.; Dabiri, M.; Bazgir, A. Palladium Nanoparticle Decorated High Nitrogen-Doped Graphene with High Catalytic Activity for Suzuki–Miyaura and Ullmann-Type Coupling Reactions in Aqueous Media. *App. Cat. A* **2014**, *488*, 265–274.

(23) Brant, P.; Benner, L. S.; Balch, A. L. X-Ray Photoelectron Spectra of Binuclear Palladium-Palladium-Bonded Complexes and Their Insertion Products. *Inorg. Chem.* **1979**, *18* (12), 3422–3427.

(24) Venkatesan, R.; Prechtl, M. H. G.; Scholten, J. D.; Pezzi, R. P.; Machado, G.; Dupont, J. Palladium Nanoparticle Catalysts in Ionic Liquids: Synthesis, Characterisation and Selective Partial Hydrogenation of Alkynes to Z-Alkenes. *J. Mater. Chem.* **2011**, *21*, 3030–3036.

(25) I. Aruna; B. R. Mehta; L. K. Malhotra; Shivaprasad, S. M. Size Dependence of Core and Valence Binding Energies in Pd Nanoparticles: Interplay of Quantum Confinement and Coordination Reduction. *J. App. Phys.* **2008**, *104*.

(26) Orzali, T.; Agnoli, S.; Sambi, M.; Granozzi, G. Reactive Deposition of NiO Ultrathin Films on Pd (100). *Surf. Sci.* **2004**, *569* (1–3), 105–117.

(27) Xiong, Y.; Chen, J.; Wiley, B.; Xia, Y.; Yin, Y.; Li, Z.-Y. Size-Dependence of Surface Plasmon Resonance and Oxidation for Pd Nanocubes Synthesized via a Seed Etching Process. *Nano Lett.* **2005**, *5* (7), 1237–1242.

(28) Avrami, M. Kinetics of Phase Change. I General Theory. *J. Chem. Phys.* **1939**, *7*, 1103–1112.

(29) Wang, C. M.; Heller, A.; Gerischer, H. Palladium Catalysis of O_2 Reduction by Electrons Accumulated on TiO_2 Particles during Photoassisted Oxidation of Organic Compounds. *J. Am. Chem. Soc.* **1992**, *114* (13), 5230–5234.

(30) Goncalves, G.; Marques, P. A. A. P.; Granadeiro, C. M.; Nogueira, H. I. S.; Singh, M. K.; Grácio, J. Surface Modification of Graphene Nanosheets with Gold Nanoparticles: The Role of Oxygen Moieties at Graphene Surface on Gold Nucleation and Growth. *Chem. Mater.* **2009**, *21* (20), 4796–4802.

(31) Gerber, R.; Blacque, O.; Frech, C. M. Suzuki Cross-Coupling Reactions Catalyzed by an Aliphatic Phosphine-Based Pincer Complex of Palladium: Evidence for a Molecular Mechanism. *ChemCatChem* **2009**, *1* (3), 393–400.

(32) Li, Y.; Boone, E.; El-Sayed, M. A. Size Effects of PVP−Pd Nanoparticles on the Catalytic Suzuki Reactions in Aqueous Solution. *Langmuir* **2002**, *18*, 4921–4925.

(33) Zhang, W.; Chen, C. H.-T.; Lu, Y.; Nagashima, T. A Highly Efficient Microwave-Assisted Suzuki Coupling Reaction of Aryl Perfluorooctylsulfonates with Boronic Acids. *Org. Lett.* **2004**, *6*, 1473–1476.

(34) LeBlond, C. R.; Andrews, A. T.; Sun, Y.; Sowa, J. R. Activation of Aryl Chlorides for Suzuki Cross-Coupling by Ligandless, Heterogeneous Palladium. *Org. Lett.* **2001**, *3*, 1555–1557.

(35) Sakurai, H.; Tsunoyama, H.; Tsukuda, T. Oxidative Homo-Coupling of Potassium Aryltrifluoroborates Catalyzed by Gold Nanocluster under Aerobic Conditions. *J. Organomet. Chem* **2011**, *692* (1–3), 368–374.

Chapter Seven:

Conclusions

7.1 Conclusions

In this Ph.D. project, we have investigated different strategies to develop catalysts and electrocatalysts based on 2D Materials to be used in the fields of *Green Energy* and *Green Chemistry.* On one hand, TMDCs-based electrocatalysts represent green electrocatalysts for hydrogen generation, exploiting different strategies to tailor innovative material properties for the final application. On the other hand, the *Green Chemistry* approach was followed to prepare heterogenized catalysts on graphene-based scaffolds. This goal was reached by taking advantage of the uniform surface functionalization of GA. As a whole this approach proved that the design of the scaffold is essential to obtain highly performing catalysts.

The common points between all the addressed catalysts are two:

- the use of state-of-the-art 2D materials, to exploit their intrinsic innovative properties;
- the approach which is associated to the fundamental role that is played by materials design, and the great impact that a rationally driven synthesis may have on the ultimate performances.

The chemical nature and the morphology of the catalysts have been deeply investigated together with their functional properties in order to establish rigorous structure-activity relationships. This fundamental knowledge represents the cornerstone for the development of novel materials to be applied in specific applications. To achieve these results, we have employed a large set of tools offered by Surface and Materials Science, exploring advanced synthesis methods and combining different characterization techniques.

In Chapter Two we investigated the design of three-dimensional MoS_2 structures doped with different Ni doses, in order to boost HER activity of MoS_2, especially aiming at optimizing it in alkaline electrolytes. The reason for such an issue is that, while alkaline environment is commonly used in electrolyzers, in such a condition the HER activity of MoS_2 is strongly hindered. We performed a detailed structural characterization followed by an extensive electrochemical characterization of the Ni 3D-MoS_2 materials, both in acidic and alkaline electrolytes, to find out a rational interpretation of the final performances and reaction kinetics. The main outcome was that sites induced by Ni on the MoS_2 edges are selectively active in alkaline electrolyte, by lowering the H_2O dissociation energy barrier. On the contrary, no beneficial effects were observed in acidic environment. On the other hand, Ni sites generated in MoS_2 basal plane were found to enhance more effectively HER in acid than in base.

In Chapter Three, we designed a procedure for preparing amorphous MoS_2/Ag_2S hybrid using recycled DVD as an easy&cheap support; converting an abundant waste into an added-value material. Interesting values in HER activity (i.e. 198 mV as overpotential at 10 mA/cm^2 and 41 mV/dec as Tafel slope) were found, confirming that effective and cheap electrocatalyst can be prepared through our procedure. Moreover, thanks to the presence of n-p junctions, an extra 10% performance enhancement under visible light irradiation was observed.

In Chapter Four, we optimized a one-pot hydrothermal synthesis for growing $MoS_{2(1-x)}Se_{2x}$ nanosheets on N-rGO. The Se:S ratio was evaluated through a combination of spectroscopic methods. The materials that we obtained were found to be amorphous due to low temperature process. Therefore strategy took two different routes: i) the as-produced materials were tested for HER in acidic environment, and ii) crystalline

materials, obtained by annealing the amorphous ones at 600 °C, were designed for testing photoinduced HER. HER activity and kinetics of all the produced samples was firstly investigated in dark, revealing that, in the case of amorphous samples, the introduction of Se had no beneficial effects, since amorphous MoS_2/N-rGO was the best performing material. On the other hand, after annealing the intrinsic defectivity of Se-containing samples completely reverted the trend: photoinduced HER measurements revealed that intermediate values of Se:S ratio allow to reach both the best performances in dark and the best light-induced enhancement.

In Chapter Five, we investigated the catalytic properties of ferrocene (Fc) after its grafting to GA and GO. The resulting Fc-modified graphene derivatives were tested as heterogeneous catalysts for the C-H insertion of aryl diazonium salts in some arene substrates. The catalytic activity and kinetics were monitored *via* NMR, resulting not only in a successful heterogenization of Fc but also in a higher performance of GA as scaffold with respect to GO. The tests performed on different substrates (naphthalene, anthracene and pyrene) revealed higher conversions for substrates with higher number of condensed rings and we could attribute the higher activity of the GA-Fc catalyst to a better interaction with the substrate, as a result of the more uniform distribution of surface functional moieties compared to GO-Fc. The heterogenized catalysts revealed fully recyclable after several reiterations of the whole process

In Chapter Six, we have grown Pd nanoparticles on GA to prepare a catalyst for Suzuki-Miyaura cross coupling reaction. We could prove the importance of scaffold surface chemistry in the nanoparticles formation by testing several amounts of Pd precursor (25%, 50%, 100% and 200%at. vs –COOH moieties), resulting in narrow size distributions and highlighting the role of surface carboxylic acids as nucleation sites. Regarding the catalytic activity, we found that our GA-Pd systems were able to perform selectively and in green conditions both Suzuki-Miyaura and boronic acid homocoupling reactions by a simple control of the reagents involved. Moreover, the ability of producing narrow particles distributions allowed to highlight the size-dependent behaviour of these reactions.

Making an *excursus* through the different case studies, it is once more confirmed the importance of materials design to tailor and improve the final performances. The investigation of the structure-activity relationships, based on detailed structural and functional characterization stages, revealed quite essential to reach the goal.

Moreover, our work underlined the strong potentiality of 2D-Materials in this field. The final catalysts, even if based only on two types of 2D materials (GA and TMDCs) have shown a remarkable versatility. Therefore, it is clear that investing in the research on these materials could allow to acquire the necessary knowledge to develop materials for multiple purposes, which would be a key step for transferring 2D-Materials from the labs to real life.

List of acronyms and abbreviations

2D	Two Dimensional
3D	Three Dimensional
3DG	3D Graphene Architectures
3D-MoS_2	3D-structured MoS_2
ATM	Ammonium Tetrathiomolybdate
BDT	Benzenediazonium Tetrafluoroborate
BE	Binding Energy
CB	Conduction Band
C_{DL}	Double-layer capacitance
CMG	Chemical Modified Graphene
CRR	CO_2 Reduction Reaction
CV	Cyclic Voltammetry
CVD	Chemical Vapour Deposition
DCC	Dicyclohexylcarbodiimide
DMDSe	Dimethyl Diselenide
DMF	N,N-dimethylformamide
DVD	Digital Versatile Disc
EDX	Energy Dispersive X-Ray Analysis
E_F	Fermi Level
EIS	Electrochemical Impedance Spectroscopy
FC	Fuel Cell
Fc	Ferrocene
FET	Field Effect Transistor
GA	Graphene Acid
g-C_3N_4	Graphitic Carbon Nitride
G-CN	Cyanographene
GO	Graphene Oxide
GRM	Graphene-Related Material
h-BN	Hexagonal Boron Nitride
HER	Hydrogen Evolution Reaction
HOBt	Hydroxybenzotriazole
HOR	Hydrogen Oxidation Reaction
ICP-MS	Inductively Coupled Plasma Mass Spectrometry
IEA	International Energy Agency
IPCE	Incident Photons to Current Efficiency
LED	Light Emitting Diode
MS	Mott-Schottky
NEt_4BF_4	Tetraethylammonium Tetrafluoroborate

NIR	Near Infrared
NMP	N-methylpyrrolidone
NMR	Nuclear Magnetic Resonance
NP	Nanoparticle
N-rGO	Nitrogen doped reduced Graphene Oxide
OER	Oxygen Evolution Reaction
ORR	Oxygen Reduction Reaction
PDA	Propylene Diamine
PEC	Photoelectrochemical
PGM	Platinum Group Metals
rGO	Reduced Graphene Oxide
RHE	Reversible Hydrogen Electrode
SCE	Standard Calomel Electrode
SEM	Scanning Electron Microscopy
TEM	Transmission Electron Microscopy
TMDC	Transition Metal Dichalcogenide
TOF	Turnover Frequency
TON	Turnover Number
UHV	Ultra-High Vacuum
UV-Vis	UV-Visible Absorption Spectroscopy
VB	Valence Band
WEO	World Energy Outlook
WLED	White light LED
WS	Water Splitting
XPS	X-Ray Photoemission Spectroscopy
XRD	X-Ray Diffraction Analysis
$\eta_{10mA/cm2}$	Overpotential at 10 mA/cm^2

List of Publications (published, submitted and in preparation)

Updated September 2018:

1. G. Marafon, D. Mosconi, D. Mazzier, B. Biondi, M. De Zotti, A. Moretto; *RSC Adv.* **2016**, 6, 73650;
2. A. Privitera, M. Righetto, D. Mosconi, F. Lorandi, A. A. Isse, A. Moretto, R. Bozio, C. Ferrante, L. Franco; *Phys. Chem. Chem. Phys.* **2016**, 18, 31286;
3. D. Mazzier, D. Mosconi, G. Marafon, A. Reheman, C. Toniolo, A. Moretto; *J. Pept. Sci.* **2016**, 23, 155;
4. M. Righetto, A. Privitera, I. Fortunati, D. Mosconi, M. Zerbetto, M. L. Curri, M. Corricelli, A. Moretto, S. Agnoli, L. Franco, R. Bozio, C. Ferrante; *J. Phys. Chem. Lett.* **2017**, 8, 2236;
5. T. Kosmala, D. Mosconi, G. Giallongo, G. A. Rizzi, G. Granozzi; *ACS Sustainable Chem. Eng.* **2018**, 6, 7818;
6. D. Garoli, D. Mosconi, E. Miele, N. Maccaferri, M. Ardini, G. Giovannini, M. Di Palo, S. Agnoli, F. De Angelis; *Nanoscale* **2018**, *10, 17105;*
7. G. Tuci, D. Mosconi, A. Rossin, L. Luconi, S. Agnoli, M. Righetto, C. Pham-Huu, H. Ba, S. Cicchi, G. Granozzi, G. Giambastiani; *Chem. Mater.* **2018**, *Accepted;*
8. D. Mosconi, A. Jacassi, P. Ponzellini, G. Giovaninni, N. Maccaferri, M. Di Palo, F. De Angelis, S. Agnoli, D. Garoli; *Sci. Rep.* **2018**, *Submitted;*
9. D. Mosconi, M. Blanco, T. Gatti, L. Calvillo, M. Otyepka, A. Bakandritsos, E. Menna, S. Agnoli, G. Granozzi; *Small* **2018**, *Submitted*;
10. D. Mosconi, P. Till, L. Calvillo, T. Kosmala, D. Garoli, A. Martucci, S. Agnoli, G. Granozzi; *Promotion of the hydrogen evolution kinetics by Ni-doping of 3D-structured MoS_2 in acid and alkaline media*; <u>*In preparation*</u>;
11. D. Mosconi, M. Blanco, D. Badocco, P. Pastore, M. Otyepka, A. Bakandritsos, C. Tubaro, W. Ren, S. Agnoli, G. Granozzi; *Homo- and cross-coupling palladium nanoparticles – graphene acid system as stable and recyclable bifunctional green catalyst*; <u>*In preparation*</u>;
12. D. Mosconi, T. Kosmala, S. Agnoli, G. Granozzi; *One-pot solvothermal synthesis of hierarchical $MoS_{2(1-x)}Se_{2x}$/N-rGO hybrids for photoenhanced HER*; <u>*In preparation*</u>.

Acknowledgements

Alla fine ce l'abbiamo fatta, dopo tre anni che sarebbe riduttivo definire movimentati, anche il dottorato è finito. È stata una faticaccia, però alla fine l'obiettivo è raggiunto: tra poco potrò firmarmi ufficialmente come Dr. Mosconi e NESSUNO potrà impedirmelo.

Data la mia naturale tendenza a disturbare le persone, quelle da ringraziare sono davvero tante, sicuramente ne mancherà qualcuna, ma spero di averla ringraziata al momento, che alla fine è quello che conta. Comincio con il ringraziare la mia famiglia, che mi ha permesso di studiare e di arrivare a questo traguardo con la consapevolezza di averli alle spalle a sostenermi, il che dà una tranquillità che non tutti hanno la fortuna di avere. A mia sorella Ilaria, l' "altra" Dr.ssa Mosconi, ribadisco il ringraziamento per avermi indirizzato alla via della ricerca (qualche anno fa ormai, ma conta uguale) e il fatto che penso ancora che io sia più bravo e più bello. Non volermene.

Ringrazio il mio supervisore, il Prof. Gaetano Granozzi, per avermi accolto nel suo gruppo di ricerca nel momento accademicamente più difficile. Mi ha dato fiducia, mi ha aspettato, mi ha guidato, mi ha consigliato, mi ha strigliato e in ognuno di questi frangenti ho imparato qualcosa di nuovo, che sono certo al 110% mi servirà nella ricerca e fuori. Senza di lui non so davvero come sarebbe finito questo dottorato, mentre ora mi trovo a scrivere i ringraziamenti di una tesi perlomeno dignitosa, nonostante la mancanza di un anno di esperimenti. Grazie.

Ringrazio il Prof. Stefano Agnoli, una delle persone più brillanti che abbia mai conosciuto e che, possedendo in aggiunta una disumana conoscenza della Scienza dei Materiali, è facile immaginare quanto sia stato importante per me in questi due anni e in generale per tutto il nostro gruppo. Grazie inoltre a Laura, che avuto la pazienza di farmi un corso accelerato di "Scrittura articoli for Dummies" e non si è mai risparmiata nel dare consigli. Grazie al Prof. Rizzi sia per avermi coinvolto nel progetto sul DVD sia, anche lui, per avermi sempre consigliato col sorriso. Un discorso a parte lo merita Francesco con cui, insieme anche a Marcello, Alberto ed Andrea, abbiamo cominciato la nostra vita di sofferenze da Scienziati di Materiali, prima da studenti universitari e poi da giovani ricercatori. Ci sarebbe dovuto essere stato anche Enrico, che il suo dottorato non ha potuto finirlo per una tragica fatalità, una distrazione di un attimo. Spero che il mio grazie ti arrivi lassù o dovunque tu sia. Infine un ringraziamento in generale a tutte le persone del gruppo di *Surface Science and Catalysis*: tutti, chi più chi meno, mi hanno dato qualcosa in questi due anni. CIAO PANJUAN!!

I would like to address a special thanks to Tomasz and Matias, who have been friends before than colleagues. I shared great moments with them, both at University and outside as well. Because "2 macchiati e un lungo" and "2 Campari-Cynar e uno spritz Aperol" is a way of life. And yes, Tomasz, this is the only part in English in the whole acknowledgments paragraph because you have still to learn Italian after two geological eras. Shame on you.

Ringrazio tutti i miei amici al di fuori dell'Università, che essendo al di fuori dell'Università vedo una volta ogni tre secoli (noi Scienziati dei Materiali stiamo MOLTO all'Università), ma che so che bene o male ci sono.

Dulcis in fundo (un quasi Dr. deve sapersi esprimere in un certo modo), un ringraziamento per lei, Anna. Sei la mia persona,[1] ormai sono quasi 10 anni che mi sopporti, 2 che viviamo insieme nella nostra casa e ne abbiamo passate davvero di ogni in questa parte delle nostre vite. Sarei già contento di me stesso avessi fatto per te metà di quelle che tu hai fatto per me. Tu ti sei beccata il mio peggio, i miei scleri, le mie giornate con la testa ancora in laboratorio e quelle in cui ero troppo stanco anche per sollevare il telecomando (ma non la birra). Il tutto in dosi molto più alte di tutte le altre persone, eppure sei ancora qui a incitarmi, a supportarmi ad ogni minima esitazione e a farmi credere di essere molto meglio di quanto non sia probabilmente nella realtà. Questo lavoro e questo traguardo sono anche un po' tuoi, senza te sono sicuro non sarebbe andata altrettanto bene e non basterebbe un altro capitolo di questa tesi per ringraziarti di tutto quello che hai fatto.

(1) Yang, C.; Grey, M. Grey's Anatomy. *Am. Broadcast. Co. Season 5*, Episode 2.